

**Production and Analysis of Alloy
Composites Exhibiting Improved Bonding
Using a Novel Vacuum Casting Process**

**A thesis submitted in fulfilment of
the requirements of the degree of
Doctor of Philosophy**

by

**Paul Huggett
MSc, BAppSc(Hons)(Mat)**

Faculty of Science



University of Technology, Sydney

***In memory of my daughter
Lisa Michelle Huggett***

ABSTRACT

A new composite manufacturing process has been developed that permits the production of white iron/steel composites. The key differences of the new vacuum casting process compared to other current processes for composite manufacture include:

- i. Elimination of machining or grinding
- ii. Removal of brazing alloy
- iii. Enhanced design flexibility
- iv. Enhanced control of microstructural features
- v. Lower cost of production

The new vacuum casting process involves the following key steps:

- Heating a white cast iron and steel substrate together within a vacuum furnace until the temperature inside the vacuum furnace is typically 50°C above the liquidus of the white cast iron.
- Before the white cast iron becomes molten, adding a partial pressure of inert gas (typically nitrogen) into the vacuum furnace to increase the pressure of the chamber above the vapour pressure of the liquid white cast iron.
- Holding the temperature above the liquidus of the white cast iron to allow the white iron to partially dissolve the steel substrate.

The experimental work outlined in this research has permitted the development of a low melting point white cast iron having the nominal composition of Fe-12Cr-1.6Mn-1.0Ni-0.5Si-4.1C, with a measured liquidus temperature of 1209°C. The microstructure of the low melting point alloy consists of a small volume fraction of primary austenite, with a eutectic of M_7C_3 carbides and austenite. Some of the M_7C_3 carbides have undergone a quasi-peritectic reaction. The austenite has undergone a partial transformation to form ledeburite (ferrite plus M_3C carbide in the form of cementite).

The microstructures of the vacuum cast samples show the presence of four zones within the interface region.

- i. Zone 1 – original steel substrate, consisting of hypoeutectoid steel
- ii. Zone 2 – heat affected zone steel substrate
- iii. Zone 3 – “carbide-free” area of low melting point white cast iron adjacent to interface
- iv. Zone 4 – low melting point white cast iron

Manufacturing and field trials have been conducted on a range of composite products to establish the potential benefit of using composite white iron/steel components in mining wear applications. The vacuum casting process has been used successfully to produce a significant volume of trial wear parts, indicating the process is robust enough to be considered for repetitive production, and can also be adapted to manufacture a wide range of products.

DECLARATION OF ORIGINALITY

I certify that this thesis has not been submitted previously for any degree and is not being submitted as part of candidature for any degree. The research work presented was performed under the guidance of Associate Professor Besim Ben-Nissan and Dr Greg Heness of the Department of Chemistry, Materials and Forensic Science (UTS). I certify that I have written the thesis and that help that I have received in its preparation, and all sources used, have been duly acknowledged.

Production Note:

Signature removed prior to publication.

Paul Huggett

ACKNOWLEDGMENTS

I would like to express my sincere gratitude to my supervisor and mentor Associate Professor Besim Ben-Nissan for his patience, guidance, and understanding throughout this research and in particular during the period of grieving after the loss of my daughter Lisa to cancer in 2003.

I would also like to thank my co-supervisor and friend Dr Greg Heness for his support and guidance.

Special thanks is also extended to Dr Richard Wuhrer for his support and assistance with the electron microscopy and microanalysis, some of which has involved many sessions of after-hours of work.

The following people have provided assistance with various aspects of the research project:

- Dr Ron Wise and Lynton McCreery from Cape Range Wireless Ltd who assisted with project funding.
- Stan Jones for providing labour and assistance during foundry trials and alloy production.
- The staff at the AMTC Central TAFE, Subiaco Campus for the provision of foundry facilities.

Finally, I extend my sincere thanks, love and appreciation to my wife Carolyn who has not only endured her own loss and personal grieving during the course of this study, but has also provided inspiration, patience and focus when at times I was unable to see my way forward.

TABLE OF CONTENTS

Abstract	iii
Declaration of Originality	v
Acknowledgements	vi
Table of Contents	vii
List of Figures	xi
List of Tables	xxiv
Nomenclature	xxvi
Outline of Thesis	xxvii
Publications Arising from Thesis Work	xxviii
CHAPTER 1	3
CHAPTER 2	6
2.1 White Cast Iron Metallurgy	7
2.2 Classification of cast Irons	7
2.3 White Iron Microstructure	8
2.3.1 Hypoeutectic White Iron	8
2.3.2 Eutectic White Irons	9
2.3.3 Hypereutectic White Irons	11
2.4 Effect of Alloying Elements	13
2.5 Wear Characteristics of White Cast Irons	14
2.5.1 Abrasion	18
2.5.2 Adhesion	20
2.5.3 Erosion	22
2.5.4 Wear of White Irons	24
2.5.5 Effect of Mechanical Properties	24
2.5.6 Strain Accommodation	27
2.5.7 Microstructure	28
2.6 Iron-Chromium-Carbon Phase Diagram	34
2.7 Determination of Predicted Alloy Microconstituent Compositions	46

2.8	Experimental Development of Low Melting Point Alloy	51
2.9	Results and Discussion	54
2.9.1	Metallography	55
2.9.2	Thermal Analysis	58
2.9.3	Electron Microscopy and Microanalysis of Low Melting Point Alloy (C1)	70
2.10	Summary and Outcomes	75
CHAPTER 3		77
3.1	Introduction	77
3.2	Existing Processes	78
3.2.1	Vacuum Brazing	78
3.2.2	Factors Effecting the Performance of the Composite Bond	85
3.2.3	Typical Microstructures of Vacuum Brazed Joints	86
3.2.4	Examples of Finished Products	88
3.2.5	CSIRO Cast-Bond Process	90
3.3	Theory of Vacuum Casting	92
3.3.1	General Description of Vacuum Furnaces	93
3.4	Design and Construction of a Vacuum Tube Furnace	98
3.5	Design and Construction of a Hot Walled Vacuum Furnace	103
3.5.1	General Description of Furnace	103
3.6	Experimental	111
3.6.1	Vacuum Tube Furnace Trials	111
3.6.2	Hot Walled Vacuum Furnace Trials	116
3.7	Results and Discussion	121
3.7.1	Visual Analysis of Tube Furnace Samples	122
3.7.2	Optical Microscopy	127
3.7.3	Microhardness Profiles of Interface Region	131
3.7.4	Description of Vacuum Casting Process	137
3.8	Summary of Outcomes	142

CHAPTER 4		145
4.1	Introduction	145
4.2	Optical Microscopy of Interface Region	146
4.3	Electron Microscopy Analysis of Interface	150
4.3.1	Scanning Electron Microscope (SEM) Imaging	151
4.3.2	Electron Microscope Energy Dispersive Spectroscopy (EDS) Analysis	157
4.3.3	SEM X-Ray Mapping	163
4.3.4	SEM Electron Backscattered Diffraction (EBSD) Mapping	193
4.4	Diffusion of Elements Across Interface	211
4.5	Summary and Outcomes	222
CHAPTER 5		224
5.1	Performance of Existing Materials in Mining Applications	225
5.2	Manufacture of Prototype Parts	236
5.2.1	Manufacture of Full White iron Excavator Bucket Tooth	237
5.2.2	Manufacture of Laminated White Iron/Steel Bucket Tooth	238
5.2.3	Manufacture of Dredge Small Bucket Teeth	242
5.2.4	Manufacture of Wider Composite Dredge Bucket Tooth	250
5.2.5	Manufacture of Dredge Wide Bucket Lip	255
5.2.6	Manufacture of Excavator Bucket Tooth Tip	264
5.2.7	Manufacture of Wear Bars	266
5.2.8	Manufacture of Debonding (Tensile) Test Sample	269
5.3	Laboratory Wear Testing	272
5.4	Debonding (Tensile) Testing	272
5.5	Composite White Iron/Steel Material Data Sheet	274
5.6	Field Trials	275
5.6.1	Field Trial of Full White Iron Bucket Teeth on	275

	Excavator	
5.6.2	Field Trial of Laminated Bucket Teeth on Excavator	276
5.6.3	Field Trial of Bucket Teeth in Dredging Applications	278
5.7	Results and Discussion	281
5.7.1	Laboratory Wear Testing	281
5.7.2	Summary Full Scale Field Trials	283
5.8	Summary of Outcomes	287
CHAPTER 6		289
7	Future Work	292
8	References	293
9	Appendices	299

LIST OF FIGURES

Figure	Page
Figure 2.1: Hypoeutectic white iron microstructure.	9
Figure 2.2: Eutectic white iron microstructure.	10
Figure 2.3: Eutectic carbide rods (after deep etching)	11
Figure 2.4: Typical hypereutectic white iron microstructure.	12
Figure 2.5: Abrasive wear.	18
Figure 2.6: Four modes of abrasion	19
Figure 2.7: Adhesive wear	21
Figure 2.8: Erosive wear modes	23
Figure 2.9: Effect of alloy steel hardness on overall wear resistance	26
Figure 2.10: Relationship between wear resistance, hardness and fracture toughness	26
Figure 2.11: Effect of carbide volume fraction on wear of alloy white irons	29
Figure 2.12: Relationship between primary carbide volume fraction and abrasive wear rate for hypereutectic white irons	29
Figure 2.13: Abrasive wear as a function of the ratio of hardness of particle to the hardness of the material	32
Figure 2.14: Liquidus projection for the Fe-Cr-C system	35
Figure 2.15: Summary of reaction sequences for the Fe-Cr-C system	36
Figure 2.16: Fe-Si-Cr-C liquidus projection for 0.5 wt% Si after Schon and Sinatora	37
Figure 2.17: Calculated phase diagram for the Fe-30Cr-C alloy series	40
Figure 2.18: Calculated phase diagram for the Fe-10Cr-C alloy series	41
Figure 2.19: Calculated phase diagram for Fe-12Cr-C alloy series	42
Figure 2.20: Compositional end points for Fe-12Cr-C phase diagram	43
Figure 2.21: Calculated phase diagram for the Fe-12Cr-1.0Ni-0.6Si-1.6Mn-C alloy series	44
Figure 2.22: Calculated phase diagram from FACTSAGE for the Fe-12Cr-1.0Ni-0.6Si-1.6Mn-4C alloy	45
Figure 2.23: Relationship between eutectic carbide chromium	49

content and the alloy chromium/carbon ratio	
Figure 2.24: Schematic diagram for thermal analysis setup.	53
Figure 2.25: Relationship of trial alloy compositions to Fe-Cr-C phase diagram (by Thorpe and Chico)	54
Figure 2.26: Typical microstructure for the Fe-12Cr-1.6Mn-1.0Ni-0.5Si-4.1C (Alloy C1) low melting point white cast iron (etched in acid-ferric chloride)	56
Figure 2.27: Image analysis threshold selection of carbides to determine carbide volume fraction (CVF).	57
Figure 2.28: Thermal analysis cooling curve for Fe-8.0Cr-2.0Mn-0.5Si-3.4C alloy	59
Figure 2.29: Thermal analysis cooling curve for Fe-8.0Cr-2.0Mn-0.5Si-3.6C alloy	60
Figure 2.30: Thermal analysis cooling curve for Fe-8.0Cr-2.0Mn-0.5Si-3.9C alloy	61
Figure 2.31: Thermal analysis cooling curve for Fe-8.0Cr-2.0Mn-0.5Si-4.2 alloy	62
Figure 2.32: Thermal analysis cooling curve for Fe-10.0Cr-2.0Mn-0.7Si-3.3C alloy	63
Figure 2.33: Thermal analysis cooling curve for Fe-10.0Cr-2.0Mn-0.7Si-3.6C alloy	64
Figure 2.34: Thermal analysis cooling curve for Fe-10.0Cr-2.0Mn-0.7Si-4.1C alloy	65
Figure 2.35: Thermal analysis cooling curve for Fe-12.0Cr-1.6Mn-1.0Ni-0.5Si-4.1C alloy	66
Figure 2.36: Phase diagram based on experimental data for Fe-8Cr-2Mn-0.5Si-C alloy series with published data from Thorpe and Chico	67
Figure 2.37: Phase diagram based on experimental data for Fe-10Cr-2Mn-0.5Si-C alloy series with published data from Thorpe and Chico	67
Figure 2.38: Comparison of experimental data for Fe-8Cr-2Mn-0.5Si-C alloy series with predicted data from Thermocalc	68
Figure 2.39: Comparison of experimental data for Fe-10Cr-2Mn-0.5Si-C alloy series with predicted data from Thermocalc	69
Figure 2.40: Low magnification secondary electron image of Alloy C1	72
Figure 2.41: Detail of Alloy C1	72
Figure 2.42: Zeiss in-lens image of Alloy C1	73

Figure 2.43: Zeiss in-lens detail image of Alloy C1	73
Figure 2.44: High magnification Zeiss in-lens image of carbides	74
Figure 3.1: Capillary action and surface wetting	80
Figure 3.2: Hot and cold wall vacuum furnace principles	81
Figure 3.3: Schematic diagram for the vacuum brazing process for steel and white cast iron	84
Figure 3.4: Steel/White iron composite (etchant: 5% HCl acid ferric chloride)	86
Figure 3.5: Close up detail of high carbon iron/copper interface (etchant: 5% HCl acid ferric chloride)	87
Figure 3.6: General Microstructure of 15/3 CrMo iron used for the parts (etchant: 5% HCl acid ferric chloride)	87
Figure 3.7: 75mm and 90mm buttons, 50mm x 50mm blocks of different lengths, 25mm x 25mm x 300mm bars, and other assorted sized blocks	88
Figure 3.8: 50mm x 50mm x 432mm Block, 240mm x 50mm and 240x40 "Chok" Blocks, 50x50 blocks and two skid pads	89
Figure 3.9: Various sizes of skid pads	89
Figure 3.10: Schematic of typical vacuum furnace system	95
Figure 3.11: Typical components of a horizontal vacuum furnace	97
Figure 3.12: Cross-sectioned view of vacuum transfer furnace	97
Figure 3.13: Design of ceramic vacuum tube for use in tube furnace	100
Figure 3.14: Schematic design of vacuum tube furnace	100
Figure 3.15: Vacuum tube furnace used for experimental development of the vacuum casting process	101
Figure 3.16: Vacuum tube furnace used for experimental development of the vacuum casting process	101
Figure 3.17: Typical heating curve for vacuum tube furnace	103
Figure 3.18: Schematic diagram of hot-wall vacuum furnace	106
Figure 3.19: Hot wall vacuum furnace	107
Figure 3.20: Hot wall vacuum furnace with front door open	107
Figure 3.21: Internal view of heating elements and hot zone of hot wall vacuum furnace	108
Figure 3.22: View of control panel for hot wall vacuum furnace	108
Figure 3.23: View of vacuum pump and isolation valves for hot	109

wall vacuum furnace	
Figure 3.24: Typical temperature profile for hot wall vacuum furnace	110
Figure 3.25: Prepared steel substrate after surface preparation and cleaning	112
Figure 3.26: Prepared white iron Alloy C1 charge and steel substrate	113
Figure 3.27: Typical bonded steel/white iron test sample after heat treatment in the vacuum tube furnace	115
Figure 3.28: Typical suction-cutter dredge head (shown in the raised position)	118
Figure 3.29: Typical mould arrangement for suction-cutter dredge bucket teeth	119
Figure 3.30: Typical original and worn steel bucket tooth used on the suction-cutter dredge.	120
Figure 3.31: Effect of soak duration on melting of white cast iron	122
Figure 3.32: Effect of nitrogen partial pressure on melting and bonding of white cast iron	123
Figure 3.33: Detail of edge bloating on the full vacuum tested composite sample	124
Figure 3.34: Excellent melting and bonding of the white iron to the steel substrate for a soak temperature of 1259°C, partial pressure of 200mbar and soak duration of 60 minutes.	125
Figure 3.35: Relationship between temperature above liquidus and required soak time to achieve a satisfactory bond	125
Figure 3.36: Macro images of sectioned samples with variations in partial pressure (soak temperature 1259°C, 60 minute soak duration)	126
Figure 3.37: Macro images of sectioned samples with variation in soak duration (soak temperature 1209°C, 200mbar partial pressure)	126
Figure 3.38: Optical micrograph of vacuum cast interface (etchant acid ferric chloride)	128
Figure 3.39: Detail of interface area (etchant acid ferric chloride)	129
Figure 3.40: Optical micrograph of vacuum cast interface (etchant acid ferric chloride). Note the continuation of the M_3C carbides in the white cast iron from the Fe_3C carbides in the steel.	129
Figure 3.41: Location of microstructural zones on vacuum cast interface	130
Figure 3.42: Detail of carbide-free zone in interface area (etchant	131

	acid ferric chloride)	
Figure 3.43:	Typical microhardness profile for vacuum cast white iron/steel composite (+65°C above Liquidus, 60 minute soak, 200mbar partial pressure)	132
Figure 3.44:	Microhardness profile for vacuum cast white iron/steel composite (+25°C above liquidus, zero soak, 200mbar partial pressure)	134
Figure 3.45:	Microhardness profile for vacuum cast white iron/steel composite (+zero °C above liquidus, zero soak, 200mbar partial pressure)	135
Figure 3.46:	Microhardness profile for vacuum cast white iron/steel composite (+25 °C above liquidus, 30 min soak, 200mbar partial pressure)	135
Figure 3.47:	Microhardness profile for heat treated vacuum cast white iron/steel composite at 1100°C for 10 minutes (Original +50 °C above liquidus, 30 min soak, 200mbar partial pressure)	136
Figure 3.48:	Microhardness profile for heat treated vacuum cast white iron/steel composite at 1100°C for 30 minutes (Original +50 °C above liquidus, 30 min soak, 200mbar partial pressure)	136
Figure 3.49:	Schematic diagram of solid/liquid interface during the vacuum casting process	138
Figure 3.50:	Vacuum casting process flow chart	140
Figure 3.51:	Schematic diagram of steel shell for white iron/steel composite	141
Figure 4.1:	Optical bright field image of vacuum cast interface.	147
Figure 4.2:	Optical bright field image detail of vacuum cast interface.	147
Figure 4.3:	Optical bright field image detail of vacuum cast interface.	148
Figure 4.4:	Optical bright field image detail of vacuum cast interface.	148
Figure 4.5:	Optical bright field image detail of vacuum cast interface. Four distinct zones within the alloy composite can be identified.	149
Figure 4.6:	SE image of vacuum cast interface (sample unetched).	151
Figure 4.7:	SE image of vacuum cast white cast iron region	152

	(sample unetched).	
Figure 4.8:	SE image detail of Zone 4 white cast iron, with carbide and ferrous matrix (sample etched in acid-ferric chloride 20 seconds)	153
Figure 4.9:	SE image of Zone 3 white cast iron which exhibits essentially a carbide-free region, with some M_3C carbide extending perpendicular to interface	153
Figure 4.10:	SE image detail of Zone 3, with M_3C carbide extending perpendicular to interface (sample etched in acid-ferric chloride 20 seconds)	154
Figure 4.11:	SE image of Zone 2 near Zone 1, with regions of ferrite surrounded by pearlite (sample etched in acid-ferric chloride 20 seconds)	155
Figure 4.12:	SE image detail of Figure 4.11 of Zone 2 near Zone 1, with regions of ferrite surrounded by pearlite (sample etched in acid-ferric chloride 20 seconds)	155
Figure 4.13:	UTS Jeol 35CF fitted with two EDS detectors and Moran Scientific XRM System	157
Figure 4.14:	EDS analysis for ferrous region in vacuum cast composite sample	159
Figure 4.15:	EDS analysis for eutectic carbide in vacuum cast white cast iron region (analysis region is shown in yellow).	160
Figure 4.16:	EDS analyses for vacuum cast sample interface for three ferrous zones	161
Figure 4.17:	Moran Scientific Jeol 733 microprobe with three EDS x-ray detectors and three WDS detectors	164
Figure 4.18:	Pseudo colour x-ray map for low chromium white cast iron	165
Figure 4.19:	Compositional map for iron rich phase in low chromium white cast iron. Yellow colouring represents location of iron rich phase.	166
Figure 4.20:	Compositional map for chromium rich carbides in low chromium white cast iron. Yellow colouring represents location of chromium rich phase.	167
Figure 4.21:	Compositional map for low chromium carbides in low chromium white cast iron. Yellow colouring represents location of low chromium carbides.	168
Figure 4.22:	Compositional map for manganese rich phase in low chromium white cast iron. Yellow colouring represents location of manganese rich phase.	169
Figure 4.23:	Composite colour x-ray map produced from overlay of selected compositional phase areas from Figures	170

4.19 to 4.22 for the low melting point alloy.	
Figure 4.24: Back scattered electron (BSE) image and x-ray maps for vacuum cast sample interface colour x-ray map for low chromium white cast iron	171
Figure 4.25: Back scattered electron (BSE) image and compositional scatter plots for vacuum cast composite interface region for chromium, iron and manganese.	172
Figure 4.26: Compositional map for iron rich phase in vacuum cast composite. Yellow colouring represents location of iron rich phase.	173
Figure 4.27: Compositional map for chromium/iron phase in vacuum cast composite. Yellow colouring represents location of chromium/iron phase.	174
Figure 4.28: Compositional map for low chromium carbide phase in vacuum cast composite. Yellow colouring represents location of low chromium carbide phase.	175
Figure 4.29: Compositional map for main chromium carbide phase in vacuum cast composite. Yellow colouring represents location of chromium carbide phase.	176
Figure 4.30: Compositional map for chromium depleted carbide phase in vacuum cast composite. Yellow colouring represents location of chromium depleted carbide phase.	177
Figure 4.31: Compositional map for second chromium/iron phase in vacuum cast composite. Yellow colouring represents location of second chromium/iron phase.	178
Figure 4.32: Compositional map for chromium rich matrix phase in vacuum cast composite. Yellow colouring represents location of chromium rich matrix phase.	179
Figure 4.33: Composite colour x-ray map produced from overlay of selected compositional phase areas for chromium, iron and manganese from Figures 4.26 to 4.32 for the steel/white iron interface area.	180
Figure 4.34: Back scattered electron (BSE) image and compositional scatter plots for vacuum cast composite interface region for chromium, iron and nickel.	181
Figure 4.35: Composite colour x-ray map produced from overlay of selected compositional phase areas for chromium, iron and nickel for the steel/white iron interface area.	182
Figure 4.36: Secondary electron (SE) image and x-ray maps for vacuum cast sample white cast iron carbides	183
Figure 4.37: Carbon x-ray map for vacuum cast white iron/steel	184

	interface performed on a Jeol 733 Microprobe SEM	
Figure 4.38:	Single line profile from x-ray map for carbon WDS scan	185
Figure 4.39:	Relationship between carbon x-ray counts and carbon weight percent for vacuum cast alloy sample from Figure 4.38.	186
Figure 4.40:	Carbon x-ray map for vacuum cast white iron/steel interface with x-ray line scan profile overlaid showing decrease in carbon content through a linear band parallel to the interface.	187
Figure 4.41:	BSE image of sample shown in carbon map in Figure 4.37 for vacuum cast white iron/steel interface with x-ray line scan profile overlaid.	188
Figure 4.42:	Single line profile from x-ray map for multi-element EDS scan.	189
Figure 4.43:	Relationship between chromium x-ray counts and chromium weight percent for vacuum cast alloy sample from Figure 4.42.	190
Figure 4.44:	Relationship between manganese x-ray counts and manganese weight percent for vacuum cast alloy sample from Figure 4.42.	191
Figure 4.45:	Relationship between nickel x-ray counts and nickel weight percent for vacuum cast alloy sample from Figure 4.42.	192
Figure 4.46:	Typical EBSD SEM arrangement [59].	194
Figure 4.47:	Location of EBSD map for vacuum cast composite bond produced at 1274°C for 60 minute soak.	195
Figure 4.48:	EBSD Map for vacuum cast composite bond produced at 1274°C for 60 minute soak for region shown in Figure 4.47	196
Figure 4.49:	EBSD Map for vacuum cast composite bond produced at 1274°C for 60 minute soak overlaid onto SE image from Figure 4.47	197
Figure 4.50:	Higher magnification image of EBSD sample produced at 1274°C for 60 minute soak	198
Figure 4.51:	Kichuchi patterns and indexing data for M ₃ C carbide found in sample shown in Figure 4.50	199
Figure 4.52:	Kichuchi patterns and indexing data for BCC ferrite found in white iron ferrous matrix shown in Figure 4.50	200
Figure 4.53:	Kichuchi patterns and indexing data for BCC ferrite found in the “carbide-free” zone shown in Figure 4.50	201
Figure 4.54:	Kichuchi patterns and indexing data for Fe ₃ C carbide	202

	found as pearlite in the sample shown in Figure 4.50	
Figure 4.55:	Correlation of Kichuchi patterns to vacuum cast interface based on Figure 4.50 and portion of EBSD map for selected region.	203
Figure 4.56:	SE image for “carbide-free” region of the sample produced at 1274°C for 60 minute soak at higher magnification compared to Figures 4.47 and 4.50.	204
Figure 4.57:	Overlay of EBSD data for BCC ferrite onto the SE image for “carbide-free” region of the sample produced at 1274°C for 60 minute soak based on Figure 4.56.	205
Figure 4.58:	Overlay of EBSD data for M ₃ C carbides onto the SE image for “carbide-free” region of the sample produced at 1274°C for 60 minute soak based on Figure 4.56.	205
Figure 4.59:	Overlay of complete EBSD map onto the SE image for “carbide-free” region of the sample produced at 1274°C for 60 minute soak based on Figure 4.56.	206
Figure 4.60:	Detail of EBSD map for “carbide-free” region of the sample produced at 1274°C for 60 minute soak based on Figure 4.56.	207
Figure 4.61:	EBSD map overlaid onto SE image for vacuum cast interface between white cast iron and steel substrate.	208
Figure 4.62:	Lower magnification EBSD map overlaid onto SE image for vacuum cast interface between white cast iron and steel substrate.	208
Figure 4.63:	Location of higher resolution EBSD map for eutectic carbides in the white cast iron (Zone 4) of the vacuum cast composite.	209
Figure 4.64:	EBSD map for eutectic carbides in the white cast iron (Zone 4) of the vacuum cast composite.	210
Figure 4.65:	Overlay of EBSD map onto SE image for eutectic carbides in the white cast iron (Zone 4) of the vacuum cast composite.	210
Figure 4.66:	Typical steel dissolution as a result of the contact with liquid white cast iron during the vacuum casting process.	213
Figure 4.67:	Comparison between microhardness and carbon content for diffusion away from the interface in the steel substrate for the vacuum cast white iron/steel composite produced at 1274°C with a 60 minute soak. (100g HV load used).	215
Figure 4.68:	Comparison between microhardness and carbon content for diffusion away from the interface in the	216

	steel substrate for the vacuum cast white iron/steel composite produced at 1209°C with a zero soak. (100g HV load used).	
Figure 4.69:	Comparison between measured and calculated carbon content in steel substrate adjacent to vacuum cast interface. Sample produced at 1274°C for 60 minute soak.	217
Figure 4.70:	Comparison between measured and calculated carbon content in steel substrate adjacent to vacuum cast interface. Sample produced at 1209°C for zero soak.	218
Figure 4.71:	Comparison between measured and calculated chromium content in steel substrate adjacent to vacuum cast interface. Sample produced at 1274°C for 60 minute soak.	219
Figure 4.72:	Comparison between measured and calculated nickel content in steel substrate adjacent to vacuum cast interface. Sample produced at 1274°C for 60 minute soak.	219
Figure 5.1:	Excavator application in open pit mining	228
Figure 5.2:	Typical bucket tooth installation on large mining excavator bucket	229
Figure 5.3:	Bucket teeth test position	230
Figure 5.5:	Geometry of the wear of excavator bucket teeth	231
Figure 5.6:	Effect of bucket tooth position on wear rate for bucket-wheel excavator trials	233
Figure 5.7:	Relationship of wear and impact levels for different mining applications	234
Figure 5.8:	Types of rock zones experienced in open pit mining operations	235
Figure 5.9:	Full white iron cast bucket tooth (equivalent to ESCO V66RDX tooth)	237
Figure 5.10:	Comparison of cast white iron and cast steel bucket teeth	238
Figure 5.11:	Machined V66RDX steel bucket tooth ready to vacuum braze white iron wear plate on front tip	239
Figure 5.12:	Multi-laminate bucket tooth tip.	240
Figure 5.13:	Finished vacuum brazed multi-laminated bucket tooth tip.	241
Figure 5.14:	New and worn original Cr/Mo steel dredge bucket teeth (ESCO V19TY)	243
Figure 5.15:	Steel moulds coated with refractory ceramic paint,	244

	with steel parts inserted and measured white iron charge positioned in side chutes.	
Figure 5.16:	Closer view of steel part positioned with steel plate, and white iron charge located in side chute	244
Figure 5.17:	Loading the hot walled vacuum furnace with trial composite white iron/steel parts in steel moulds	245
Figure 5.18:	Close up view of hot walled vacuum furnace showing arrangement of steel moulds on furnace tray prior to final placement	246
Figure 5.19:	View of multiple steel moulds for composite white iron/steel parts placed into hot walled vacuum furnace	246
Figure 5.20:	Several finished composite white iron/steel bucket teeth with original worn steel part (a) and painted composite part (b)	247
Figure 5.21:	Detail of finished composite tooth (a), painted composite tooth (b) and original worn Cr/Mo steel tooth (c)	248
Figure 5.22:	Detail view of comparison between worn original Cr/Mo steel bucket tooth (a) and new composite white iron/steel bucket tooth (b)	249
Figure 5.23:	View of steel mould with ceramic coating on inside surfaces to assist with stopping bonding of white iron to the steel mould	250
Figure 5.24:	View of steel mould with steel part positioned using retaining plate.	251
Figure 5.25:	Completed wider tip composite part after removal from the metal mould	252
Figure 5.26:	Side view of wider tip composite white iron/steel bucket tooth	252
Figure 5.27:	Original as-received steel part and new wide tip composite wear part	253
Figure 5.28:	Front view of original as-received steel part and new wide tip composite wear part	253
Figure 5.29:	Ceramic coated mould after removal of the finished composite part	254
Figure 5.30:	Worn steel dredge wide bucket lip	255
Figure 5.31:	Side view of worn steel dredge wide bucket lip	256
Figure 5.32:	Dual attachment cavities for wide bucket lip	256
Figure 5.33:	Wide bucket tooth lip part inserted into furnace ready to start the cycle	257
Figure 5.34:	View of mould, white iron charge and steel part	257

placed into position	
Figure 5.35: View of completed wide bucket lip still in the mould after casting	258
Figure 5.36: Detail view of completed wide bucket lip still in the mould after casting.	259
Figure 5.37: View of excellent wetting between the white iron and the steel	259
Figure 5.38: Side view of steel mould and composite part after removal from the furnace	260
Figure 5.39: Finished composite wide bucket lip after removal from the mould	260
Figure 5.40: View of the finished composite wide bucket tooth prior to final painting	261
Figure 5.41: End view of wide bucket lip showing excellent bonding around the complete part	262
Figure 5.42: First production trial part with a final mass of 9.02kg. Subsequent cycles were adjusted for a total composite mass of 9.40kg.	262
Figure 5.43: Comparison of sizes of wide bucket lip composite part to ESCO V19TY bucket teeth	263
Figure 5.44: Cast chromium/molybdenum steel bucket tooth tip with cavity to receive white iron	264
Figure 5.45: As-cast composite steel/white cast iron bucket tooth tip.	265
Figure 5.46: Hot “chok” bar mould with cast parts after removal at 1000°C from furnace	266
Figure 5.47: Finished composite white iron/steel “chok” bar after casting using vacuum based process	267
Figure 5.48: Detail view of excellent bonding between white cast iron and steel backing plate.	268
Figure 5.49: As-cast composite wear bar manufactured from “C” channel with welded end caps	268
Figure 5.50: Vacuum cast composite tensile test sample dimensions	269
Figure 5.51: End view of completed composite debonding test sample	270
Figure 5.52: Composite debonding test sample	271
Figure 5.53: Detail of bonding/interface between centre rod, white cast iron and outer shell of composite tensile test sample	271
Figure 5.54: Location of trial full white iron bucket teeth on	275

	Komatsu PC1000 excavator bucket	
Figure 5.55:	Location of trial single laminate white iron/steel bucket teeth on Komatsu PC1000 excavator bucket	276
Figure 5.56:	Location of trial multi-laminate white iron/steel bucket teeth on Hitachi EX1800 excavator bucket	277
Figure 5.57:	View of suction-cutter dredge head raised from the water for maintenance.	279
Figure 5.58:	Closer view of bucket arrangement on suction-cutter dredge head. Note wide bucket lip and smaller side bucket teeth.	279
Figure 5.59:	Vacuum cast small composite bucket teeth trialled at Cable Sands Mine, Capel, Western Australia (New composite on left)	280
Figure 5.60:	Relationship Between Carbon Content and Abrasive Wear Rate for Fe-12Cr-1.6Mn-1.0Ni-0.6Si-C Alloy Series (DSRW Test based on ASTM G65-04)	282
Figure 5.61:	Comparative wear rates for chromium/molybdenum steel and white cast iron in excavator application (Greenbushes Mine)	284
Figure 5.62:	Comparative wear rates for chromium/molybdenum steel and multi-layer vacuum brazed white cast iron in excavator application (Golden Feather Mine)	285
Figure 5.63:	Comparison of Volumetric Wear Rates for Cr/Mo Steel and Composite Alloy Parts (Cable Sands Jangardup Mine Site)	286

LIST OF TABLES

Table		Page
Table 2.1:	Typical liquidus temperatures for commercial white cast irons.	6
Table 2.2:	Classification of wear modes	16
Table 2.3:	Classification of wear processes by wear mechanisms.	17
Table 2.4:	Summary of factors which influence wear	17
Table 2.5:	Hardness of minerals and microconstituents	33
Table 2.6:	Summary of Invariant Reactions	34
Table 2.7:	Comparison of predicted and observed microstructures for high chromium white irons	38
Table 2.8:	Calculated lowest liquidus temperatures for the C-Cr-Fe-Mn-Mo system	39
Table 2.9:	Typical phase microanalysis results for hypoeutectic white iron	47
Table 2.10:	Typical phase microanalysis results for eutectic white iron	47
Table 2.11:	Typical phase microanalysis results for hypereutectic white iron	48
Table 2.12:	Phase elemental distributions (based on empirical data)	50
Table 2.13:	Estimated phase compositions for proposed	50
Table 2.14:	Summary of test alloy compositions	52
Table 2.15:	Summary of alloy microstructures	56
Table 2.16:	Measured thermal arrests for trial alloys	58
Table 2.17:	EDS analysis data for Alloy C1	74
Table 3.1:	Effect of furnace atmosphere on maximum element temperature [52]	102
Table 3.2:	Test sample matrix covering variations in temperature, time at soak and partial pressure of inert gas	115
Table 3.3:	Summary of Zone 2 and 3 depths based on microhardness data for vacuum cast samples	133
Table 3.4:	Effect of heat treatment on Zone 2 depth for vacuum cast composite	134
Table 4.1:	EDS phase analysis after carbon correction for ferrous phase zones shown in Figure 4.16 for	162

	vacuum cast sample.	
Table 4.2:	EDS phase analysis after carbon correction for vacuum cast sample.	162
Table 4.3:	Estimated carbon weight % based on carbon calibration curve shown in Figure 4.39 for positions on x-ray line scan shown in Figure 4.38.	186
Table 4.4:	Estimated chromium weight % based on chromium calibration curve shown in Figure 4.3 for positions on x-ray line scan shown in Figure 4.42.	190
Table 4.5:	Estimated manganese weight % based on manganese calibration curve shown in Figure 4.44 for positions on x-ray line scan shown in Figure 4.42.	191
Table 4.6:	Estimated nickel weight % based on nickel calibration curve shown in Figure 4.45 for positions on x-ray line scan shown in Figure 4.42.	192
Table 4.7:	Carbon Diffusion Coefficients in γ iron	213
Table 4.8:	Chromium Diffusion Coefficients in γ iron	214
Table 4.9:	Nickel diffusion coefficients in γ iron	214
Table 5.1:	Summary of materials used in mining applications	226
Table 5.2:	Relative wear rates for white cast irons used for liner plates	227
Table 5.3:	Abrasive wear rates for hardfacing alloys	229
Table 5.4:	Summary of wear part life for laboratory and mine based testing	230
Table 5.5:	Summary of pendulum groove test data	232
Table 5.6:	Debonding (Tensile) test results for composite white cast iron/steel	273
Table 5.7:	Dry Sand Rubber Wheel Wear Test Results (according to ASTM G65-04)	281
Table 5.8:	Summary of field trial data for full white iron and vacuum brazed wear parts, Greenbushes Mine	283
Table 5.9:	Summary of field trial data for full white iron and vacuum brazed wear parts, Golden Feather Mine	283
Table 5.10:	Summary of field trial data for composite wear parts in dredge application	285

NOMENCLATURE

$\phi(y)$	=	Gaussian Error Function
<i>Bulk C%</i>	=	overall carbon weight percent
C_0	=	concentration of semi-infinite solid
C_s	=	surface concentration
C_x	=	concentration of diffusing species
<i>C%</i>	=	carbon weight percent
<i>Cr%</i>	=	chromium weight percent
<i>Cr/C</i>	=	chromium/carbon ratio
D	=	diffusivity or diffusion coefficient
D_0	=	temperature independent pre-exponential, m^2/s
$\frac{dC}{dx}$	=	concentration gradient
<i>EC Cr%</i>	=	eutectic Carbide Chromium Content
<i>ECVF%</i>	=	eutectic carbide volume fraction %
<i>ETC%</i>	=	eutectic trough carbon %
<i>FM Cr%</i>	=	ferrous Matrix Chromium Content %
J_x	=	flux of diffusing species
<i>PC Cr%</i>	=	primary Carbide Chromium Content
<i>PCVF%</i>	=	primary carbide volume fraction %
<i>PFMVF%</i>	=	primary ferrous matrix volume fraction %
Q_d	=	activation energy for diffusion, J/mol
R	=	Gas constant, $8.314 \text{ J}\cdot\text{mol}^{-1}\cdot\text{K}^{-1}$
t	=	time, seconds
T	=	Temperature, Kelvin
x	=	distance, mm

OUTLINE OF THESIS

Chapter One provides background information and significance of this research work.

Chapter Two describes the development of a low melting point white cast iron. The low melting point white iron development involved analysis of the Fe-Cr-C phase diagram and computer modelling using CALPHAD techniques to result in a white cast iron having a liquidus (melting point) of approximately 1200°C. The low melting point white iron was essential to enable standard electrical element materials to be adopted for the vacuum heat treatment furnace development.

Chapter Three describes the development of the vacuum casting process, providing theory of vacuum heat treatment, background to other composite alloy manufacturing processes, and the experimental work and outcomes for the new vacuum based composite alloy manufacturing process.

Chapter Four provides a detailed analysis of the composite interface developed between a steel substrate and the low melting point white cast iron. The analysis of the interface is used to provide confirmation of the vacuum casting model developed in Chapter 3, and to demonstrate the quality and power of the vacuum process to develop 100% fully bonded metallurgical bonds.

Chapter Five provides detail on the development of trial parts for use in various mining applications. The trial parts involved the manufacture of full scale parts for use on heavy duty mining equipment. Laboratory wear test results are provided and compared to field trial performance.

Chapter Six outlines the conclusion of the thesis and summarises the project outcomes.

References have been listed in the sequence of their use within the main thesis text and then numerically numbered.

Publications Arising from Thesis Work

1. P.G. Huggett and B. Ben-Nissan, "Development of a low melting point white cast iron for use in composite alloy manufacture", Proceedings of the Materials and Austceram Conference, Sydney, Australia, July 2007
2. P.G. Huggett, R. Wuhrer, B. Ben-Nissan and K. Moran, "Composite alloy wear parts for use in the mining industry", Materials Forum, 2006, Volume 30, pp23-29.
3. D. J. Attard, R. Wuhrer P. G. Huggett and K. Moran, "Sample preparation of a novel titanium-aluminium composite", 19th Australian Conference on Microscopy and Microanalysis, Sydney, NSW February 2006.
4. D.J. Attard , R. Wuhrer, P.G. Huggett and K. Moran, " Sample preparation of a novel titanium-aluminium composite for EBSD analysis", Microscopy and Microanalysis, 2006, Vol 12(suppl 2), 1052CD-1053CD.
5. P.G. Huggett, R. Wuhrer, B. Ben-Nissan and K. Moran, "A novel metallurgical bonding process and microstructural analysis of ferrous alloy composites", Materials Forum, 2005, Volume 29, pp83-88.
6. R. Wuhrer, P. Huggett, K. Moran, M.R. Phillips and B. Ben-Nissan, "EBSD and XRM of phases in vacuum cast composite alloys", Microscopy and Microanalysis, 2005, Vol 11 (suppl 2), pp1678-1679.
7. R. Wuhrer, K. Moran, P. Huggett, M.R. Phillips, B. Ben-Nissan, X-ray mapping and EBSD of phases in welded steels, Microscopy and Microanalysis, 2004, Vol 10 (suppl 2), pp912-914.
8. P. Huggett, R. Wuhrer, B. Ben-Nissan and K. Moran, "A novel metallurgical bonding process and microstructural analysis of ferrous alloy composites", Proceedings of the 3rd International Conference on Advanced Materials Processing, Edited by J.F. Nie and M. Barnett, IMEA, 2004, pp 83-88.
9. R. Wuhrer, P. Huggett, M.R. Phillips, K. Moran and B. Ben-Nissan, "X-ray mapping and electron back-scattered diffraction of welded materials", 18th Australian Conference on Microscopy and Microanalysis, Geelong, Victoria, 2004.
10. R. Wuhrer, K. Moran, P. Huggett, M.R. Phillips, and B. Ben-Nissan, "X-ray Mapping and Electron Back Scattered Diffraction of Phases in Welded Materials", Proc. of Microscopy and Microanalysis 2004, Savannah USA, Eds E. Voelkl, D. Piston, R. Gauvin, A.J. Lockley, G.W. Bailey and S. Mckernan, Published by Cambridge University Press, Vol 8 Suppl 2, 446-447

CHAPTER 1

One of the original objectives of this research study was to develop and test a composite alloy ground engaging tool (GET) for use on large earthmoving equipment typically operating throughout Western Australian mine sites. The use of composite alloy wear parts and components is not new to mining in Western Australia, however due to current limitations in manufacturing methods with respect to size, shape and complexity of composite alloys, the adoption of composites has yet to be fully utilised.

Standard wear parts used for GET are typically manufactured as cast steel components. The grade of steel is nominally a chromium/molybdenum medium carbon steel which is then hardened and tempered to achieve a combination of high bulk hardness and moderate impact strength. Original equipment manufacturers and suppliers of current GET have adopted an approach of standardization of material grades to ease the control of inventory across the broad range of mining applications.

Western Australian mine sites are characterized by hard and abrasive rock structures that challenge the GET to their limits. On some mine sites, for example at Greenbushes, located in the south west of Western Australia, the rock structures consist of hard and abrasive spodumene which result in GET wear lives of less than 24 hours.

The original direction of this research study was to investigate the potential for white iron/steel composite wear parts to be developed for some of the applications where high abrasive wear existed, and a moderate level of toughness was required. Typical examples of target applications include bucket teeth for front end loaders, bucket teeth used on dredging components, and other high wear applications such as GET for reclaim stackers and ship loading equipment.

The use of white cast irons (or white irons) in high abrasive wear applications is well documented, and further discussion on this area will be developed in Section 2 of this study. White irons are susceptible to impact fracture due to their brittle nature and dominant microstructure of hard ceramic-like carbides.

The challenge of this study was to develop a composite manufacturing process that was able to permit complex shapes and large sizes to be produced, whilst optimizing the bond produced to provide both wear resistance and toughness. Utilizing knowledge and experience gained from vacuum brazing processes, a new process was conceptualized that would effectively permit cast composites to be produced. The nature of the proposed composite process initially required the use of vacuum heat treatment equipment, and hence was limited in temperatures to less than 1300°C. This temperature limit was largely due to the standard element materials used in vacuum furnaces.

Standard white iron grades such as AS2027-Cr27 alloy have a melting point close to 1290°C, and would not necessarily be suitable for the proposed process. Hence the first stage of this research study was to develop a lower melting point white iron, preferably with a target liquidus temperature of approximately 1200°C.

In order to effectively develop a lower melting point white iron, the metallurgy, phase diagrams and microstructural features of white cast irons must first be examined in detail. A discussion on the development of the low melting point white iron is included in Section 2.

The vacuum casting process developed in this project evolved from an understanding of a specific vacuum brazing techniques currently used to bond white cast iron onto mild steel backing plates. The vacuum brazing process requires a brazing alloy to be used, typically copper, which is placed between the two layers of material to be brazed. The components are then placed into a vacuum furnace and heated until the copper melts. As the copper melts, the liquid

copper alloys with the solid iron phases of the components, and growth of an intermediate copper/iron phase progresses until a full metallurgical bond is produced. Further discussion on the vacuum brazing process is included in Section 3 of this study.

Based on the observations made from the vacuum brazing process, a theory was developed that suggested if the brazing alloy was removed (the copper), and the temperature of the heat treatment process was increased until the white iron melted, then providing an oxygen free atmosphere was maintained the molten white iron would alloy with the solid steel surface.

The research investigation detailed in this study will cover the development of the new process from its original conception to the final prototype production and mining field trials. Sections in this study will cover the following main areas:

- Development of a low melting point white iron
- Vacuum brazing theory
- Development of the new vacuum casting process
- Analysis of the bond interface for the vacuum casting process
- Production of large scale prototypes
- Field trials and performance of large scale prototypes

A significant feature of this research project was the focus on developing the technology to a level where full scale field trials on actual mining equipment could be conducted. The project has also been funded largely through personal contributions and has necessitated the acquisition of various items of equipment outside the envelope of the University, and also the design and manufacture of specific equipment to enable the manufacturing process to be studied in a systematic and investigative manner.

Ultimately the key objective for this research study was to determine if a composite white iron/steel component would provide significant life cycle improvements compared to existing commercial products, and establish a base wear rate performance that can be used to justify further research and commercialization of the technology.

This research study has been written as four main chapters, which are effectively separate studies of their own, but combined to provide the overall development of the vacuum casting manufacturing process. Each key chapter has been written as a stand alone sub-project, with its own structure of introduction, background, experimental, results, discussion and conclusion.

Chapter Two provides the development of the low melting point white cast iron, an essential part of the thesis due to anticipated limitations with upper processing temperatures for vacuum heat treatment furnaces. The practical maximum operating temperature for most commercial vacuum heat treatment furnaces is approximately 1250 to 1300°C. However many commercial white cast irons have a melting point (liquidus temperature) near this limit, and it was anticipated that some degree of casting superheat would be required to provide sound and fully bonded composite castings.

To enable the development of the low melting point white iron, a study was undertaken of the Fe-Cr-C phase diagram, and particularly focussed on the relationship of lower eutectic liquidus temperatures with decreasing chromium and increasing carbon content of the alloy.

After the development and casting of feed stock ingots from the low melting point white cast iron, the next phase of the process development involved the systematic development of the vacuum casting process, as provided in **Chapter Three**. This chapter provides a full background to the key fundamentals of how the vacuum casting process was developed, the use of similar vacuum brazing heat treatment

processes to understand the main variables, and the design and manufacture of low cost vacuum heat treatment equipment to enable the bonding process to be fully developed for large scale composite parts.

Chapter Four provides a detailed analysis of the interface region between the steel substrates and the white cast iron for the composite alloys produced. Various analysis techniques have been used, including optical microscopy and microhardness, and electron microscopy techniques including energy dispersive spectroscopy (EDS) analysis, x-ray mapping (XRM), and electron beam backscattered diffraction (EBSD) analysis.

The analysis from Chapter Four enabled the fine tuning of the manufacturing process and provided essential information on the vacuum casting process model for the steel/white cast iron composite.

Finally in **Chapter Five**, the manufacture and testing of several laboratory and full scale wear parts is detailed to provide an initial demonstration of the power of the vacuum casting process to enable the manufacture of ultra wear resistant composites for use in the mining industry. The chapter provides information on the comparison of the composite wear parts against single material alternatives, and provides an initial reference source for further wear trials in this area.

CHAPTER 2

Before the development of a new vacuum heat treatment process for bonding steel to white cast iron could be started, it was necessary to consider the raw materials and in particular the melting point (or liquidus) of the white cast iron.

Common modern vacuum heat treatment furnaces typically have an upper temperature limit of 1200 to 1300°C. Commercial white cast irons normally have a liquidus temperature above 1290°C. Examples of commercial white cast iron liquidus temperatures are provided in Table 2.1.

In order to allow standard vacuum heat treatment equipment to be used for the development of the bonding process, it was therefore necessary to develop a lower melting point white cast iron, preferably with a liquidus temperature of around 1200°C.

Table 2.1: Typical liquidus temperatures for commercial white cast irons.

Alloy Designation[1]	Description	Liquidus Temperature (°C)
Cr 27	Eutectic High Chromium White Cast Iron	1296
CrMo 15 3	Hypoeutectic Chromium – Molybdenum White Cast Iron	1246
Cr 35	Hypereutectic High Chromium White Cast Iron	1440

The work covered within this section of the report outlines the metallurgy of white cast irons and then details the development of a lower melting point white cast iron. Additional information is provided on the categorisation of wear processes and the relationship between microstructure and wear for white cast irons.

2.1 WHITE CAST IRON METALLURGY

Cast irons are heterogeneous ferrous alloys, which solidify with a eutectic phase. They contain iron, carbon and silicon as the major alloying elements and often incorporate chromium, nickel, manganese, molybdenum, copper and other elements to enhance specific chemical and mechanical properties.

The basic iron-carbon (Fe-C) binary system allows two types of solidification paths to occur:

- i. as a thermodynamically metastable iron-cementite (Fe-Fe₃C) system ; or
- ii. a stable Fe-graphite system.

If the alloy solidifies under the Fe-Fe₃C system, the carbon rich phase is the iron carbide cementite, whilst in the Fe-graphite system, the carbon rich phase is graphite.

The formation of a stable or metastable eutectic structure depends upon the chemical composition, cooling rate and nucleation potential of the liquid metal.

The two basic eutectic microstructures have significantly different mechanical properties with respect to hardness, strength, toughness and ductility. The aim of the cast iron metallurgist is to change the proportion, morphology and type of phases present to achieve the required mechanical properties.

When the metallurgy of cast irons is discussed the key factors that control the final microstructure are chemical composition, cooling rate, and heat treatment.

2.2 CLASSIFICATION OF CAST IRONS

Cast irons were historically first classified on the basis of their fracture surface. Two types were initially recognised:

- i. White Iron -having a white, fine crystalline fracture face due to fracture occurring along the carbide plates.

- ii. Grey Iron -having a grey fracture appearance due to fracture occurring along graphite flakes.

Various classifications of cast irons have been introduced, based on the nature of the phase microconstituents and the purpose of the alloy. The major groups are grey irons, white irons, malleable iron, and nodular iron. Cast irons can also be categorised by their purpose, such as corrosion resistant, heat resistant, or wear resistant irons. This study is concerned primarily with wear resistant white irons.

White irons are alloys of iron containing no free graphitic carbon. The composition is controlled so that graphitisation will be inhibited for the desired section size of the casting. The group of white irons of interest to this study are multiphase alloys, containing hard carbides within a typically austenitic ferrous matrix. The wear resistant white irons are also high alloy irons, containing high levels of chromium, nickel, molybdenum and manganese.

The ferrous matrix phase of the alloy is usually austenite, or austenitic in origin, depending on the thermal history of the alloy. Structures such as Martensite, Pearlite and Bainite are possible in addition to the austenite.

2.3 WHITE IRON MICROSTRUCTURE

The iron-chromium-carbon alloy system used for this study typically exhibits three main microstructural types depending on the nature of the proeutectic phase. These are a hypoeutectic, eutectic and hypereutectic alloy. The phases present for each of these types of alloys are essentially the same, consisting of a hard carbide and a softer ferrous structure, only differing in the nature of the proeutectic phase formed. The ferrous phase can be either austenite, ferrite, or various transformation products such as martensite, pearlite and ledeburite.

2.3.1 HYPOEUTECTIC WHITE IRON

If the alloy is hypoeutectic in composition, then austenite will typically be the proeutectic phase (primary phase). The carbides will be contained within the eutectic structure, forming between the austenite dendrite arms. The ferrous structure is the

first phase to nucleate, forming a network of dendrites. At the eutectic temperature boundary, the remaining liquid alloy solidifies along the eutectic temperature trough, forming the ferrous/ M_7C_3 eutectic product.

Since the carbide growth occurs over a narrow temperature range along the eutectic trough, the carbide size is extremely small. A typical micrograph for a hypoeutectic white iron is shown in Figure 2.1.

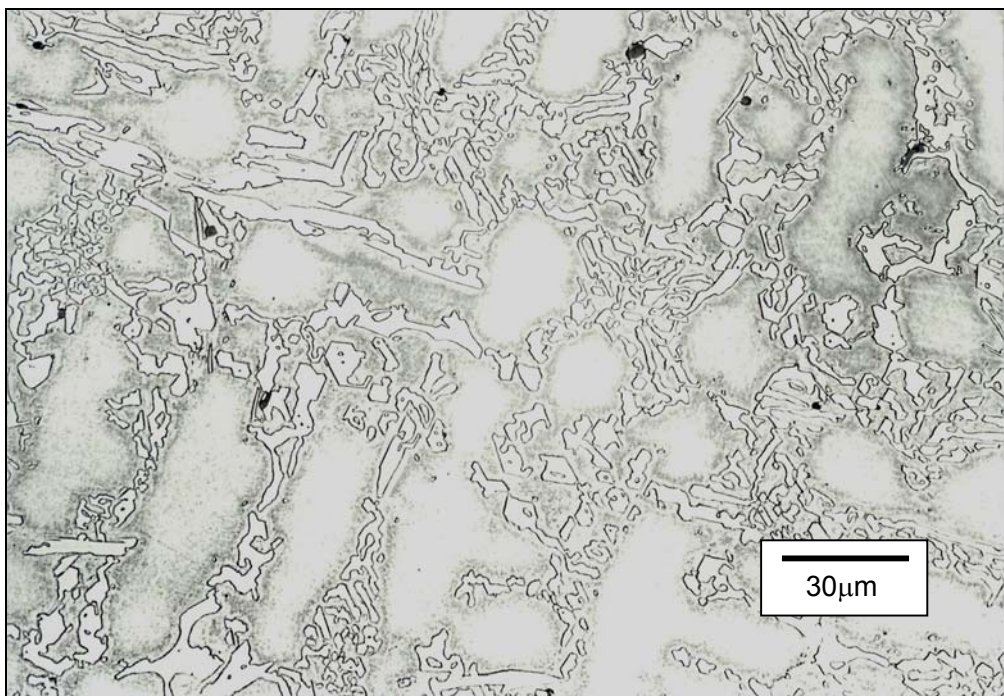


Figure 2.1: Hypoeutectic white iron microstructure.

2.3.2 EUTECTIC WHITE IRONS

Eutectic irons remain in the molten state during cooling until the eutectic trough is reached. When the liquid alloy reaches the austenite/ M_7C_3 trough, the temperature of the remaining liquid during eutectic solidification decreases as its composition follows the eutectic boundary. Both carbide and austenite phases solidify simultaneously, resulting in an interlaced structure. The exact nature of the eutectic structure is dependant on the alloying elements present. A typical microstructure for a eutectic white iron is shown in Figure 2.2.

Eutectic white irons have a continuous carbide network. If the composition lies directly on the eutectic, the microstructure is extremely fine and difficult to resolve at low magnifications during examination. Typically in alloy white iron, the presence of molybdenum, manganese, chromium and nickel alter the eutectic significantly, so that a true eutectic may not be achieved. The major carbide formed is the M_7C_3 type. The carbides have the shape of long rods [2]. The crystal structure is hexagonal close packed. The structure of the eutectic carbide is shown in Figure 2.3.

The size of the eutectic carbides are essentially controlled by the rate of heat removal during solidification along the eutectic boundary.

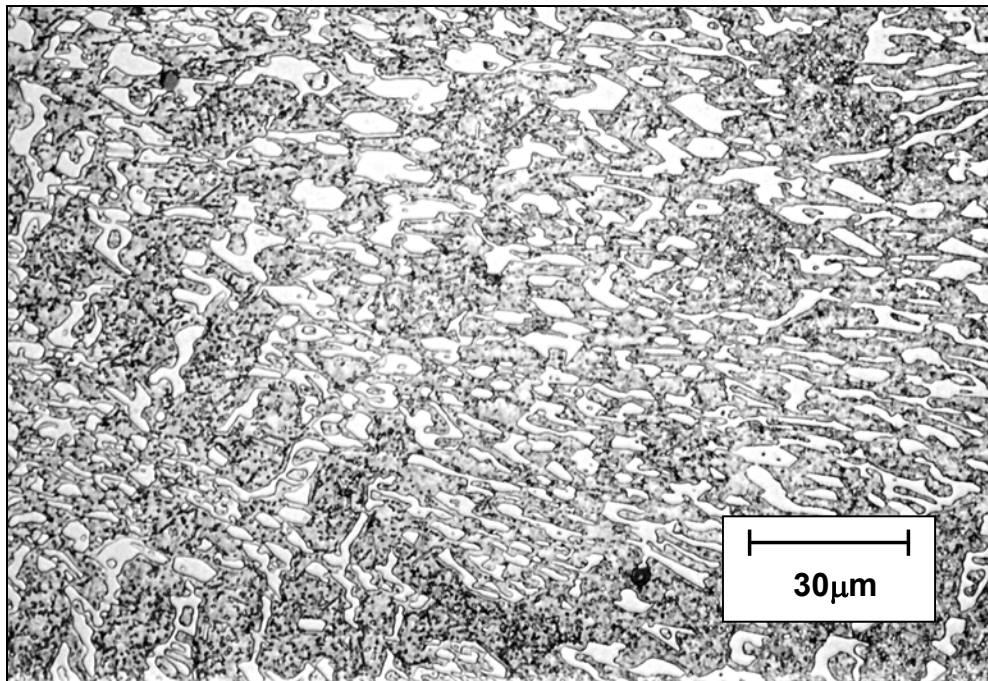


Figure 2.2: Eutectic white iron microstructure.

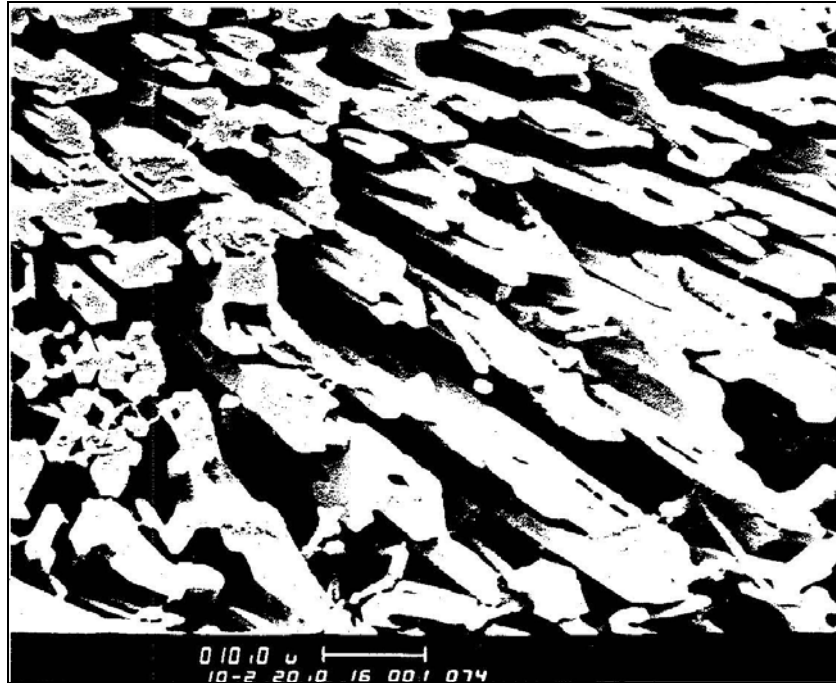


Figure 2.3: Eutectic carbide rods (after deep etching) [2]

2.3.3 HYPEREUTECTIC WHITE IRONS

Hypereutectic white irons consist of proeutectic (primary) M_7C_3 carbides within an eutectic matrix. The first phase to solidify from the melt is the discontinuous hexagonal M_7C_3 carbide. These carbides have a high hardness due to their high proportion of chromium and carbon. As the temperature decreases, these carbides grow in size, until the eutectic trough is reached, upon which the remaining liquid alloy solidifies along the austenite/ M_7C_3 trough, arresting the primary carbide growth.

The eutectic matrix of the hypereutectic alloy is similar to that of the eutectic composition alloy previously discussed in section 2.3.2. The phases present in the eutectic are a continuous M_7C_3 carbide with austenite. The nature, size and distribution of the primary carbides are controlled by the composition and thermal history of the alloy casting. A typical hypereutectic white iron microstructure is shown in Figure 2.4

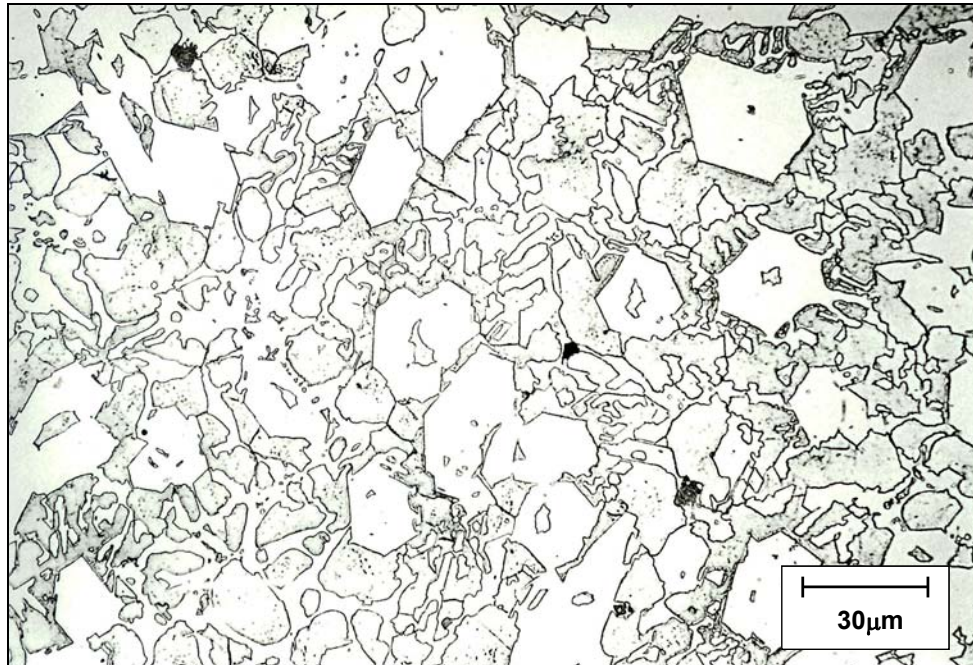


Figure 2.4: Typical hypereutectic white iron microstructure.

The volume fraction of total carbide (both primary and eutectic) is determined by the overall chromium and carbon content. An empirical formula has been derived which estimates the carbide volume fraction [2]. However this formula takes into account the secondary carbides produced after heat treatment of the alloy, and is not an accurate guide when determining the carbide formed as a result of solidification.

$$\% \text{ Carbides} = 12.33 \times \text{C}\% + 0.55 \times \text{Cr}\% - 15.2 \quad \text{equ 1}$$

Typically a more accurate method for predicting the carbide content is to utilise the lever rule method applied to the isopleth for the Fe-Cr-C phase diagram.

2.4 EFFECT OF ALLOYING ELEMENTS [3]

Chromium is the major alloying element used in white irons in addition to iron and carbon. Chromium is a strong carbide former, and can form a variety of carbides depending on the overall composition and carbon level. The form of the carbides is designated by a simple notation, where 'M' represents the major metallic alloying element(s) and carbon is represented by 'C'. The following carbide types can be typically found in chromium white irons:

- i. M_7C_3 where M usually consists of chromium and iron.
- ii. M_3C where M is usually iron (cementite).
- iii. M_2C where M is usually molybdenum.
- iv. $M_{23}C_3$ where M is usually chromium and iron, and occurs when the chromium/carbon ratio is high.

More than one element may combine with the carbon to form the hard carbides, and typically iron is present along with the chromium, creating a complex carbide $(Fe,Cr)_7C_3$. Elements such as vanadium and niobium can also be used as alloying elements, creating more complex carbides. As the amount of the alloying element exceeds the solid solubility, then this element will form carbides on its own.

This carbide formation usually occurs at a higher temperature than the major solidification temperature for the iron/chromium M_7C_3 carbides and can also occur during subsequent heat treatment of the alloy casting.

The presence of complex carbides promotes a higher hardness for the alloy. The presence of high melting point carbides can promote the nucleation of the M_7C_3 carbides by acting as a seed.

Silicon is generally added to increase fluidity for the molten alloy during casting. Normally up to one percent silicon is added for fluidity enhancement. Increasing silicon above 1.5 weight percent usually results in the stabilisation of delta ferrite from the solidus temperature, and a wholly ferritic ferrous matrix at room temperature. As the alloy cools from the solidus temperature, the solubility of carbon in the ferrite dramatically reduces, and the carbon is expelled from the ferrite forming fine carbide precipitates. Silicon in high concentrations can give good chemical resistance.

Manganese in small quantities acts in a similar manner to silicon in providing enhanced fluidity of the molten alloy. Generally one percent manganese is added to give better fluidity. Manganese also acts as a strong austenite stabiliser providing the residual carbon level of the ferrous phase is sufficient. The manganese content is often varied to enhance the hardenability of the castings for variations in section thickness during subsequent heat treatment.

Nickel acts as a potent austenite stabiliser for white cast irons. Nickel is also a major alloying element for chemical resistance.

Molybdenum has a dual function when alloyed with iron and chromium. Small quantities of molybdenum, generally up to one percent, act as an austenite stabiliser. Above one percent additions, the molybdenum begins to form hard complex molybdenum/chromium/iron carbides. The molybdenum carbides generally partition to the grain boundaries, causing a decrease in alloy toughness.

2.5 WEAR CHARACTERISTICS OF WHITE CAST IRONS

Wear is a complex process by which materials lose mass under the influence of mechanical deformation, and can manifest itself in many forms. Avery [4] describes wear as the unintentional deterioration due to use or the environment, and is usually a surface phenomenon. The classification of various wear modes by Avery (Table 2.2) separates wear into three basic categories; mechanical, thermal and chemical. Under each major category, several causes for wear are listed, along with various modes of interactions. Erosion was classed by Avery as a form of Abrasion, involving velocity, impact, stress and shear. Wear is not just a function of the surface material, but is a characteristic of the overall system. In the majority of mining application, the major form of wear is abrasion, although the other forms of wear are present. The wear process does not usually result in catastrophic failure of the material, but a gradual loss of material from the surface, which may lead to failure.

A summary of the descriptions of wear was also compiled by Zum Gahr [5]. A list of the major classification of wear is given in Table 2.3. The preferred system for the classification of wear is to describe the processes as either abrasion, adhesion, erosion, corrosion or surface fatigue.

- i. Abrasion is the removal of materials due to scratching.
- ii. Adhesion is the formation and breaking of interfacial bonds.
- iii. Erosion is the damage caused by a second phase under motion induced by a carrier medium.
- iv. Corrosion is the chemical degradation of the surface.
- v. Surface fatigue is the damage caused by cyclic applied stresses.

A more recent report published by the Australian Mineral Industries Research Association Ltd (AMIRA) [6] describes the current understanding about wear mechanisms and basic material selection for the mining industry.

The AMIRA report still generalises wear as 'abrasion', however the study was extensive, and covered most of the fundamentals related to wear. The wear of the component was described to be controlled by three main factors; the properties of the wear material, the properties of the abrasive material, and the nature of the interaction between the abrasive and wear materials. A summary of the main factors affecting wear is given in Table 2.4.

Table 2.2: Classification of wear modes [4]

BASIC FACTOR	NOMINAL CAUSE	DESCRIPTION OF WEAR (Variables)
MECHANICAL	IMPACT	Battering (Stress, Deformation), Rupture (Stress, Deformation, Brittleness), Cavitation (Stress)
	FRICTION	Smoothing (Stress, Shear) Seizing (Stress, Deformation, Welding) Galling (Stress, Deformation, Welding, Shear)
	ABRASION	Erosion (Velocity, Impact, Stress, Shear) Scratching (Low Stress, Shear) Grinding (High Stress, Shear, Deformation) Gouging (High Stress, Shear, Impact, Deformation)
	VIBRATION	Fatigue (Stress reversals, Time, Cracking) Corrosion Cracking (Stress)
THERMAL	HEAT	Creep (Stress, Softening, Time, Deformation) Sealing (Oxidation, Corrosion) Crazing (Expansion, Stress, Deformation, Reversal, Time, Cracking, Fatigue) Growth (Graphitisation, Phase Change, Oxidation) Transformations (Expansion, Contraction, Stress, Phase Change)
CHEMICAL	CORROSION	Solution (Heat, Time, Chemical Action) Erosion (Solution, Velocity, Stress) Intergranular (Time, Chemical Action) Electrolytic Action (Heat, Dissimilar Phases) Scaling (Heat, Time, Chemical Action, Diffusion) Galvanic (Electrolytic, Dissimilar Phases) Pitting (Electrolytic, Dissimilar Media)

Table 2.3: Classification of wear processes by wear mechanisms [5].

1. Burwell and Strange [7]: Abrasion, Adhesion, Corrosion, Surface Fatigue, Fretting, Erosion and Cavitation.
2. Jahanmir [8]: Adhesion, Delamination, Fretting, Abrasion, Erosion, Impact, Surface, Fatigue, Corrosion, Diffusion, and Electrical Contact Wear.
3. Godfrey [9]: Mild Adhesive, Severe Adhesive, Abrasion, Erosion, Fatigue, Delamination, Corrosive, Electrocorrosive, Fretting, Corrosive, Cavitation, Electrical Discharge and Polishing.
4. Rise [10]: Adhesion, Abrasion, Fatigue, Corrosion and Electrical.
5. DIN 50320 [11]: Adhesion, Abrasion, Fatigue, Tribochemical Reaction.

Table 2.4: Summary of factors which influence wear [6]

ABRASIVE MATERIAL	CONTACT CONDITIONS	WEAR MATERIAL
particle shape	force/impact level	hardness
particle size	velocity	yield strength
particle/material hardness	impact angle	elastic modulus
yield strength	sliding/rolling	ductility
fracture properties	temperature	toughness
concentration	wet/dry	strain hardening
characteristics	pH/corrosivity	fracture toughness
		microstructure
		corrosion resistance

2.5.1 ABRASION

The term 'Abrasion' has been used loosely in the past to cover the majority of wear descriptions. However, it is important to differentiate between the various types of wear because their mechanisms and results are different. Abrasion is the loss of material due to hard particles or protrusions, forced against the surface at tangential angles [12] (see Figure 2.5). Hard particles may be products of the process, such as the case with crushing and milling, or an outside component which enters the system. Hard particles can also take the form of protuberances, especially on a microscopic scale. A range of processes may occur during abrasion depending on the specific duty. Abrasive wear can be classified as either two-body or three-body, depending on the presence of free moving particles.

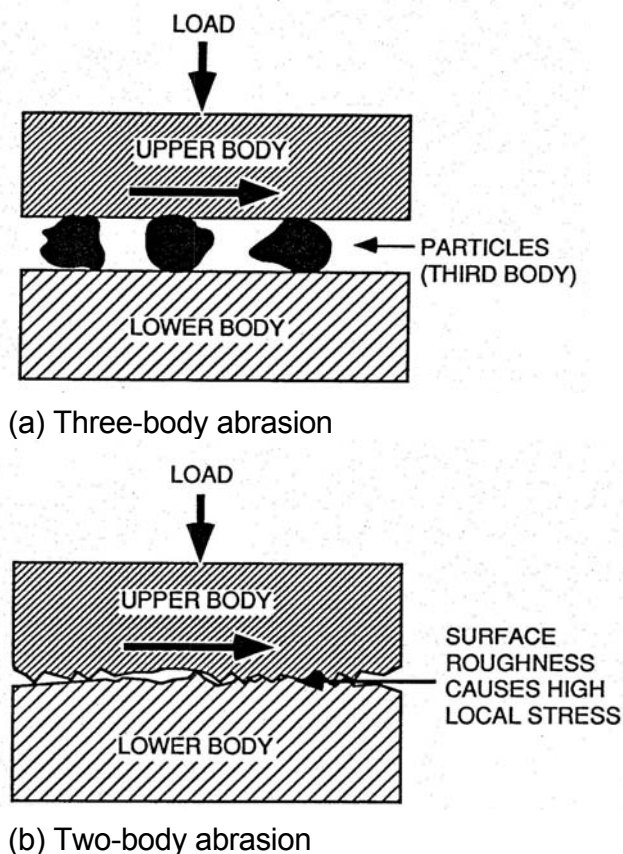


Figure 2.5: Abrasive wear.

Four modes of abrasion are recognised (see Figure 2.6)[5];

- i. microploughing,
- ii. microcutting,
- iii. microfatigue and
- iv. microcracking.

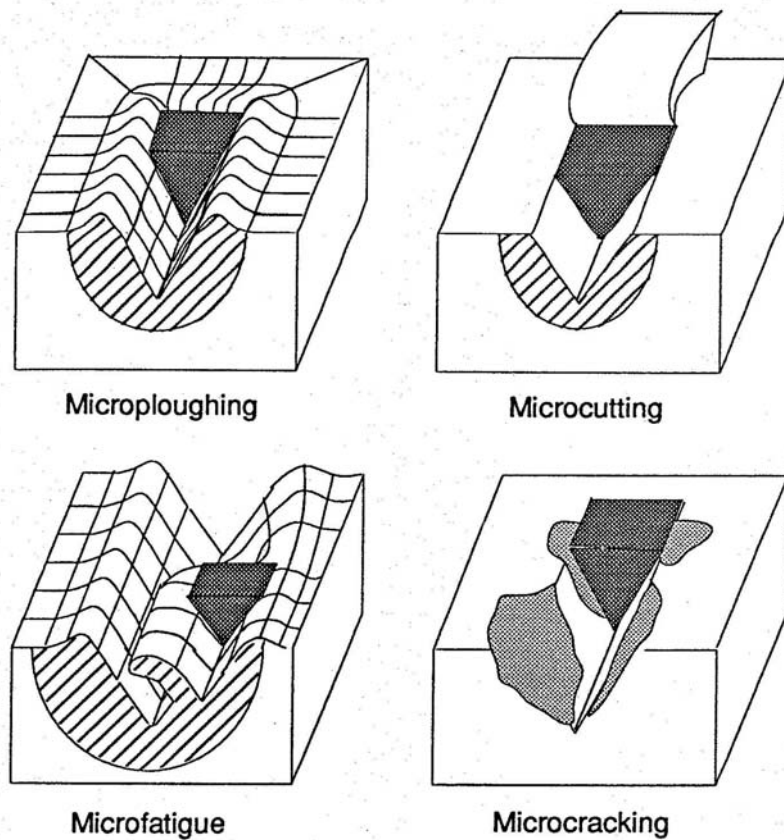


Figure 2.6: Four modes of abrasion [5]

Microploughing occurs when the abrasive particle moves across the material surface and produces a deformation groove. The surface can accommodate the deformation by allowing material to flow around the abrasive particle.

Material loss from microploughing is negligible since rupture of the surface does not occur.

Microcutting occurs when the movement of the abrasive particle across the material surface results in the formation of a chip. The surface does not flow around the particle, but is removed by the machining action of the particle.

Microfatigue occurs under cyclic microploughing conditions. When several particles cause grooving of the material surface, the extruded material results in the formation of lips. Removal of the material surface occurs when subsequent particle abrasion shears off the extruded lips.

Microcracking occurs when the material surface is brittle, and the abrasive particle is harder compared to the surface hardness. As the particle moves across the material the surface is grooved, and the material chips at the particle / surface interface. The microcracks can interconnect under repeated abrasion conditions, resulting in spalling of the material surface.

The nature of the abrasive wear of a given material will be a function of the material's mechanical properties. The rate of material loss will depend on the nature of the abrasive material and the applied load. Abrasion is not velocity dependant as the volume of material removed does not increase with increasing velocity [13]. However, increasing the frequency of abrasion cycles will increase the amount of wear.

2.5.2 ADHESION

Adhesive wear is the material transfer or loss between two surfaces, due to localised bonding between two contacting solid surfaces [12] (see Figure 2.7). Adhesive wear can occur when surfaces slide against each other. Local asperities produce high contact pressures between two contacting surfaces, and result in plastic flow, and adhesion of two surfaces. Movement of the joint causes rupture at the junctions created by the asperities. The tendency of a surface couple to form adhesive bonds was a function of the physical and chemical properties of the materials in contact, applied load, surface purity and roughness [5].

Alternatively, adhesion can result from the joining of two bodies using a third body (called an adhesive). This form of adhesion requires both mechanical locking of

molecules and chemical bonding. The adhesive on a molecular level flows between the asperities of the surface, providing the mechanical joint.

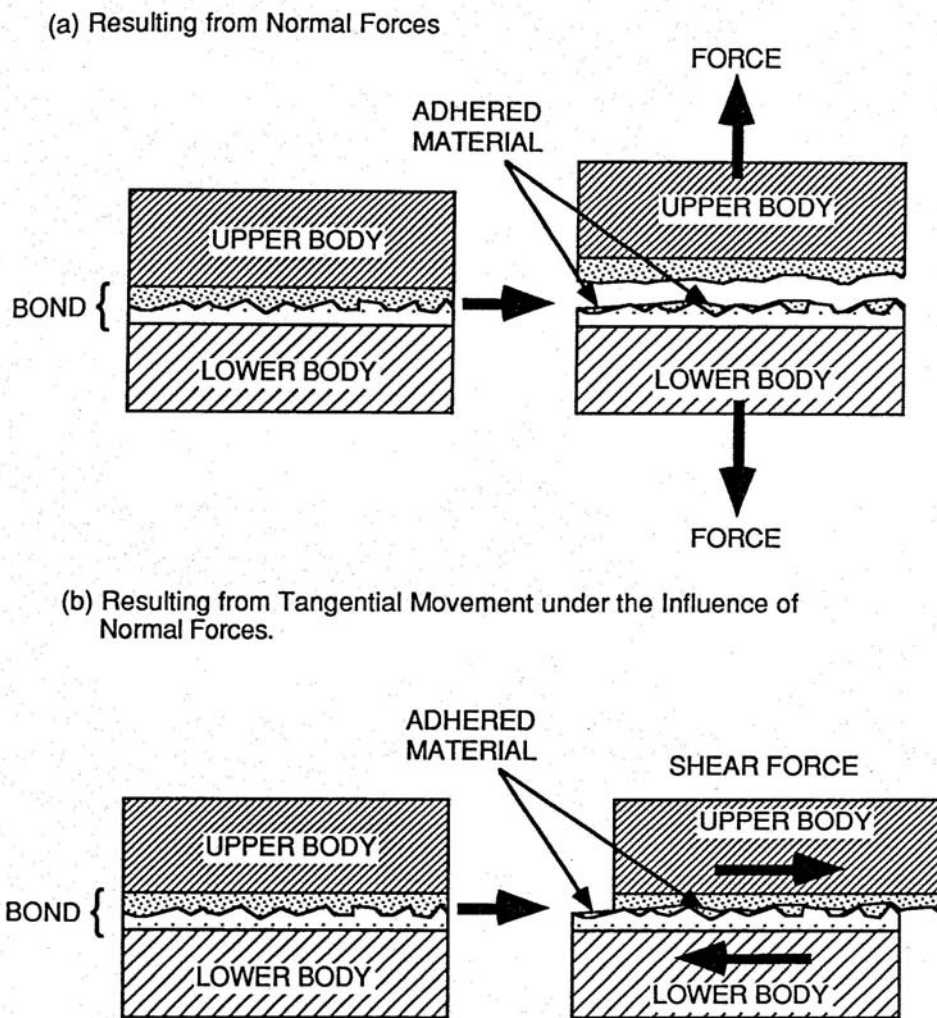


Figure 2.7: Adhesive wear

2.5.3 EROSION

When the wear particles are transported by a gas or fluid at high speeds, the principal mode of wear is called erosion [6]. The contact stress between the particle and the material results from the kinetic energy of the particles. Erosion can then be described as the loss of material from a solid surface due to a mechanical interaction between that surface and a fluid, gas or solid particles [12] (see Figure 2.8). Erosion is a velocity controlled process, but other slurry variables also have an effect on the erosion rate. Erosion differs from abrasion since erosion involves the transfer of kinetic energy from the impacting particle to produce surface deformation. Avery [4] suggests the role of impact must be considered carefully. Impacting particles can cause high mechanical stresses, resulting in surface compressive stresses. When the stress from the impact exceeds the elastic limit of the material surface, plastic flow will occur. This results in deformation which can lead to cracking or failure. Repeated impacts of erosive particles may lead to a system involving fatigue.

Erosive wear is generally an open system, and can be divided into several major types. One classification by Zum Gahr [5] differentiates between blast erosion, flush erosion, cavitation-erosion, erosion-corrosion, rain erosion and thermal erosion. The most appropriate classification is to divide erosion into three modes [14];

- i. directional impingement,
- ii. random impingement, and
- iii. sliding bed erosion.

Directional impingement (Figure 2.8a) consists of particles hitting the alloy surface at a common angle. Erosion has a heavy dependence on the angle of incidence of the impacting particles, and this relationship varies between materials.

In many mineral processing applications, there is always a complex system of erosive wear, with a range of angles of impingement occurring.

Random impingement (Figure 2.8b) occurs where there is a local variation in the angle of incidence of the particles. This process is usually associated with eddy currents and vortices. Since the angle of impingement of the particles is varied, this type of erosion is difficult to model and predict.

Sliding-bed erosion (Figure 2.8c) occurs where impact angles are low, and the local density of solids is high. Particle-particle as well as particle-material interactions occur. This type of erosion is similar to low-stress abrasion. Since erosion is a velocity dependant process, the wear can be controlled to a small degree by adjusting the velocity of the particles. In mineral processing applications, it is desirable to operate at low velocities to minimise the wear of the components.

Low stress abrasion and erosion usually involve contact stresses which do not exceed the crushing strength of the abrasive particle.

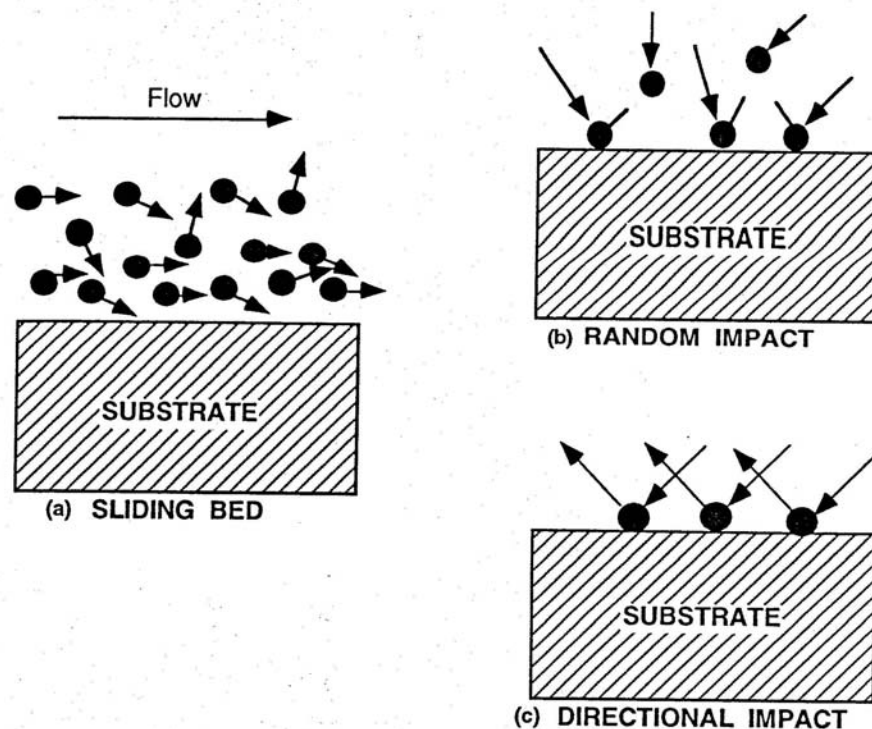


Figure 2.8: Erosive wear modes [15]

2.5.4. WEAR OF WHITE IRONS

The wear of white irons is governed by the overall microstructure. The effect of the microstructure on the wear rate is dependant on the nature and scale of the wear system [6]. When the wear involves damage from abrasion or erosion with large particles, the bulk material properties generally effect the wear rate, and the nature of the microstructural features are not as important. In fine particle systems, the nature of the microconstituents has the most effect on the overall wear rate.

The ultimate performance of white irons is dependant on the two major microconstituents, carbide and matrix [16]. The wear rate is generally believed to be a function of the alloy hardness, although it has proved difficult for researchers to quantify this relationship. The wear of white irons has been described as the martensitic structure being removed from around the carbides, followed by the carbides spalling off [16]. The carbides are often as hard as the wear particles, and offer the major protection to the alloy. The matrix, usually martensitic, with some residual austenite, is worn at a faster rate than the carbides. The rate of matrix removal has been shown to be controlled by the inter-carbide spacing (mean free path of the matrix phase) [16].

Chemical composition, microstructures and strain-hardening ability [17] have been shown to play an important role in controlling the wear resistance of an alloy. In general, the alloy hardness remains the only easily measurable property which can give an estimate of the potential performance [17]. High alloyed materials, such as high chromium irons, provide the highest wear resistance [18]. The most wear resistant materials have been found to have a low relative hardness difference when comparing the hardness of the slurry particles to the hardness of the material.

2.5.5 EFFECT OF MECHANICAL PROPERTIES

The bulk indentation hardness of an alloy can be used as a rough guide to the performance of the alloy in wear situations. Homogeneous alloys (single phase) generally follow the trend of increasing wear resistance with increasing hardness [18]. The relationship of hardness with wear for multiphase alloys (heterogeneous) is not clear, but in general the wear reduces as the hardness of the alloy increases [18]. In

the case of alloy steels, there are several trends depending on the level of alloying and type of microstructure (see Figure 2.9).

There is no direct relationship for bulk hardness compared to the wear resistance of alloy white irons, however the overall trend is for increasing resistance with increasing hardness [6].

Sare's work on fracture toughness [19] showed the fracture toughness and low stress abrasion resistance to be the greatest for austenitic matrices. The plain-strain fracture toughness of white cast irons was found to be sensitive to changes of the matrix, and that austenite had a greater ability to arrest brittle cracks from propagating from carbide to carbide.

The maximum wear resistance was obtained when the ratio of the fracture toughness to the bulk hardness was high, and the overall hardness of the alloy was high compared to that of the particle. The relationship between metal wear, hardness and fracture toughness is shown in Figure 2.10. When the fracture toughness of the alloy is low, fragmentation is the predominant mode of material removal. As the fracture toughness increases, the wear resistance increases, until the mechanism of wear changes to that of cutting and ploughing.

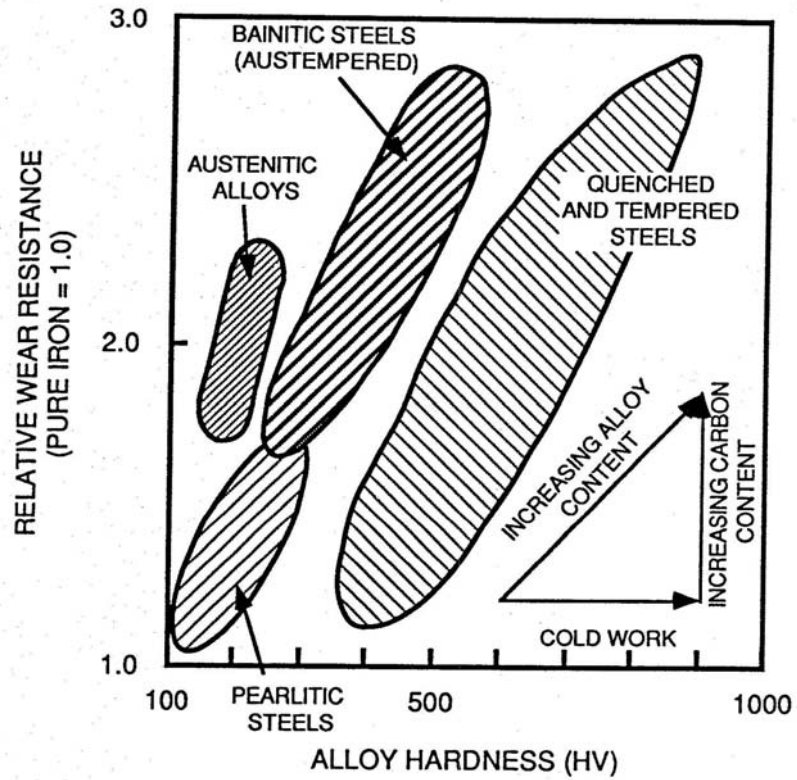


Figure 2.9: Effect of alloy steel hardness on overall wear resistance [20]

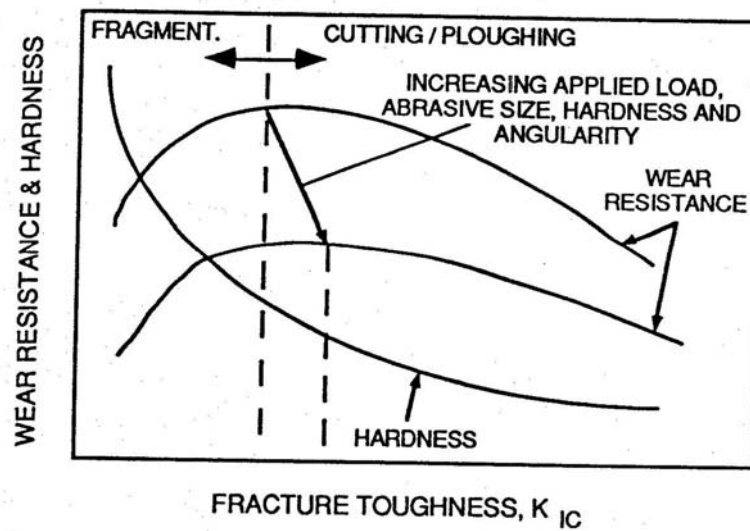


Figure 2.10: Relationship between wear resistance, hardness and fracture toughness [5].

As the fracture toughness increases, the hardness of the alloy typically decreases. A combination of high hardness and high fracture toughness is required in the alloy to maximise wear resistance [5]. The transition from fragmentation to cutting and ploughing for alloys is dependant on the contact stress, and the maximum size of the groove caused by the particles. As the severity of the wear environment increases (increasing particle size, angularity, hardness), the alloy requires a higher fracture toughness to reduce the wear. In extremely large particle applications, such as dredge pumping, the alloys used are generally more ductile to enhance the fragmentation resistance [6].

2.5.6 STRAIN ACCOMMODATION

Carbide fracture has long been considered to be the dominant mechanism in controlling carbide removal caused by wear. The carbides can be chipped by microfracture, initiated by cyclic elastic contacts [21]. The wear rate has been found to be influenced by the presence of lateral cracks around the carbides.

Ball [22] showed that the wear process can involve plastic deformation, ductile and brittle modes of microfracture of the various phase structures, and stress induced phase transformation. The overall wear involves an incubation period, followed by a steady state wear period. A wear resistant material would have a long incubation period, followed by a low steady state wear rate. Ball also showed that alloy wear resistance was controlled by strain accommodation, as opposed to high indentation hardness to strength.

The ability of a material to accommodate strain is related to the material's dislocation density [23]. As a material is worn, the strain increases from the stress-free state in the bulk, to a critical value at the surface involving an increase in dislocation density. Repeated impacts of particles, whether they be water droplets or sand grains, result in an increase in the dislocation density at the materials surface. As the dislocation density increases at grain boundaries and the surface, a stage is reached where the surface can not accommodate further strain, and surface damage and material loss results.

The best performing materials would have a high plastic strain capacity, and excellent microfracture behaviour. A mismatch of elastic and plastic strain in a microstructure encourages the initiation of fracture, by allowing the dislocations to build up around regions of high elastic strain, such as carbides and graphite [24,25]. The high localised strains generated by eroding particles accentuate the problems associated with heterogeneous materials.

2.5.7 MICROSTRUCTURE

The carbide volume fraction (CVF) in white irons plays an important role in controlling the wear rate of the alloy [24]. The CVF can control the mechanism of material removal, as shown in Figure 2.11. Increasing the CVF above 30% for alloys having a low carbide hardness changes the mechanism of wear from ploughing and cutting to fragmentation.

When the matrix and carbide compositions are held constant, the wear resistance passes through a maximum near the eutectic composition for quartz abrasives, and increases with increasing CVF for alumina particles (see Figure 2.11). Spalling and pitting of the massive primary carbides was observed for hypereutectic white irons using quartz abrasives, but was not observed for the alumina particles.

Under low stress conditions, wear resistance is primarily a function of carbide morphology [19], with the matrix providing mechanical support. The matrix can also control the fracture toughness of the alloy, by arresting brittle cracks as they propagate through carbides [19]. Low stress abrasion resistance is greatest for austenite matrices. The wear resistance is also a factor of carbide volume fraction, and dispersion of carbides [19]. Other studies on low stress abrasion [13] have shown that no carbide cracking occurs, and the matrix is not preferentially removed.

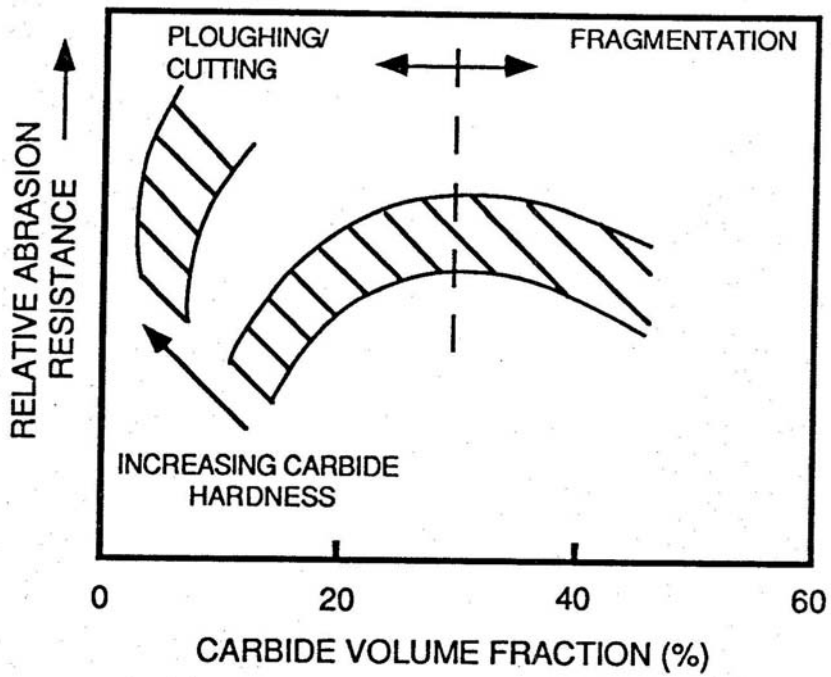


Figure 2.11: Effect of carbide volume fraction on wear of alloy white irons [6]

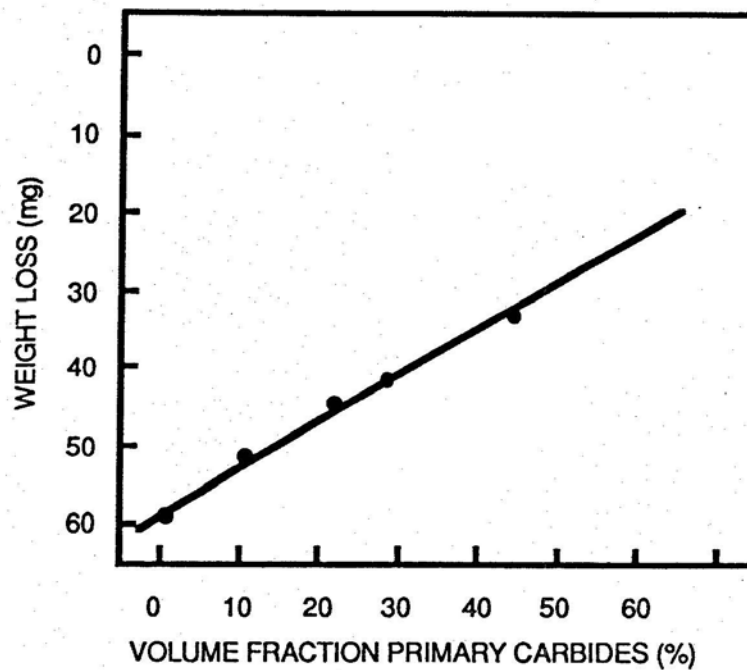


Figure 2.12: Relationship between primary carbide volume fraction and abrasive wear rate for hypereutectic white irons [26].

The performance of the alloy has been shown to be a function of the hardness of the microconstituents of the irons [13]. Hardened alloys also perform better than as cast structures [13], however this is in contrast to the concept that austenitic structures provide better wear resistance [19].

The actual optimal matrix phase may be dependant on the nature of the wear particles. Size, shape and hardness of the particle have a significant effect on the erosion mechanism, and different phases may be required for a given duty [17].

The ductility of steels may be a better guide to the wear resistance than other physical properties [27]. Hardness, strength, fracture toughness and impact strength had little effect on the wear behaviour. The benefit of ductile materials was due to their ability to dissipate the kinetic energy of the wear particle by deforming around the area of the impact zone. The higher ductility materials could accommodate higher levels of strain.

To obtain an understanding of the mechanism of wear for white irons, it is necessary to study the wear mechanisms of the individual structures. Various studies have been conducted on single phase alloys, and alloys containing predominantly one major phase.

The most comprehensive results have been provided by Stauffer [18]. In general, Stauffer's results showed martensitic structures to be more wear resistant than austenitic structures. As the degree of alloying increased to enable better hardening of steels, the wear resistance also increased. Stauffer's results do not conclusively show that wear resistance is directly proportional to bulk alloy hardness.

Inclusions and carbides within the microstructure are not effectively measured using standard hardness tests, which may effect the establishment of hardness as a criterion to wear resistance. The results of grinding tests carried out by Avery [4] show that martensite has a higher wear resistance than bainite, austenite, pearlite and ferrite. The individual microhardness of each phase present, associated with the relative proportion of each phase, may provide a better relationship to erosion resistance. Stauffer's results also showed no correlation between tensile strength and overall elongation with wear resistance.

Stauffer's results show that alloys containing titanium, boron, tungsten and other hard metal alloying elements have superior wear resistance to lower alloyed grades. Alloy sinters containing tungsten carbide were more resistant than alloys containing titanium carbides. Boron carbide also provided excellent wear resistance.

Pearce [28] has found that martensitic matrices gave higher wear resistance than austenitic or pearlite structures, under high stress abrasion duties. Increasing the bulk hardness increased the wear resistance, however this relationship did not follow for all of the test results. Cracking of the matrix between the eutectic carbide lamellae was observed. Irons with continuous carbides were suggested to provide a higher wear resistance since there was better attachment of the carbides to the matrix, in addition to the micromachining of the matrix. Under non-impact conditions, cracking of the carbides did not lead to carbide removal providing the carbides were continuous.

The effect of matrix microstructure on the erosion of a series of steels was investigated by McCabe, Sargent and Conrad [29]. They found that spheroidal and pearlite microstructures eroded in a ductile manner. Material removal of martensitic structures occurred as a brittle mode of erosion. The four microstructures investigated were ranked against erosion in the following order of increasing resistance; spheroidite, pearlite, tempered martensite and martensite. The erosion rates were determined using Alumina particles, which are significantly harder than the steel, and harder than the minerals typically transported in mineral processing applications.

The fracture toughness of the alloy, or the individual phase components, may provide an improved guide to the performance of the white irons.

Gundlach and Parks [30] suggest that the hardness of the abrasive used in wear tests influences the wear rates significantly. The rate of wear was found to increase with increases in abrasive hardness (see Figure 2.12). The type of abrasive used altered the ranking of the white irons tested. A list of abrasives and microconstituents with their corresponding hardness values is given in Table 2.5.

Tests with silicon carbide and alumina showed austenitic white irons exhibited lower wear rates than heat treated white irons. However, tests conducted using garnet, a softer abrasive, showed the martensitic structures to be more resistant than the austenitic alloys. Softer particles will provide a greater differentiation between various white irons since the hardness of the abrasive is close to that of the hard carbide phases found in high alloyed white irons. Gundlach and Parks also suggest that when the abrasive is softer than the carbide phase, the martensitic structures provide greater wear resistance, and when the abrasives are harder than the carbides, the austenitic structures show the greater wear resistance.

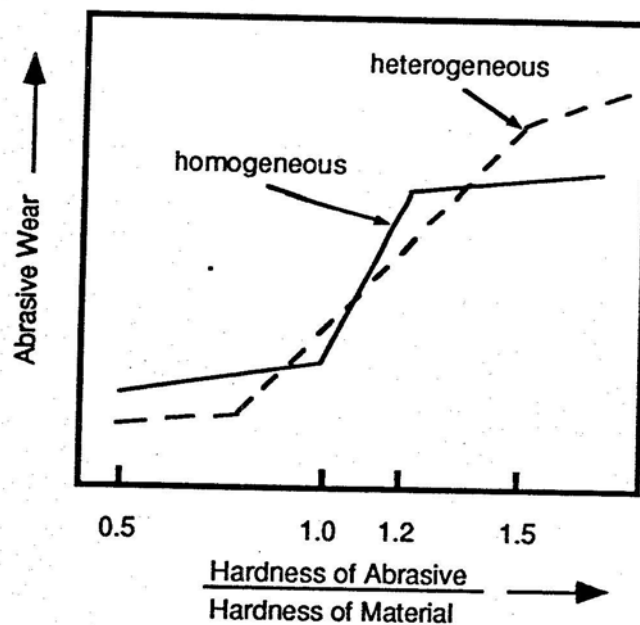


Figure 2.12: Abrasive wear as a function of the ratio of hardness of particle to the hardness of the material [5]

Table 2.5: Hardness of minerals and microconstituents [30]

MINERAL	HARDNESS KNOOP	HARDNESS VICKERS
TALC	20	-
CARBON	35	-
GYPSUM	40	36
CALCITE	130	140
FLUORITE	175	190
APATITE	335	540
GLASS	455	500
FELSPAR	550	600-750
MAGNETITE	575	-
ORTHOCLASE	620	-
FLINT	820	950
QUARTZ	840	900-1280
TOPAZ	1330	1430
GARNET	1360	-
EMERY	1400	-
ALUMINA	2020	1800
SILICON CARBIDE	2585	2600
DIAMOND	7575	10000
MATERIAL OR MICROCONSTITUENT		
FERRITE	235	70-200
PEARLITE (UNALLOYED)	-	250-320
PEARLITE (ALLOYED)	-	300-460
AUSTENITE (12% Mn)	305	170-230
AUSTENITE (LOW ALLOY)	-	250-350
AUSTENITE (HIGH Cr IRON)	-	300-600
MARTENSITE	500-800	500-1010
CEMENTITE	1025	840-1100
CHROMIUM CARBIDE	1735	1200-1600
MOLYBDENUM CARBIDE	1800	1500
TUNGSTEN CARBIDE	1800	2400
VANADIUM CARBIDE	2660	2800
TITANIUM CARBIDE	2470	3200
BORON CARBIDE	2800	3700

2.6 IRON-CHROMIUM-CARBON PHASE DIAGRAM

A large systematic study of the iron-rich corner of the Fe-Cr-C system was conducted by Bungardt et al [31]. Subsequent studies by Jackson [32], and Thorpe and Chicco [33] have resulted in more accurate representations of the system. For the purpose of this study, the liquidus projection used comes from the work conducted by Thorpe and Chicco, and is shown in Figure 1.

Based on the liquidus projection represented in Figure 1, four proeutectic or primary phases can occur on solidification depending on the composition of the alloy:

- a) austenite (γ Fe)
- b) ferrite (α Fe)
- c) M_7C_3 carbide
- d) M_3C carbide

The invariant liquidus reactions that are shown in the liquidus projection (Figure 2.13) are summarised in Table 2.6:

Table 2.6: Summary of Invariant Reactions

Invariant Location	Invariant Liquidus Reaction
U1	$L + \alpha \text{ Fe} \rightarrow \gamma \text{ Fe} + M_7C_3$
U2	$L + M_7C_3 \rightarrow \gamma \text{ Fe} + M_3C$
P1	$L + \alpha \text{ Fe} \rightarrow \gamma \text{ Fe}$
e1	$L \rightarrow \gamma \text{ Fe} + Fe_3C$

The reaction sequence for the Fe-Cr-C metastable system based on the study by Thorpe and Chicco is shown in Figure 2.14.

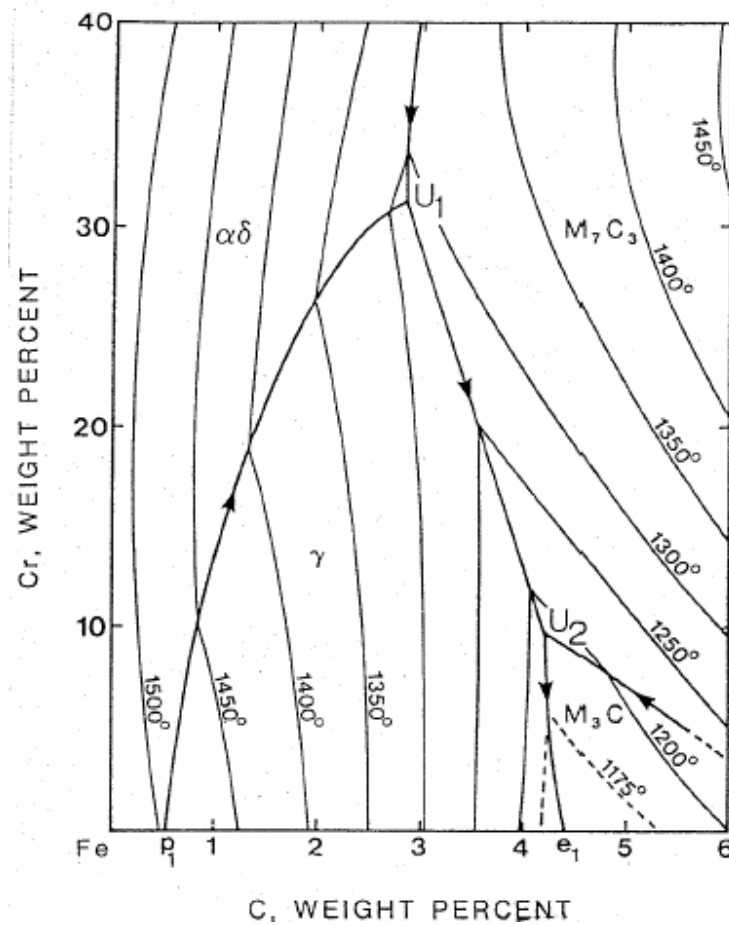


Figure 2.13: Liquidus projection for the Fe-Cr-C system [33].

Study of the Fe-Cr-C phase diagram shows the eutectic trough follows a reducing temperature as it approaches the U2 triple point. At a composition of approximately 4 wt% carbon and 10% chromium, the liquidus temperature is estimated to be 1200°C.

This composition is not considered practical from a commercial manufacturing perspective, and the effect of adding silicon, manganese and other minor alloying elements needs to be considered.

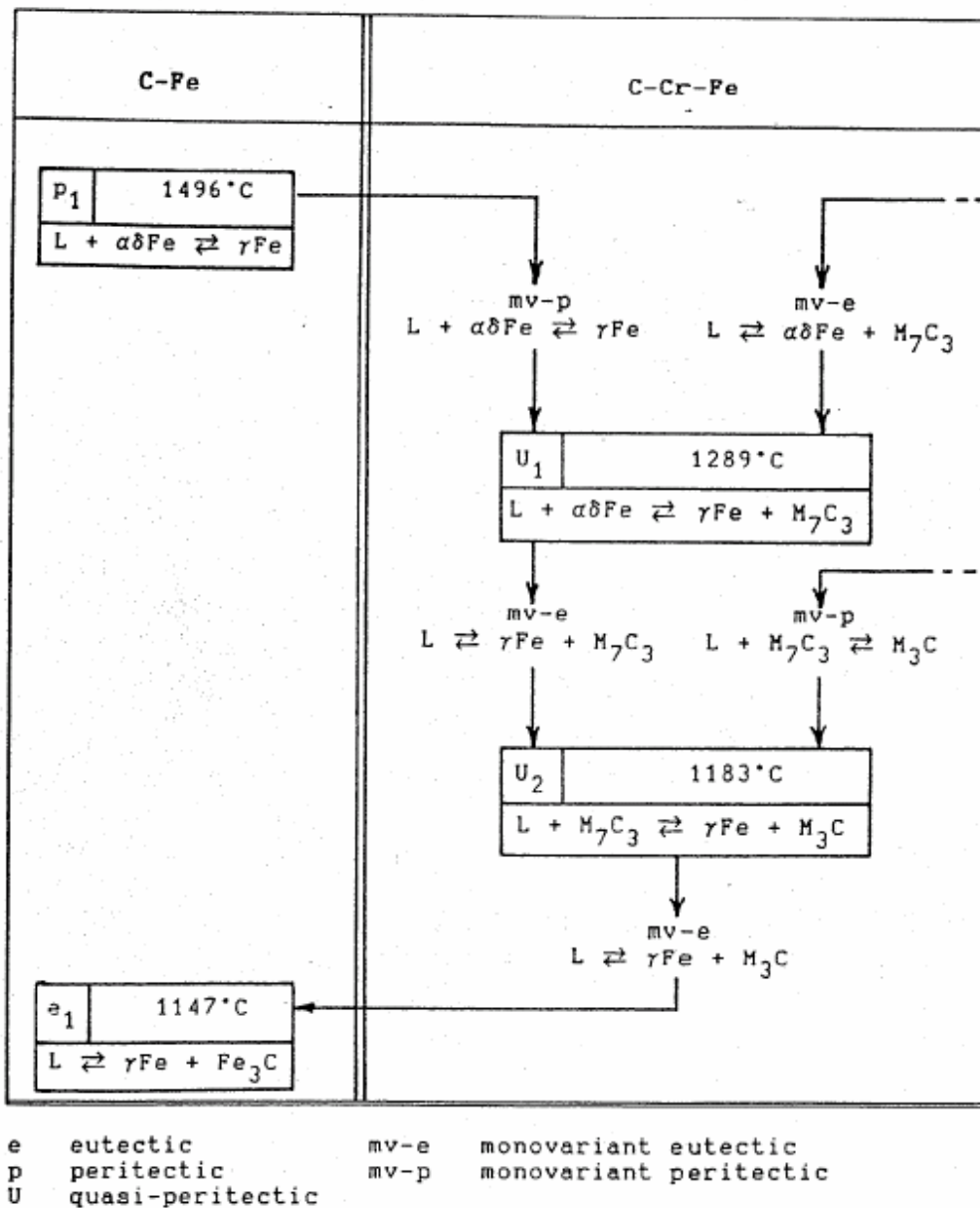


Figure 2.14: Summary of reaction sequences for the Fe-Cr-C system [33].

In recent years computer aided phase diagrams (CALPHAD) have become a popular tool for studying the effects of alloy composition variations. Commercial computer software programs such as Thermocalc [34] allow a range of compositions to be studied, and isopleths to be established. These computer aided calculations can then be compared with actual thermal analysis data from production melts to provide a comparison of accuracy.

In a study conducted by Schon and Sinatora [35] on the simulation of solidification paths for the Fe-Si-Cr-C alloy system, a range of computer predicted microstructures were compared to experimentally observed microstructures. Figure 2.15 shows the range of alloys reviewed and their predicted position on the liquidus projection.

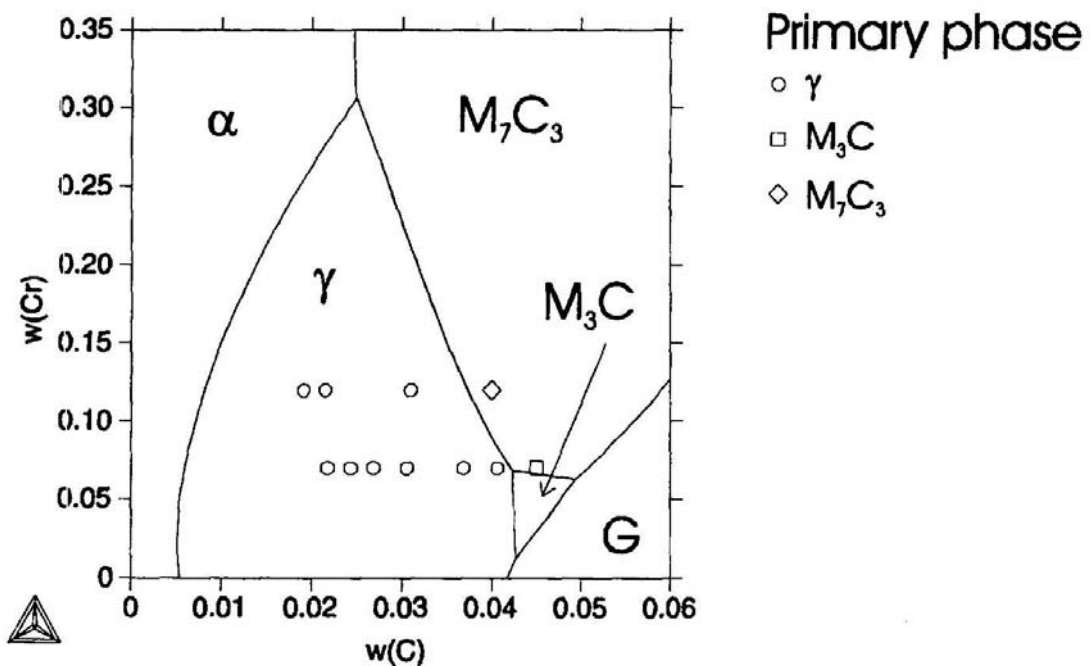


Figure 2.15: Fe-Si-Cr-C liquidus projection for 0.5 wt% Si after Schon and Sinatora [35].

The experimental results obtained from the Schon and Sinatora study showed close correlation between the predicted and the observed microstructures (see Table 2.7). In particular the target composition for this study of Fe-12Cr-4C would be expected to have a microstructure of M_7C_3 eutectic carbide, with M_3C carbide surrounding M_7C_3 carbide particles, and ledeburite, and as discussed in Section 2.5 would be expected to have good wear resistance. The M_3C carbides surrounding the M_7C_3 carbide particles was a result of the quasi-peritectic reaction U2 observed in Thorpe and Chico's data [33] and shown in Figure 2.14.

Table 2.7: Comparison of predicted and observed microstructures for high chromium white irons [35]

Alloy	Predicted Microstructure	Observed Microstructure
7.3Cr-2.17C	Austenite, M_7C_3 eutectic	Austenite, M_7C_3 eutectic
7.0Cr-2.43C	Austenite, M_7C_3 eutectic	Austenite, M_7C_3 eutectic, M_3C covering M_7C_3 particles
7.1Cr-2.68C	Austenite, M_7C_3 eutectic, secondary M_3C	Austenite, M_7C_3 eutectic, M_3C covering M_7C_3 particles
7.0Cr-3.05C	Austenite, M_7C_3 eutectic, type II peritectic	Austenite, M_7C_3 eutectic, M_3C covering M_7C_3 particles, ledeburite
7.1Cr-3.68C	Austenite, M_7C_3 eutectic, type II peritectic, ledeburite	Austenite, M_7C_3 eutectic, M_3C covering M_7C_3 particles, ledeburite
6.9Cr-4.06C	Austenite, M_7C_3 eutectic, type II peritectic, ledeburite	Austenite, M_7C_3 eutectic, M_3C covering M_7C_3 particles, ledeburite
7.0Cr-4.50C	M_7C_3 , M_7C_3 eutectic, secondary M_3C	Primary M_3C , ledeburite
11.7Cr-1.91C	Austenite, M_7C_3 eutectic	Austenite, M_7C_3 eutectic
11.7Cr-2.15C	Austenite, M_7C_3 eutectic	Austenite, M_7C_3 eutectic
12.0Cr-3.10C	Austenite, M_7C_3 eutectic	Austenite, M_7C_3 eutectic
13.0Cr-4.00C	M_7C_3 , M_7C_3 eutectic, secondary M_3C	M_7C_3 , M_7C_3 eutectic, M_3C covering M_7C_3 particles, ledeburite

In a separate study by Du and Morral [36], a prediction was made for the lowest melting point eutectic in the Fe-Cr-Mo-V-C alloy system. Du and Morral's data showed small variations in liquidus temperatures between the predicted and the experimental data.

Gomez-Acebo *et al* [37] presented a further study on the low melting point eutectics in the Fe-Cr-Mn-Mo-C alloy system. A summary of the calculated lowest liquidus temperatures within this system are shown in Table 2.8.

Figure 2.16 represents the predicted phase diagram for the Fe-30Cr-C alloy series. This phase diagram was calculated using the Thermocalc [34] software package.

Table 2.8: Calculated lowest liquidus temperatures for the C-Cr-Fe-Mn-Mo system [37]

System	T _{min} (K)	Reaction	Reaction type	Composition (wt%)
<i>Binary</i>				
C-Cr	1806	$L = bcc + M_{23}C_6$	Eutectic	3.53C-96.5Cr
	1771	$L = bcc + M_{23}C_6$	Eutectic	3.2C-96.8Cr
C-Fe	1427	$L = fcc + C$	Eutectic	4.34C-95.7Fe
	1427	$L = fcc + C$	Eutectic	4.26C-95.7Fe
C-Mn	1504	$L = fcc + bcc$	Eutectic	0.25C-99.7Mn
	1493	$L = fcc$	Congruency	1.3C-98.7Mn
C-Mo	2478	$L = bcc + M_2C$	Eutectic	2.54C-97.5Mo
	2478	$L = bcc + M_2C$	Eutectic	2.5C-97.5Mo
Cr-Fe	1788	$L = bcc$	Congruency	20Cr-80Fe
	1789	$L = bcc$	Congruency	21Cr-79Fe
Cr-Mn	1519	$L = bcc$	Melting point Mn	100Mn
	1519	$L = bcc$	Melting point Mn	100Mn
Cr-Mo	2133	$L = bcc$	Congruency	79Cr-21Mo
	2093	$L = bcc$	Congruency	79.1Cr-20.9Mn
Fe-Mn	1507	$L = fcc + bcc$	Eutectic	12.7Fe-87.3Mn
	1505	$L = fcc + bcc$	Eutectic	13Fe-87Mn
Fe-Mo	1723	$L = bcc + R$	Eutectic	64.0Fe-36.0Mo
	1722	$L = bcc + R$	Eutectic	64Fe-36Mo
Mn-Mo	1519	$L = bcc$	Melting point Mn	100Mn
	1519	$L = bcc$	Melting point Mn	100Mn
<i>Ternary</i>				
C-Cr-Fe	1425	$L = fcc + M_3C + C$	Eutectic	4.38C-0.49Cr-95.1Fe
	1426	$L = fcc + C$	Eutectic C-Fe	4.26C-95.7Fe
C-Cr-Mn	1456	$L = fcc + bcc + M_{23}C_6$	Eutectic	1.35C-13.6Cr-85.1Mn
C-Cr-Mo	1739	$L = bcc + M_2C + M_{23}C_6$	Eutectic	3.39C-51.8Cr-44.8Mo
C-Fe-Mn	1350	$L = fcc + M_3C$	Quasibinary eutectic	4.03C-65.7Fe-30.3Mn
	1373	$L = fcc + M_3C$	Quasibinary eutectic	4.25C-45.7Fe-50Mn
C-Fe-Mo	1338	$L = fcc + M_3C + M_2C$	Eutectic	4.25C-81.3Fe-14.5Mo
	1358	$L = fcc + M_3C + M_2C$	Eutectic	3.63C-82.6Fe-13.7Mo
C-Mn-Mo	1485	$L = fcc + bcc + M_2C$	Eutectic	0.84C-82.9Mn-16.3Mo
Cr-Fe-Mn	1507	$L = fcc + bcc$	Eutectic Fe-Mn	12.7Fe-87.3Mn
	1505	$L = fcc + bcc$	Eutectic Fe-Mn	13Fe-87Mn
Cr-Fe-Mo	1726	$L = bcc + R$	Eutectic Fe-Mo	64.0Fe-36.0Mo
	1618	$L = bcc + R + \tau$	Eutectic	11.0Cr-59.0Fe-30.0Mo
Cr-Mn-Mo	1519	$L = bcc$	Melting point Mn	100Mn
Fe-Mn-Mo	1501	$L = fcc + bcc + \sigma$	Eutectic	25.5Fe-60.3Mn-14.3Mo
<i>Quaternary</i>				
C-Cr-Fe-Mn	1362	$L = fcc + M_3C + M_7C_3$	Quasiternary eutectic	3.77C-3.74Cr-58.1Fe-34.4Mn
C-Cr-Fe-Mo	1338	$L = fcc + M_3C + M_2C$	Eutectic C-Fe-Mo	4.25C-81.3Fe-14.5Mo
C-Cr-Mn-Mo	1456	$L = fcc + bcc + M_{23}C_6$	Eutectic C-Cr-Mn	1.35C-13.6Cr-85.1Mn
C-Fe-Mn-Mo	1309 ^a	$L = fcc + M_3C + M_2C + M_7C_3$	Eutectic	3.99C-64.2Fe-21.4Mn-10.4Mo
Cr-Fe-Mn-Mo	1501	$L = fcc + bcc + \sigma$	Eutectic Fe-Mn-Mo	25.5Fe-60.3Mn-14.3Mo
<i>Quinary</i>				
C-Cr-Fe-Mn-Mo	1309	$L = fcc + M_3C + M_2C + M_7C_3$	Eutectic C-Fe-Mn-Mo	3.99C-64.2Fe-21.4Mn-10.4Mo

^a Lowest melting point eutectic.

Figure 2.17 represents the predicted phase diagram for the Fe-10Cr-C alloy series which was suggested earlier from the Fe-Cr-C liquidus projection as exhibiting a low melting point close to 1200°C. The eutectic point from Figure 2.16 shows the

predicted value is close to the experimental data determined by Thorpe and Chico [33].

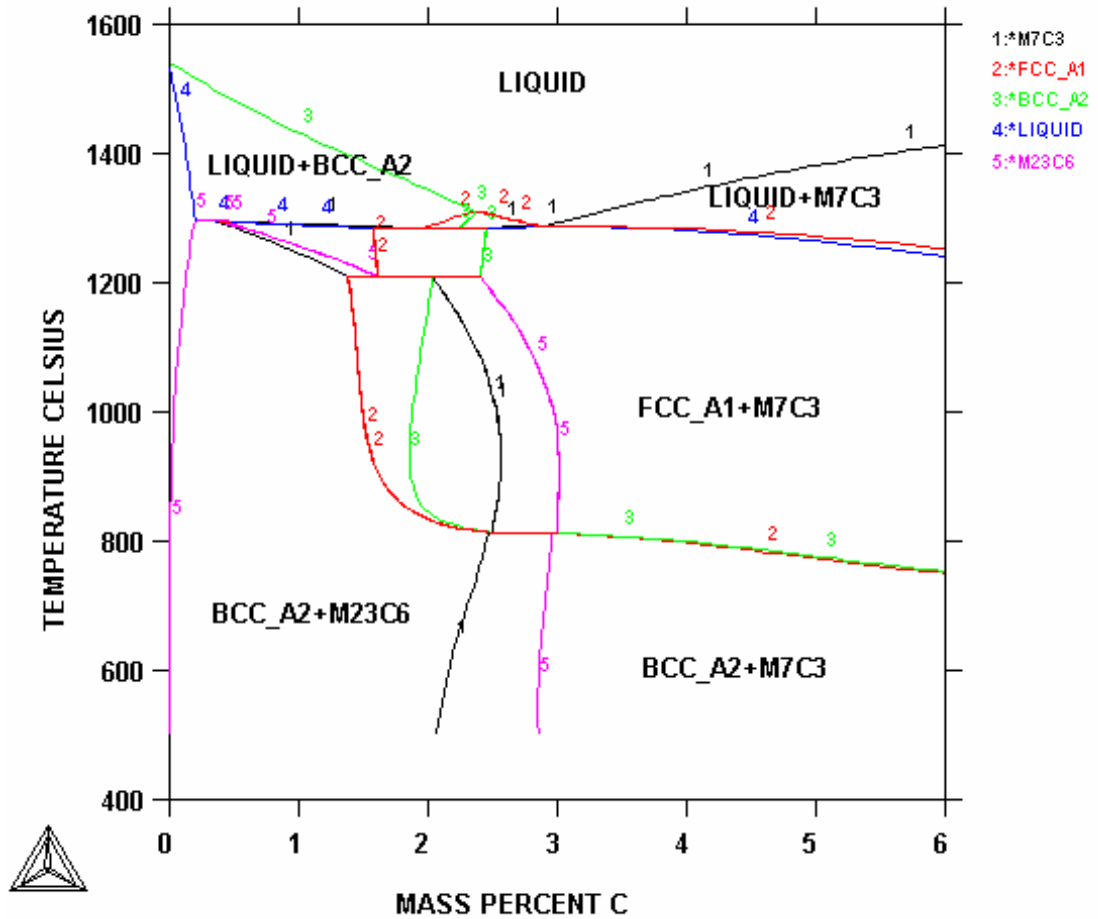


Figure 2.16: Calculated phase diagram for the Fe-30Cr-C alloy series [34]

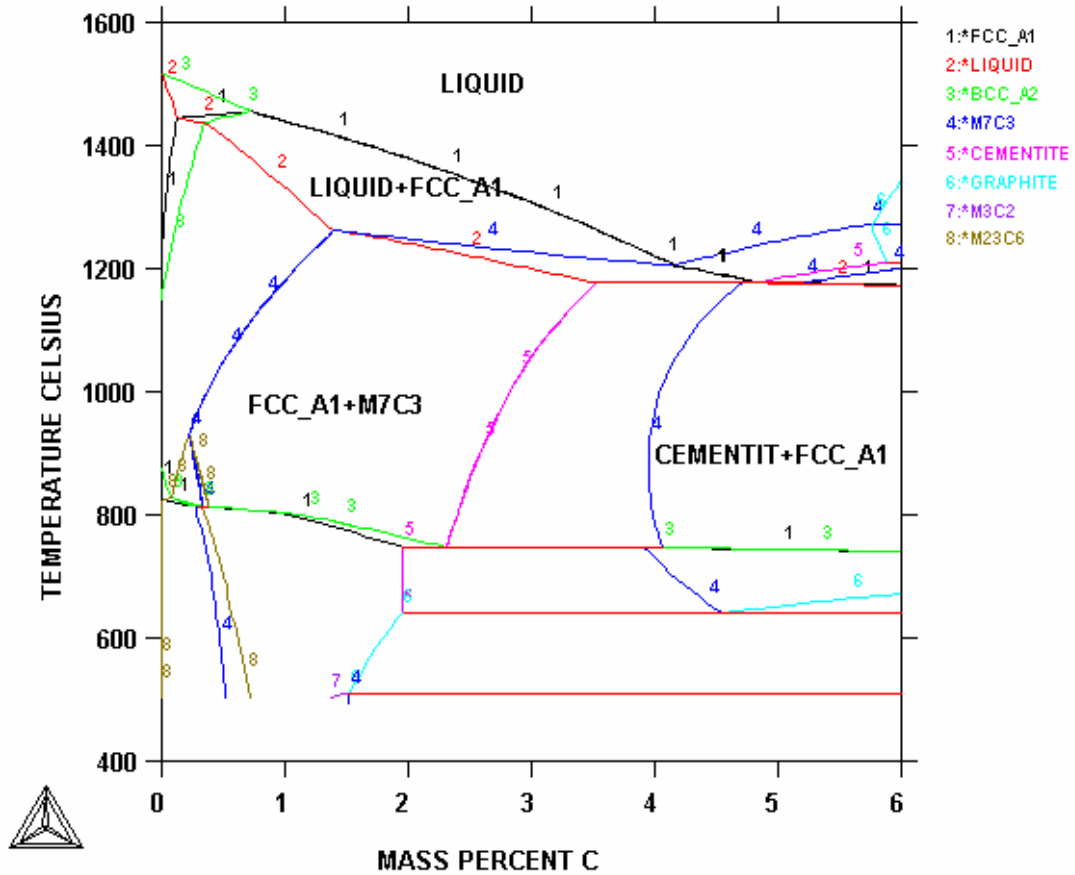


Figure 2.17: Calculated phase diagram for the Fe-10Cr-C alloy series [34]

Commercial alloys normally contain approximately 0.5 weight percent silicon, and nominally 1.0 weight percent manganese. The target alloy microstructure for a balanced combination of toughness and wear resistance should contain a high proportion of retained austenite with a high carbide volume fraction. Increasing the manganese content and adding nickel to the alloy will provide an increased proportion of retained austenite in the as-cast microstructure.

If the chromium content drops too low beyond the 10 to 12 weight percent chromium level towards the U2 triple point (refer Figure 2.13), the carbide formed will be a combination of M_7C_3 with some M_3C . The M_3C carbide has a lower hardness compared to the M_7C_3 carbide and will potentially reduce the wear performance of the low melting point alloy.

To overcome the potential for the formation of M_3C carbide, the chromium content should be increased to approximately 12 weight percent. The predicted phase diagram for the Fe-12Cr-C alloy system is shown in Figure 2.18.

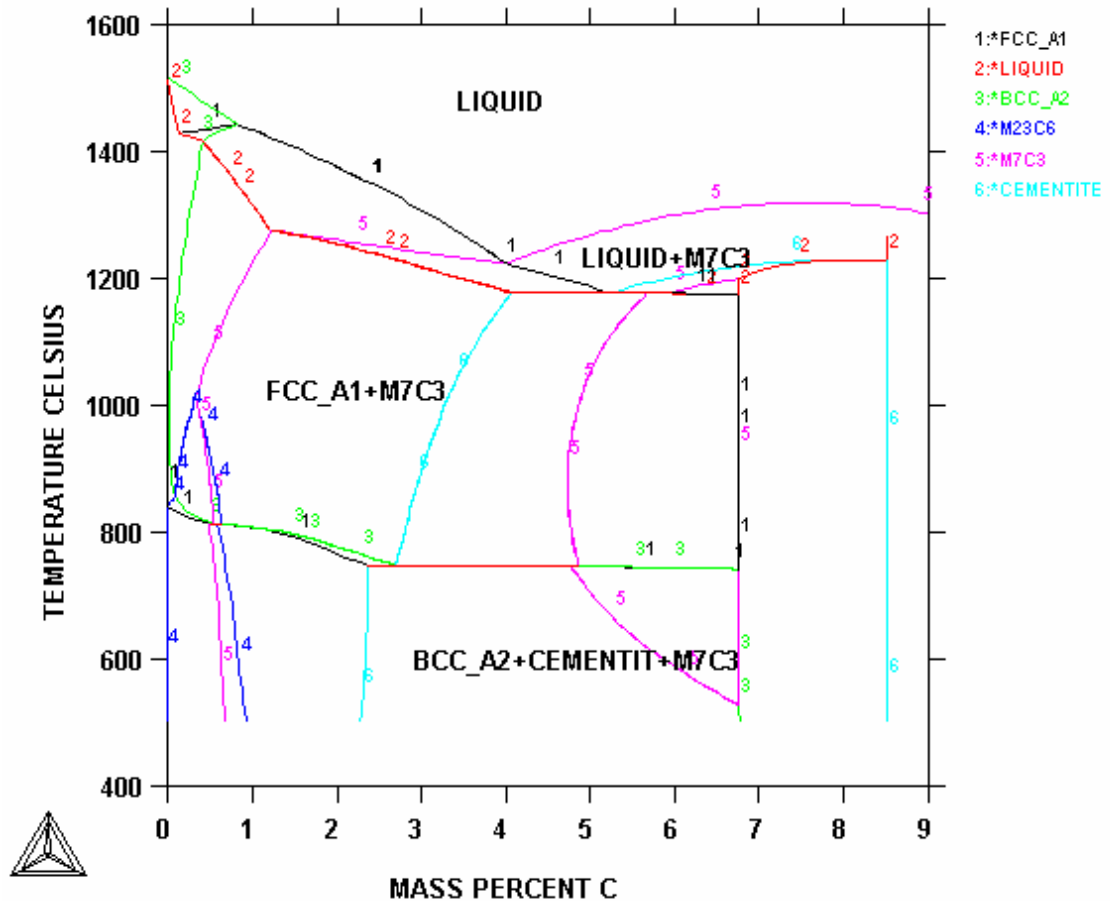


Figure 2.18: Calculated phase diagram for Fe-12Cr-C alloy series [34]

Figure 2.18 suggests the target alloy composition of Fe-12Cr-4C should have a liquidus temperature of approximately 1200°C.

Using the Lever Rule the estimated carbide volume fraction (CVF) can be determined for the eutectic composition as follows (refer to Figure 2.19):

$$\text{CVF} = \frac{(4.0 - 1.2)}{(8.6 - 1.2)} \times 100 \% = 37.8 \%$$

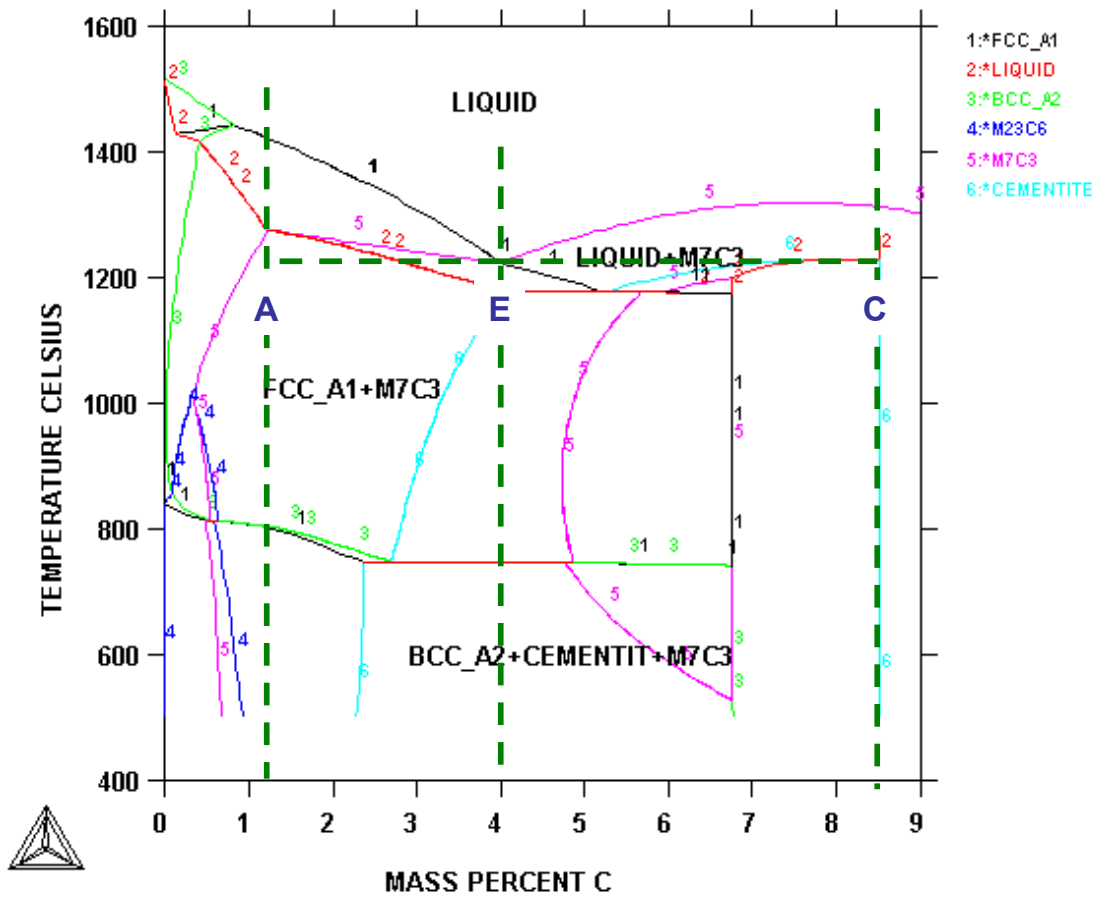


Figure 2.19: Compositional end points for Fe-12Cr-C phase diagram [34]

The potential effect for addition of silicon, manganese and nickel to the Fe-12Cr-C alloy system predicted phase diagram is shown in Figure 2.20 (based on ThermoCalc). Note the addition of the silicon, manganese and nickel has increased the predicted liquidus temperature to approximately 1230°C. The eutectic carbon content has also slightly reduced to approximately 3.6 to 3.7 weight percent.

Figure 2.20 also suggests the presence of a quasi-peritectic reaction of:



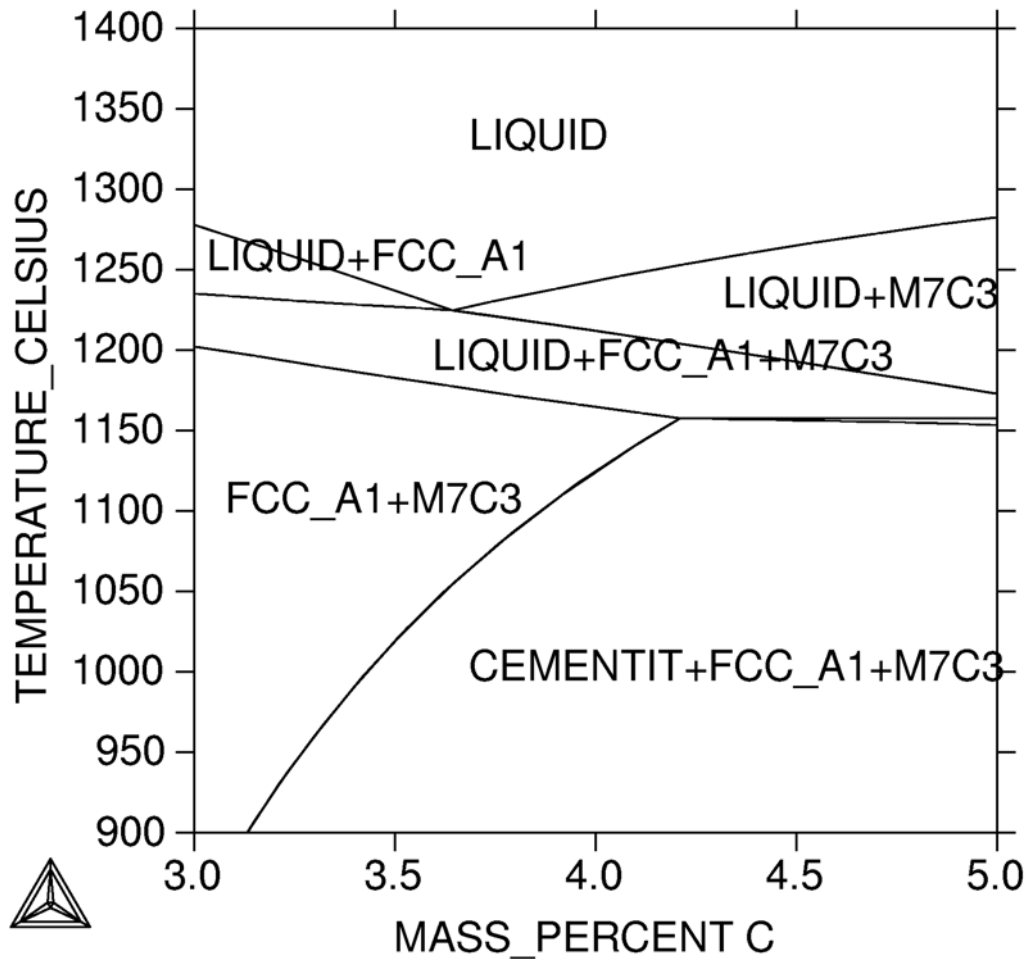


Figure 2.20: Calculated phase diagram for the Fe-12Cr-1.0Ni-0.6Si-1.6Mn-C alloy series [38]

The results of the phase diagram analysis for the Fe-12Cr-C alloy series suggest the liquidus temperature will be close to the target of 1200°C, and the microstructure should be near the eutectic of M_7C_3 carbides with an austenitic (with some M_3C peritectic) ferrous matrix.

The predicted phase diagram for the same Fe-12Cr-1.0Ni-0.6Si-1.6Mn-4C alloy from a separate computer software package, FACTSAGE, is shown in Figure 2.21.

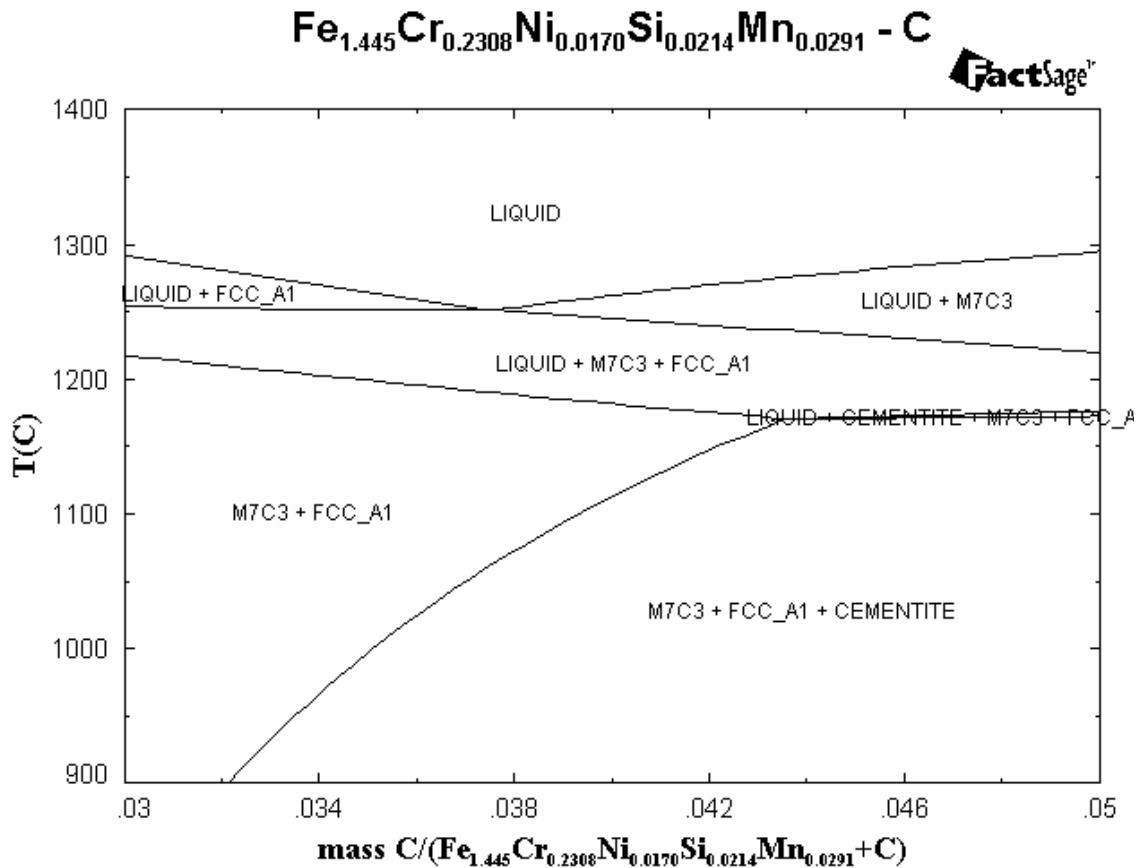


Figure 2.21: Calculated phase diagram from FACTSAGE for the Fe-12Cr-1.0Ni-0.6Si-1.6Mn-4C alloy [39]

In summary, the review of past work conducted on the Fe-Cr-C phase diagram suggests an alloy having the a nominal composition of Fe-12Cr-1.0Ni-0.6Si-1.6Mn-4.0C will exhibit a eutectic microstructure consisting of M_7C_3 eutectic carbide, with M_3C carbide surrounding M_7C_3 carbide particles, with austenite and ledeburite. The estimated liquidus temperature for this alloy is 1200°C. The computer generated phase diagrams predict a higher eutectic temperature of approximately 1230°C.

2.7 DETERMINATION OF PREDICTED ALLOY MICROCONSTITUENT COMPOSITIONS

Previous work [40] has been conducted to determine the phase compositions for a series of white cast irons using energy dispersive spectroscopy (EDS) from a scanning electron microscope (SEM). The dispersion of elements including carbon, chromium, manganese, silicon, nickel and molybdenum were determined for the carbides and ferrous matrix, and compared to the overall bulk chemical analysis for each sample. The data from this previous work is summarised in Table 2.9 to 2.11 for the hypoeutectic, eutectic and hypereutectic alloy compositions.

The following generalisations can be extracted from the data shown in Tables 2.9 to 2.11:

- i. Chromium partitions to the carbides;
- ii. The presence of primary carbides in the microstructure will result in higher chromium content in the primary carbides compared to the eutectic carbides
- iii. Manganese and nickel partition more to the ferrous matrix, but are still found in the carbides;
- iv. Silicon preferentially partitions to the ferrous matrix, and is essentially excluded from the carbides;
- v. Carbon is primarily taken up by the formation of the carbides, and the residual carbon of the ferrous matrix will be dependent on the final phase at room temperature.
- vi. Austenitic ferrous phases can contain up to 1.2 weight percent carbon
- vii. Ferritic ferrous phases have negligible carbon present
- viii. Molybdenum has a low solid solubility in the ferrous phases (both austenite and ferrite), and excessive molybdenum will form separate Mo_2C carbides.

Table 2.9: Typical phase microanalysis results for hypoeutectic white iron [40]

PHASE ANALYSIS FOR Fe-30Cr-2.1C-2Mn-0.5Si ALLOY

Element	Primary Fe	Eutectic Fe	Eutectic M_7C_3	BULK SEM CALC	BULK OES ACT
Fe	75.9	76.1	23.9	66.3	65.0
Cr	20.6	20.3	65.3	28.7	30.2
Mn	1.9	2.1	1.6	2.0	1.8
Si	0.7	0.7	<0.1	0.6	0.5
C	0.6	0.6	8.8	2.1	2.1
vol %	20.6	60.8	18.6		

Table 2.10: Typical phase microanalysis results for eutectic white iron [40]

PHASE ANALYSIS FOR Fe-30Cr-3.0C-2Mn-0.5Si ALLOY

Element	Fe Matrix	Eutectic M_7C_3	Primary M_7C_3	BULK SEM CALC	BULK OES ACT
Fe	78.7	27.8	27.3	64.7	64.2
Cr	17.9	61.2	62.2	29.8	30.0
Mn	1.9	1.8	1.4	1.9	2.0
Si	0.7	<0.1	<0.1	0.5	0.5
C	0.8	8.8	8.8	3.0	2.9
vol %	72.6	25.0	2.4		

Table 2.11: Typical phase microanalysis results for hypereutectic white iron [40]

PHASE ANALYSIS FOR Fe-30Cr-4.4C-2Mn-0.5Si ALLOY

Element	Fe Matrix	Eutectic M ₇ C ₃	Primary M ₇ C ₃	BULK SEM CALC	BULK OES ACT
Fe	83.7	37.6	33.3	63.5	62.8
Cr	11.2	51.3	56.3	29.1	30.0
Mn	2.3	2.0	1.4	2.0	2.1
Si	1.1	<0.1	<0.1	0.6	0.5
C	1.2	8.7	8.8	4.4	4.4
vol %	58.2	19.3	22.5		

Based on the liquidus projection shown in Figure 2.13, the following empirical relationships can be established to estimate the phase volume fractions for the Fe-Cr-C alloy series:

$$\begin{aligned} \text{Eutectic trough carbon \% (ETC\%)} &= 5.8245 \times 10^{-5} (\text{Cr\%})^3 - 3.2460 \times 10^{-3} (\text{Cr\%})^2 \\ &\quad - 3.9451 \times 10^{-3} (\text{Cr\%}) + 4.4769 \end{aligned} \quad (\text{Equ 2})$$

where: Cr% = overall chromium weight percent of alloy

$$\text{Eutectic carbide volume fraction \% (ECVF\%)} = \frac{(\text{ETC\%} - 1.2)}{(8.8 - 1.2)} \times 100 \quad (\text{Equ 3})$$

$$\text{Primary carbide volume fraction (PCVF\%)} = \frac{(\text{Bulk C\%} - \text{ETC\%})}{(8.8 - \text{ETC\%})} \times 100 \quad (\text{Equ 4})$$

where: Bulk C% = overall carbon weight percent of alloy

$$\text{Primary ferrous matrix volume fraction (PFMVF\%)} = \frac{(\text{ETC\%} - \text{Bulk C\%})}{(\text{ETC\%} - 1.2)} \times 100 \quad (\text{Equ 5})$$

Using the chemical analysis data presented in Tables 2.9 to 2.11, and Equations 2 to 5, the following empirical relationships can be established to estimate the individual phase compositions:

$$\begin{aligned} \text{Eutectic Carbide Chromium Content \% (EC Cr\%)} = & 3.8596 \times 10^{-2} (\text{Cr/C})^4 - 1.2063 \times 10^{-1} (\text{Cr/C})^3 \\ & + 8.1039 \times 10^{-1} (\text{Cr/C})^2 + 6.3714 (\text{Cr/C}) \\ & - 3.1681 \times 10^{-2} \end{aligned}$$

(Equ 6)

Where: Cr/C = Chromium/carbon ratio

The relationship between Eutectic Carbide chromium content and the alloy chromium/carbon ratio is shown in Figure 2.22.

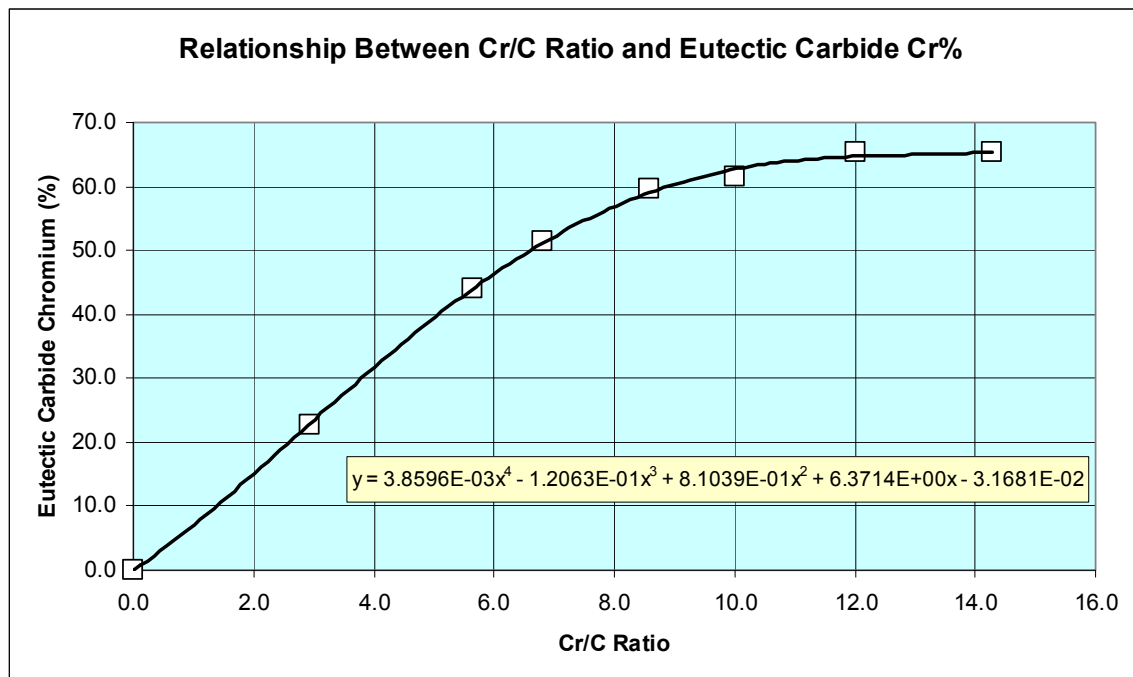


Figure 2.22: Relationship between eutectic carbide chromium content and the alloy chromium/carbon ratio

$$\text{Primary Carbide Chromium Content \% (PC Cr\%)} = (\text{EC Cr\%}) \times (-0.0254 (\text{Cr/C}) + 1.2719) \quad (\text{Equ 7})$$

$$\text{Ferrous Matrix Chromium Content \% (FM Cr\%)} = (\text{EC Cr\%}) \times (0.0088 (\text{Cr/C}) + 0.199) \quad (\text{Equ 8})$$

Additional elemental relationships can be summarised as provided in Table 2.12.

Table 2.12: Phase elemental distributions (based on empirical data) [40]

Element	Ratio of Phase Element % to Total Alloy Element %			
	Primary Carbide	Eutectic Carbide	Eutectic Ferrous Matrix	Primary Ferrous Matrix
Mn	0.7	0.9	1.2	1.3
Ni	0.6	0.8	1.1	1.3
Si	0.0	0.0	1.4	1.6

Based on the proposed target composition of Fe-12Cr-1.0Ni-0.6Si-1.6Mn-4.0C, the formulas in Equations 6 to 8 and the ratios shown in Table 2.12 can be used to determine the estimated phase compositions. The estimated compositions are summarised in Table 2.13.

Table 2.13: Estimated phase compositions for proposed Fe-12Cr-1.0Ni-0.6Si-1.6Mn-4.0C alloy

Alloy Composition	Weight (%)	Primary Carbide	Eutectic Carbide	Eutectic Matrix	Primary Matrix	Estimated Bulk Analysis
C	4.0	8.8	8.8	1.2	1.2	4.0
Cr	12.0	28.0	23.4	5.3	0.0	11.9
Mn	1.6	0.0	1.4	1.9	2.1	1.6
Si	0.6	0.0	0.0	0.8	1.0	0.5
Ni	1.0	0.0	0.8	1.1	1.3	1.0
Mo	0.0	0.0	0.0	0.0	0.0	0.0
Volume Fraction (%)		0.0	36.8	61.0	2.2	100.0

2.8 EXPERIMENTAL DEVELOPMENT OF LOW MELTING POINT ALLOY

The experimental development of the low melting point alloy involved the systematic melting and casting of a range of alloy compositions and incorporating analytical measurements including thermal analysis, chemical analysis and metallography.

The range of alloy compositions studied is summarised in Table 2.14.

Each alloy composition (charge) was produced from commercial foundry grade raw materials including ferrochrome, ferrosilicon, electrolytic manganese, nickel pellets, steel scrap and graphite. The charge was then melted in an Inductotherm 75kW, 50kg pop-up induction melting furnace using clay graphite crucibles and heated to a temperature of 1500°C.

When the molten charge was at the required temperature, a small sample was obtained from the melt using refractory insulated cups and poured into a steel chemical analysis mould to produce an analysis button. The analysis button was then surface ground and the chemical composition measured using a Hilger Optical Emission Spectrometer calibrated against standard white iron alloys.

Minor additions to adjust the chemical analysis to the required composition were then added to the melt, and a final chemical analysis button obtained.

After the composition was confirmed as correct, a large refractory cup was used to remove a 1kg sample of superheated alloy for thermal analysis recording. The molten alloy was poured into an insulated refractory cup which had been placed into a sand bucket. A glass-sheathed Type R thermocouple was positioned into the insulated cup so that the tip of the thermocouple sits at the centre of the cup. The Type R thermocouple is connected to a commercially available thermal analysis system, MeltLab, which records the cooling temperature of the insulated cup at 1

second intervals. The setup for the thermal analysis is shown diagrammatically in Figure 2.23.

After the recording of the temperature cooling curve was completed, a small addition of carbon was then added to the molten charge still in the furnace, and further progressive thermal curves collected.

At the completion of the thermal analysis, each sample was sectioned and polished to check and review the microstructure, and collated against the thermal cooling curve. The thermal cooling curves were then analysed to determine the thermal arrests representing the liquidus and solidus reactions.

Table 2.14: Summary of test alloy compositions

Alloy	Element Composition (weight %)					
	Cr	C	Si	Mn	Ni	Fe
A1	8.0	3.4	0.5	2.0	0.0	Bal
A2	8.0	3.6	0.5	2.0	0.0	Bal
A3	8.0	3.9	0.5	2.0	0.0	Bal
A4	8.0	4.2	0.5	2.0	0.0	Bal
B1	10.0	3.3	0.5	1.6	1.0	Bal
B2	10.0	3.6	0.5	1.6	1.0	Bal
B3	10.0	4.1	0.5	1.6	1.0	Bal
C1	12.0	4.1	0.6	1.6	1.0	Bal

Selected scanning electron microscopy (SEM) was conducted on the final alloy selected for the low melting point to determine the individual microconstituent phase analyses using energy dispersive spectroscopy, and to examine the microstructure in more detail. X-ray Mapping (XRM) using EDS spectra was collected for the selected low melting point alloy using a Moran Scientific Chemical Analysis system.

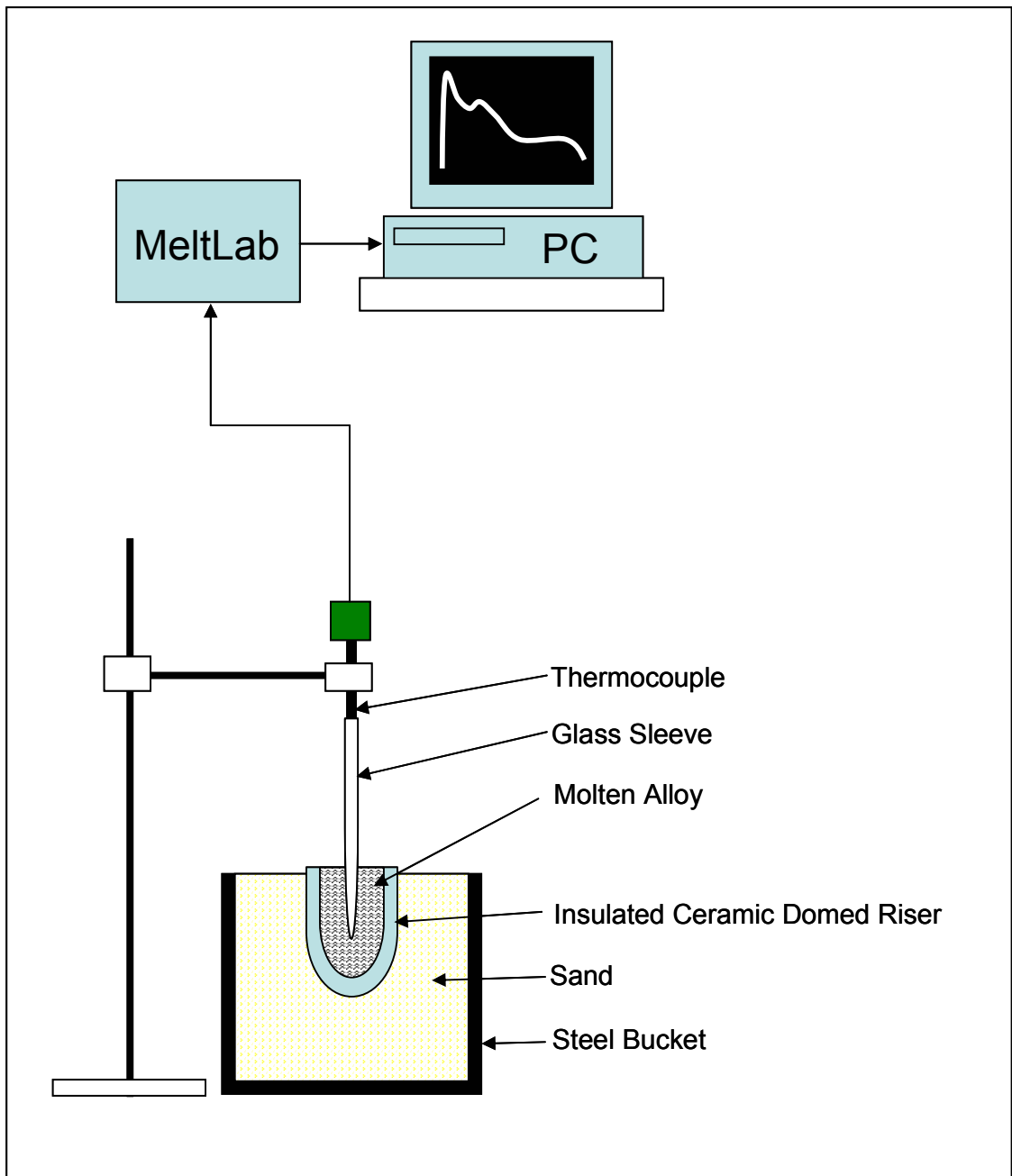


Figure 2.23: Schematic diagram for thermal analysis setup.

2.9 RESULTS AND DISCUSSION

The alloy compositions that make up the group of trial alloys from the range shown in Table 2.14 are shown relative to the published data from Thorpe and Chico [33] in Figure 2.24.

The proximity of the Fe-8Cr-2Mn-0.5Si-C series to the M_3C phase boundary suggests these alloys will form predominantly M_3C carbides during solidification.

Based on the position of the Fe-10Cr-2Mn-0.5Si-4.1C alloy to the liquidus projection, it would be expected this alloy to be essentially eutectic in nature.

The Fe-12Cr-1.6Mn-1.0Ni-0.5Si-4.1C alloy is also shown overlaying the eutectic trough for the liquidus projection.

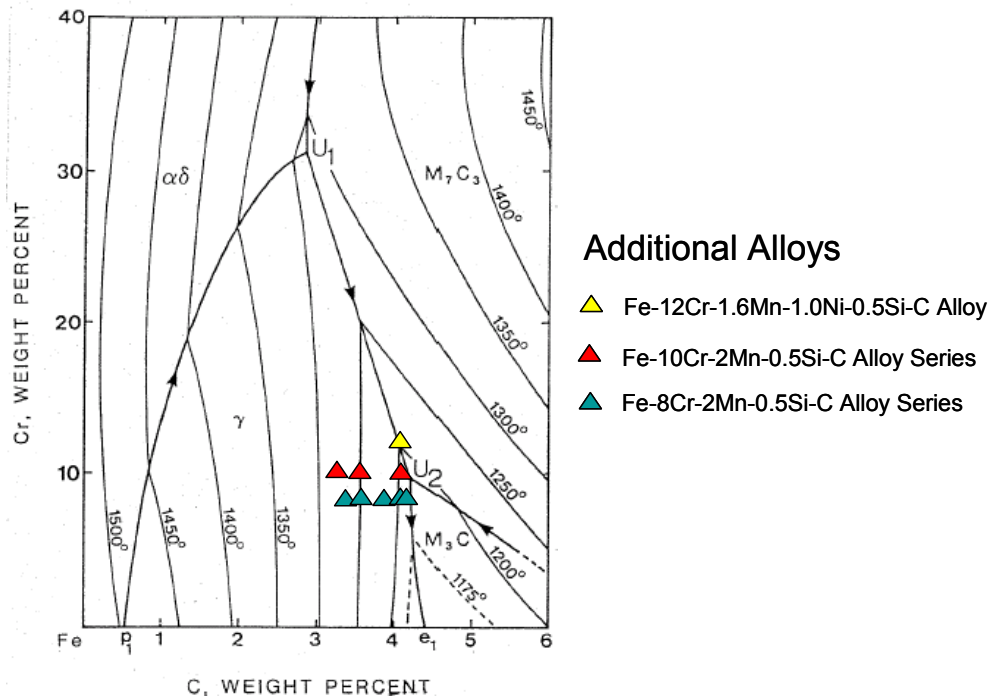


Figure 2.24: Relationship of trial alloy compositions to Fe-Cr-C phase diagram (by Thorpe and Chico [33])

Each of the alloy melts produced in the induction furnace exhibited excellent melting characteristics with minimal slag development, high fluidity and clean, oxide free metal. Pouring of the alloy melts was highly compatible with standard high chromium white irons, with minimal dross and inclusions. The liquid melt surface exhibited low oxide formation and exhibited high flow movement under power from the induction furnace. Overall all of the trial alloys exhibited favourable characteristics for foundry applications.

2.9.1 Metallography

The microstructures for the test alloys are summarised in Table 2.15.

The microstructure for the target composition low melting point alloy (Alloy C1) is shown in Figures 2.25 and 2.26. The microstructure consists of eutectic M_7C_3 carbides with some M_3C carbide covering the M_7C_3 carbides as a result of the quasi-peritectic reaction, and a ferrous matrix of ledeburite with retained austenite.

Using the Image Tool [41] software, thresholding of the grey scale image was used to determine the carbide volume fraction (CVF) for the alloy. The CVF was measured to be 38% which compares favourably with the predicted CVF from Section 2.6 of this report of 37.8%.

Table 2.15: Summary of alloy microstructures

Alloy	Microstructure
A1	Primary austenite with partial transformation to ledeburite, and eutectic M_7C_3 with substantial M_3C covering the M_7C_3 carbides
A2	Primary austenite with partial transformation to ledeburite, and eutectic M_7C_3 with substantial M_3C covering the M_7C_3 carbides
A3	Primary austenite with partial transformation to ledeburite, and eutectic M_7C_3 with substantial M_3C covering the M_7C_3 carbides
A4	Primary austenite with partial transformation to ledeburite, and eutectic M_7C_3 with substantial M_3C covering the M_7C_3 carbides
B1	Primary austenite with partial transformation to ledeburite, and eutectic M_7C_3 with M_3C covering M_7C_3 particles
B2	Primary austenite with partial transformation to ledeburite, and eutectic M_7C_3 with M_3C covering M_7C_3 particles
B3	Primary austenite with partial transformation to ledeburite, and eutectic M_7C_3 with M_3C covering M_7C_3 particles
C1	M_7C_3 eutectic, M_3C covering M_7C_3 particles, ledeburite and retained austenite

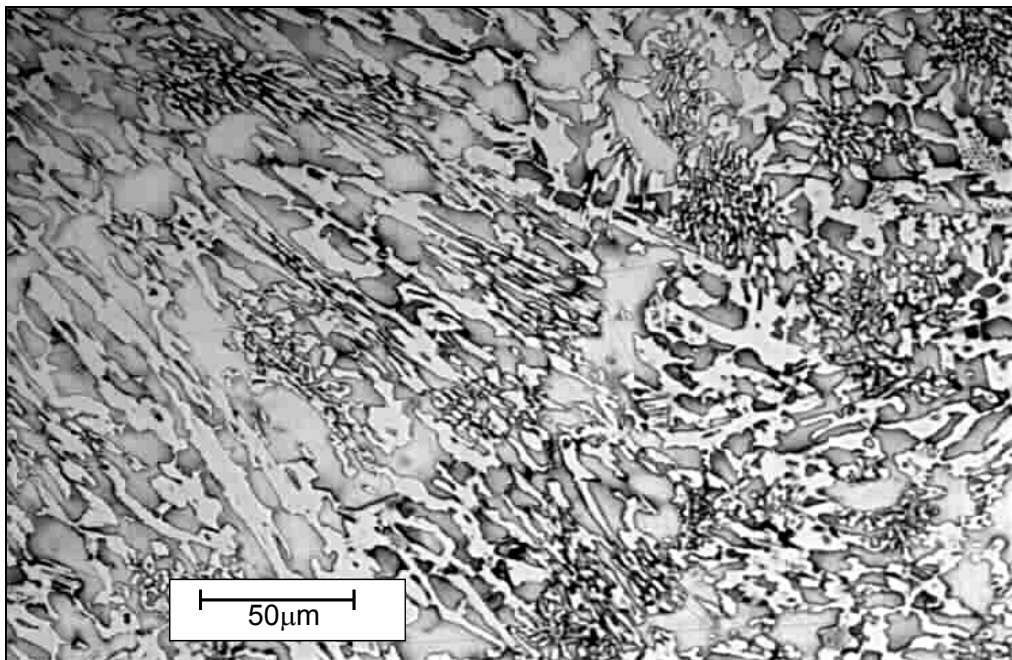


Figure 2.25: Typical microstructure for the Fe-12Cr-1.6Mn-1.0Ni-0.5Si-4.1C (Alloy C1) low melting point white cast iron (etched in acid-ferric chloride)

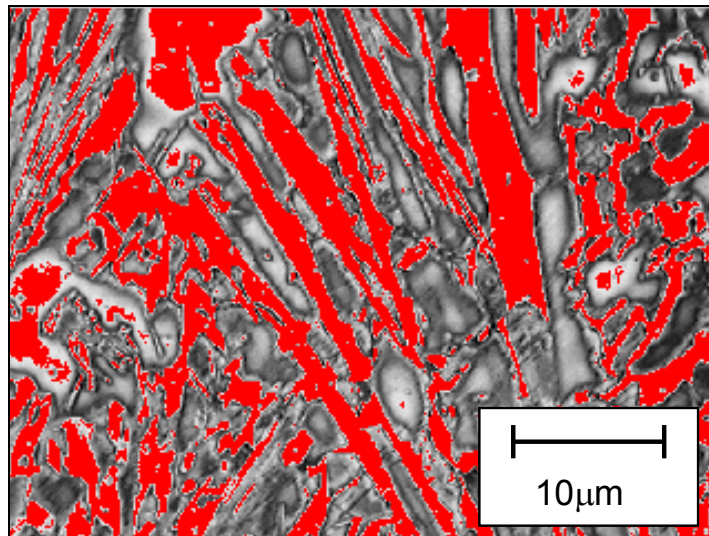


Figure 2.26: Image analysis threshold selection of carbides to determine carbide volume fraction (CVF). Calculated CVF = 38%.

The initial alloy series produced was the Fe-8Cr-2Mn-0.5Si-C series. The liquidus temperatures were not considered low enough to satisfy the requirements for the vacuum heat treatment phase of the study, and the presence of the high volume fraction of M_3C carbide would potentially reduce the abrasive wear performance of the alloy.

The chromium in the alloy was increased to 10 weight percent and the “B” alloy series showed improved liquidus temperature data, and a higher volume fraction of M_7C_3 carbides, however there was still further room for lowering the liquidus temperature and avoiding the detrimental M_3C carbides. It was possible that the presence of manganese may have been acting as a chromium substitute in the alloy. Based on the previous studies on element distribution shown in Table 2.12, nickel partitions slightly less to the carbides compared to manganese, and therefore providing a greater austenite stabilising benefit to the ferrous matrix.

The final target alloy of Fe-12Cr-1.6Mn-1.0Ni-0.5Si-4.1C successfully resulted in a low liquidus temperature and a high volume fraction of retained M_7C_3 carbide. The

addition of nickel has suppressed the transformation of the austenite to ledeburite at moderate cooling rates.

2.9.2 Thermal Analysis

The thermal analysis cooling curves for each alloy are shown in Figures 2.27 to 2.34. Each thermal analysis curve shows an enlarged view for the liquidus and solidus regions. The thermal arrests observed from the thermal analysis cooling curves are summarised in Table 2.16.

The liquidus and solidus for each alloy series is summarised in the form of an experimental phase diagram in Figures 2.35 and 2.36, and compared to the CALPHAD predicted phase diagrams in Figures 2.37 and 2.38.

Table 2.16: Measured thermal arrests for trial alloys

Alloy	Liquidus (°C)	Solidus (°C)
A1	1271	1185
A2	1265	1184
A3	1226	1179
A4	1247	1181
B1	1277	1201
B2	1272	1200
B3	1257	1197
C1	1209	1194

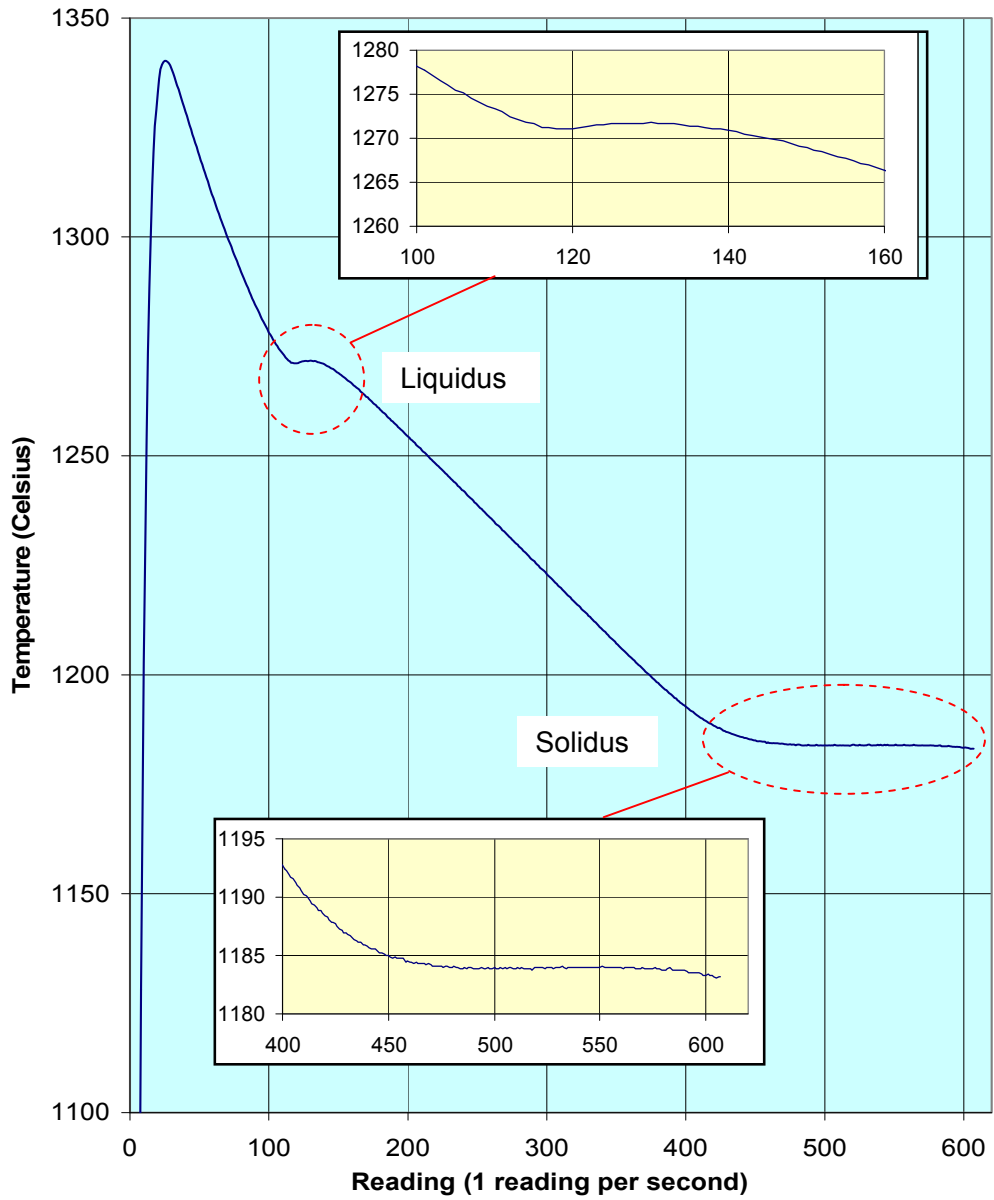


Figure 2.27: Thermal analysis cooling curve for Fe-8.0Cr-2.0Mn-0.5Si-3.4C alloy

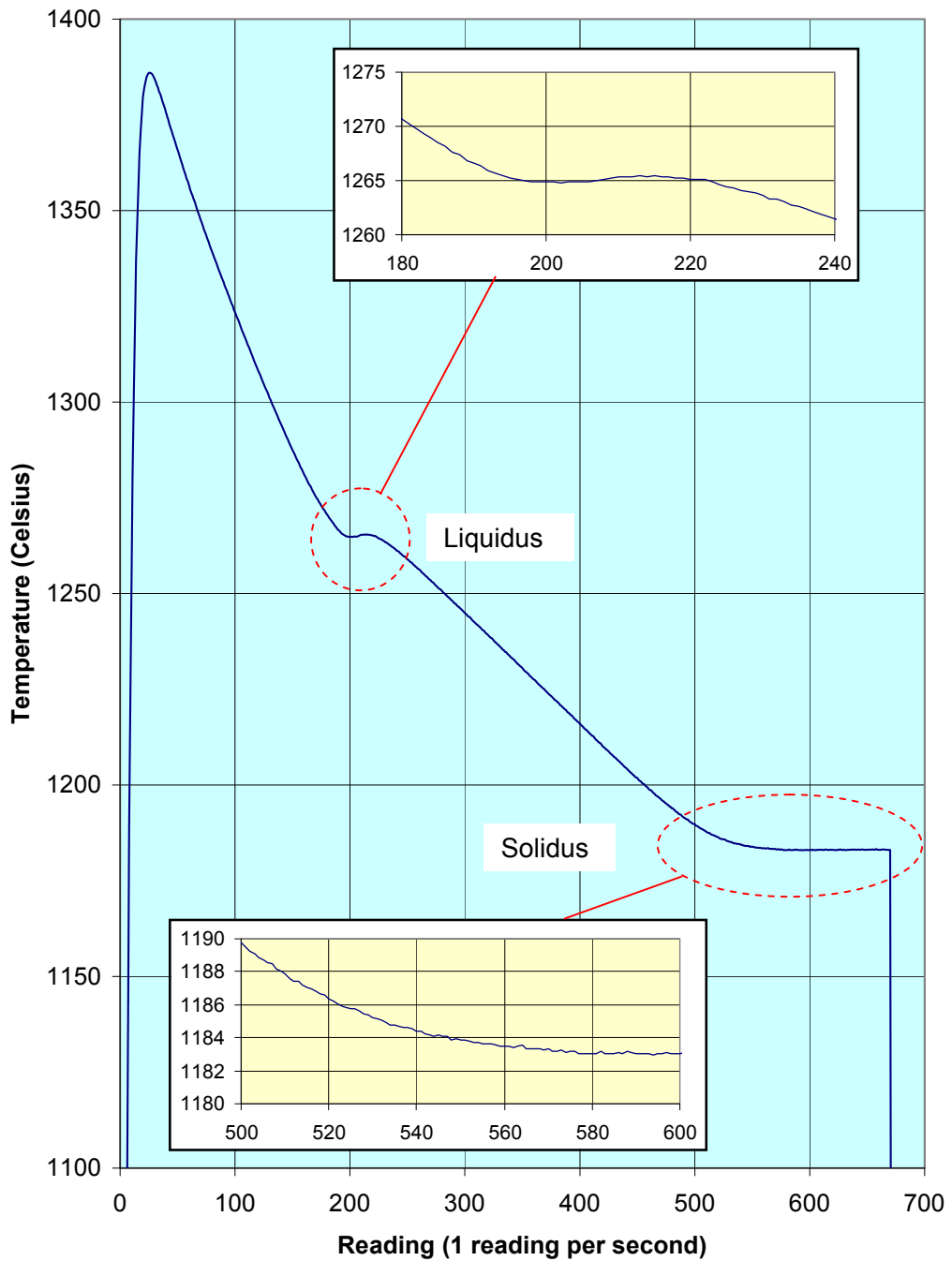


Figure 2.28: Thermal analysis cooling curve for Fe-8.0Cr-2.0Mn-0.5Si-3.6C alloy

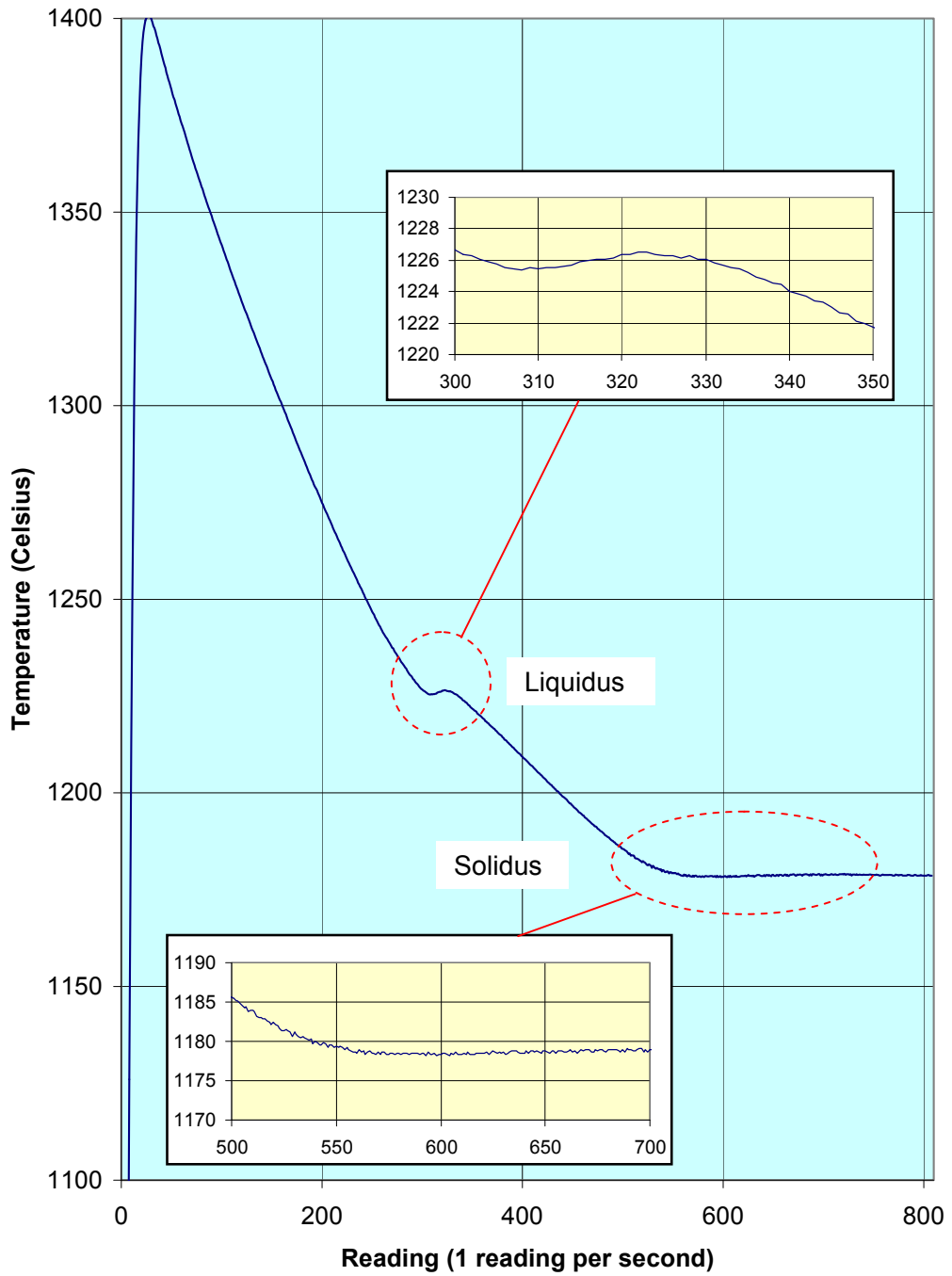


Figure 2.29: Thermal analysis cooling curve for Fe-8.0Cr-2.0Mn-0.5Si-3.9C alloy

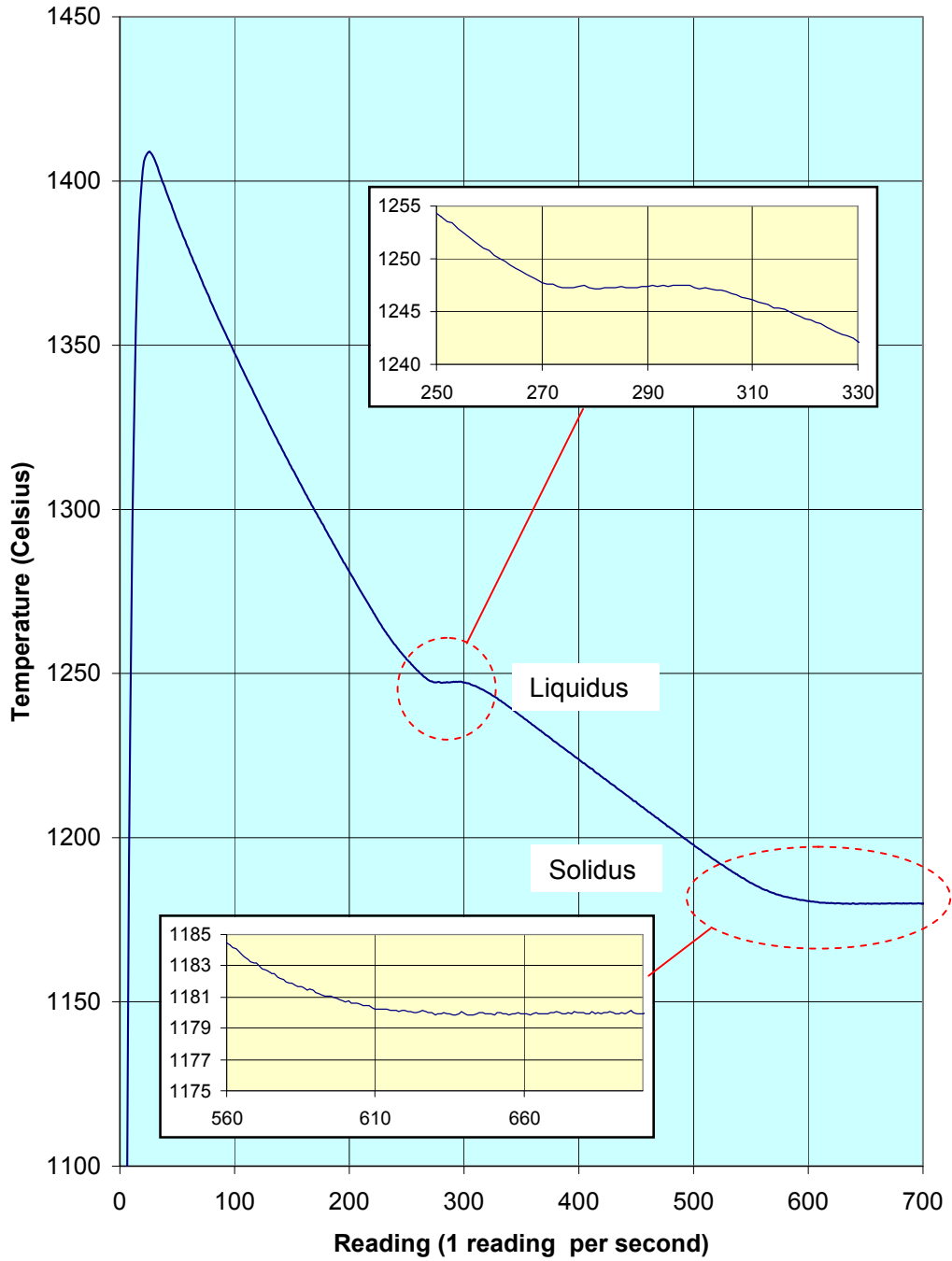


Figure 2.30: Thermal analysis cooling curve for Fe-8.0Cr-2.0Mn-0.5Si-4.2 alloy

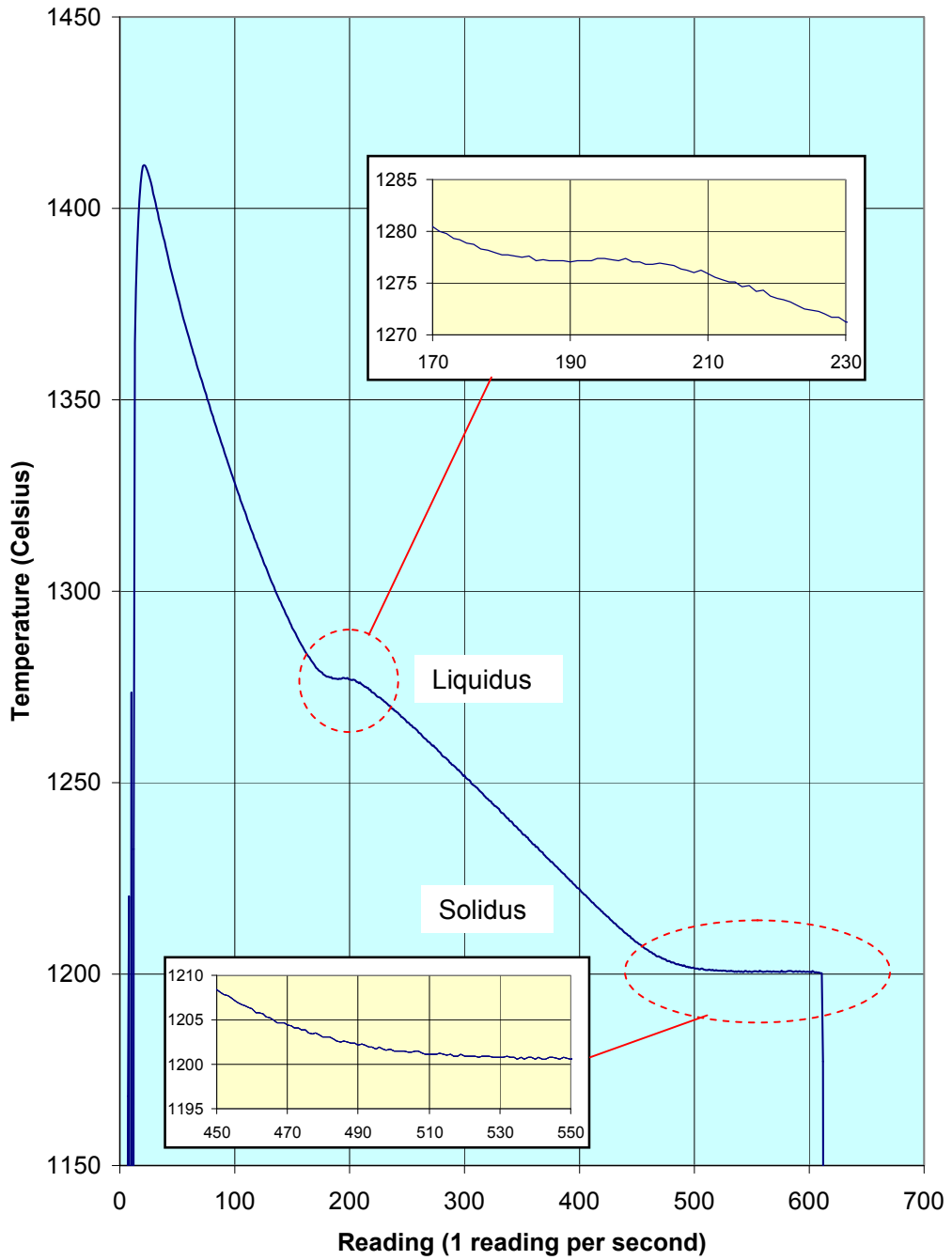


Figure 2.31: Thermal analysis cooling curve for Fe-10.0Cr-2.0Mn-0.7Si-3.3C alloy

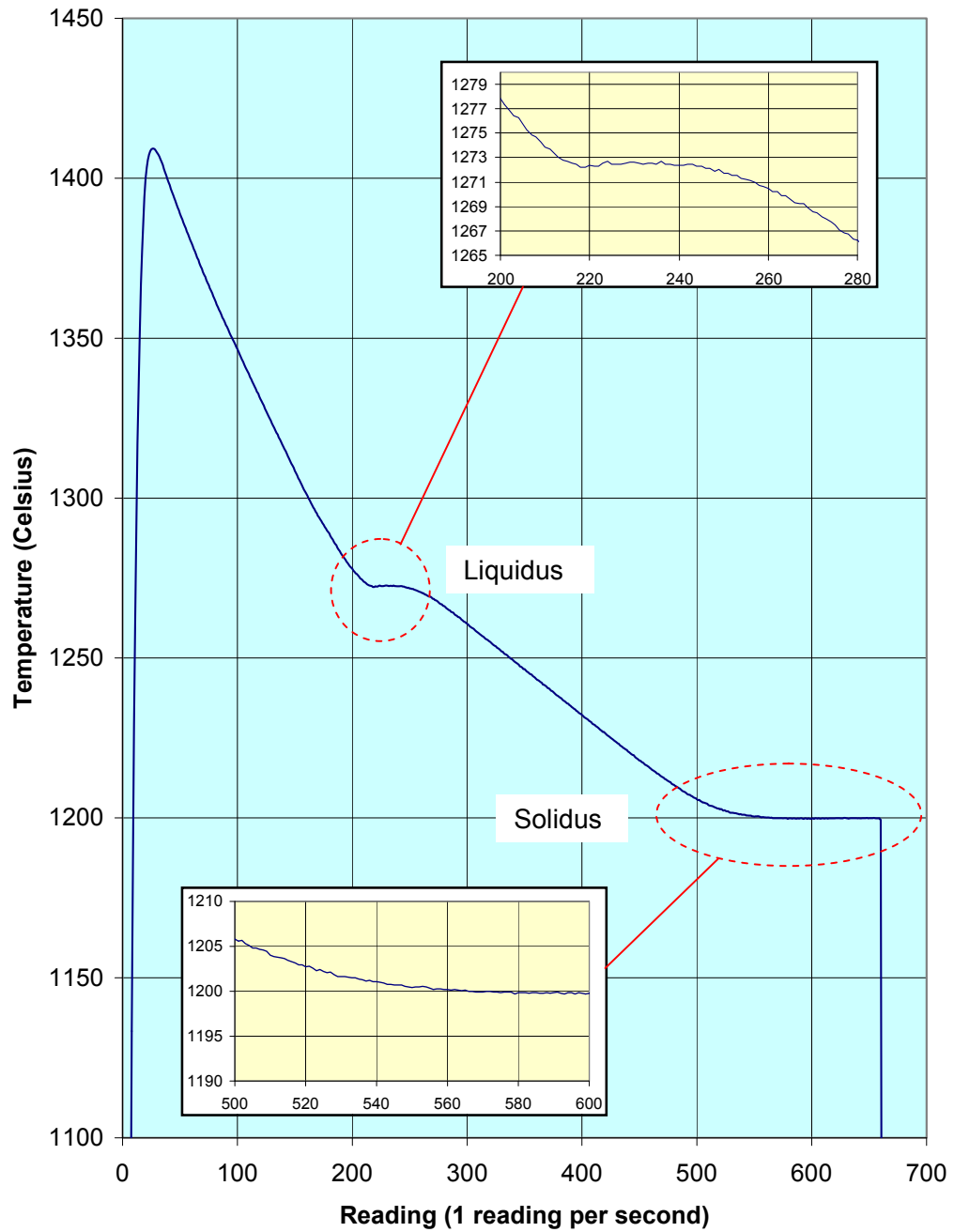


Figure 2.32: Thermal analysis cooling curve for Fe-10.0Cr-2.0Mn-0.7Si-3.6C alloy

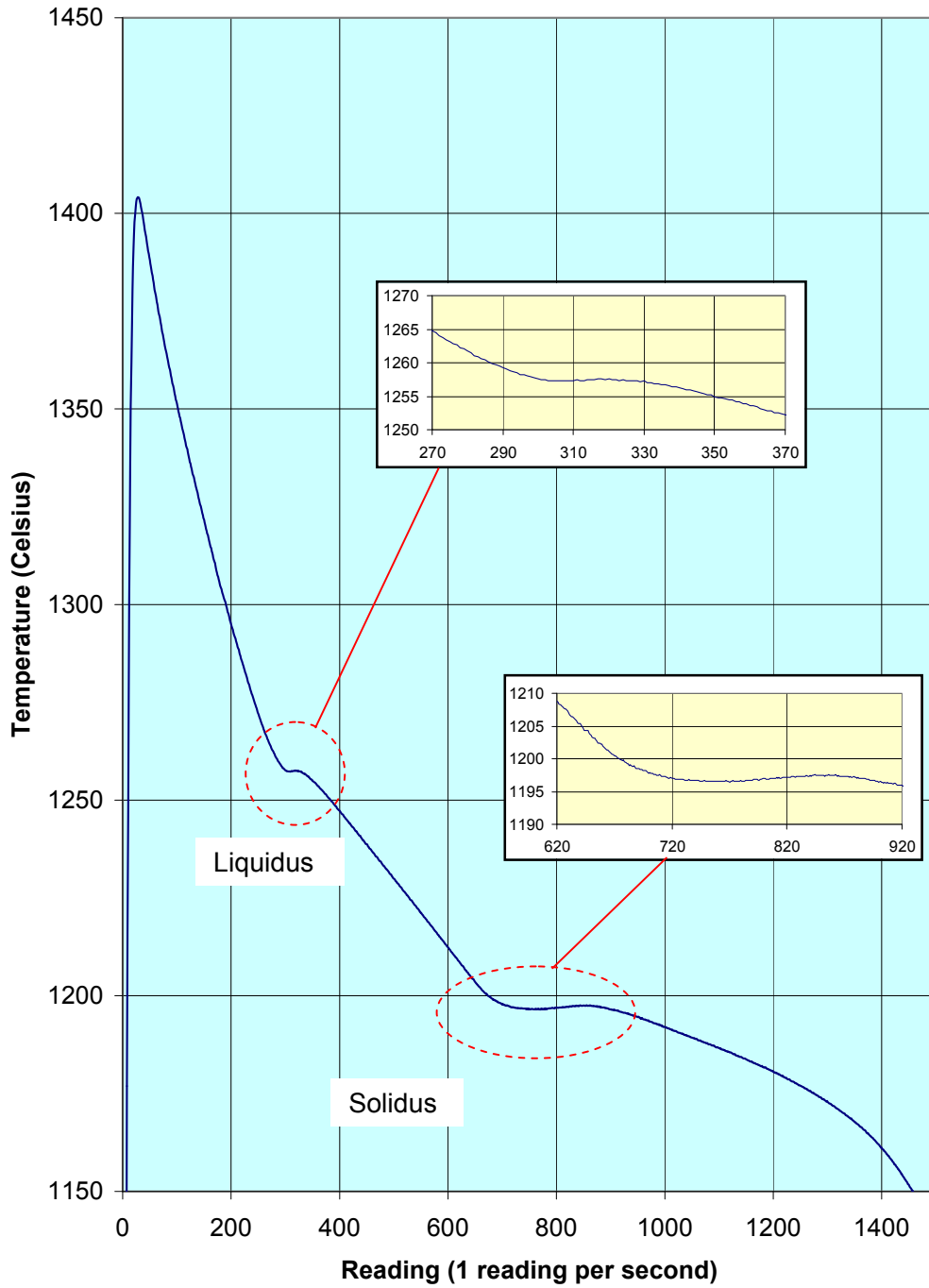


Figure 2.33: Thermal analysis cooling curve for Fe-10.0Cr-2.0Mn-0.7Si-4.1C alloy

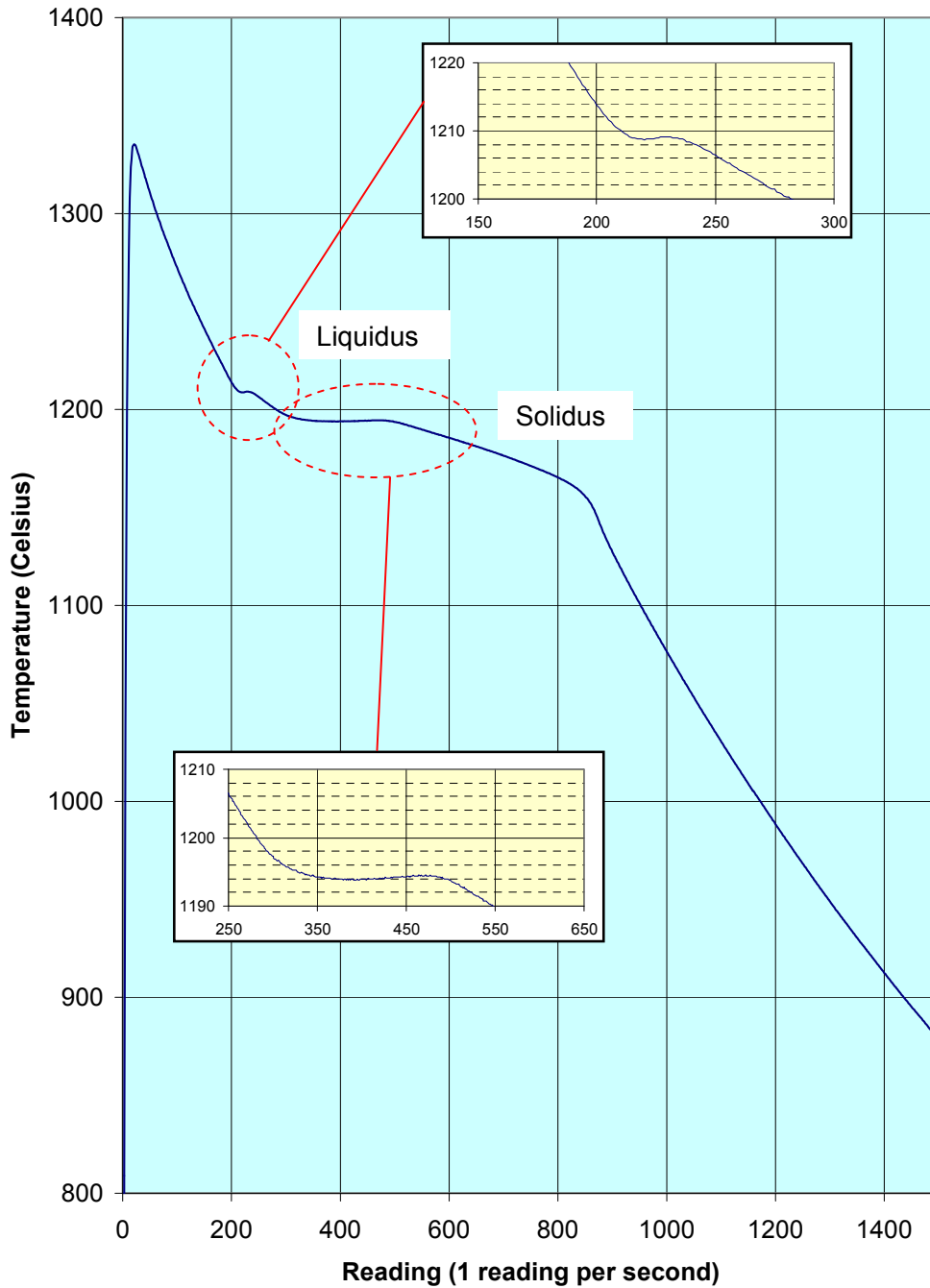


Figure 2.34: Thermal analysis cooling curve for Fe-12.0Cr-1.6Mn-1.0Ni-0.5Si-4.1C alloy

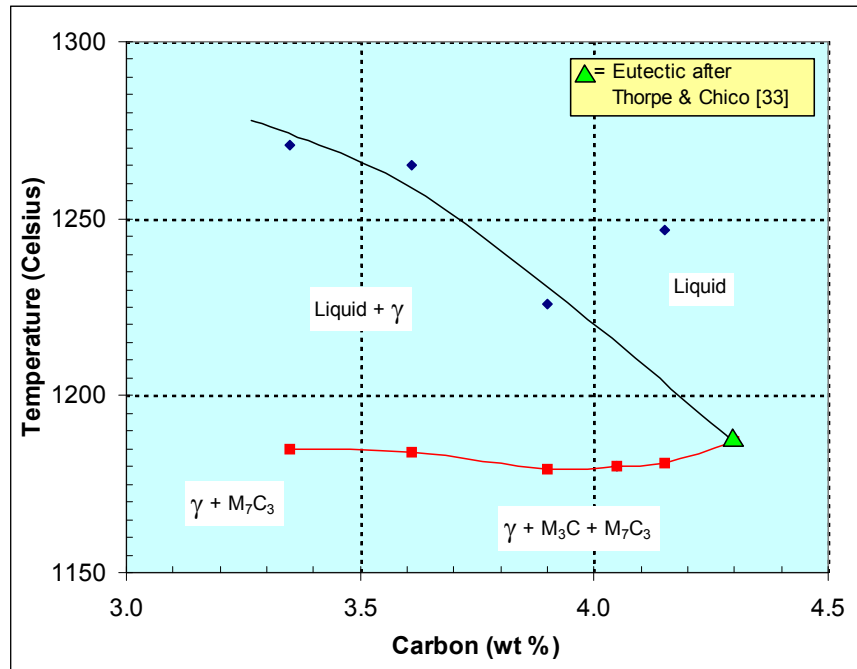


Figure 2.35: Phase diagram based on experimental data for Fe-8Cr-2Mn-0.5Si-C alloy series with published data from Thorpe and Chico [33]

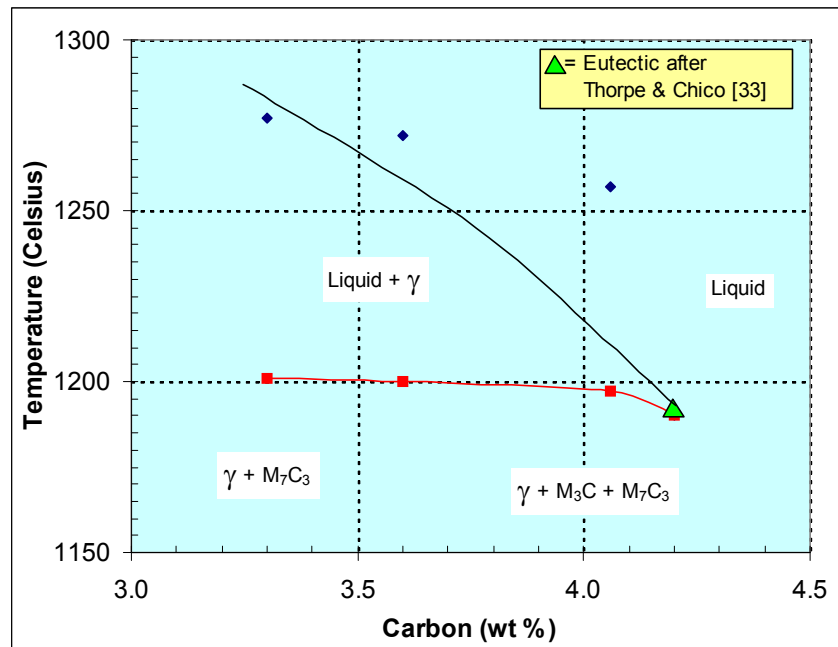


Figure 2.36: Phase diagram based on experimental data for Fe-10Cr-2Mn-0.5Si-C alloy series with published data from Thorpe and Chico [33]

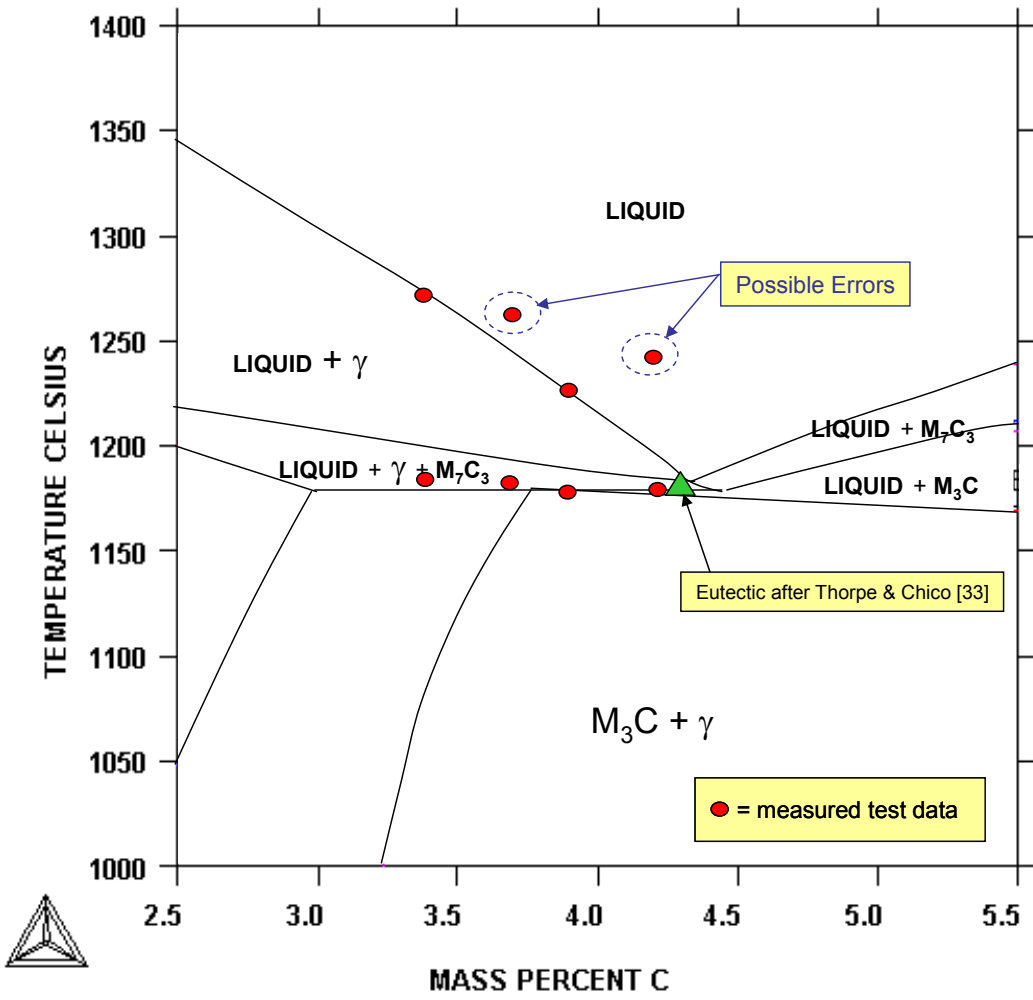


Figure 2.37: Comparison of experimental data for Fe-8Cr-2Mn-0.5Si-C alloy series with predicted data from Thermocalc [34]

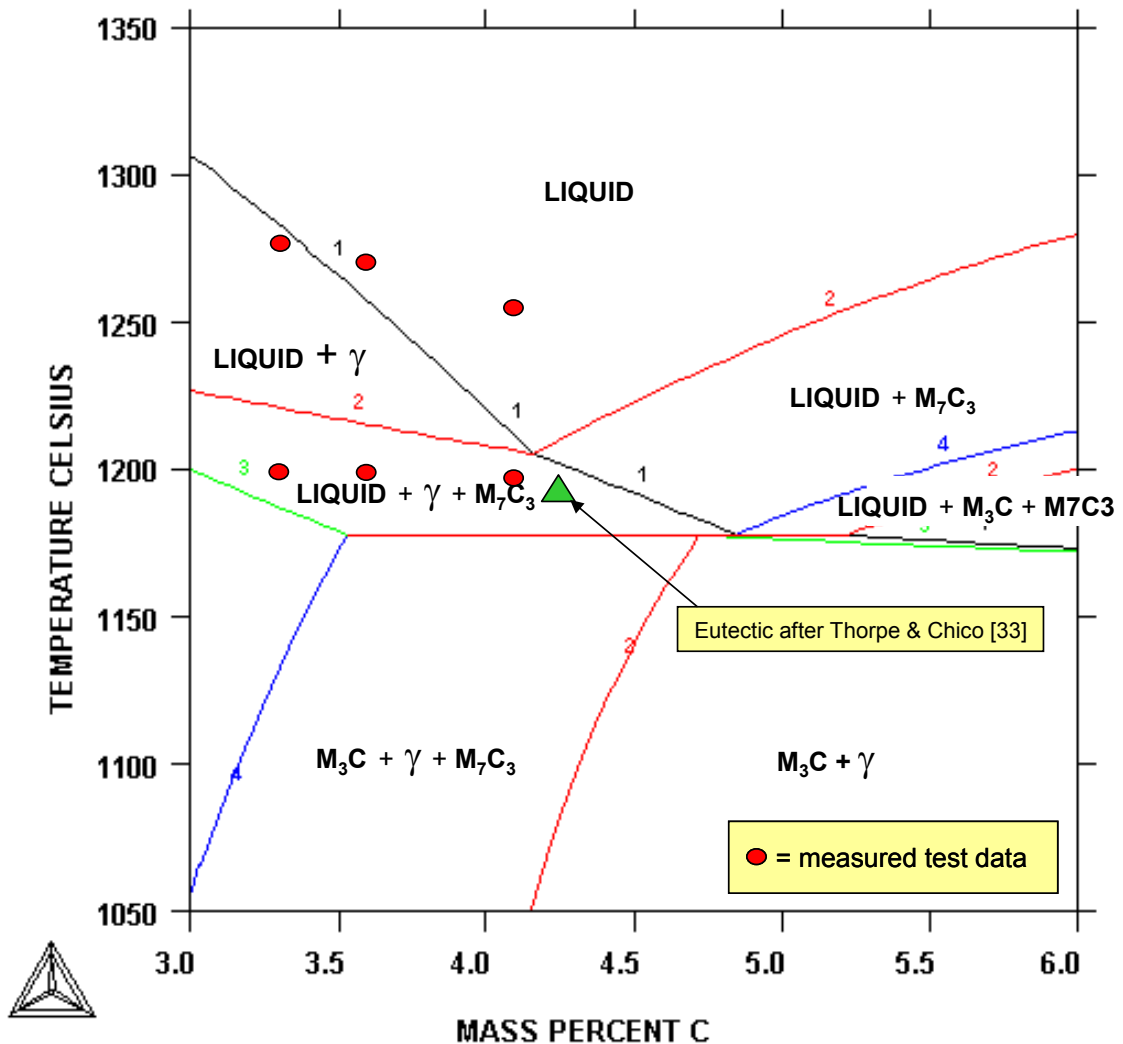


Figure 2.38: Comparison of experimental data for Fe-10Cr-2Mn-0.5Si-C alloy series with predicted data from Thermocalc [34]

There is generally a close agreement between the experimental data obtained through this study and the published and predicted phase diagrams. In both the “A” and “B” series of experimental data there appears to be errors with the measured liquidus temperatures, and this could be the result of possible chemical composition differences, particularly the addition of manganese and silicon to the experimental melts.

Significantly the proposed low melting point alloy having the composition Fe-12Cr-1.6Mn-1.0Ni-0.5Si-4.1C exhibits a near eutectic composition, which is also confirmed by the fine carbide structure shown in the microstructure (refer Figure 2.25).

Errors were observed with the experimental data collected from this study, and this could be the result of either:

- i. Chemical composition variations
- ii. Non-equilibrium cooling conditions
- iii. Variations in starting pouring temperature
- iv. Variations in positioning of thermocouple

The thermal analysis data obtained from this study represents a practical application of thermal measurement for foundry applications and is fully representative of the cooling rates and alloy conditions experienced within a foundry. The data is therefore applicable when considering transfer of the technology to pilot scale and full scale production trials.

2.9.3 Electron Microscopy and Microanalysis of Low Melting Point Alloy (C1)

A Jeol 35CF and Zeiss Scanning Electron Microscopes were used to obtain secondary electron images of the low melting point alloy C1, and to conduct energy dispersive spectroscopy and elemental x-ray mapping to assist with identification of the chemical phase present.

Figure 2.39 shows the typical microstructure of the alloy C1 at low magnification. Higher magnification images as shown in Figure 2.40

Figures 2.41 to 2.43 show the In-Lens images from the Zeiss SEM. The In-Lens images show the presence of compositional variations within the carbides, and confirm the quasi-eutectic reaction that occurs during solidification. The centre of the carbides are the M_7C_3 type, with the outer regions of the carbides being M_3C carbides. Additional investigation and discussion is presented in Section 4 of this study.

The energy dispersive spectroscopy (EDS) analysis results for the alloy C1 are summarised in Table 2.17. The EDS analysis was not capable of resolving the variation in composition within the carbides, and the data shown for the carbide is therefore an average value for the two different types of carbides present. In Section 4 of this report a more detailed analysis of the microstructures with respect to chemical analysis is presented using x-ray mapping and electron beam back scattered diffraction (EBSD) mapping. The EBSD in particular was able to highlight the carbide crystallographic differences.

The EDS data for the carbides shows the chromium level in the carbides is approximately 22 weight percent compared to approximately 60 weight percent for high chromium alloys such as Cr27 alloy. This reduced chromium content will potentially alter the carbide hardness as has been shown in previous work [40]. The reduced carbide hardness will have some effect on the abrasive wear resistance for the alloy. However the increase in carbide volume fraction for this alloy will offset the effect from the reduction in carbide hardness.

The chromium content of the ferrous matrix is between 5 to 7 weight percent which provides sufficient chromium to develop a good hardenability response after heat treatment. The EDS data also confirms the ratios of elemental segregation suggested in Table 2.12.

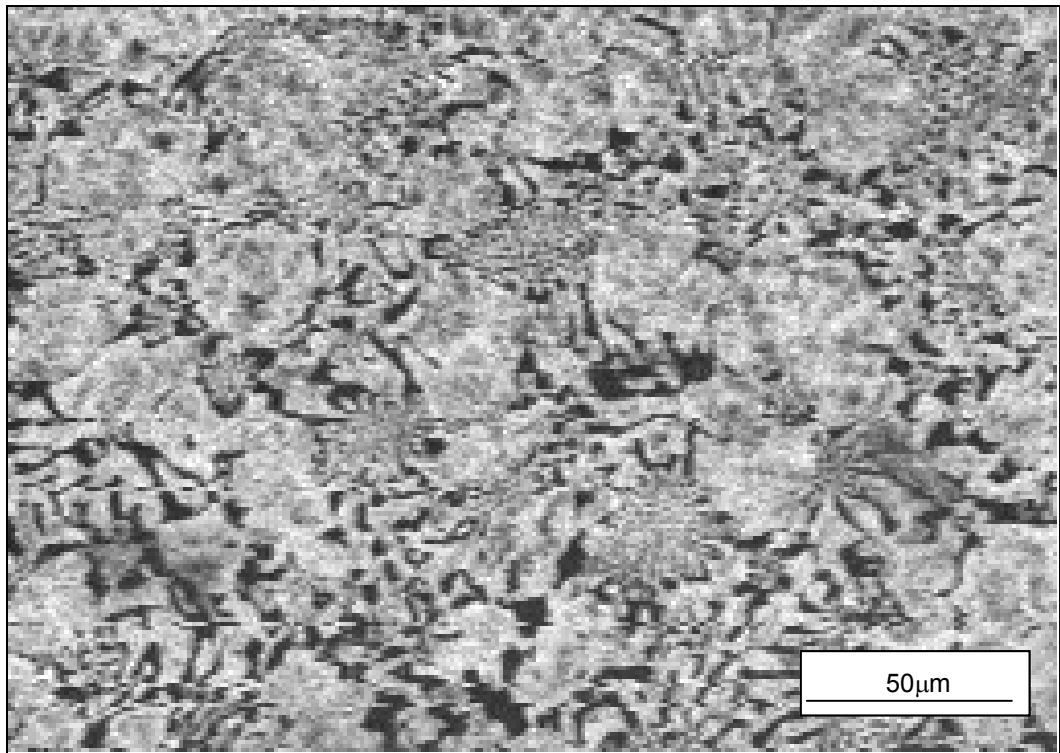


Figure 2.39: Low magnification secondary electron image of Alloy C1

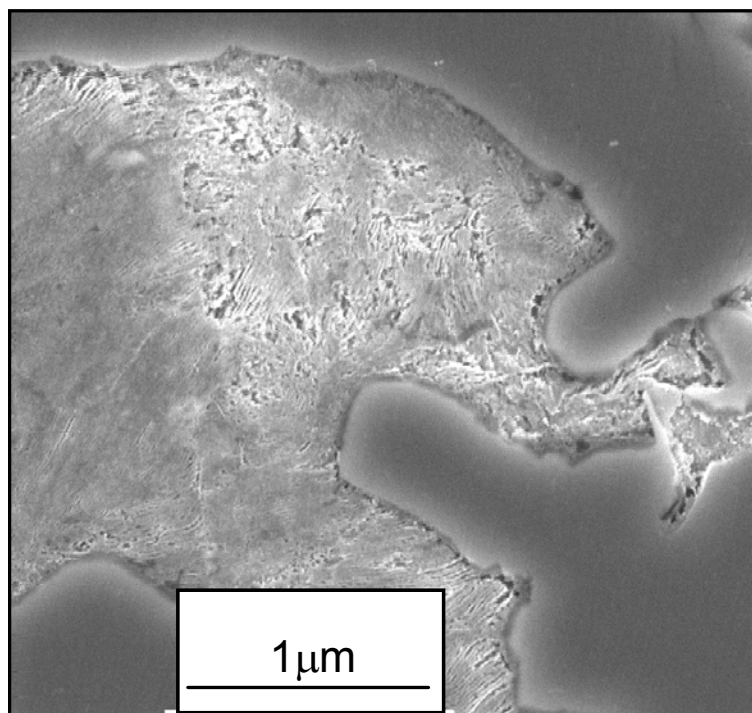


Figure 2.40: Detail of Alloy C1

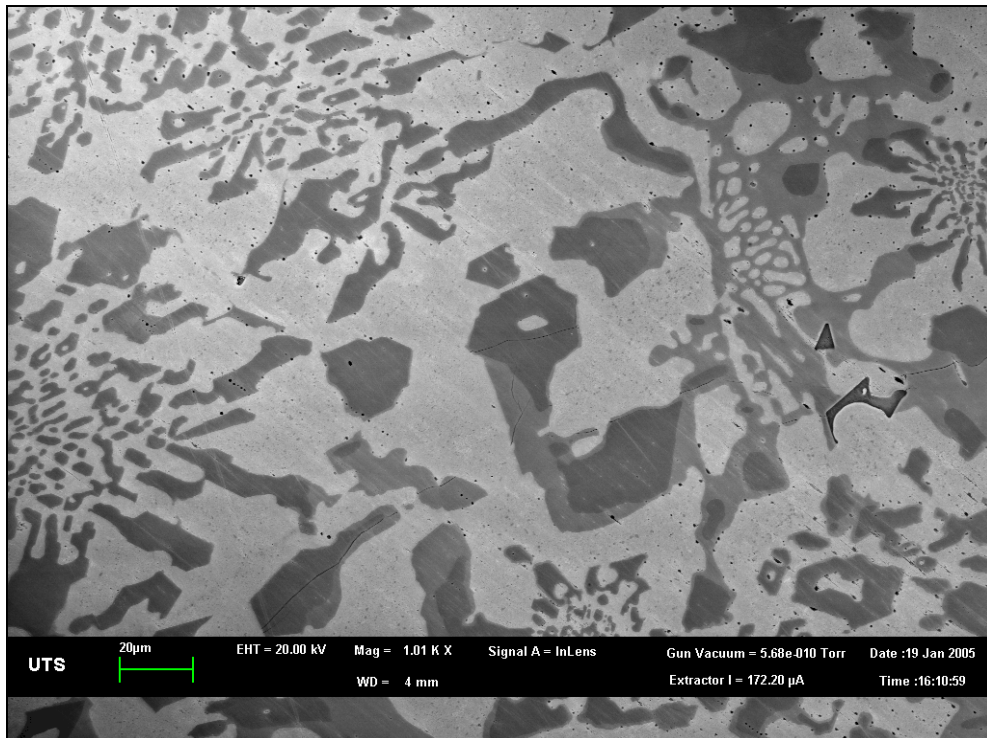


Figure 2.41: Zeiss in-lens image of Alloy C1

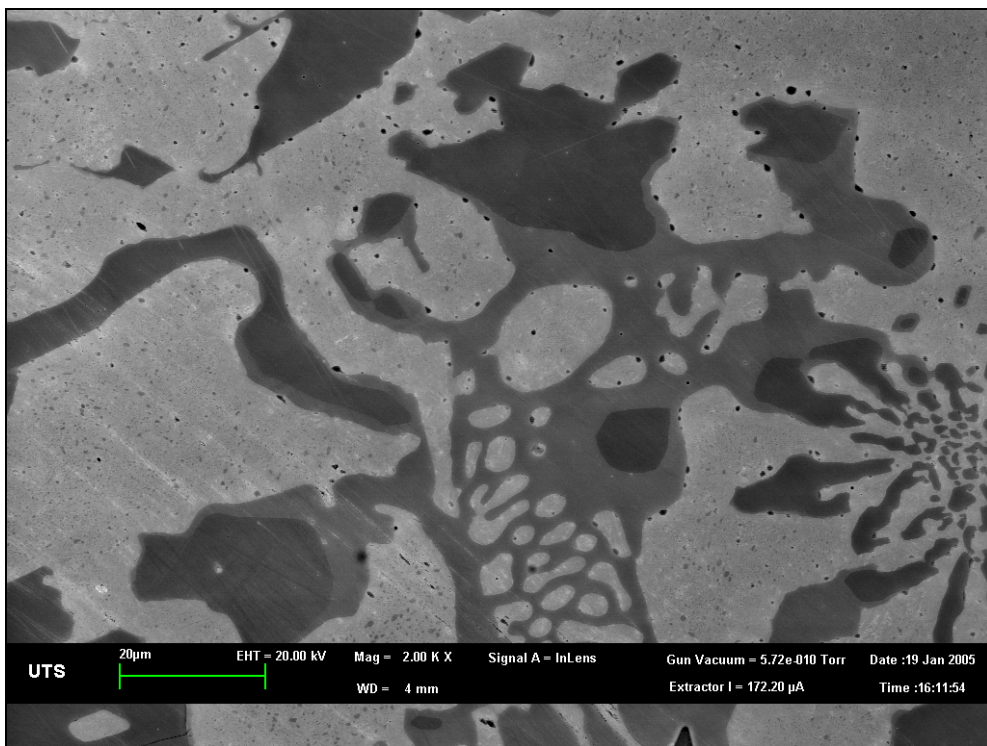


Figure 2.42: Zeiss in-lens detail image of Alloy C1

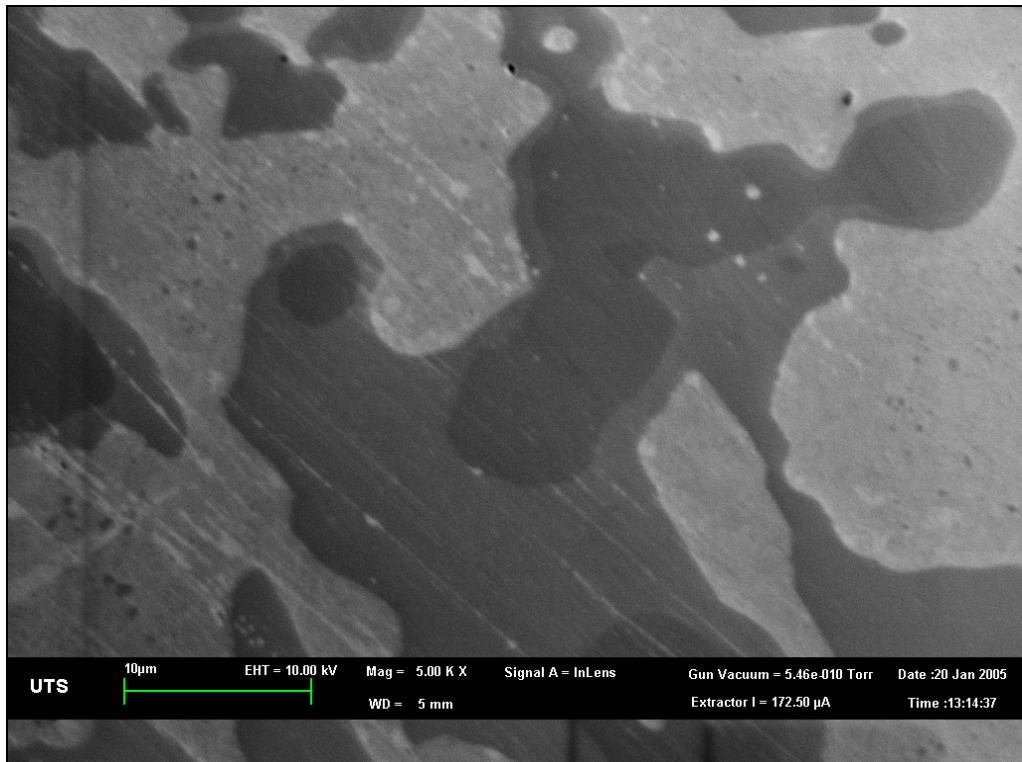


Figure 2.43: High magnification Zeiss in-lens image of carbides

Table 2.17: EDS analysis data for Alloy C1

PHASE ANALYSIS FOR Fe-12Cr-1.6Mn-1.0Ni-0.5Si-4.1C ALLOY

Element	Primary Fe	Eutectic Fe	Eutectic M_7C_3	BULK SEM CALC	BULK OES ACT
Fe	87.1	89.6	67.3	66.3	80.7
Cr	7.2	5.1	22.7	11.5	12.0
Mn	2.3	2.1	0.5	1.6	1.6
Ni	1.3	1.1	0.8	1.0	1.0
Si	0.9	0.9	<0.1	0.6	0.6
C	1.2	1.2	8.7	3.0	4.1
vol %	2	62	36	100	100

2.10 SUMMARY AND OUTCOMES

The experimental work outlined in this chapter has permitted the development of a low melting point white iron having the nominal composition of:

Carbon	=	4.1 weight %
Chromium	=	12.0 weight %
Manganese	=	1.6 weight %
Nickel	=	1.0 weight %
Silicon	=	0.5 weight %
Iron	=	Balance

The liquidus temperature for the alloy (C1) was measured as 1209°C, and the solidus temperature was measured as 1194°C.

The measured thermal arrests are in close agreement with published thermal data for the Fe-Cr-C phase diagram [33]. The measured thermal arrests are lower compared to predicted thermal data from CALPHAD software results [34, 38].

The microstructure of the low melting point alloy (C1) consists of a small volume fraction of primary austenite, with a eutectic of M_7C_3 carbides and austenite. Some of the M_7C_3 carbides have undergone a quasi-peritectic reaction which has been previously observed and described by Thorpe and Chico [33]. The austenite has undergone a partial transformation to form ledeburite (ferrite plus M_3C carbide in the form of cementite).

The alloy C1 should provide the ability to be melted within a normal commercial vacuum heat treatment furnace having a maximum operating temperature of approximately 1300°C.

The test results from this study show that low chromium white irons having less than approximately 10 weight percent chromium have the tendency to form high volume fractions of M_3C carbides. The M_3C carbides form as the result of a quasi-peritectic reaction which has been observed in previous studies. The M_3C carbides are also less wear resistant compared to M_7C_3 carbides.

The thermal analysis data developed from this study is in close agreement with previously published data for the Fe-Cr-C alloy system. The experimental data varies from the CALPHAD predicted data, and there were some errors observed with the experimental data that suggested possible chemical composition variations, thermocouple position variations or potential non-equilibrium cooling conditions within the alloy melts.

The data presented in this study for the development of the low melting point alloy has been obtained from pilot scale foundry production using typical melting and casting methods of larger foundry applications. The data is therefore typical of practical foundry practice. The measured thermal data, observed microstructures and alloy compositions are all achievable using standard foundry equipment.

CHAPTER 3

3.1 INTRODUCTION

White iron alloys have been successfully adopted in the mining industry to combat high wear problems, but suffer from failure when used in impact conditions. The white iron has been used mainly in the form of castings, hard faced wear plates, and vacuum brazed composites of white iron and steel. The use of steel with the white iron as a composite will impart toughness to the wear parts, whilst providing a means for more flexible attachment of the composites to equipment requiring wear protection.

Even though white cast iron and steel are both ferrous alloys, they have different microstructural features which limit their ability to be joined by many of the common processes such as welding, soldering and gas-flame brazing. The large cross-sectional areas to be joined also makes it difficult for standard joining processes to achieve full bonding across the entire interface.

The following sections provide an understanding of the most significant joining processes for white iron to steel and the equipment used. The development of the new vacuum casting process is then described detailing how this process was developed from an understanding of the mechanisms of the vacuum brazing process and the critical parameters of oxidation control and surface wetting.

3.2 EXISTING PROCESSES

Historically ferrous alloy composites have been produced using welding or brazing processes that require the two alloys being joined to have similar mechanical properties. The welding process relies on the minimisation of weld dilution between the weld parent metal and the filler material or overlay in combination with control of the energy input to provide an optimum joint strength, appropriate mechanical properties and microstructure. The strength of the brazed joint is limited to the predominant mechanical properties of the materials used, and to the close tolerances between the mating surfaces required.

Extensive research has been conducted on vacuum brazing [42 to 49] which has been used successfully to join white irons to mild steel through the use of typically copper brazing alloys. During the vacuum brazing cycle, parts are heated to a temperature above the melting point of copper to allow the copper to wet both surfaces. The molten copper alloys with the iron present in both the steel and the white iron to produce a columnar growth of binary copper/iron alloy grains across the interface, with other elements diffusing across the interface.

3.2.1 VACUUM BRAZING

Vacuum brazing has been used as a metal joining process since the 1950's, and permits the joining of materials which would normally not be able to be joined by other methods. The versatility of vacuum brazing surpasses furnace-brazing in protective gas atmospheres. Good vacuum brazing produces sound, strong, ductile joints.

Standard brazing is a joining technique where a filler metal is heated until it is molten, and through capillary action, wets the surfaces of the materials to be

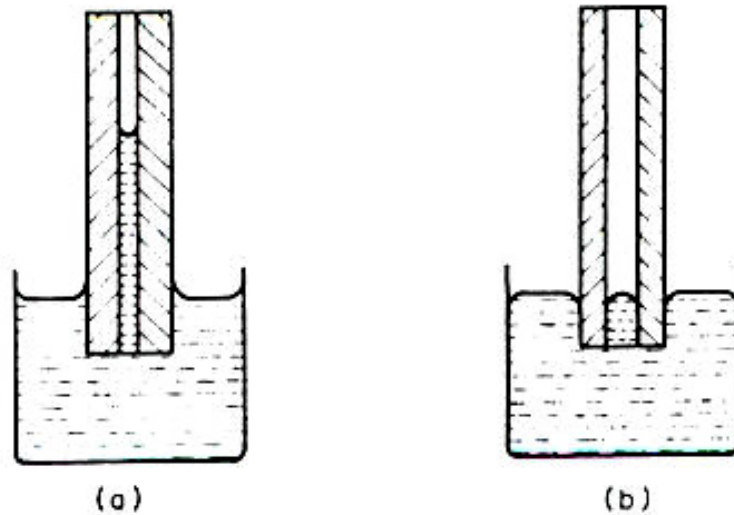
joined, and solidifies to a strong joint upon cooling. The principal of capillary action and surface wetting are shown in Figure 3.1 below [43].

To achieve the optimum brazed joint, a high liquid surface tension, and low contact angle are highly desirable.

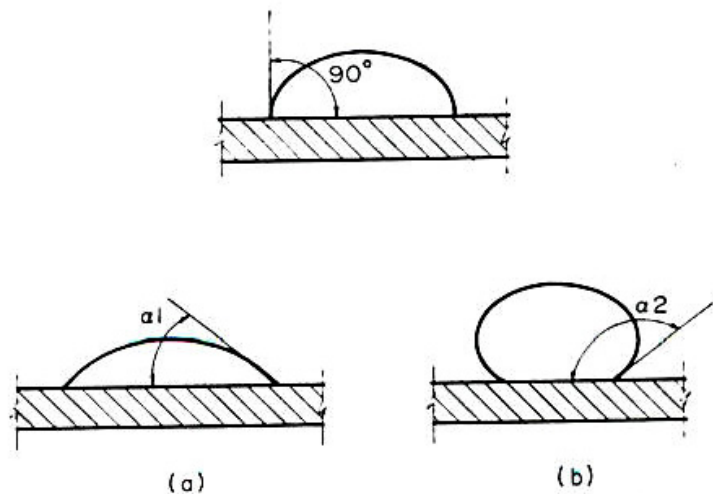
In traditional brazing methods where a gas torch is used to heat the products prior to being joined with the filler wire, a flux is used to enhance the wetting of the joint surfaces, and inhibit oxidation. The presence of oxidation may prevent a satisfactory joint from being achieved.

Whilst the normal brazed joints are relatively strong compared to the parent material, there is usually no alloying of the filler metal to the parent metal, as with normal welding methods.

Inert gas brazing, and subsequent vacuum brazing techniques were developed to permit a wider range of materials to be joined in a more uniform and controlled manner, without the need for fluxes, which typically are limit the temperatures to less than 800°C. If successful brazing of alloys using filler metals other than silver solder was required, then a vacuum brazing process was the best choice since the filler alloys would typically oxidise and scale at higher temperatures.



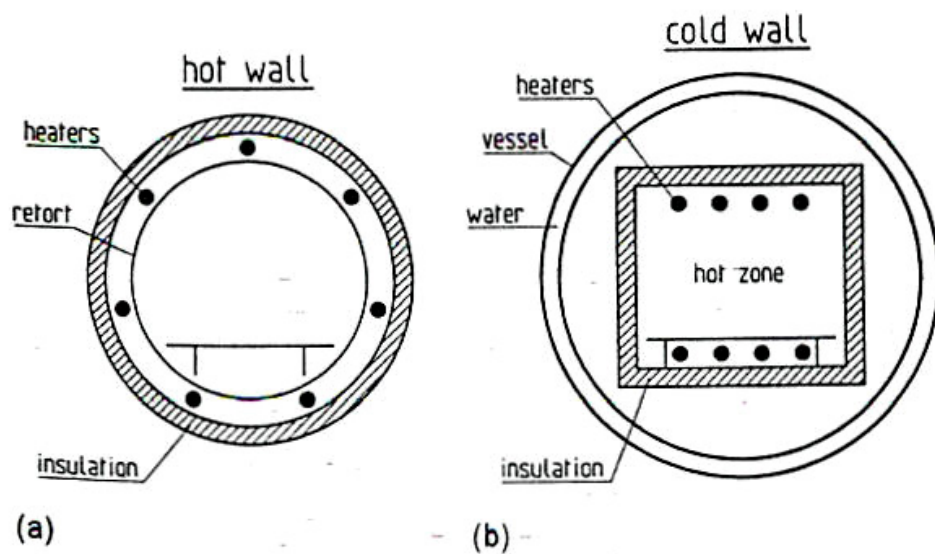
Principal of capillary action (a) Water: wetting, level rises;
 (b) Mercury: no wetting, level depressed



Sessile drop and contact angles: (a) contact angle less than 90° – wetting;
 (b) contact angle greater than 90° – no wetting

Figure 3.1: Capillary action and surface wetting [43]

Early work on vacuum brazing was carried out in ceramic tube furnaces [44], and through development of the technology, these have been replaced by cold wall designs which provide faster heating and cooling rates and less restrictions on the size and shape of the furnaces. Figure 3.2 shows the general principle of hot and cold wall furnaces.



Vessel design for (a) hot-wall and (b) cold-wall vacuum furnaces

Figure 3.2: Hot and cold wall vacuum furnace principles [45]

Vacuum brazing is a batch process where the charge of pre-assembled components is heated within a vacuum chamber until the braze material is molten. Once the braze material has flowed the charge is then cooled back to room temperature, often using the recirculation of inert gas.

The process is capable of a high degree of automation once the loading of the cycle has been completed.

The free flowing nature of most braze alloys, coupled with the elimination of any need for fluxes normally results in the production of crevice free joints.

In copper brazing of ferrous based alloys, the base metal (steel and white iron) dissolves into the molten copper until the iron in the molten copper reaches an equilibrium state fixed by the brazing temperature.

The low carbon iron from the steel backing plate dissolves into the molten copper and diffuses towards the high carbon white iron boundary and reaches the boundary through capillary action due to narrow joint clearances. When the low carbon iron/copper columnar grains progress across the interface toward the high carbon iron surface, the columnar grains combine with carbon from the high carbon white iron to form a high carbon iron. The high carbon in the iron in molten copper exceeds its equilibrium quantity fixed by the brazing temperature, and excess high carbon iron then deposits as a columnar Fe-Cu-C alloy phase from the high carbon steel boundary at a constant brazing temperature.

This phenomenon has been noted in the literature as “dissolution and deposit of base metal” [46,47]

In order to achieve the optimum bond, vacuum brazing requires close tolerances, which can only normally be achieved through machining or grinding. The process is also reliant on the use of a brazing alloy such as copper (or sometimes nickel or other alloys). Design and use of these brazed ferrous alloy composites has been limited only to blocks and plates, which can be cost effectively cast in a foundry and machined to the required tolerances.

Additional complications arise in vacuum brazing between the two alloys being joined commonly exhibiting differences in thermal expansion. The high stresses induced into the parts from the variation in thermal expansion/contraction can result in post heat treatment cracking of the parts, and substantial distortion.

The vacuum brazing process for the steel/white iron composite is shown schematically in Figure 3.3. The process involves the following general steps:

- i. The surface to be brazed for the steel and white iron are machined or ground to a surface flatness of 0.10 mm;

- ii. The surfaces and parts are then cleaned and degreased to remove any residue;
- iii. A copper shim of nominally 0.10 mm thickness is placed in between the machined/ground surfaces;
- iv. The parts to be brazed are then placed into a vacuum furnace, and heated under vacuum until a temperature of typically 1000°C is reached;
- v. A partial pressure of inert gas (typically nitrogen) is then purged into the vacuum furnace until the partial pressure inside the vacuum furnace is above the vapour pressure of liquid copper at its melting point of 1083°C;
- vi. The temperature is increased to approximately 1100 to 1120°C and held (soak period) for a period of at least 30 minutes to permit the wetting of the molten copper across the joint surfaces and allow the dissolution of iron into the liquid copper;
- vii. After the soak is completed, the temperature of the furnace is allowed to cool to approximately 1000°C. The inert gas inside the furnace is now recirculated using a blower and heat exchanger to develop a faster cooling rate that will enable the white iron to undergo the martensitic phase transformation.

The Vacuum Brazing Process for Iron Based Alloys

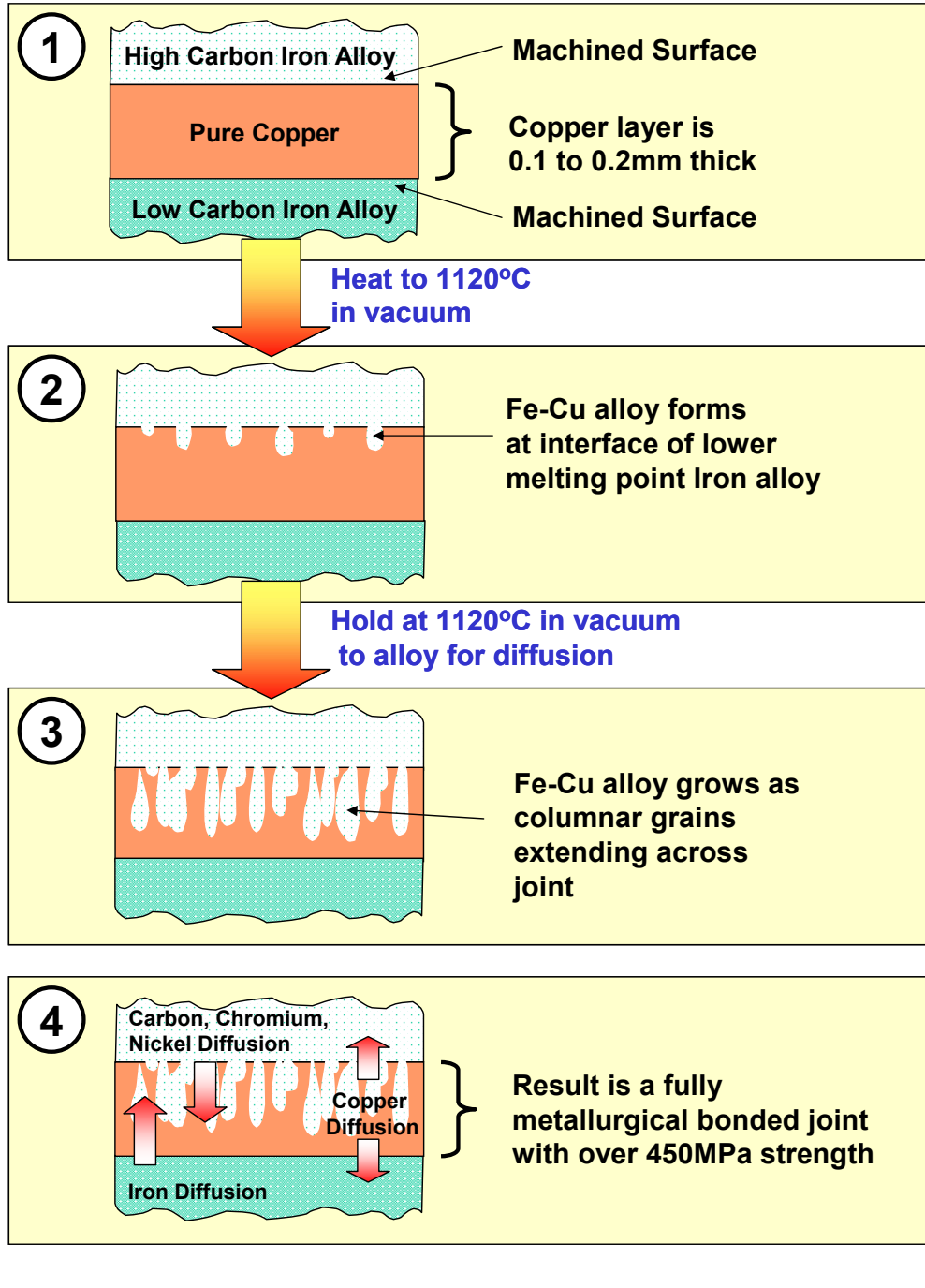


Figure 3.3: Schematic diagram for the vacuum brazing process for steel and white cast iron

3.2.2 FACTORS AFFECTING THE PERFORMANCE OF THE COMPOSITE BOND

Key factors that affect the performance of the vacuum brazing process for steel/white iron composites include:

- Vacuum or pressure inside the chamber will directly control the amount of oxygen that is present. Oxygen will quickly oxidise the machined surfaces being brazed, especially at higher temperatures. It only takes a surprisingly small amount of residual oxygen to prevent the process from working successfully.
- Flatness of the surfaces to be bonded using vacuum brazing techniques are critical if good capillary flow is to be achieved. Molten copper requires a maximum gap of 0.1 to 0.3mm. The smaller the gap, the stronger the resulting bond. If a steel/white iron composite part is vacuum brazed, residual machining stresses will relieve during the heating cycle, and will result in some distortion of the parts near the joint. This distortion could result in the gap between the two components increasing beyond the maximum limit of 0.1 to 0.3mm.
- Surface roughness aids the wetting of the surface by increasing the turbulence of the flow of the molten copper across the interface. The increased turbulence provides a means for increasing the dissolution of the ferrous phase into the copper, increasing the performance of the final joint. Too much surface roughness will result in the joint touching on the high points and may result in a gap in excess of the 0.1mm to 0.3mm maximum.
- Presence of oxides may limit the wetting of the surface, even in a vacuum based system. It is extremely important with normal vacuum brazing to

keep all surfaces to be wetted clean from grease, oxides and other potential contaminants. The presence of even dust particles could prevent the joint from achieving a clearance less than the maximum 0.1 to 0.3mm limit.

- Cleanliness of the products to be braised will have a direct impact on joint quality and performance of the vacuum system. Dirty components placed in the vacuum chamber will result in contamination of the vacuum pump oil, which will cause both undue wear of the pumps, and also decrease the performance of the pumps hence restricting their pumping capacity and resulting in an increased chamber pressure.

3.2.3 TYPICAL MICROSTRUCTURES OF VACUUM BRAZED JOINTS

The following photomicrographs show typical vacuum brazed joints for the steel/white iron composites produced on samples manufactured by the author during this study, and highlight the columnar grains produced during the process.

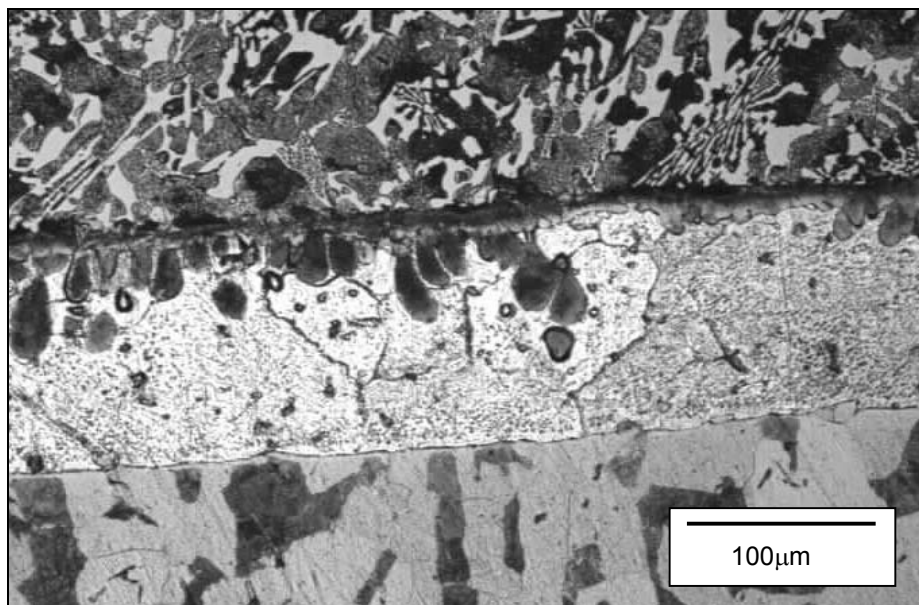


Figure 3.4: Steel/White iron composite (etchant: 5% HCl acid ferric chloride) White iron is on the top of picture, steel is on the bottom. Note the presence of the dissolution deposited columnar grains adjacent to the white iron/copper interface.

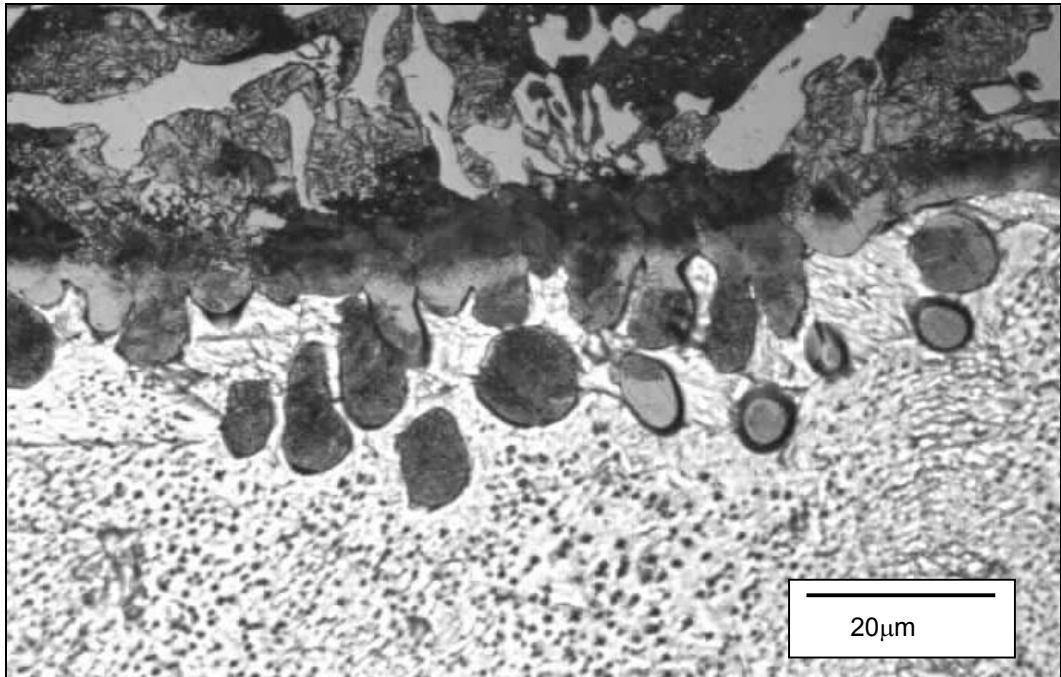


Figure 3.5: Close up detail of high carbon iron/copper interface (etchant: 5% HCl acid ferric chloride)

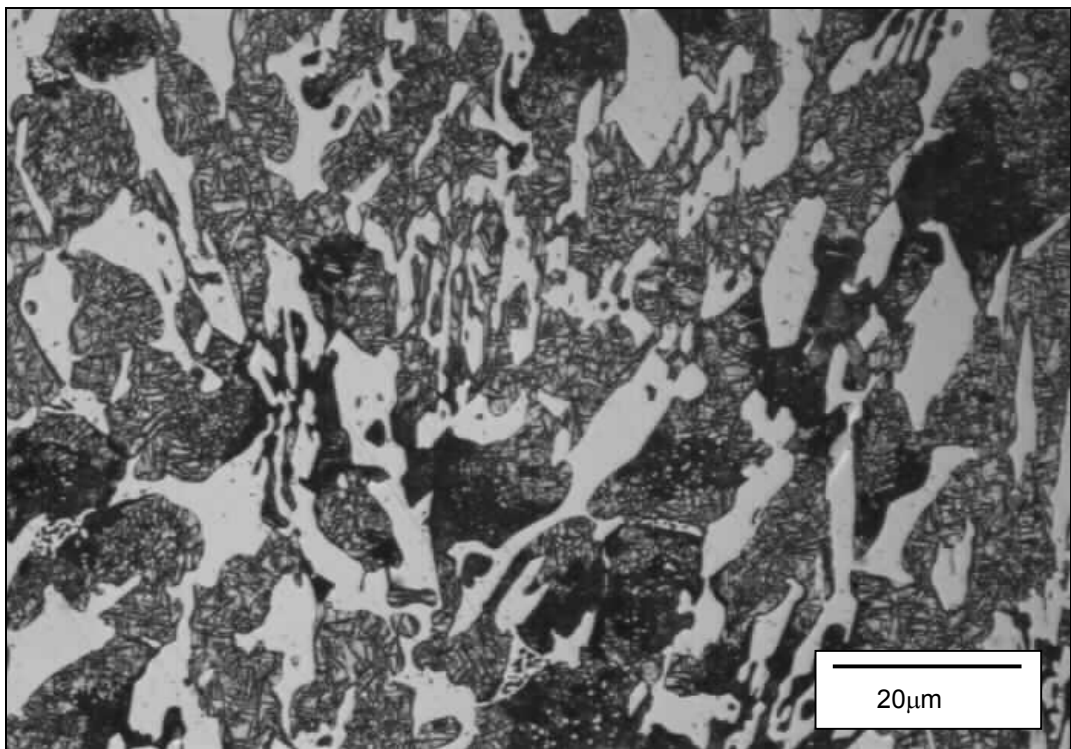


Figure 3.6: General Microstructure of 15/3 CrMo iron used for the parts (etchant: 5% HCl acid ferric chloride)

3.2.4 EXAMPLES OF FINISHED PRODUCTS

The following figures show a sample of the typical products produced using the vacuum brazing process.



Figure 3.7: 75mm and 90mm buttons, 50mm x 50mm blocks of different lengths, 25mm x 25mm x 300mm bars, and other assorted sized blocks



Figure 3.8: 50mm x 50mm x 432mm Block, 240mm x 50mm and 240x40 "Chok" Blocks, 50x50 blocks and two skid pads

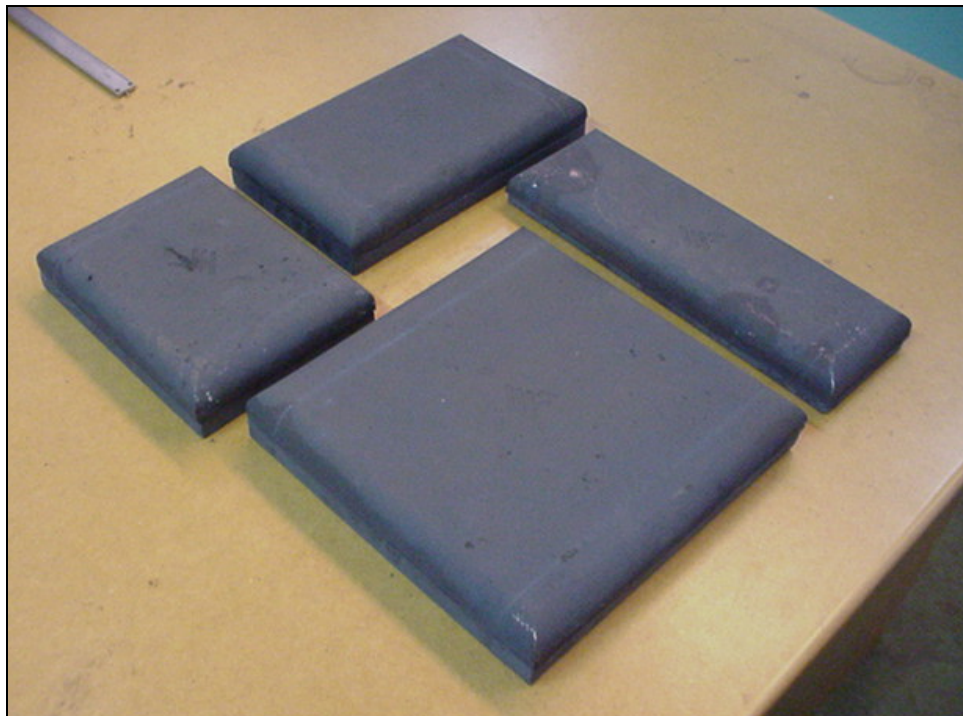


Figure 3.9: Various sizes of skid pads

3.2.5 CSIRO CAST-BOND PROCESS

A process called Cast-Bonding [50,51] has been developed where white iron is cast directly onto steel substrates in a standard air atmosphere. The process requires the use of fluxes coating the steel substrate to limit oxidation and improve surface wetting of the liquid alloy. The steel substrate and mould are preheated to a moderate temperature of approximately 300 to 400°C, and the white iron cast directly onto the steel. The Cast-Bond process was successful in producing high quality bonds between the steel and the white iron, however until now only a minor amount of research was conducted on the interface bonding mechanisms.

The keys to the establishment of a satisfactory bond using the CSIRO Cast-Bond process were:

- i. Having sufficient preheat on the steel and sufficient superheat on the molten white iron to establish a combined temperature when poured above the liquidus of the white iron for sufficient time to permit wetting and steel surface dissolution;
- ii. Having a typical white iron to steel mass ratio of a minimum 2:1, and typically 4:1;
- iii. Coating the steel surface to be bonded with a flux to help minimize oxidation and enhance surface wetting.

As an example, assuming a steel preheat of 400°C, with a mass of 10kg, and a required white iron addition of 20kg (minimum 2:1 ratio) with a liquidus of 1295°C (as for Cr27 alloy), and a pouring temperature of 1600°C, the estimated joint temperature immediately after pouring would be:

$$\begin{aligned}
\text{Joint Temperature (}^{\circ}\text{C)} &= \frac{10}{30} \times 400 + \frac{20}{30} \times 1600 \\
&= 133 + 1067 \text{ }^{\circ}\text{C} \\
&= 1200 \text{ }^{\circ}\text{C}
\end{aligned}$$

In the above example, the average joint temperature based on using the whole mass balance would be estimated at 1200°C. However since the exposed surface of the steel will heat up quicker compared to the bulk of the alloy, the surface of the steel at the interface would be expected to be significantly higher in initial temperature.

Assuming that some time at the temperature above the liquidus of the white iron is required to achieve a satisfactory bond, then in the above case a higher steel preheat and white iron superheat would be required.

Increasing the steel preheat to say 500°C, and a superheat of the white iron of 1700°C, the estimated interface temperature based on mass balance would be 1300°C.

It can be seen from the above basic calculations that increasing the proportion of white iron to steel will effectively reduce the required steel preheat and white iron superheat.

One of the advantages of the CSIRO Cast Bond process is the ability cast more complex shapes to form a composite, as opposed to the plate/block nature of the vacuum brazing process.

The main disadvantages of the CSIRO Cast-Bond process are the need to place the steel to be bonded inside a sand mould (or centrifugal casting unit if lining pipe), and then establishing a method of preheating the steel within the sand mould. This would normally be done using a gas flame in a foundry which provides complications and hazards to the casting area.

The steel insert will also act as a chill even if preheated to a temperature of around 400 to 500°C. This chilling effect will affect the manner in which the liquid white iron feeds the casting, and there is a potential for shrinkage defects and other issues associated with using chills.

3.3 THEORY OF VACUUM CASTING

The theory behind the vacuum casting process for steel/white iron composites was developed from the vacuum brazing concepts. As discussed previously, during the vacuum brazing process, the copper shim is heated until it becomes liquid, and then begins a dissolution/alloying process that establishes the growth of iron/copper columnar grains across the interface.

The fundamental processes for copper based vacuum brazing were believed to be:

- i. Having a oxygen free environment;
- ii. Having a minimum temperature of the process of at least the liquidus temperature of the copper alloy;
- iii. The ferrous based alloys and the copper exhibit a degree of solubility.

The theory behind the proposed vacuum casting process was to place the steel and the white iron into the vacuum heat treatment furnace and heat them together until the white iron was liquid. At this temperature, the liquid white iron would react with the solid steel substrate to create a bond.

If the white iron was placed in a reservoir above the steel substrate, at the temperature it becomes liquid, the white iron will flow onto the steel substrate, which can be encased in a suitable mould to create a finished white iron/steel composite.

Unlike the vacuum brazing process, a bonding agent (eg. copper) would not be required, and surface preparation requirements are greatly simplified.

Also, compared to the Cast-Bond process, the flux is not required due to the use of the vacuum furnace, and the issue of preheating the steel substrate is eliminated as it is placed into the same furnace at the same temperature as the white iron charge.

The vacuum casting process would also permit the introduction of other compatible alloying materials into the composite using one process. For example, tungsten carbide particles could be introduced into the white iron region of the composite to further increase the wear resistance of the material.

To enable a thorough discussion of the process of vacuum casting, the following sections will discuss the general types and construction methods for vacuum furnaces, the design and construction of a vacuum tube furnace to enable basic experimentation of the proposed method of manufacture, and the design and construction of a pilot scale hot-walled vacuum furnace to enable prototype test parts to be manufactured for mining field trials.

3.3.1 GENERAL DESCRIPTION OF VACUUM FURNACES

The design of vacuum furnaces generally depends on the size of the load, the pressure and temperature to be attained, and the medium to be used to cool the load. The main parts of the vacuum furnace include:

- The recipient
- Pumping system
- Heating chamber
- Temperature-measuring control system
- Cooling system

The recipient is basically the vacuum chamber, and can be grouped into two main types as either 'hot wall' or 'cold wall' chambers (see Figure 3.1).

A hot wall vacuum furnace uses insulation surrounding the heating elements to contain the heat. The outer shell of the furnace has no cooling other than normal air passing over the outside. Internally, the load sits on a support frame, which must be capable of supporting the furnace load at high temperature without distortion or slumping. Normally hot walled vacuum furnaces are limited in operation to maximum temperatures of 1100 -1150°C.

A cold wall furnace uses a cooling jacket surrounding an inner vacuum chamber, usually with water as the cooling fluid, to contain the heat inside the furnace. Minimal insulation is used inside the heating chamber to permit faster heating and cooling cycles. Cold wall furnaces are typically capable of achieving higher vacuum levels compared to hot wall furnaces, and can operate at higher temperatures between 1200 – 1400°C.

The construction of the vacuum pumping system depends on the following factors:

- The volume of the recipient
- The surface of the recipient and the type of furnace parts inside
- The degassing of the charge
- The time required for evacuation down to the working pressure

Pumping systems are usually divided into two sub-systems, the roughing pump, and the high vacuum pump. In some furnace designs/requirements, a single roughing pump is sufficient. Figure 3.10 shows an example of a typical vacuum pumping system.

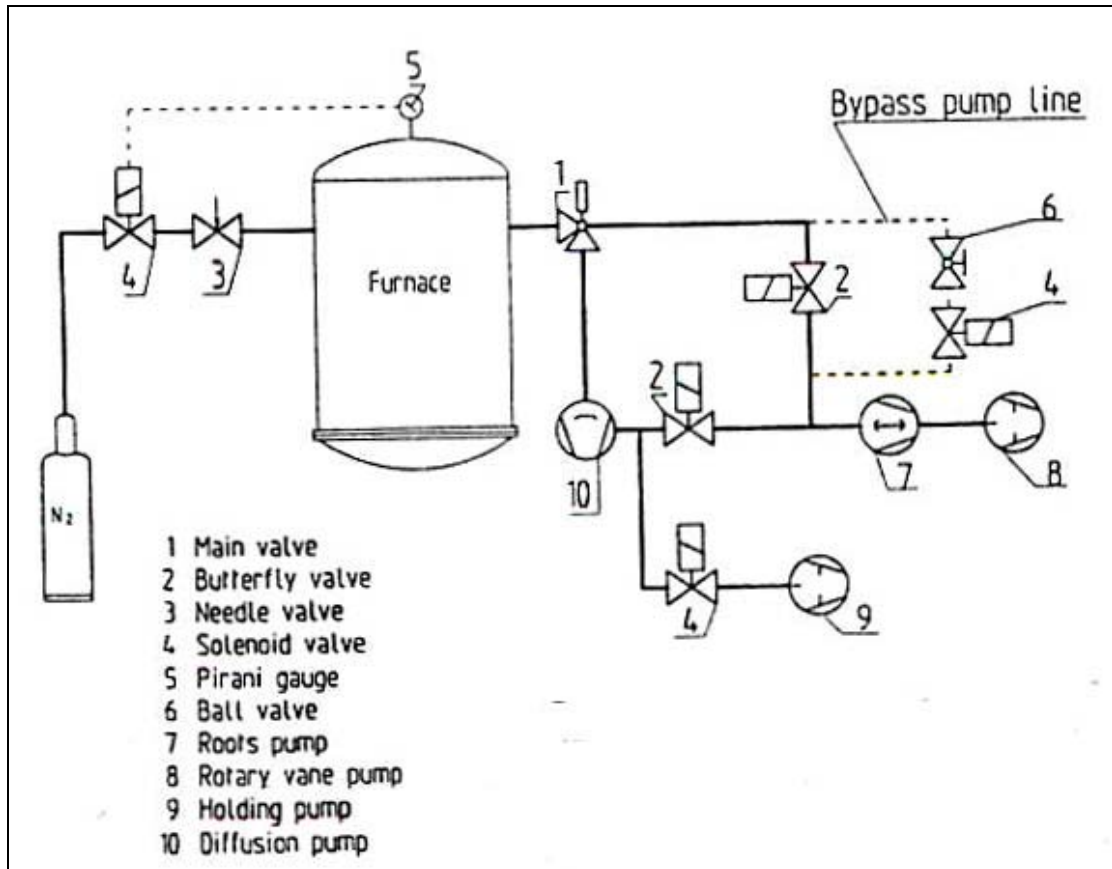


Figure 3.10: Schematic of typical vacuum furnace system [45]

The heating chamber is a critical feature of all vacuum furnaces. The insulation of the hot zone usually involves using at least one of the following components:

- Radiation shields
- Combination of radiation shields and ceramic insulation Material
- Multiple-layer insulation (sandwich)
- Graphite insulation

Radiation shields can be made from tungsten, tantalum (max operating temp 2400°C), molybdenum, stainless steel or nickel alloys. Combinations of ceramic insulation wool and various radiation shield materials as listed above can also be used. Graphite fibre sheets are the most expensive for use in insulation, but they

have lower heat losses and hence can be used with smaller thicknesses, and have less absorption of gasses.

The heating elements are made from one of the following materials:

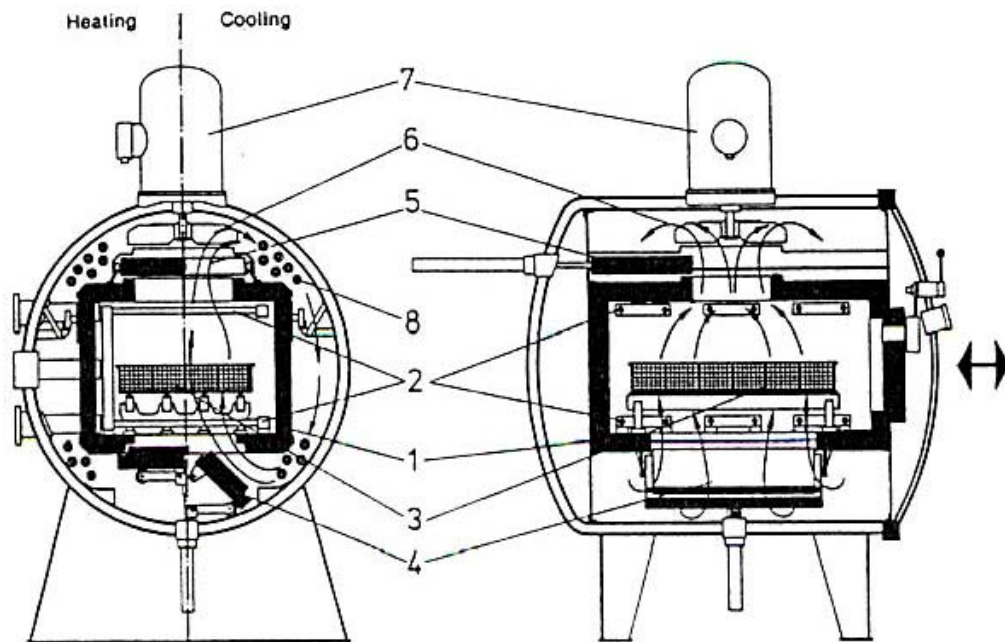
- Chrome-nickel alloy (commonly called Kanthal), with a maximum temperature limit of 1150 -1250°C in vacuum.
- Silicon carbide , maximum temperature 1150 – 1200°C (in vacuum)
- Molybdenum, maximum temperature limit of 1700°C
- Graphite, maximum temperature 2000°C
- Tantalum, maximum temperature 2400°C

In designing the placement and distribution of the heating elements within the hot zone, the primary aim is to provide a uniform heat distribution.

Control of the furnace temperature and vacuum is provided through micro-processor controlled systems that provide constant measurement of the temperature and in some cases the vacuum pressure.

Thermocouples used for most temperatures below 1175°C are the K-type, which are a nickel-nickel/chromium type. It should be noted that all metals used in a vacuum will have a lower operating temperature compared to use in a normal oxidising atmosphere. The life of the thermocouple will depend greatly on the maximum temperatures being achieved inside the furnace, and the level of the vacuum.

Typical components of a vacuum furnace are shown in Figures 3.11 and 3.12.



1. Heating chamber; 2. heating elements; 3. charge carrier; 4. bottom vent; 5. top vent; 6. fan; 7. fan motor; 8. heat exchanger

Figure 3.11: Typical components of a horizontal vacuum furnace [45].

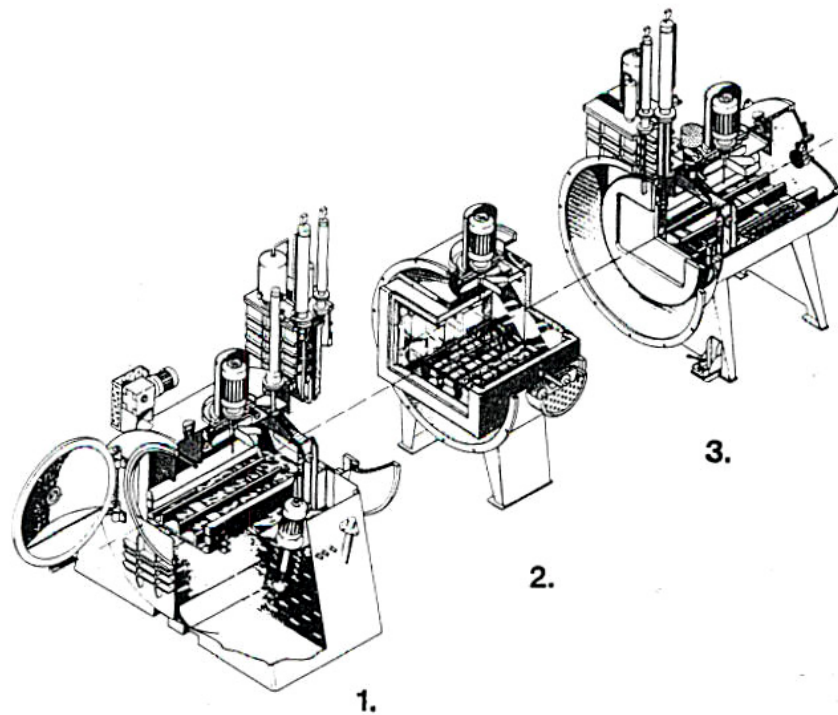


Figure 3.12: Cross-sectioned view of vacuum transfer furnace [45].

3.4 DESIGN AND CONSTRUCTION OF A VACUUM TUBE FURNACE

In order to test the theory behind the proposed vacuum casting process, it was necessary to design and construct a small vacuum tube furnace.

The concept behind a vacuum tube furnace is the sample is placed inside a ceramic tube which is sealed at one end (domed end), and has a flanged manifold at the other end (see Figure 3.13). The ceramic tube can then be evacuated to a medium vacuum level and inserted into a standard tube furnace heating element.

The tube furnace designed for this study incorporated a single phase, 20Amp element design, using Kanthal A1 material elements capable of reaching an operating temperature of 1300°C. A schematic diagram of the tube furnace is shown in Figure 3.14, and an actual photo of the constructed tube furnace is shown in Figures 3.15 and 3.16.

One of the key benefits of using a tube furnace is the fact the elements operate in a normal oxidizing environment, which is how they are designed to be used. Kanthal A1 heating elements contain a small addition of aluminium. When used in an air atmosphere, the oxygen present oxidises the surface aluminium in the alloy to form aluminium oxide which helps to protect the element from further oxidation. When using standard elements such as Kanthal A1 inside a vacuum chamber, the aluminium in the element alloy is not able to develop a protective oxide layer and hence the maximum operating temperature is significantly reduced to less than 1200°C (refer Table 3.1) [52]. Even silicon carbide elements which would normally have an operating temperature up to 1600°C in air can only be used to approximately 1200°C within a vacuum.

A standard rotary vane vacuum pump was connected to the tube furnace manifold to enable the ceramic tube to be pumped down to a vacuum of 3×10^{-3} Torr. A

manual needle valve is used on the manifold to control the pumping of the ceramic tube.

A second needle valve connected to the manifold allows inert gas to be back-filled into the ceramic tube as required.

A Type K mineral filled/stainless steel sleeved thermocouple is inserted through a gland on the manifold and extends into the hot zone of the ceramic tube to permit temperature control from the sample inserted into the tube furnace. The thermocouple is connected to a standard ramp/soak temperature controller.

The hot zone of the vacuum tube furnace is approximately 300mm long, and the inside diameter of the ceramic tube permits a maximum sample size of approximately 50mm x 50mm cross section to be inserted into the tube furnace.

The commissioning of the new vacuum tube furnace was successful, and a maximum vacuum of 3×10^{-3} Torr was achieved at a temperature of 1280°C. A typical heating curve for the vacuum tube furnace is shown in Figure 3.17.

A stainless steel “boat” is used to enable easy insertion and removal of samples. The sample is placed on ceramic paper inside the boat, and the boat is then pushed into the end of the tube using a push-rod. At the completion of the heat treatment cycle, the push-rod is used to hook the lip of the boat and the sample is then removed.

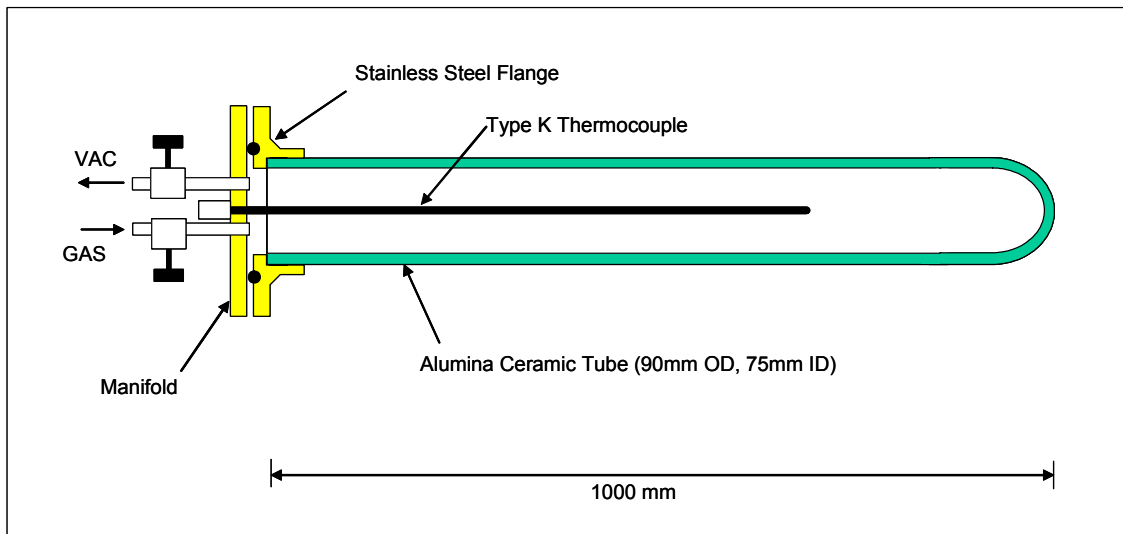


Figure 3.13: Design of ceramic vacuum tube for use in tube furnace

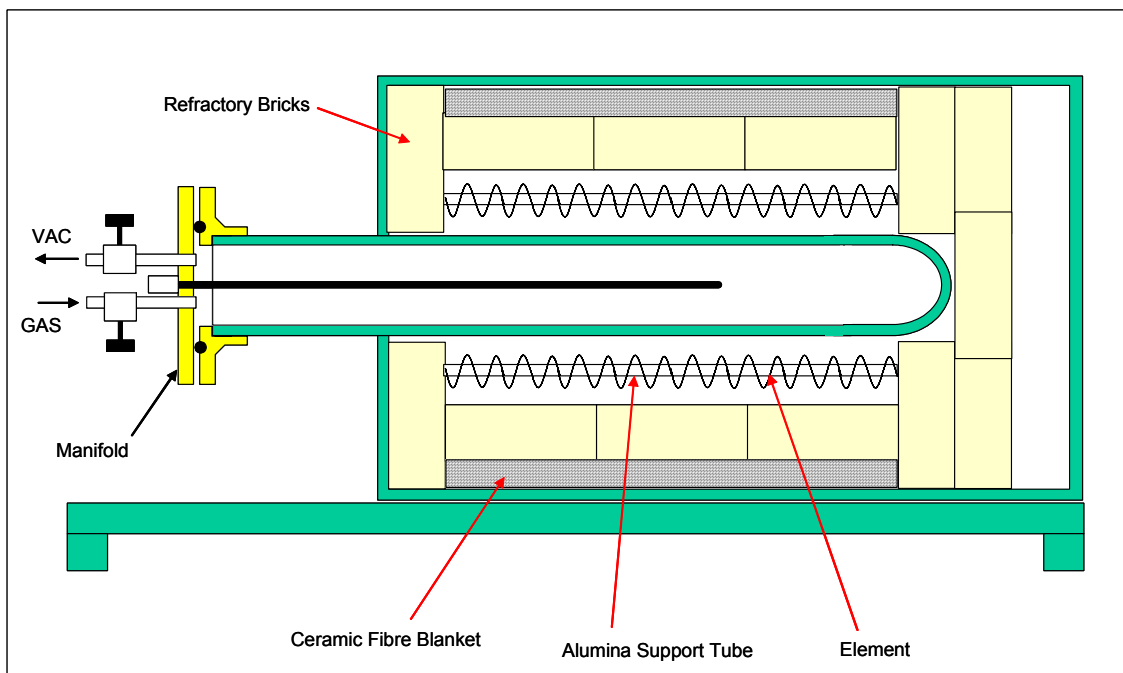


Figure 3.14: Schematic design of vacuum tube furnace



Figure 3.15: Vacuum tube furnace used for experimental development of the vacuum casting process



Figure 3.16: Vacuum tube furnace used for experimental development of the vacuum casting process

Table 3.1: Effect of furnace atmosphere on maximum element temperature [52]

	KANTHAL A-1 and APM °C	KANTHAL AF °C	KANTHAL D °C	NIKROTHAL 80 and 70 °C	NIKROTHAL 60 °C	NIKROTHAL 40 °C
Oxidizing:						
Air, dry	1400 ^{a)}	1300	1300	1200 ^{d)}	1150	1100
Air, moist	1200	1200	1200	1150	1100	1050
Neutral:						
N ₂ , Nitrogen ^{b)}	1200	1250	1150	1250	1200	1150
Ar, Argon	1400 ^{a)}	1300	1300	1250	1200	1150
Exothermic:						
10 CO, 15 H ₂ , 5 CO ₂ , 70 N ₂	1150	1150	1100	1100 ^{c)}	1100	1100
Reducing:						
Endothermic:						
20 CO, 40 H ₂ , 40 N ₂	1050	1050	1000	1100 ^{c)}	1100	1100
H ₂ , Hydrogen	1400 ^{a)}	1300	1300	1250	1200	1150
Cracked ammonia:^{e)}						
75 H ₂ , 25 N ₂	1200	1200	1100	1250	1200	1150
Vacuum:						
10 ⁻³ torr	1150	1200	1100	1000	900	900

a) Max 1425°C for APM

b) The higher values apply for pre-oxidized material.

c) Please note risk of "green rot" formation in carburizing atmospheres. Use KANTHAL AF or NIKROTHAL 70.

d) 1250°C for NIKROTHAL 70.

e) An atmosphere created by cracked ammonia, that contains uncracked ammonia, will lower the max. permissible temperature.

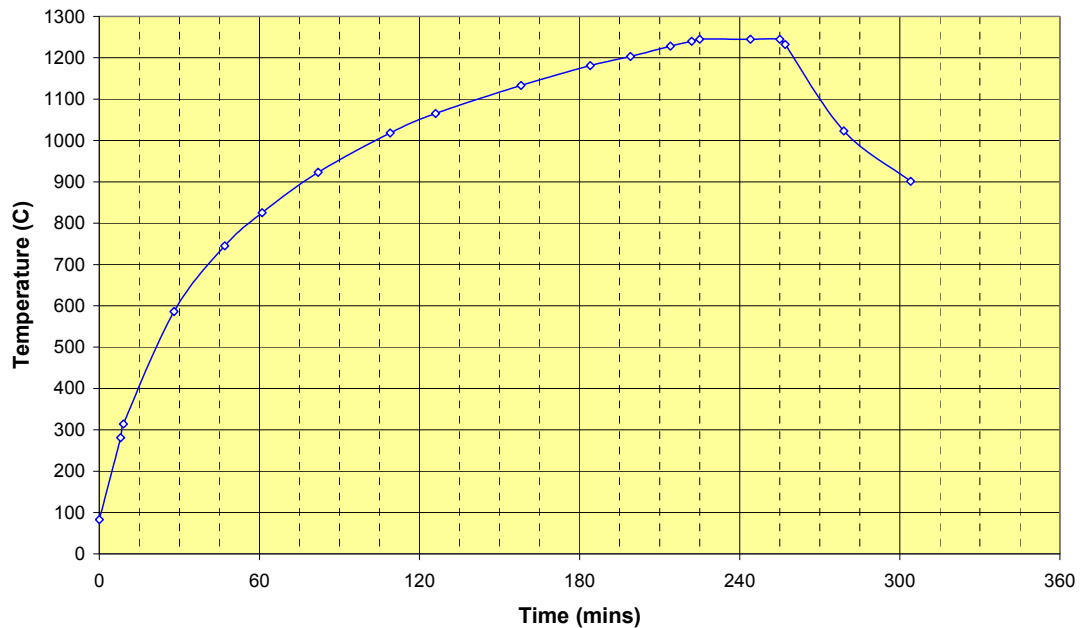


Figure 3.17: Typical heating curve for vacuum tube furnace

3.5 DESIGN AND CONSTRUCTION OF A HOT WALLED VACUUM FURNACE

To enable the production of larger field trial samples, a small Hot Walled vacuum furnace was designed and constructed. Typical commercial vacuum furnaces can be very expensive, and are generally cold-walled style furnaces, and can operate with very clean vacuums. After the early work conducted with the vacuum tube furnace, it was observed the vacuum did not have to be high in order to achieve a successful bond. Hence the emphasis on the design for the small hot walled furnace was to have a lower vacuum level compared to normal commercial furnaces.

3.5.1 GENERAL DESCRIPTION OF FURNACE

The hot wall vacuum furnace is a single steel walled vacuum vessel into which a standard electric kiln has been placed. The vacuum chamber was designed to handle a pressure greater than 0.1mbar. The schematic design of the hot wall vacuum furnace is shown in Figure 3.18.

Heating is provided via four elements inside the kiln (two of which run in series) operating at 60 volts stepped down through a transformer. The total power used by the heating elements is 14kW. The elements are made from Kanthal A1 material, and have been used successfully up to 1275°C at a pressure of 0.1mbar.

The hot zone is lined with ceramic wool fibre, with a layer of 1400°C rated fibre next to the elements, with 1260°C wool fibre behind this layer in contact with the stainless steel shell of the electric kiln.

The hot zone/electric kiln was designed to support a load of 200kg (including the furnace trays).

The recipient (vacuum chamber) is made from rolled mild steel, with the seal flange rolled from angle stock then seam welded to the main vessel. The chamber door is a single plate with C-channel cross braces, and is supported on the vessel through a single pin hinge.

The vacuum pressure of 0.1mbar is achieved using a single rotary vane vacuum pump fitted with air ballast. The pump will evacuate the vacuum chamber in approximately 20 minutes to a pressure of 0.5mbar.

A single rubber o-ring is fitted into the chamber opening flange, and is made of nitrile rubber. A smear of grease should be applied to the rubber o-ring occasionally to help provide the optimum vacuum seal.

The control of the vacuum chamber pressure is provided through isolating ball valves which have electronic activated servo motors fitted to allow remote operation via the control panel. The ball valves are rated to a vacuum level of 0.1mbar.

Inert gas such as nitrogen can be vented into the chamber through a separate manifold and control valve, which is also activated from the control panel.

A vent/exhaust tube is fitted to the vacuum pump and vent valve to permit the chamber vapor to exit the building, or allow air to be vented into the chamber to open the vessel door.

The following Figures 3.19 to 3.23 show various views of the constructed hot wall vacuum furnace.

A typical temperature profile for the hot wall vacuum furnace after commissioning is shown in Figure 3.24.

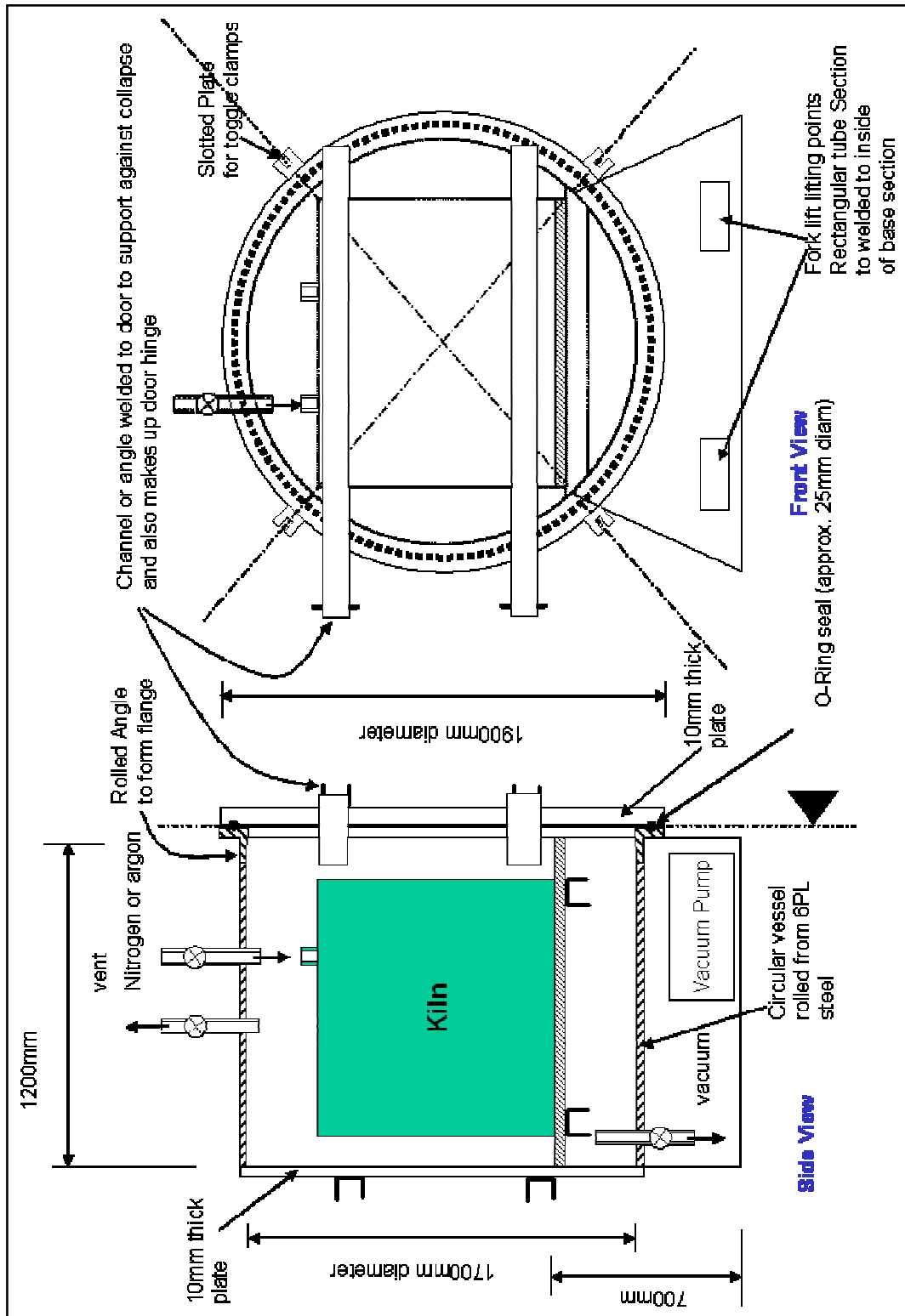


Figure 3.18: Schematic diagram of hot-wall vacuum furnace



Figure 3.19: Hot wall vacuum furnace

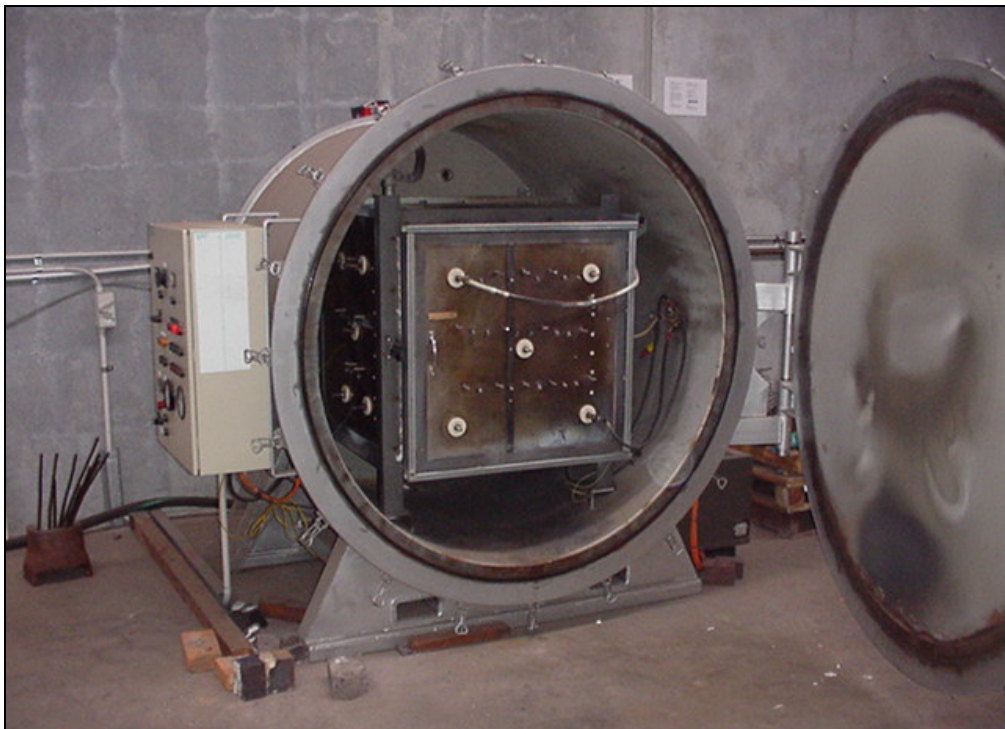


Figure 3.20: Hot wall vacuum furnace with front door open. NB: Electrical circuit must be isolated on control panel prior to opening front door.

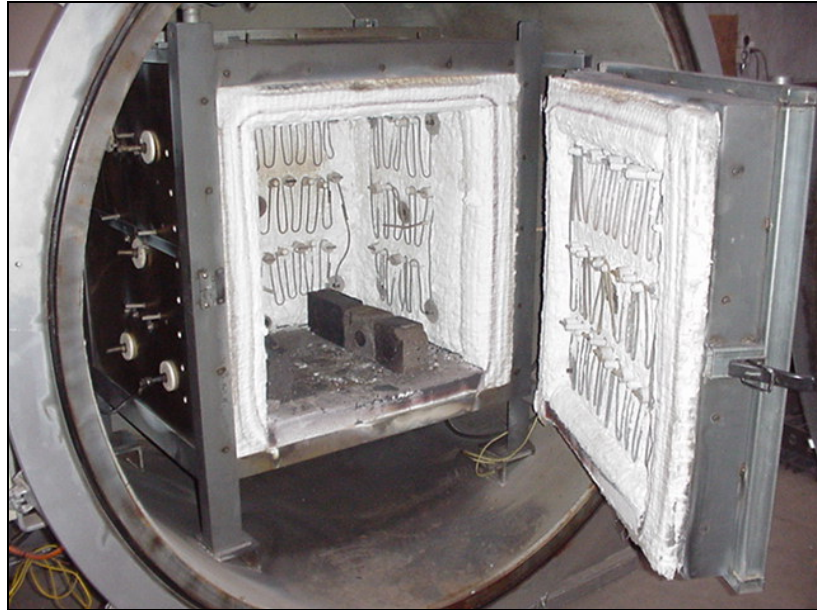


Figure 3.21: Internal view of heating elements and hot zone of hot wall vacuum furnace



Figure 3.22: View of control panel for hot wall vacuum furnace



Figure 3.23: View of vacuum pump and isolation valves for hot wall vacuum furnace

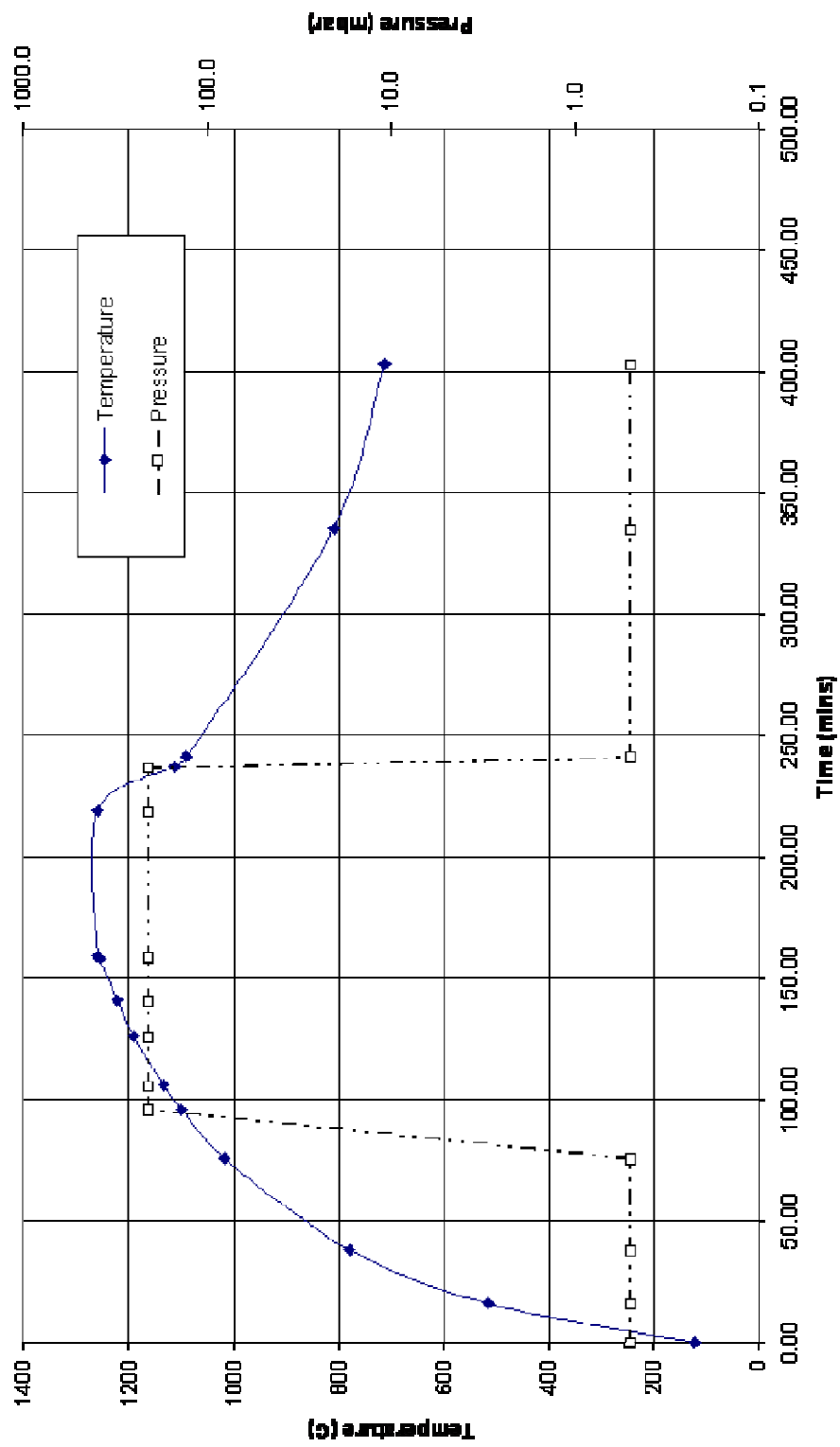


Figure 3.24: Typical temperature profile for hot wall vacuum furnace

3.6 EXPERIMENTAL

The aims of the experimental development of the vacuum casting process were as follows:

- i. Prepare test samples and conduct heat treatment cycles within the vacuum tube furnace using the low melting point alloy developed from Section 2 of this study to confirm that the vacuum casting process works;
- ii. Determine the optimum furnace cycle parameters that enable a successful bond between the steel and white iron;
- iii. Using the optimum furnace cycle parameters, conduct trials on larger components in the hot walled vacuum furnace to develop an understanding of the effect of scale on the optimum process;

3.6.1 VACUUM TUBE FURNACE TRIALS

To initially test the principals and theory behind the proposed vacuum casting process, steel substrates were prepared from “C” channel mild steel by welding two end caps to short cut sections approximately 75mm long. An example of the “C” channel with the welded end caps is shown in Figure 3.25.

Each welded steel sample was cleaned by surface grinding to remove any residual processing scale and oxide, then rinsed with acetone to degrease and remove any remaining grit.

The internal volume of the test steel substrate was measured and calculated.

A segment of the low melting point alloy C1 was selected of the equivalent mass to be less than the internal cavity volume based on the alloy density of the alloy C1. The alloy C1 sample was then cleaned and degreased prior to inserting the alloy “charge” into the prepared steel substrate (see Figure 3.26).

The steel substrate and white iron charge were then inserted into the vacuum tube furnace positioned on top of the stainless steel boat with a small segment of ceramic paper between the steel substrate and the stainless steel boat. One of the key purposes of the stainless steel boat was to protect the ceramic tube from any potential damage from molten white iron should the white iron penetrate completely through the steel substrate wall.



Figure 3.25: Prepared steel substrate after surface preparation and cleaning

The vacuum tube furnace manifold flange was then bolted to the ceramic tube, and the ceramic tube pumped down to achieve the maximum roughing vacuum of 3×10^{-3} Torr.

The needle valve for the vacuum pump was then closed, and the Nitrogen gas valve opened to back-fill the ceramic tube with a partial pressure of Nitrogen.

The gas valve was then closed and the vacuum valve reopened to evacuate the chamber a second time. Using this method of evacuating the chamber followed by partial pressure back-fill diluted any possible remaining oxygen significantly. A total of three Nitrogen back-fills and vacuum pump down cycles were performed prior to the kiln cycle starting.



Figure 3.26: Prepared white iron Alloy C1 charge and steel substrate

Each heat treatment cycle was then conducted based on the following steps:

- i. The soak set point on the temperature controller was set, and the soak period also set on the kiln controller;
- ii. The furnace cycle was then started to heat up at the fastest rate possible;

- iii. The first set of tests were run to the soak temperature on full vacuum, then allowed to soak and cool to room temperature before removing the samples for visual inspection;
- iv. The first set of samples using the full vacuum showed signs of bloating and porosity of the white iron (this will be discussed further in Section 3.5);
- v. The subsequent vacuum tube furnace cycles involved heating each sample to a temperature of 1100°C, at which point the vacuum valve was closed, and a partial pressure of Nitrogen was added to the ceramic tube to suppress the vapour pressure of the white cast iron;
- vi. The temperature was then allowed to increase to the required set-point and allowed to soak for the required duration.
- vii. Each test sample was then allowed to furnace cool and then removed from the vacuum tube furnace for visual inspection;
- viii. Each test sample was then cross-sectioned using a water cooled metallographic cutting saw to allow inspection of the internal white iron material to observe the presence of any defects such as porosity;
- ix. Selected samples were then mounted and polished for optical microscopy examination to determine the quality of the bond between the steel substrate and the white cast iron.

In order to determine the effect of soak time, test temperature and partial pressure of nitrogen, a test sample matrix was used as shown in Table 3.2.

A typical test sample after completion of the vacuum tube furnace cycle is shown in Figure 3.27.

Table 3.2: Test sample matrix covering variations in temperature, time at soak and partial pressure of inert gas

Pressure = 200mbar

Temperature (°C)	Soak Time					Set Point (°C)
	0 mins	15 mins	30 mins	60 mins	90 mins	
Liq + 0	<input checked="" type="checkbox"/>	<input checked="" type="checkbox"/>	<input checked="" type="checkbox"/>	<input checked="" type="checkbox"/>	<input checked="" type="checkbox"/>	1209
Liq + 10	<input checked="" type="checkbox"/>	<input checked="" type="checkbox"/>	<input checked="" type="checkbox"/>	<input checked="" type="checkbox"/>	<input checked="" type="checkbox"/>	1219
Liq + 25	<input checked="" type="checkbox"/>	<input checked="" type="checkbox"/>		<input checked="" type="checkbox"/>		1234
Liq + 50	<input checked="" type="checkbox"/>	<input checked="" type="checkbox"/>	<input checked="" type="checkbox"/>	<input checked="" type="checkbox"/>	<input checked="" type="checkbox"/>	1259
Liq + 65				<input checked="" type="checkbox"/>		1274

Soak Time = 60 mins

Temperature (°C)	Partial Pressure (mbar)					Set Point (°C)
	Air	800	500	200	0.1	
Liq + 0				<input checked="" type="checkbox"/>	<input checked="" type="checkbox"/>	1209
Liq + 10				<input checked="" type="checkbox"/>		1219
Liq + 25				<input checked="" type="checkbox"/>	<input checked="" type="checkbox"/>	1234
Liq + 50	<input checked="" type="checkbox"/>	<input checked="" type="checkbox"/>	<input checked="" type="checkbox"/>	<input checked="" type="checkbox"/>	<input checked="" type="checkbox"/>	1259
Liq + 65				<input checked="" type="checkbox"/>	<input checked="" type="checkbox"/>	1274



Figure 3.27: Typical bonded steel/white iron test sample after heat treatment in the vacuum tube furnace

3.6.2 HOT WALLED VACUUM FURNACE TRIALS

After the tests with the vacuum tube furnace established the optimum temperature, soak time and partial pressure parameters for the vacuum casting process, a number of trials were conducted using the hot walled vacuum furnace to allow the process to be scaled-up, and to better understand issues such as moulding, volume of white iron melted, casting methodology (feeding, gating, etc).

To make the process simulate as close as possible to full scale production a suction-cutter dredge bucket tooth was selected with a nominal mass of 3kg that could be conveniently vacuum cast within the hot walled vacuum furnace.

A suction-cutter dredge is a floating barge that is used to mine mineral sands. A boom which has a rotating cutting head is lowered into the water until it comes into contact with the floor of the mining area. As the suction-cutter rotates, the sand is scooped through the buckets and then suction from a slurry pump draws the sand slurry to the surface where it is transported to the sand separation plant.

A typical suction-cutter dredge head is shown in Figure 3.28.

To successfully trial the manufacture of the suction-cutter dredge teeth, a steel mould was prepared based on the arrangement shown in Figure 3.29.

After the steel part was cleaned and surface ground, it was placed into a steel mould which had an internal shape of the desired final white iron surface.

The white iron charge mass was determined by weighing the steel part and subtracting the effective volume from the estimated volume of the finished part.

The required white iron was then placed into the chute attached to the steel mould.

During the heating cycle of the vacuum casting process, the white iron will melt and flow down the chute of the steel mould to fill the cavity formed by the steel mould. Whilst the molten white iron is held within the steel cavity, the white iron will start to dissolve the steel substrate to form the bond between the steel substrate and the white cast iron.

Obviously if the mould was manufactured from steel, then the molten white iron would also bond to the mould. To overcome this problem, a range of ceramic coatings were trialled on the inside of the mould.

The original and worn steel bucket teeth from the suction-cutter dredge are shown in Figure 3.30.

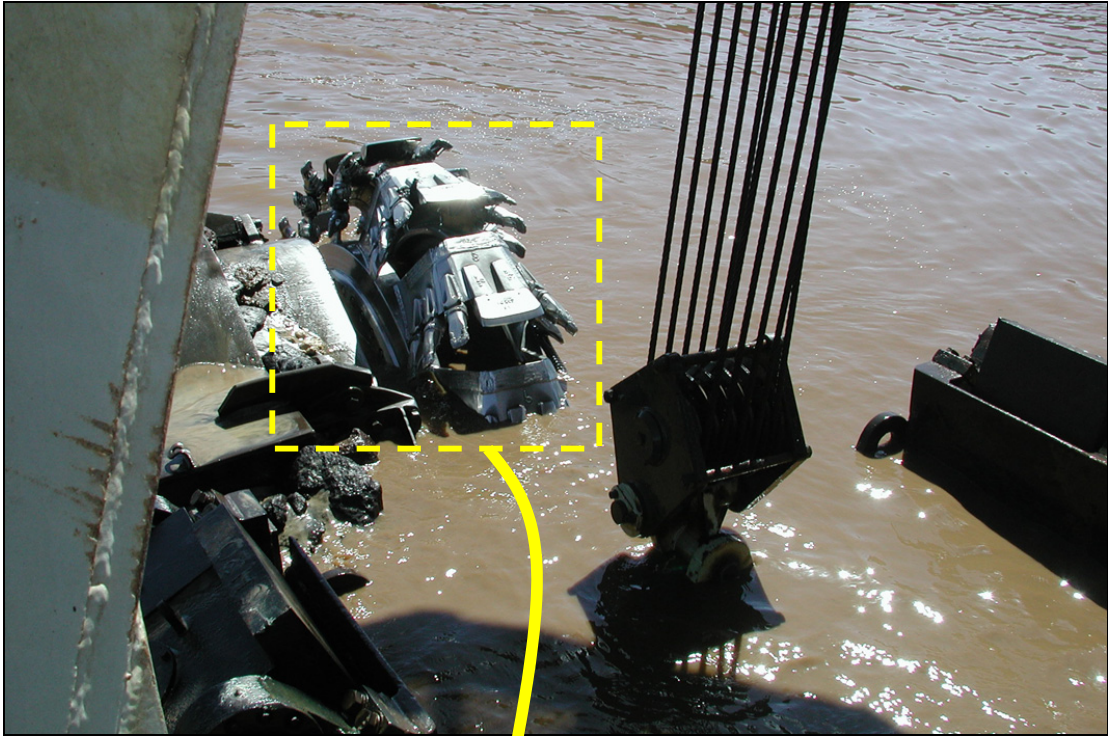


Figure 3.28: Typical suction-cutter dredge head (shown in the raised position)

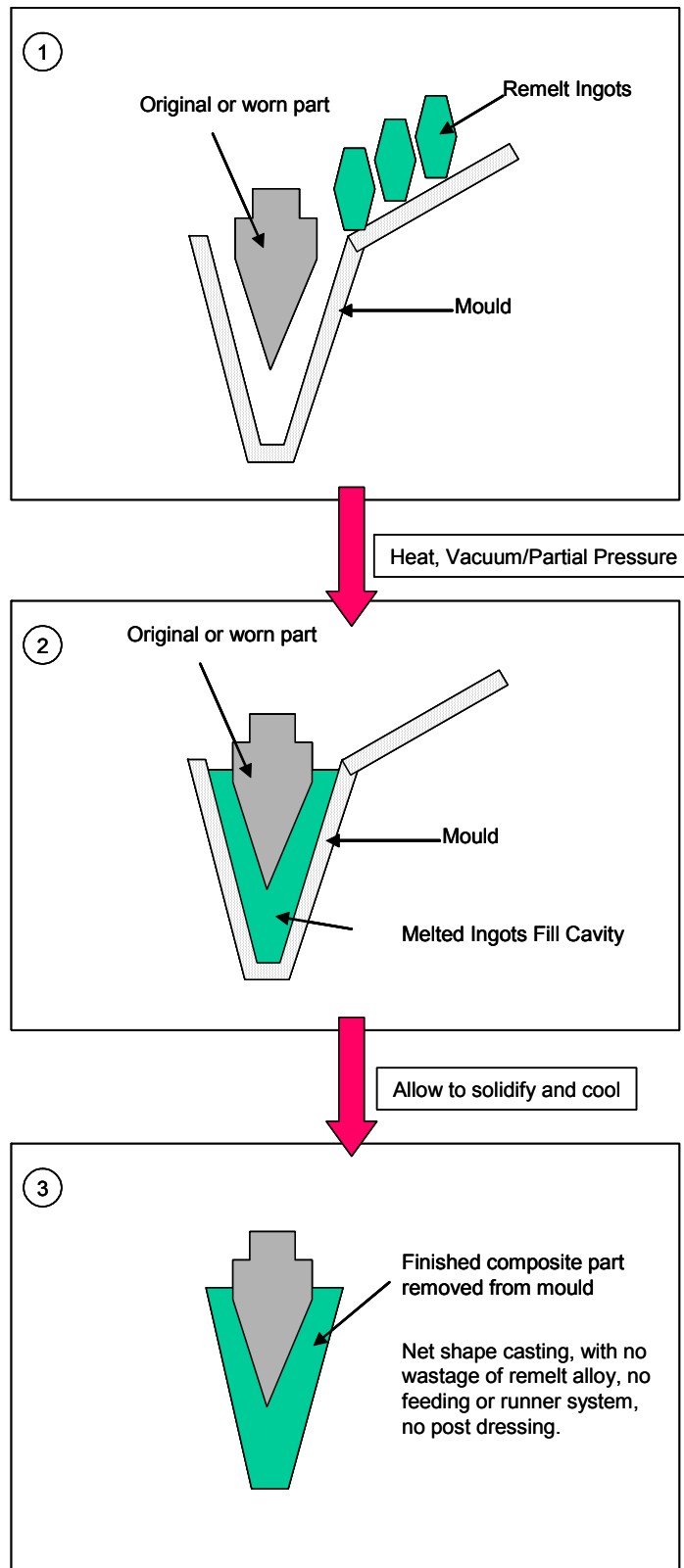


Figure 3.29: Typical mould arrangement for suction-cutter dredge bucket teeth



Figure 3.30: Typical original and worn steel bucket tooth used on the suction-cutter dredge.

3.7 RESULTS AND DISCUSSION

The testing and commissioning of both the vacuum tube furnace and the hot walled vacuum furnace were very successful, with both furnaces achieving their required duty/operating conditions.

The vacuum tube furnace was suitable for testing samples of a maximum size of 50mm x 500mm x 250mm with approximately 3 kg in mass, and could achieve a maximum vacuum with a rotary vane roughing pump of 3×10^{-3} Torr. The maximum operating temperature for the kiln was consistently tested at 1280°C.

Typical cycle times for the vacuum tube furnace was 3.5 to 4.0 hours to achieve a temperature of approximately 1250°C, with an expected cool down to room temperature of approximately 12 hours. These times produced a research furnace capable of testing one sample per day.

Similarly, the hot walled vacuum furnace was also successfully tested and commissioned to achieve a maximum operating temperature of approximately 1250°C, at a maximum vacuum of 0.1 mbar.

Typical cycle times for the hot walled vacuum furnace was a heating cycle of approximately 6 hours, with a cool down period of approximately 10 hours, depending on the load placed inside the furnace.

The initial trials to conduct the vacuum casting within the tube furnace were surprisingly very successful, and essentially the first trial sample tested produced an excellent bond between the steel substrate and the white cast iron.

There was however a number of issues that arose from the initial tests, which will be covered in the following sections of the study.

3.7.1 VISUAL ANALYSIS OF TUBE FURNACE SAMPLES

After the completion of each vacuum tube furnace cycle, the test sample was removed, labelled with the cycle number, and then photographed to enable visual comparison with other samples. A range of test samples were then sectioned through the middle to view the presence of any macro casting defects.

Figure 3.31 shows the effect of increasing the soak duration at the maximum cycle temperature on the quality and degree of melting of the white cast iron. The sample shown for zero minutes has actually partially bonded to the steel without any significant melting on a macro scale. It can be seen from the final sample for the 60 minute soak duration that full melting of the white iron has been achieved.

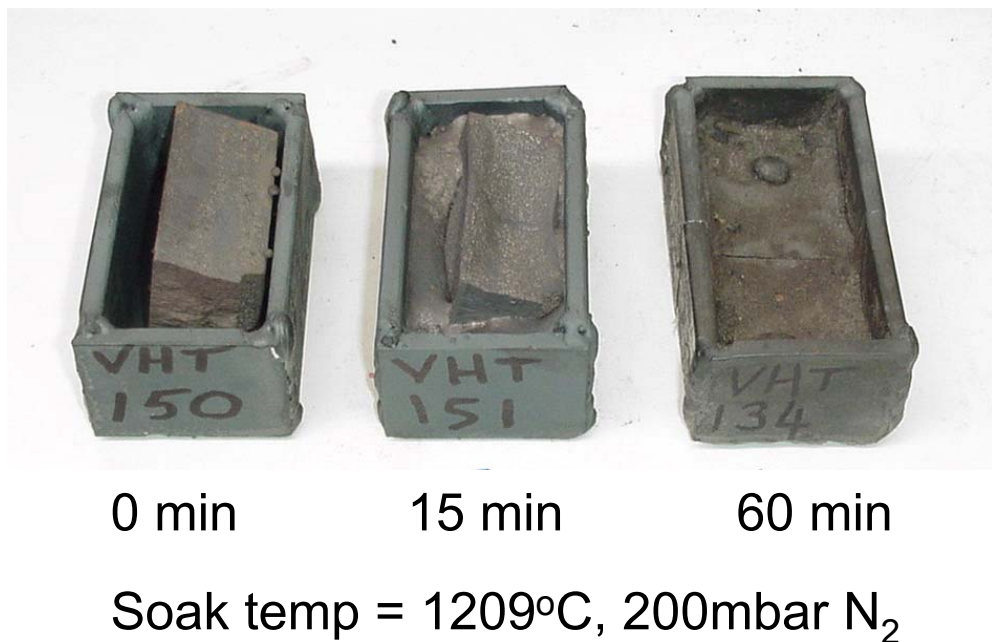


Figure 3.31: Effect of soak duration on melting of white cast iron



Air 800mbar 200mbar 0.1mbar

Soak temp = 1259°C, 60 min

Figure 3.32: Effect of nitrogen partial pressure on melting and bonding of white cast iron

The effect of changing the partial pressure on the melting and bonding of the white cast iron is shown in Figure 3.32. The sample tested in air has melted, however has left a significant slag on the surface of oxidizing white iron. Similarly, the sample tested with a partial pressure of 800mbar shows some surface slag, however bonding has improved.

The sample produced with a full vacuum shows bloating at the edges of the sample. This bloating is a result of cavitation within the liquid white iron during the melting phase of the cycle, where the vapour pressure of the liquid white iron is higher than the residual vacuum pressure in the tube furnace. Figure 3.33 shows a more detailed view of the bloating on the sample.

Based on the visual observations in Figure 3.32, the optimum partial pressure is approximately 200mbar, and this provides a sample with excellent bonding between the white iron and the steel substrate, and excellent surface finish. An

example of the test sample produced based on the ideal cycle parameters is shown in Figure 3.34.

Using the test matrix shown in Table 3.2, it was possible through visual inspection to initial assess the performance of each cycle to produce a relationship between soak temperature and soak duration for the recommended partial pressure of 200mbar. The relationship shown in Figure 3.35 shows that as the soak temperature is increased, the time required to achieve satisfactory melting and bonding of the white iron is decreased.

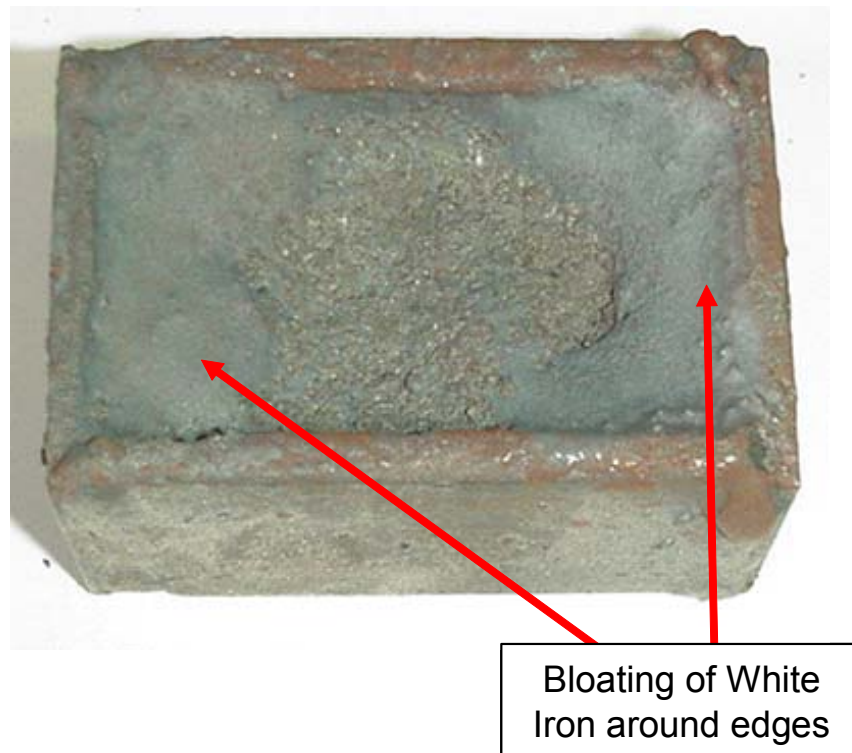


Figure 3.33: Detail of edge bloating on the full vacuum tested composite sample



Soak temp = 1259°C, 60 min,
200mbar partial pressure N₂

Figure 3.34: Excellent melting and bonding of the white iron to the steel substrate for a soak temperature of 1259°C, partial pressure of 200mbar and soak duration of 60 minutes.

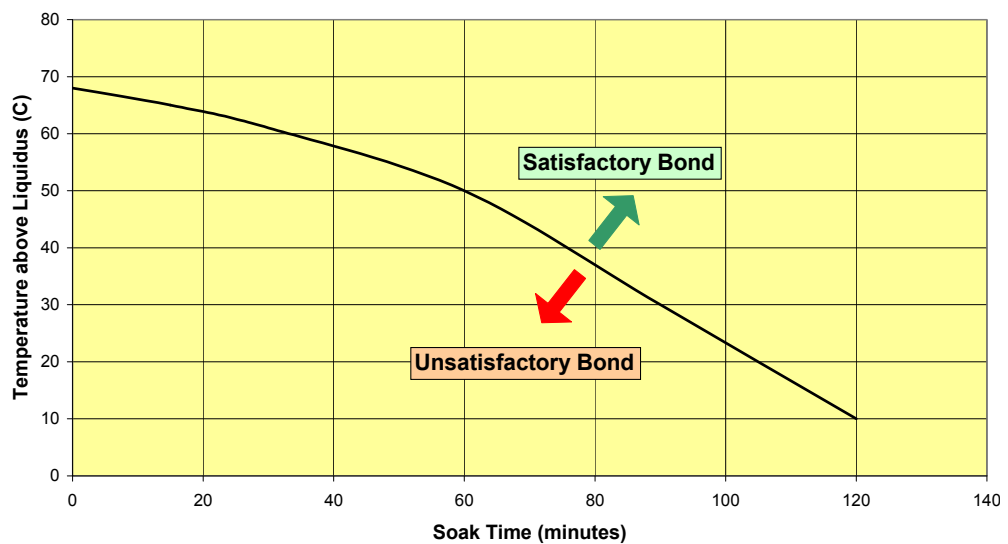


Figure 3.35: Relationship between temperature above liquidus and required soak time to achieve a satisfactory bond

Macros of the sample cross-sections for the variations in partial pressure clearly show the effect of the partial pressure on casting quality and the level of porosity. Based on the cross-sections in Figure 3.36, the ideal conditions are a partial pressure of 200mbar.

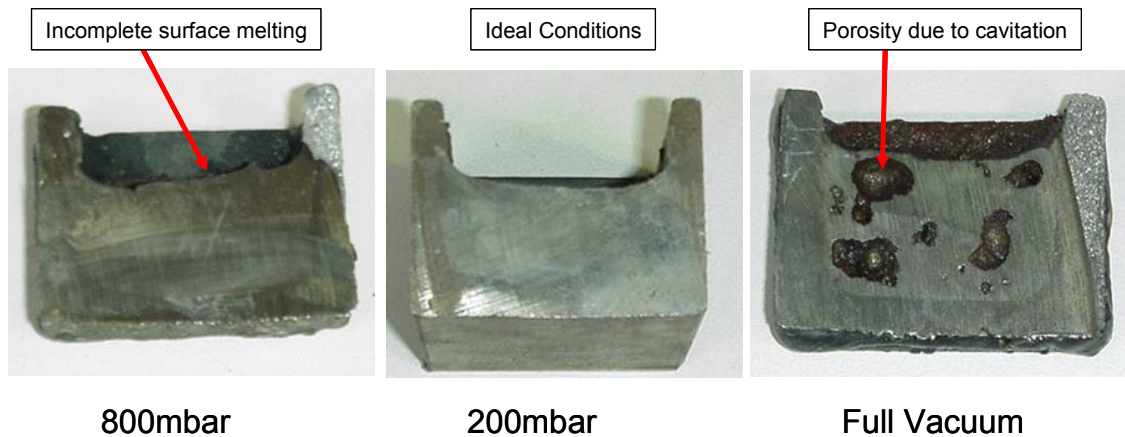


Figure 3.36: Macro images of sectioned samples with variations in partial pressure (soak temperature 1259°C, 60 minute soak duration)

Similarly, the effect of the duration at soak is shown in the cross-section macros of Figure 3.37. Even though the zero soak time samples exhibited limited melting, the white iron has still partially bonded to the steel substrate.

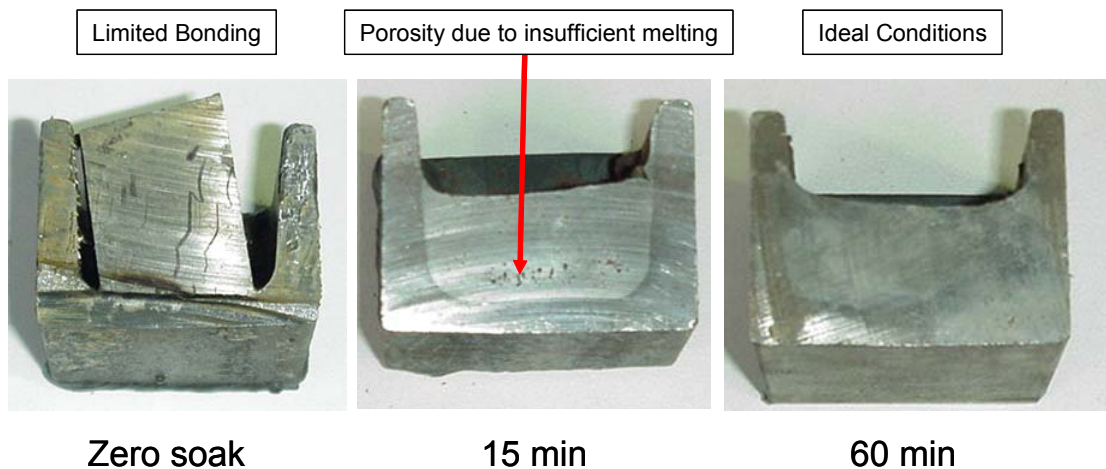


Figure 3.37: Macro images of sectioned samples with variation in soak duration (soak temperature 1209°C, 200mbar partial pressure)

The results of the visual macro inspection of the various test samples suggest the ideal vacuum casting furnace parameters are as follows:

- i. Soak temperature to be +50oC above the liquidus of he white cast iron;
- ii. At the time of soak, the partial pressure inside the furnace to be typically 200mbar
- iii. The duration of soak to be nominally 60 minutes
- iv. If a higher soak temperature is used, the duration of the soak can be shortened.

3.7.2 OPTICAL MICROSCOPY

A typical optical micrograph of the vacuum cast sample is shown in Figures 3.38 to 3.40. No brazing agent has been used to produce this sample. The micrograph demonstrates the excellent bonding between the two ferrous alloys, with no evidence of cracking at the interface.

The interface developed from the vacuum casting process exhibits four distinct zones as shown in Figure 3.41. Zone 1 is the parent steel substrate, which in this study was 0.2% C steel. This region consists of 75% ferrite and 25% pearlite.

Zone 2 is the transformed parent steel adjacent to the liquid/solid interface with the white iron. This zone exhibits a transformed microstructure of hypereutectoid steel, predominantly of pearlite, with some Fe₃C carbides precipitating along a perpendicular alignment to the primary steel/white iron interface. The transformation of the low carbon steel to eutectoid steel in Zone 2 is the result of carbon diffusion from the liquid white iron which has a significantly higher carbon content of 4.1 weight % compared to the low carbon steel.

During the melting phase of the vacuum casting cycle, the liquid white iron is in intimate contact with the solid steel substrate. It would be expected that carbon and to a lesser extent chromium would diffuse into the steel. The level of eutectoid steel in the microstructure of Zone 2 decreases as the distance away from the interface increases until the parent steel is reached in Zone 1.

Zone 3 is the white iron region adjacent to the liquid/solid interface, and is remarkable for the absence of eutectic carbides of the M_7C_3 type normally associated with high chromium white irons. Significantly, M_3C carbides have formed as a continuation of the Fe_3C carbides in Zone 2. The eutectoid Fe_3C carbide in Zone 2 appears to be acting as nucleation sites for the M_3C carbide, which then grows and extends perpendicular to the interface between Zone 2 and Zone 3.

Zone 4 represents the remainder of the white iron region, exhibiting eutectic M_7C_3 carbides, M_3C quasi-peritectic carbides with a ferrous matrix.

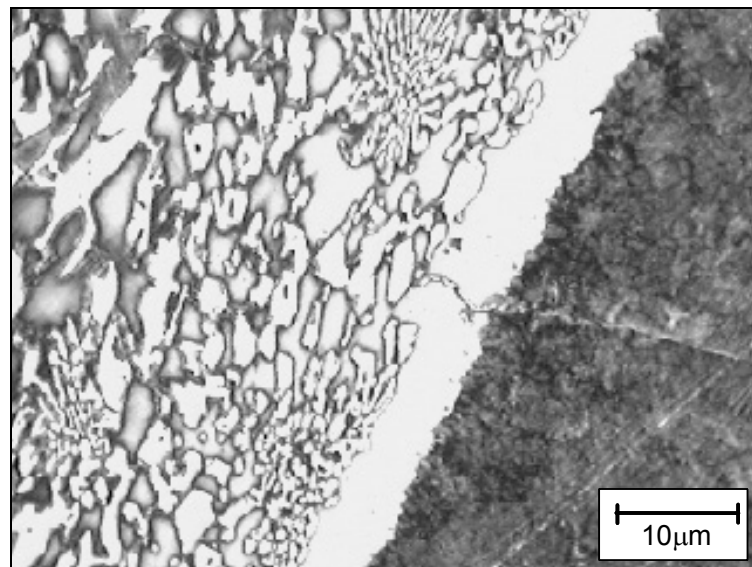


Figure 3.38: Optical micrograph of vacuum cast interface (etchant acid ferric chloride)

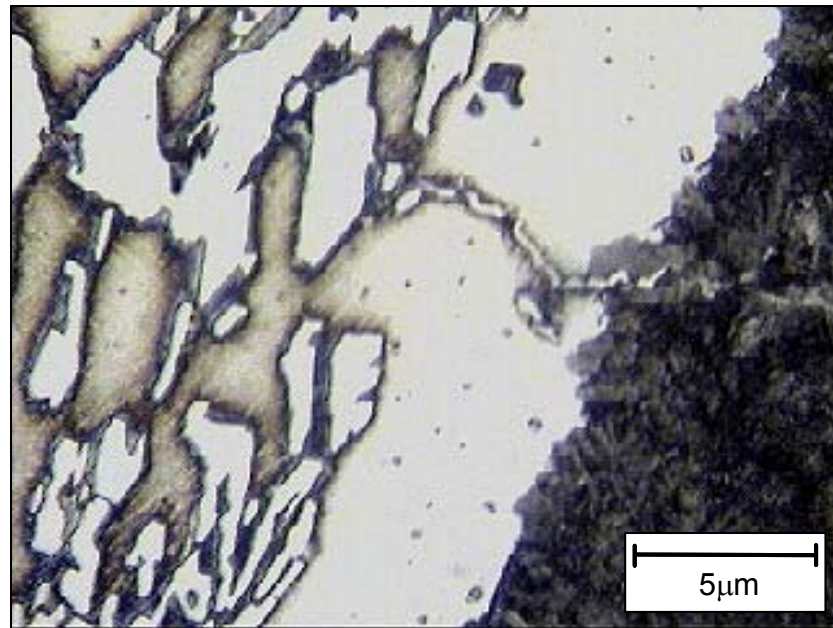


Figure 3.39: Detail of interface area (etchant acid ferric chloride)

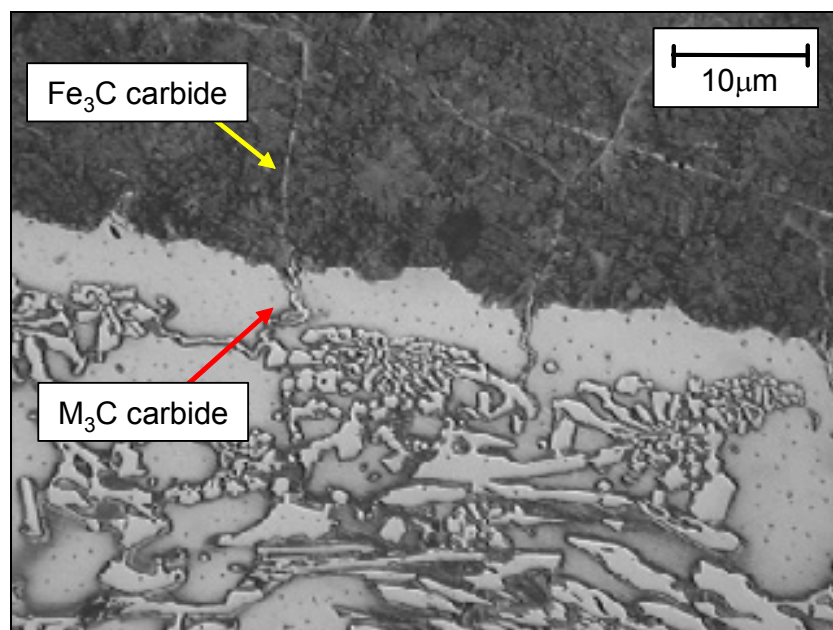


Figure 3.40: Optical micrograph of vacuum cast interface (etchant acid ferric chloride). Note the continuation of the M_3C carbides in the white cast iron from the Fe_3C carbides in the steel.

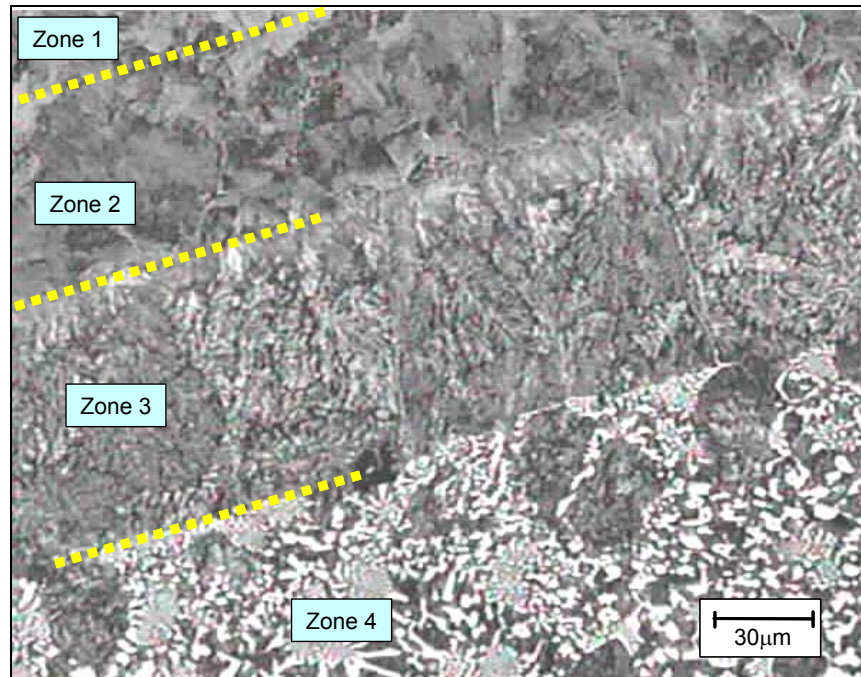


Figure 3.41: Location of microstructural zones on vacuum cast interface

The quality of the bond between the steel and the white iron produced from the vacuum casting process is highlighted in Figure 3.42. Along the length of the bond area, there is no evidence of inclusions or porosity, and there is no evidence of any detrimental cracking, such as that would be observed with hard facing composites of steel and white cast iron.

A number of significant observations were initially made after the review of the optical microscopy as follows:

- i. The width of Zone 3 increased with increasing soak duration and increasing temperature above the liquidus
- ii. The width of Zone 2 increased with increasing soak duration, increasing temperature above the liquidus, and increasing time of cooling at the completion of the cycle

In order to quantify the effects of soak duration and temperature on the Zone 2 and 3 microstructures, a series of microhardness profiles on a range of test samples were conducted.

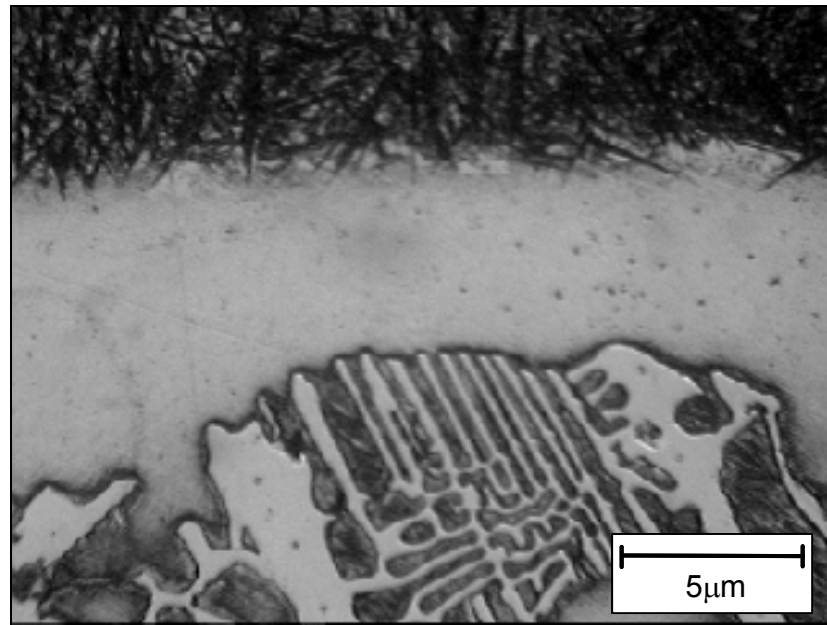


Figure 3.42: Detail of carbide-free zone in interface area (etchant acid ferric chloride)

3.7.3 MICROHARDNESS PROFILES OF INTERFACE REGION

In order to better understand the relationships between microstructure and test cycle conditions a series of microhardness profiles were conducted on a range of samples.

During the vacuum casting process, it would be expected that both liquid state diffusion and solid state diffusion would occur for elements across the interface. Liquid state diffusion would occur for carbon and chromium from the white cast iron into the solids steel substrate. Since carbon is a significantly smaller atomic size compared to chromium, nickel and manganese, it would be expected the diffusion rates into the steel for carbon to be much higher compared to other alloying

elements, as the carbon is dissolved interstitially and therefore diffuses faster compared to the substitutional solutes.

The solid state diffusion rates would be expected to be slower compared to the liquid state diffusion rates.

Figure 3.43 shows a typical microhardness profile for the vacuum cast conditions of +65°C above the liquidus, 60 minute soak time, and 200mbar partial pressure.

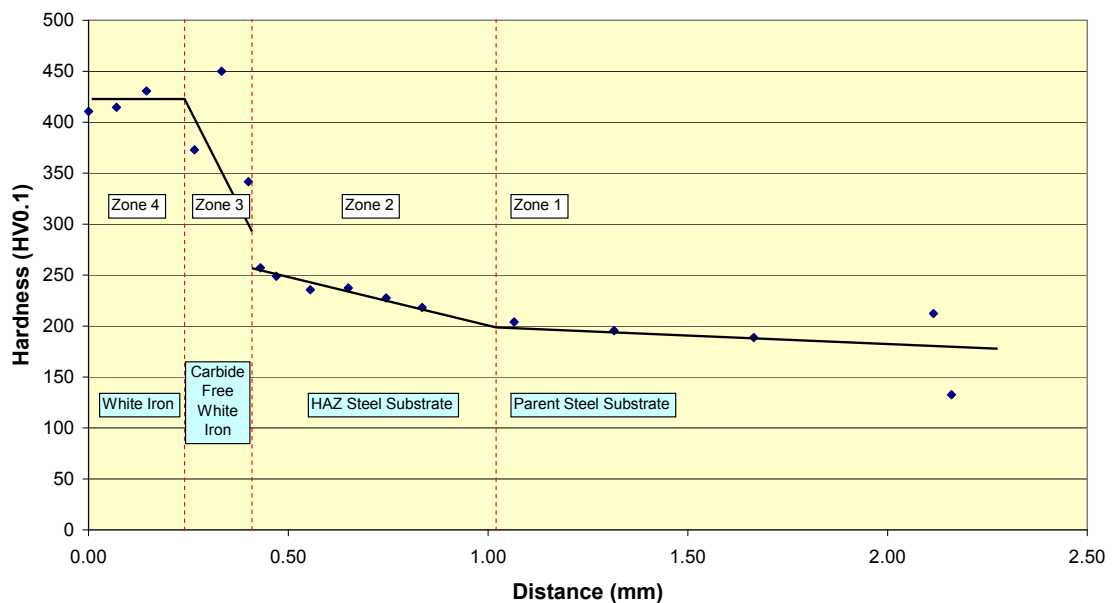


Figure 3.43: Typical microhardness profile for vacuum cast white iron/steel composite (+65°C above Liquidus, 60 minute soak, 200mbar partial pressure)

The data in Figure 3.43 shows that the white iron ferrous matrix hardness decreases in the Zone 3 area, most likely due to the decrease alloying elements as a result of diffusion into the steel substrate. The decrease in alloying elements would affect the hardenability of the white cast iron, resulting in a greater propensity to form a pearlitic ferrous matrix upon cooling.

The hardness of the Zone 2 Heat Affected Zone (HAZ) Steel Substrate is higher compared to the Zone 1 Parent Steel Substrate due to the diffusion of carbon into Zone 2. Based on the measured microhardness values in Figure 3.43, the HAZ distance can be determined as 0.6mm of depth.

Similar microhardness test data were obtained for a range of test samples produced from the vacuum tube furnace, and additional test data examples are provided in Figures 3.44 to 3.46. The microhardness data was then used to determine the depth of the Zone 3 and Zone 2 layers within each vacuum cast sample. The depth of the Zone 2 layer should be able to be correlated against the temperature data to determine the liquid state diffusion rate for the white iron into the steel. Longer soak times and higher soak temperatures increase the depth of the Zone 2 layer. The Zone 2 and 3 depth data obtained from the microhardness data is summarised in Table 3.3.

Table 3.3: Summary of Zone 2 and 3 depths based on microhardness data for vacuum cast samples

Soak Above Liquidus (°C)	Soak Duration (min)	Partial Pressure (mbar)	Zone 3 Depth (mm)	Zone 2 Depth (mm)
0	0	200	0.075	0.150
0	60	200	0.140	0.300
25	0	200	0.080	0.220
50	30	200	0.086	0.370
65	60	200	0.155	0.630

In order to determine the solid state diffusion rates for the elements in the vacuum cast samples, the vacuum cast sample for +50°C above the liquidus and soaked for 30 minutes was sectioned into several samples, then heat treated at 1100°C for 10 and 30 minutes to determine the change in microhardness profiles. Any movement observed with the Zone 2 depth would be directly attributable to the solid state diffusion rate.

The microhardness profiles for the heat treated samples are provided in Figures 3.47 and 3.48. The change in Zone 2 depth after heat treatment is summarised in Table 3.4.

Table 3.4: Effect of HEAT TREATMENT ON Zone 2 depth for vacuum cast composite

Description	Zone 2 Depth (mm)
+50°C Soak, 30 min, 200mbar	0.37
Heat Treated @ 1100°C for 10 min	1.42
Heat Treated @ 1100°C for 30 min	2.50

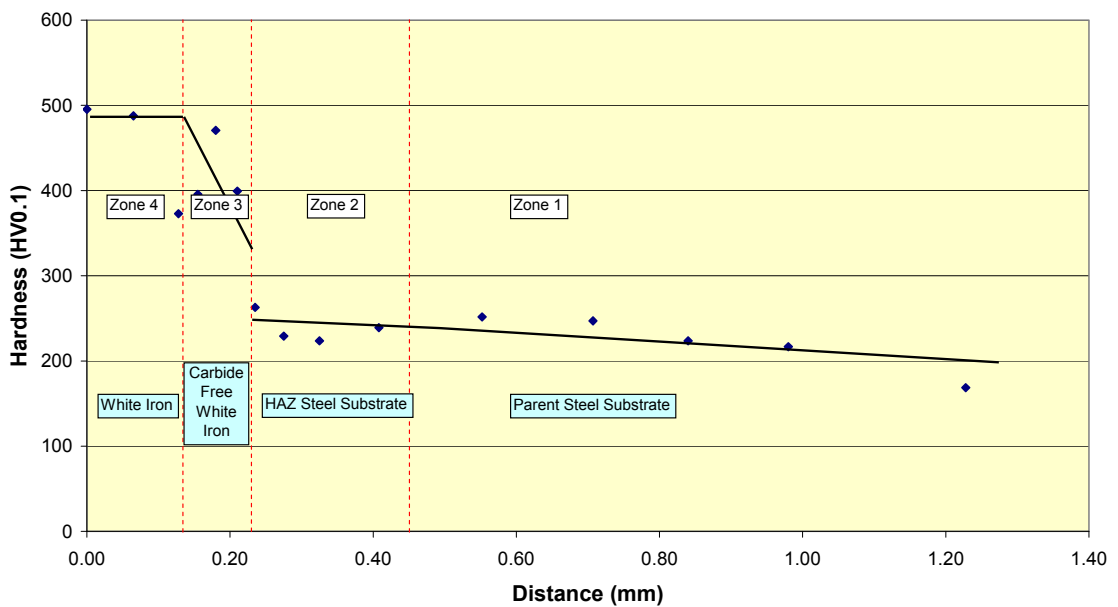


Figure 3.44: Microhardness profile for vacuum cast white iron/steel composite (+25°C above liquidus, zero soak, 200mbar partial pressure)

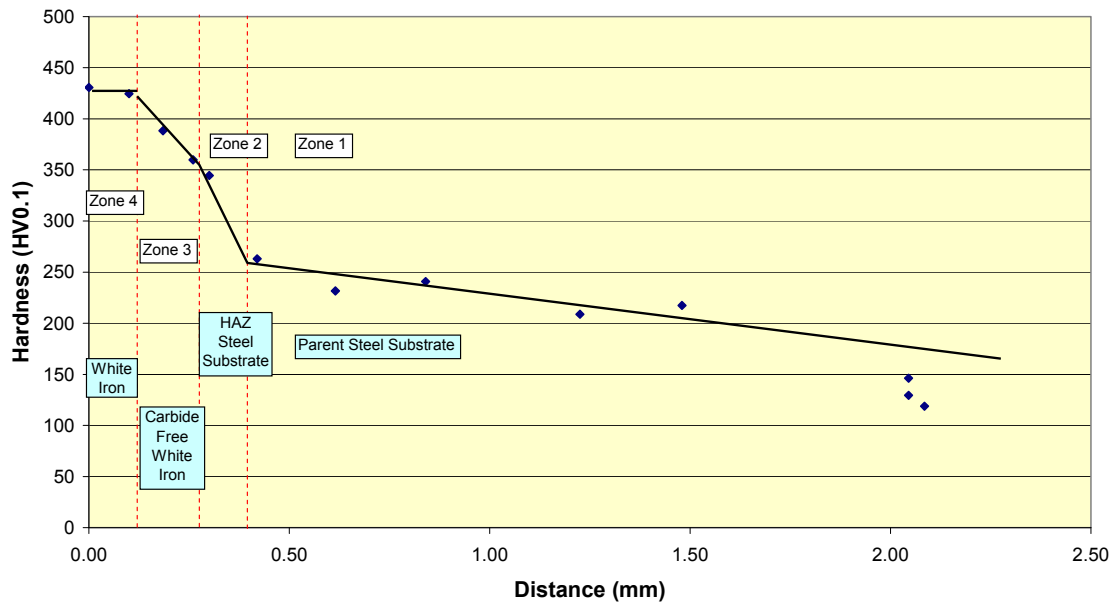


Figure 3.45: Microhardness profile for vacuum cast white iron/steel composite (+zero °C above liquidus, zero soak, 200mbar partial pressure)

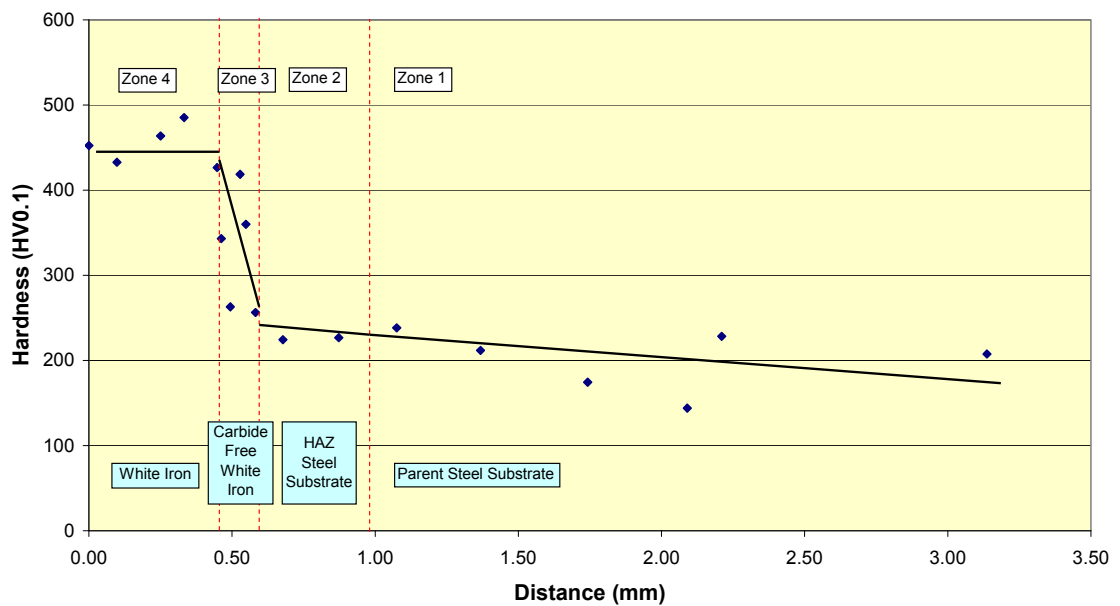


Figure 3.46: Microhardness profile for vacuum cast white iron/steel composite (+25 °C above liquidus, 30 min soak, 200mbar partial pressure)

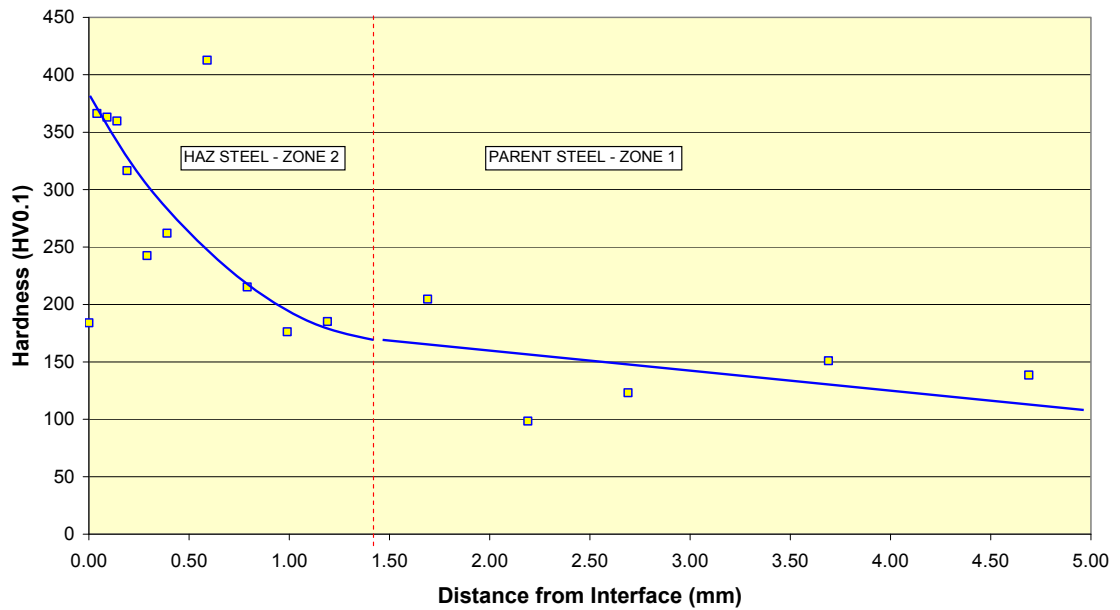


Figure 3.47: Microhardness profile for heat treated vacuum cast white iron/steel composite at 1100°C for 10 minutes (Original +50 °C above liquidus, 30 min soak, 200mbar partial pressure)

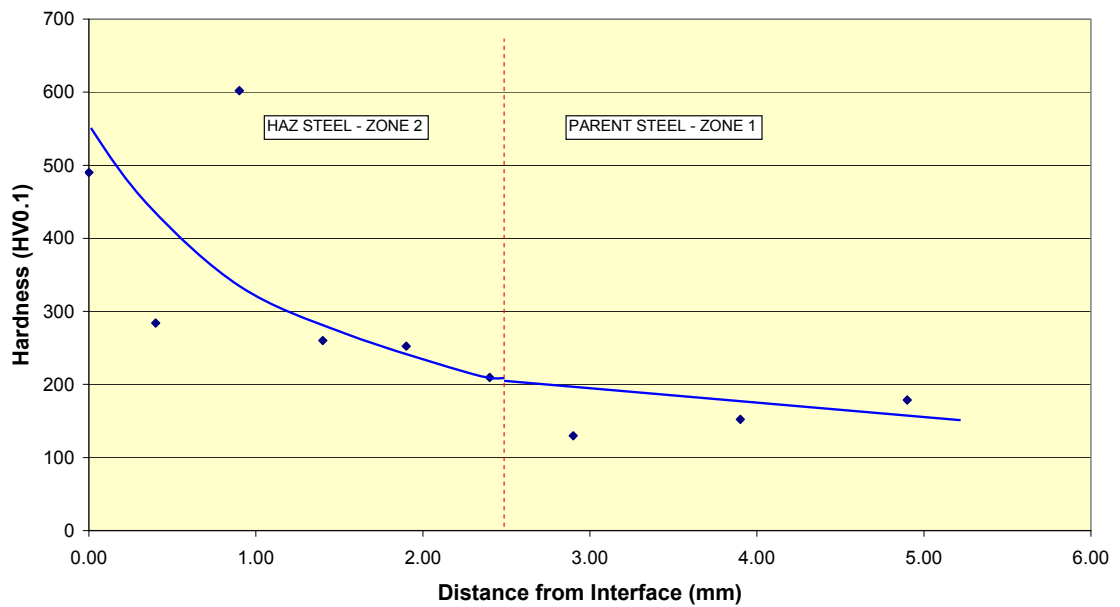


Figure 3.48: Microhardness profile for heat treated vacuum cast white iron/steel composite at 1100°C for 30 minutes (Original +50 °C above liquidus, 30 min soak, 200mbar partial pressure)

3.7.4 DESCRIPTION OF VACUUM CASTING PROCESS

During the vacuum casting process, the white iron alloy forms a liquid phase, which under the exclusion of oxygen improves the wetting of the steel substrate. The key factors determined for controlling successful bonding between the white iron and the steel were:

- i. quality of vacuum – medium vacuum of 3×10^{-3} Torr, with a back-filling of the chamber with a partial pressure of 200mbar of inert gas, typically nitrogen, to suppress porosity in the finished casting;
- ii. temperature of soak – optimum temperature is $+50^{\circ}\text{C}$ above the liquidus of the white cast iron; and
- iii. duration of soak – a period of 60 minutes provides good quality bonding.

When the white iron is liquid within the vacuum chamber, the vapour pressure of the white iron is higher than the residual pressure within the chamber, and results in cavitation of the white iron alloy. The cavitation results in significant porosity within the resultant composite white iron.

Adding a partial pressure to the vacuum chamber of inert gas, such as argon or nitrogen, increases the vacuum chamber pressure to a level such that cavitation does not occur, and a sound casting is produced.

The solid/liquid reaction during the melting phase of the vacuum casting process is shown diagrammatically in Figure 3.49.

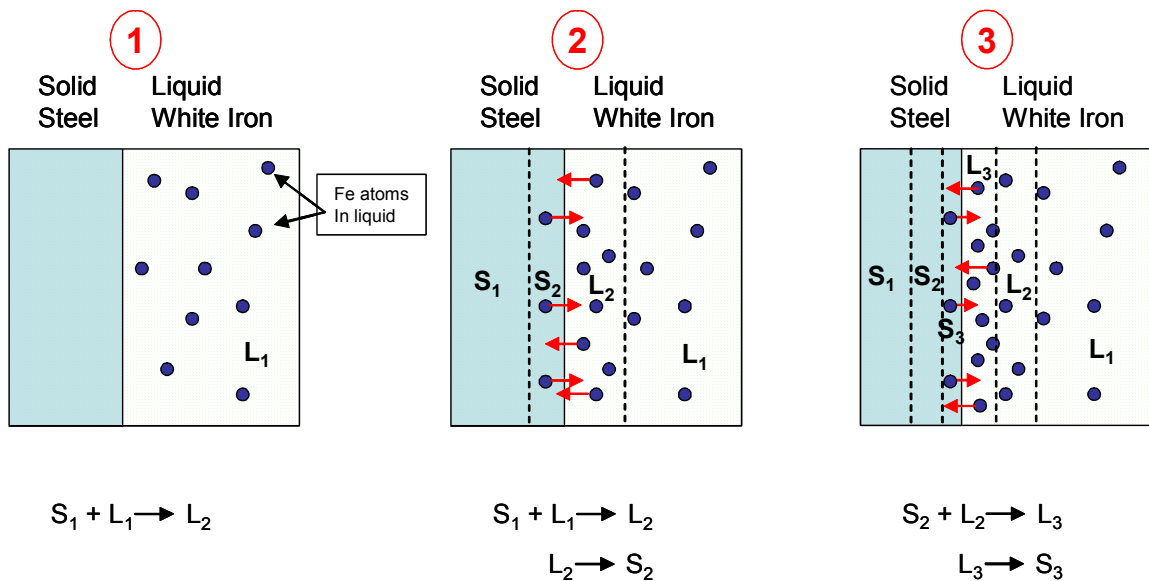


Figure 3.49: Schematic diagram of solid/liquid interface during the vacuum casting process

When the white iron is molten and initially in contact with the steel substrate (solid), the liquid alloy will start to dissolve the solid, and principally iron is dissolved into the liquid alloy. The increase in iron into the liquid alloy produces a locally rich liquid zone in the absence of any stirring or relative velocity of liquid metal. In the Fe-Cr-C alloy system, when the percentage of iron increases in the white iron, the melting point of the liquid increases.

Hence locally at the solid/liquid interface, the melting point of the liquid increases, and some solidification of this new composition will occur, albeit for only a relatively small period as the bulk of the material adjacent is still liquid.

The remaining liquid then begins to dissolve the adjacent solid, which is now of a slightly different composition to the original steel. The process continues producing a gradual dissolution of the steel substrate into the liquid white iron.

Parameters such as soak temperature, soak duration, white iron composition, cleanliness of the original steel substrate, vacuum pressure, etc. all have an influence on the resulting bond.

The complete vacuum casting process as developed by this study is summarised in Figure 3.50.

The new vacuum casting process involves the use of a metal shell or ceramic mould which is heated inside a vacuum furnace, and contains a low melting point white iron in the form of beads, pellets or small ingots (see Figure 3.51).

The alloy shells are typically cast or fabricated from mild steel, then shot blasted and cleaned prior to use, or alternatively, a steel shape can be positioned inside a ceramic shell into which the molten white iron will fill the cavity.

The shells are heated inside the vacuum furnace to a temperature greater than the liquidus temperature of the remelt alloy. Typically the liquidus of the remelt alloy is 1200 to 1210°C. After the shells containing the remelt alloy achieve the required temperature, the temperature is held constant for a period, allowing the remelt alloy to become molten and flow into the shell cavity. Oxidation is minimised through the use of the vacuum furnace.

After the required soak time, the furnace is allowed to cool until the new composite parts are at a temperature of 1000°C. At this temperature the furnace can be opened if desired to atmosphere and the charge removed to allow to air cool and achieve the required white iron alloy hardness.

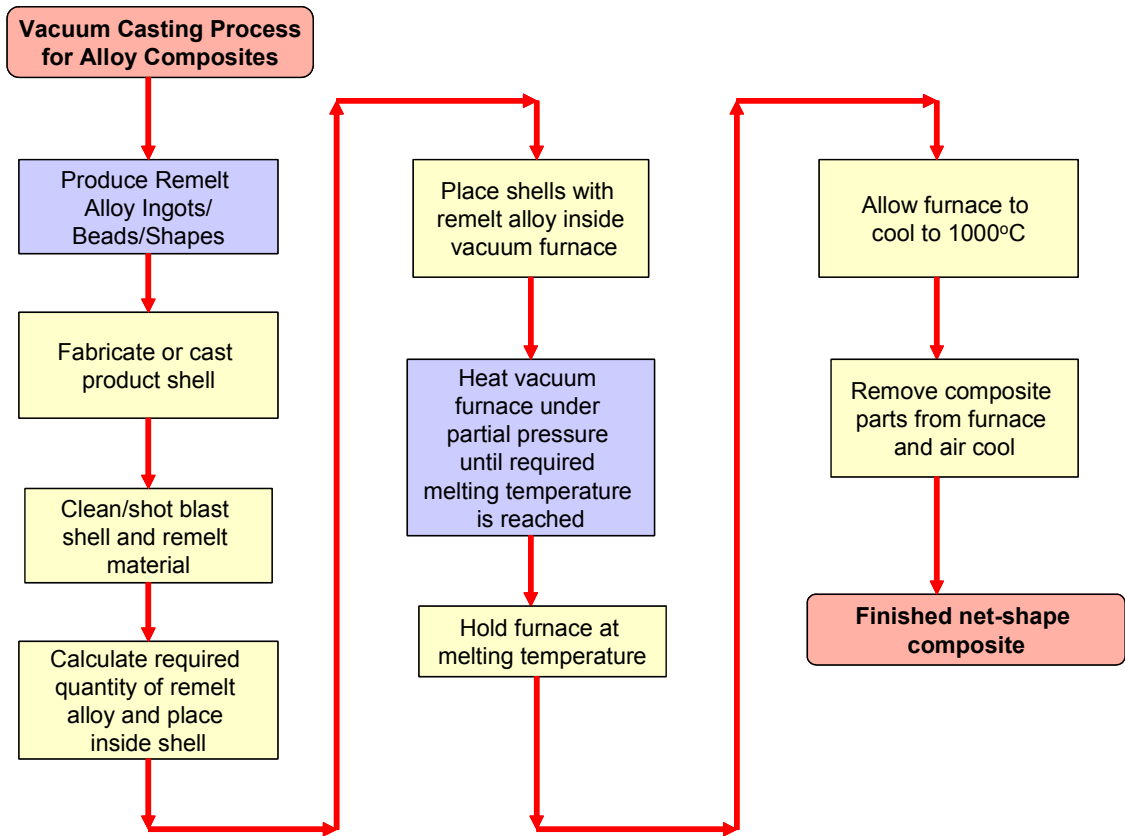


Figure 3.50: Vacuum casting process flow chart

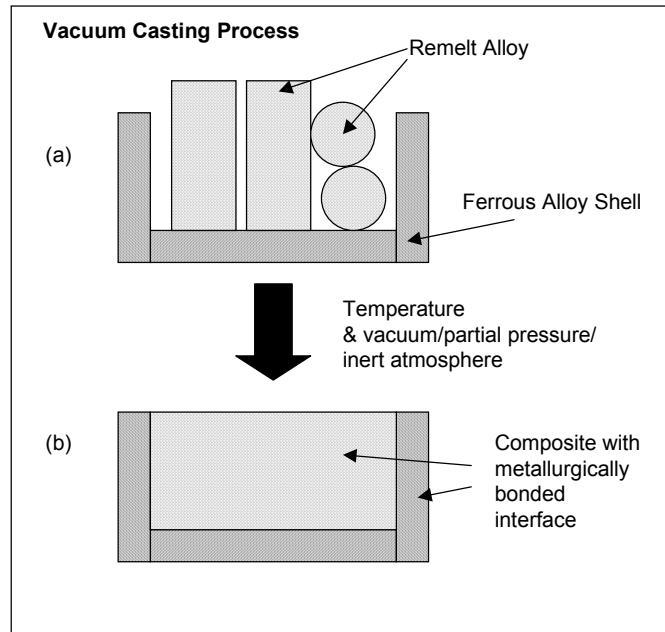


Figure 3.51: Schematic diagram of steel shell for white iron/steel composite

The interface developed from the vacuum casting process exhibits four distinct zones as shown in Figure 3.41. Zone 4 is the parent white iron, which typically consists of complex chromium carbides supported within a ferrous matrix. Zone 3 is a carbide depleted region adjacent to the bond interface, with the composition of this phase typically the equivalent to the ferrous phase of the Zone 4 white iron alloy. Zone 3 has intergranular M_3C carbides which extend perpendicular to the interface. Zone 2 is the steel region adjacent to the bond interface, and consists almost entirely of the eutectoid transformation phase pearlite, with some intergranular M_3C carbides. Further away from the interface within the steel the original steel parent alloy is Zone 1.

The presence of the liquid white iron adjacent to the steel during the vacuum casting process provides a high source of carbon that can readily diffuse into the steel, as with carburizing processes. Microhardness testing of the Zone 2 HAZ steel confirms the increase in hardness as a result of the diffusion of carbon. The effect of the carbon diffusion is also seen visually with optical microscopy in the form of increased eutectoid pearlite formation near the interface.

3.8 SUMMARY OF OUTCOMES

A new composite manufacturing process has been developed that permits the production of white iron/steel composites. The key differences of the new vacuum casting process compared to other current processes for composite manufacture include:

- i. • Elimination of machining or grinding
- ii. • Removal of brazing alloy
- iii. • Enhanced design flexibility
- iv. • Enhanced control of microstructural features
- v. • Lower cost of production

The new vacuum casting process involves the following key steps:

- Producing a steel substrate to which the white iron will be bonded. The steel substrate can either be in the form of a shell that will retain the white iron when cast, or can be an inert that is positioned into a ceramic mould (or ceramic lined steel mould);
- After cleaning the steel substrate by either grit blasting or surface grinding, the white iron and steel substrate are placed together into a vacuum furnace and heated until the temperature inside the vacuum furnace is typically 50°C above the liquidus of the white cast iron.
- Before the white iron becomes molten, a partial pressure of inert gas (typically nitrogen) is back-filled into the vacuum furnace to increase the pressure of the chamber above the vapour pressure of the liquid white cast iron.
- After the white iron is liquid, it flows and fills the cavity and comes into contact with the steel substrate.

- The liquid white iron begins to partially dissolve the steel substrate, forming a liquid/solid reaction front. After a suitable soak period, sufficient reaction with the steel substrate will have occurred, and upon subsequent cooling of the sample, a full metallurgical bond will be achieved.

Compared to existing vacuum brazing and welding methods, the new process enables the following:

- i. Greater flexibility in design and shape due to the elimination of surface machining or grinding;
- ii. Can produce white iron/steel composites not normally possible using conventional processes;
- iii. Reduction in cost for comparable vacuum brazed wear blocks and plates;
- iv. Elimination of need for machining or grinding, and the elimination of the need of a brazing alloy as compared with conventional vacuum brazing;
- v. Excellent joint strength with minimum dilution;
- vi. Permits the use of a variety of additional composite materials within the same process concept;
- vii. Can be used to repair white iron castings without the need for welding. Welding is extremely difficult for white cast irons, and can often result in component failure;
- viii. Finished composites are net-shape requiring minimal post heat treatment dressing, and no waste remelt material usually associated with cast processes;
- ix. No casting shrinkage is present in remelted portion of finished products;
- x. Ability to control solidification rate of remelt alloy through control of the vacuum furnace which enables control of the microstructure through grain size refinement.

The results of the experimental work conducted in this study have shown the optimum conditions for the vacuum casting include the following:

- Soak temperature should be nominally +50°C above the liquidus of the white iron;
- The soak duration should be typically 60 minutes;
- The partial pressure of gas should be 200mbar to avoid porosity in the casting and maximise the wetting of the steel substrate with the liquid white iron.

CHAPTER 4

4.1 INTRODUCTION

The success of the vacuum casting process detailed in Chapter 3 of this study demonstrates the excellent performance of the process to produce a quality composite alloy product. In order to understand the process from an atomic level, and to further demonstrate the quality of the bonds produced from the vacuum casting process, the interface region of the composite has been examined using both classical metallurgical processes and more modern electron microscopy techniques.

The aims of the electron microscopy were to establish:

- High resolution imaging of the four zones within the vacuum cast composite;
- Quantify the chemical composition of the various phases found within the alloy composites;
- Conduct extensive quantitative x-ray mapping to study the diffusion of elements such as carbon, chromium and nickel, and to observe the presence of various chemical phases within the four zones of the composite interface;
- Conduct electron backscattered diffraction (EBSD) on various samples to quantify the crystallography of the four zones observed in the composite interface; and
- To calculate and compare diffusion based elemental compositions with the measured data from the x-ray mapping.

4.2 OPTICAL MICROSCOPY OF INTERFACE REGION

Optical micrographs were obtained for various vacuum cast samples by sectioning the steel “C” section samples produced in Chapter 3 of this study. Each sample was sectioned from the same region of the steel cross-section in order to provide some capacity to quantify differences resulting from vacuum casting process variables such as process temperature, duration of soak, and partial pressure of the vacuum chamber. The samples were then polished to a 1 micron finish then etched in a 5% HCl acid-ferric chloride solution for 20 seconds to reveal the underlying microstructure.

Bright field optical images were obtained for the various samples using a Reichert MeF inverted stage microscope with the Polaroid camera system replaced with a low light digital microscope camera to enable recording and processing of images of the interface.

Figures 4.1 and 4.2 show a typical bright field image for the vacuum cast interface. The steel substrate (Zone 2) has etched dark indicating a high volume fraction of pearlite adjacent to the interface. The pearlite also has the presence of some pro-eutectoid Fe_3C carbide between the prior austenite grain boundaries. M_3C carbides can be seen extending perpendicular to the interface into the Zone 3 region of the white cast iron, also known as the “carbide depleted” zone. Figure 4.3 also highlights the Fe_3C and M_3C carbides in Zones 2 and 3.

In the examples shown in Figures 4.1 and 4.2, the ferrous matrix of the white cast iron is essentially wholly austenitic. Other samples as shown in Figure 4.5 show a partially pearlitic white cast iron ferrous matrix.

The detail of the interface between Zone 2 and Zone 3 is highlighted in Figure 4.4. The shape of the eutectic carbides in the white cast iron suggests the carbides consist of M_7C_3 and M_3C type carbides.

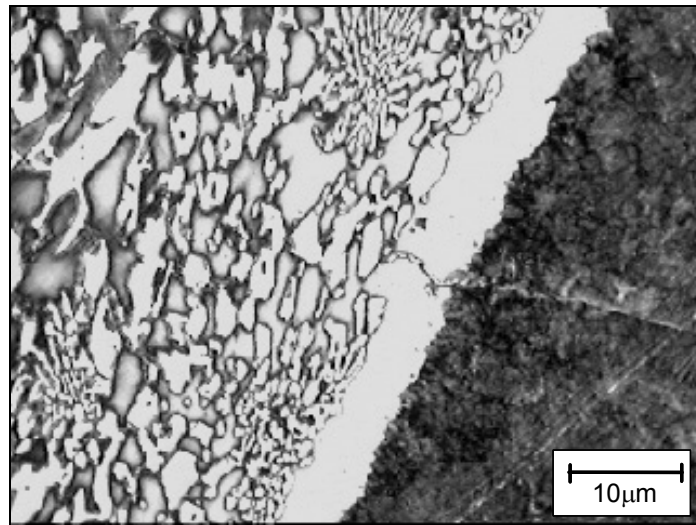


Figure 4.1: Optical bright field image of vacuum cast interface. White cast iron is on the left of the image, and steel substrate is on the right of the image. Interface is between the middle white carbide free band and the right hand side steel substrate (sample etched in acid-ferric chloride for 20 seconds).

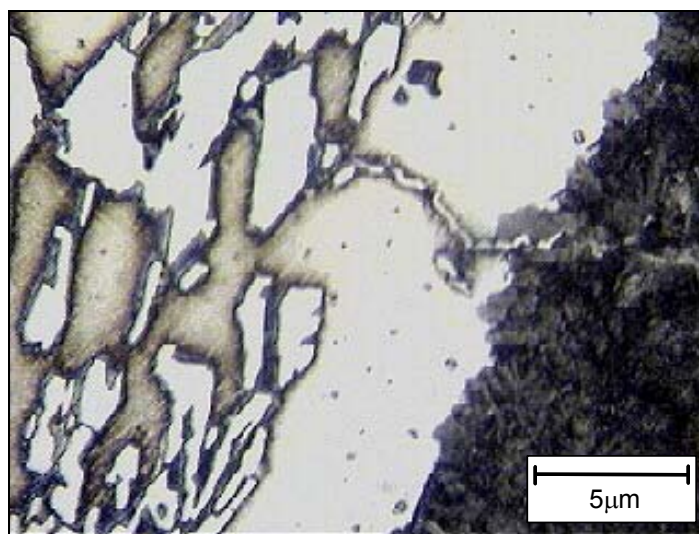


Figure 4.2: Optical bright field image detail of vacuum cast interface. White cast iron is on the left of the image, and steel substrate is on the right of the image. Interface is between the middle white carbide free band and the right hand side steel substrate (sample etched in acid-ferric chloride for 20 seconds).

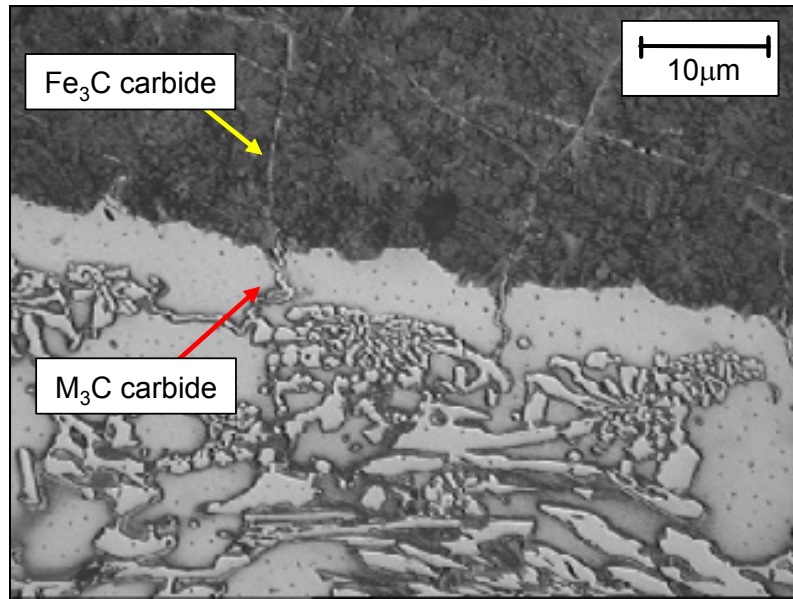


Figure 4.3: Optical bright field image detail of vacuum cast interface. White cast iron is on the bottom of the image, and steel substrate is on the top of the image. M₃C carbide in “carbide-free” white iron region have extended from proeutectoid Fe₃C carbides in the steel substrate (sample etched in acid-ferric chloride for 20 seconds).

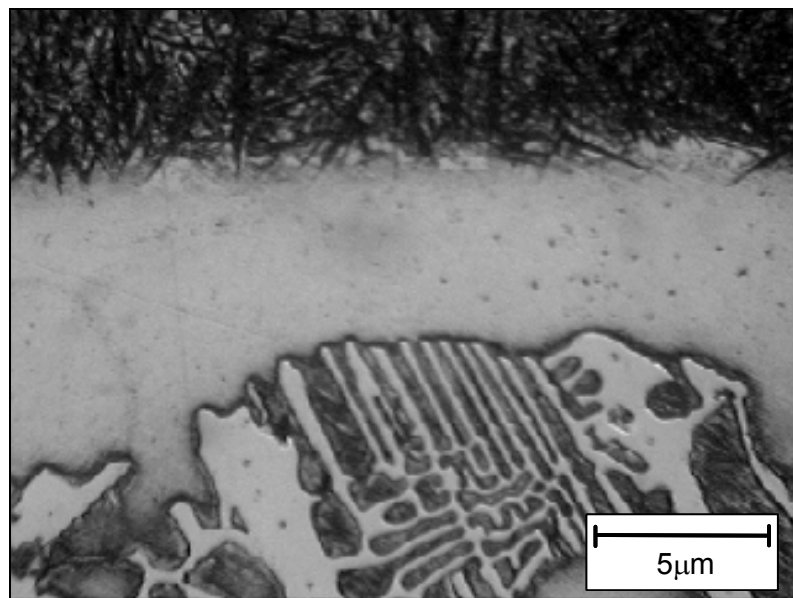


Figure 4.4: Optical bright field image detail of vacuum cast interface. White cast iron is on the bottom of the image, and steel substrate is on the top of the image. “Carbide-free” white iron region is shown in between the steel substrate and the white cast iron (sample etched in acid-ferric chloride 20 seconds).

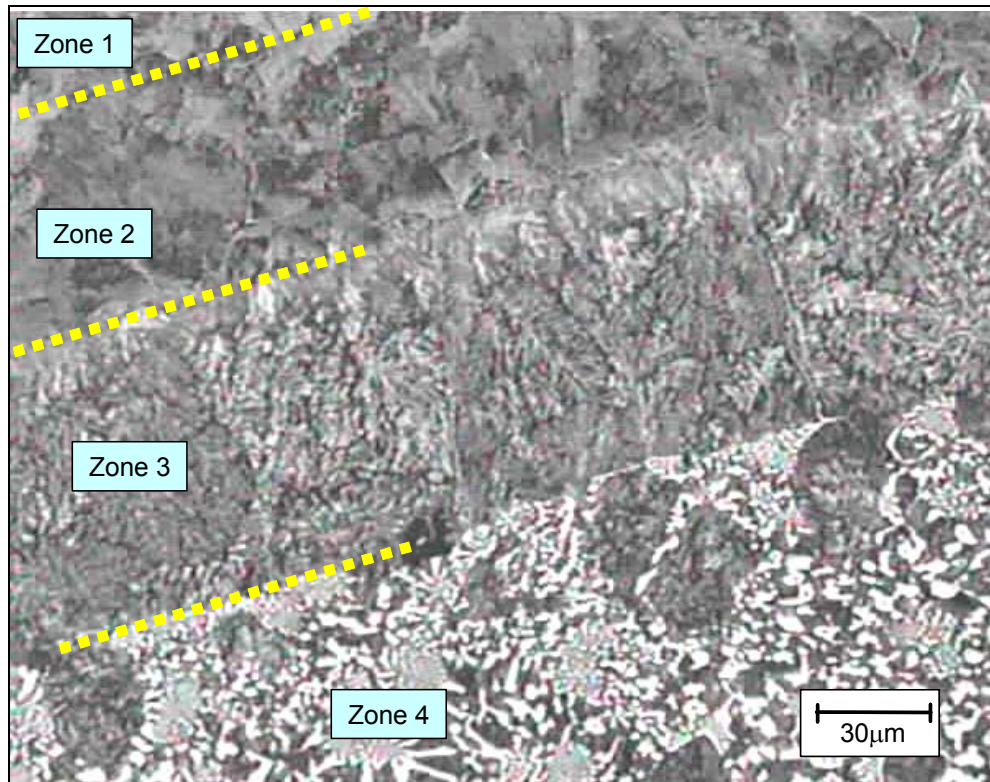


Figure 4.5: Optical bright field image detail of vacuum cast interface. Four distinct zones within the alloy composite can be identified (sample etched in acid-ferric chloride 20 seconds).

Figures 4.1 to 4.4 show the Zone 3 width is approximately 5 to 10 μm , whereas the width of the Zone 3 in Figure 4.5 is greater at 50 μm . Based on the optical microscopy conducted and the measurement of the widths of the four zones present in the samples, the width of Zone 3 has been observed to be essentially independent of the vacuum casting process parameters, and no specific correlation has been observed to date which can quantify this microstructural feature.

4.3 ELECTRON MICROSCOPY ANALYSIS OF INTERFACE

The vacuum cast interface was viewed and analysed using several electron microscopes and techniques. Initial high resolution imaging was conducted using a Jeol 35CF scanning electron microscope (fitted with dual EDS detectors), Jeol 6300 electron microscope, Jeol 733 microprobe (fitted with three EDS x-ray detectors and three WDS detectors) and Zeiss Supra 55VP scanning electron microscope.

Standard samples were prepared for imaging and x-ray mapping analysis by polishing to a 1 μ m finish then etching in 5% HCl acid ferric-chloride solution for 20 seconds. Samples for electron beam backscattered diffraction (EBSD) analysis were prepared using a more automated polishing process to provide a super-flat surface. The method used for polishing the samples for EBSD analysis was developed from careful selection of the grinding and polishing media, and using chemical-mechanical polishing with automatic polishing equipment to produce a scratch-free surface in all zones of the alloy composite. During the polishing stage, each step in the method was also repeated using a lighter load, to minimise the sub-surface deformation.

The EBSD polishing method used is summarised as follows:

Step	Surface ¹	Abrasive	Grain Size, μ m	Lubricant ³	Force, N ⁴	Rotation ⁵	Direction ⁶	Time/Minutes
1	Abrasive paper	Silicon carbide	30 (P500)	water	Hand pressure	150rpm	Opposite	Until plane
2	MD-Largo, composite disc	Polycrystalline Diamond	15	DP-Green	30	150rpm	Opposite	5
3	MD-Largo, composite disc	Polycrystalline Diamond	15	DP-Green	15	150rpm	Opposite	5
4	MD-Largo, composite disc	Polycrystalline Diamond	3	DP-Green	30	150rpm	Opposite	5
5	MD-Largo, composite disc	Polycrystalline Diamond	3	DP-Green	15	150rpm	Opposite	5
6	MD-Plus, long nap synthetic	Polycrystalline Diamond	3	DP-Green	30	150rpm	Opposite	5
7	MD-Plus, long nap synthetic	Polycrystalline Diamond	3	DP-Green	15	150rpm	Opposite	5
8	MD-Nap, short nap synthetic	Polycrystalline Diamond	1	DP-Green	30	150rpm	Opposite	5
9	MD-Chem, porous synthetic	Colloidal Silica ²	0.04	water	20	150rpm	Opposite	10
10	MD-Chem, porous synthetic	Colloidal Silica ²	0.04	water	10	150rpm	Opposite	5
11	MD-Chem, porous synthetic	none		water	10	150rpm	Opposite	5

1) All grinding and polishing surface are magnetic to ensure flatness. This is important to prevent edge rounding of specimens. I have given the description of the polishing cloths, but for your record they were Struers items.

2) Colloidal silica has a pH of 9.8.

3) DP-Green is a Struers water-based lubricant used with diamond suspensions for general polishing of most materials.

4) The force applied to the samples during polishing. This is in single force mode for 25mm diameter samples.

5) The rotational speed of the grinding surface and the specimens.

6) The rotational direction of the samples relative to the grinding surface.

The EBSD samples were not etched prior to viewing and analysis with EBSD methods.

4.3.1 SCANNING ELECTRON MICROSCOPE (SEM) IMAGING

Secondary electron images (SEI) were obtained during the course of x-ray mapping and EBSD mapping to provide a more detailed understanding of the microstructural features at higher resolutions compared to optical microscopy. Figures 4.6 to 4.12 show various detail SEI images for the various zones observed within the composite alloy samples.

Figure 4.6 provides a low magnification image of the vacuum cast interface as observed from the In-lens SEI from the Zeiss Supra 55VP SEM. At higher magnifications within the white iron Zone 4 region, the compositional differences between the M_7C_3 and M_3C eutectic carbides can be seen as shown in Figure 4.7. The M_7C_3 carbides are in the centre of the carbide regions, with the quasi-peritectic M_3C carbides formed surrounding the M_7C_3 carbides.

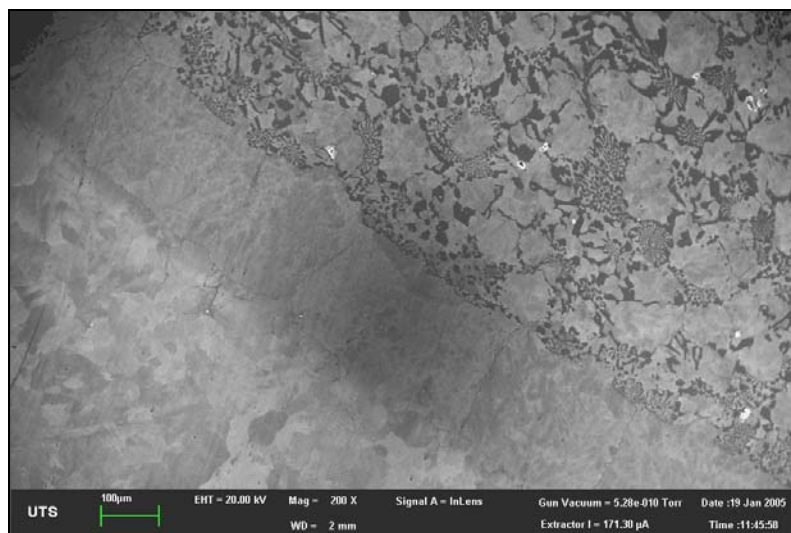


Figure 4.6: SE image of vacuum cast interface. White cast iron is on the top of image, and steel substrate is on the bottom of the image. Interface is between the middle and bottom bands (sample unetched).

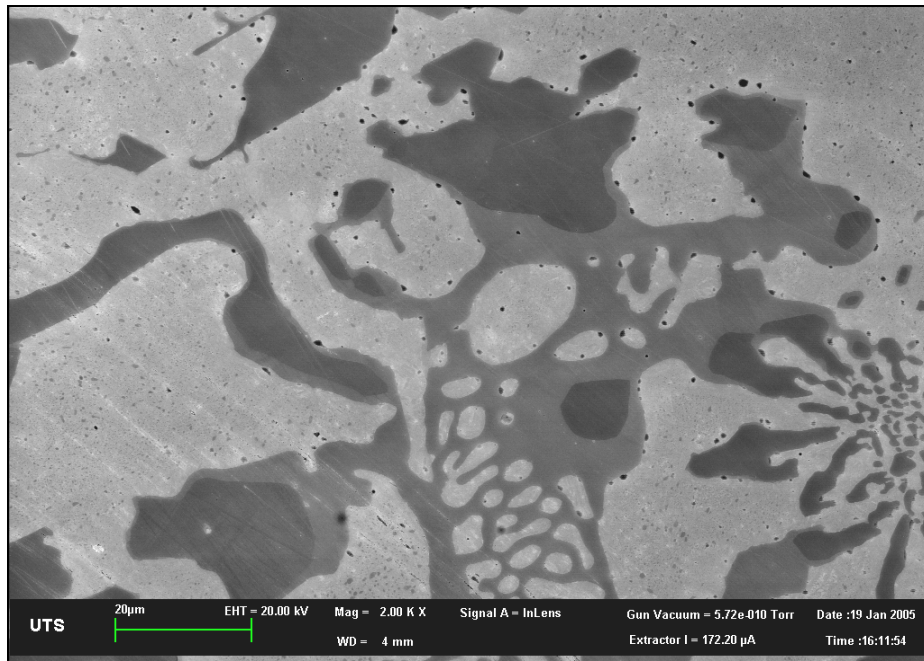


Figure 4.7: SE image of vacuum cast white cast iron region. Compositional changes represented by the change in grey scale contrast can be seen within the carbide phase which represents a carbide centre of M_7C_3 structure surrounded by M_3C carbide (sample unetched).

Etched samples that were viewed in the Jeol 35CF SEM as part of the x-ray mapping show the formation of pearlite in the ferrous matrix surrounding the eutectic white cast iron carbides. Figure 4.8 shows the formation of a fine pearlite structure, and some retained austenite is also present.

In the “carbide-free” Zone 3 of the white iron, there is the presence of fine intergranular carbides extending perpendicular from the interface towards the Zone 4 white iron. Figure 4.9 shows the fine intergranular carbides which are the M_3C carbide form. At higher resolutions, as shown in Figure 4.10, more detail on the nature and intergranular form of these carbides can be observed.

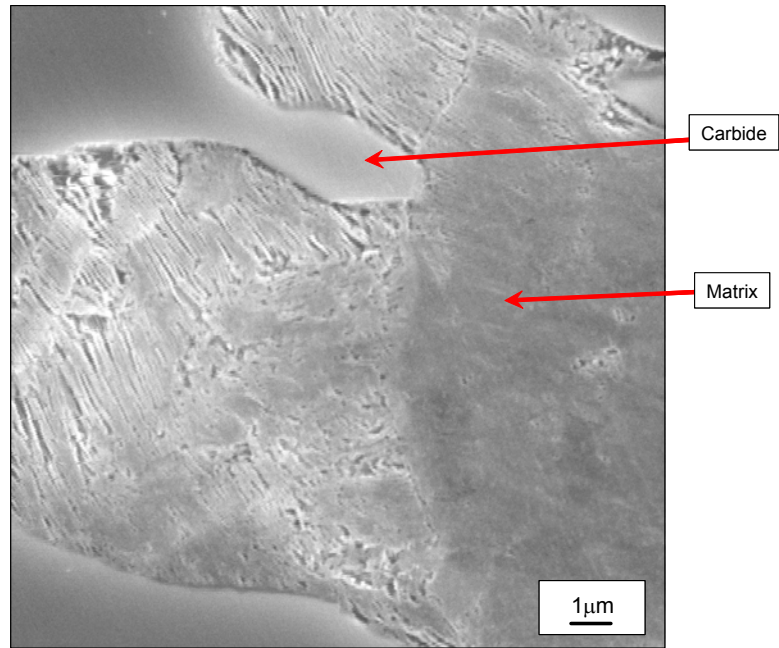


Figure 4.8: SE image detail of Zone 4 white cast iron, with carbide and ferrous matrix (sample etched in acid-ferric chloride 20 seconds)

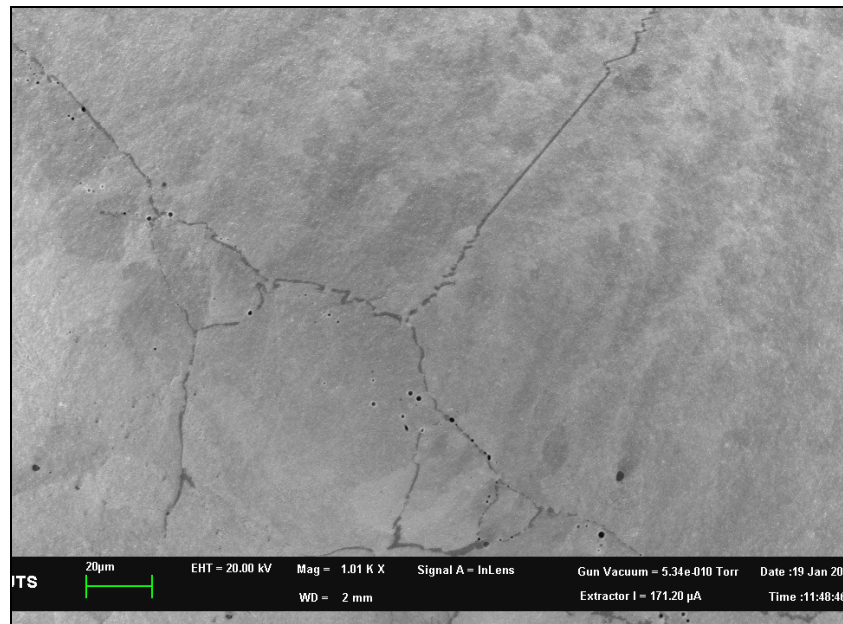


Figure 4.9: SE image of Zone 3 white cast iron which exhibits essentially a carbide-free region, with some M_3C carbide extending perpendicular to interface

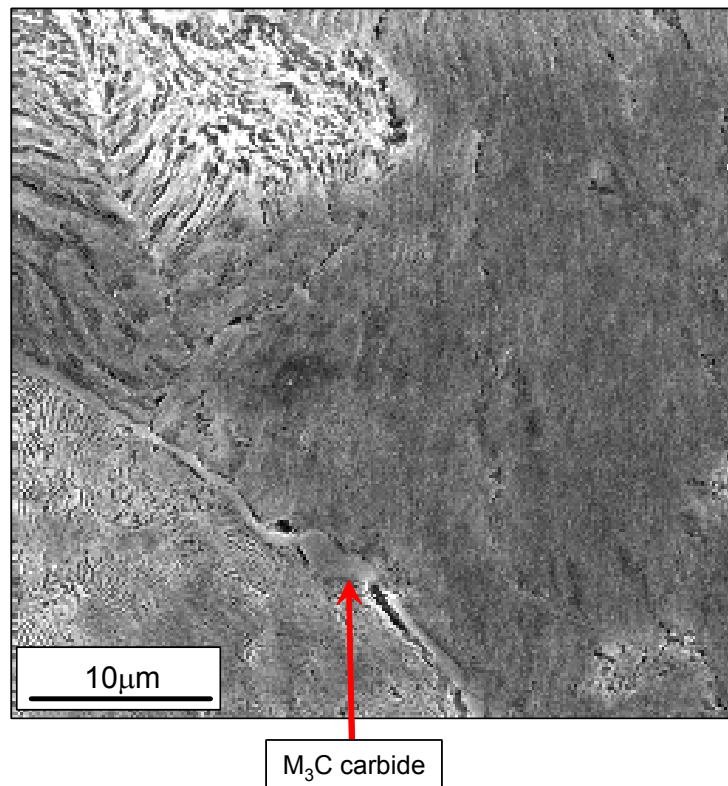


Figure 4.10: SE image detail of Zone 3, with M_3C carbide extending perpendicular to interface (sample etched in acid-ferric chloride 20 seconds)

Imaging of the steel after the vacuum casting process has been conducted show the development of a significant heat affected zone (HAZ) in which the diffusion of carbon from the white cast iron has produced a strong formation of eutectoid product within the steel. The base steel has a nominal 0.2wt% carbon content, which would normally result in a 25 volume % of eutectoid pearlite within the microstructure. The image shown in Figure 4.11 is close the boundary between the Zone 1 base steel (normally 25 volume % pearlite) and the HAZ of Zone 2 adjacent to the white iron. Figure 4.11 shows a significantly increased volume percent of pearlite, whilst immediately adjacent to the Zone 3 “carbide-free” white cast iron the microstructure is hypereutectoid pearlite with some intergranular proeutectoid Fe_3C carbide.

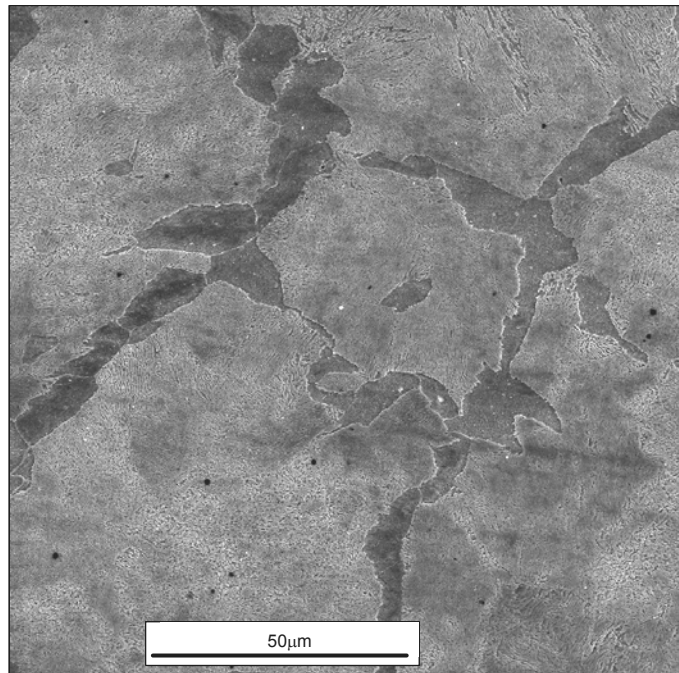


Figure 4.11: SE image of Zone 2 near Zone 1, with regions of ferrite surrounded by pearlite (sample etched in acid-ferric chloride 20 seconds)

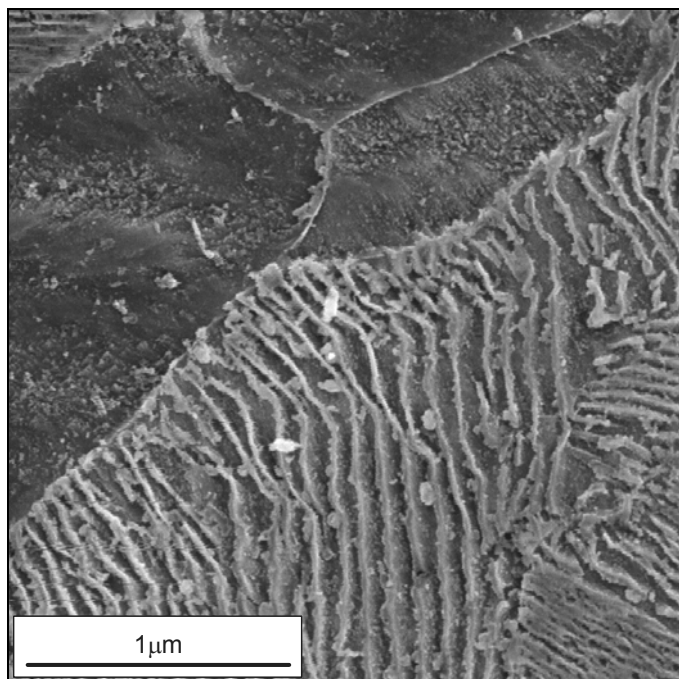


Figure 4.12: SE image detail of Figure 4.11 of Zone 2 near Zone 1, with regions of ferrite surrounded by pearlite (sample etched in acid-ferric chloride 20 seconds)

At higher resolution the Zone 2 pearlite can be seen to consist of coarse lamella Fe_3C carbide and ferrite. The development of the hypereutectoid steel microstructure within Zone 2 of the microstructure is further confirmation of the strong diffusion of carbon into the steel that has resulted from the excellent bonding between the white cast iron and the steel substrate during the vacuum casting process.

4.3.2 ELECTRON MICROSCOPE ENERGY DISPERSIVE SPECTROSCOPY (EDS) ANALYSIS

Multi-element energy dispersive spectroscopy (EDS) analysis was conducted on various samples for the individual phases present within the four zones of the interface. EDS spectra were collected at 20kV and 30kV accelerating voltage using a Moran Scientific energy dispersive x-ray analysis and mapping system attached to a Jeol 35CF SEM fitted with multi-detector EDS system (see Figure 4.13).



Figure 4.13: UTS Jeol 35CF fitted with two EDS detectors and Moran Scientific XRM System

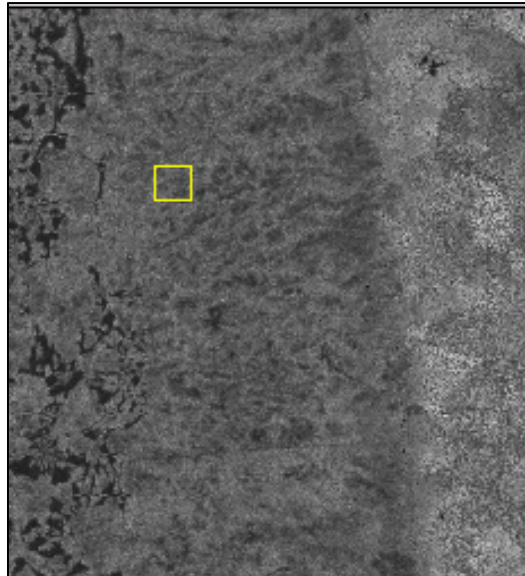
In addition to point measurements using the EDS system, additional chemical data was obtained using the Moran Scientific software by processing the data collected from x-ray maps for specific microstructural areas of interest.

The typical chemical analysis for the “carbide-free” Zone 3 ferrous matrix is shown in Figure 4.14. Since the analysis was performed with a Beryllium window-based EDS detector, light elements such as carbon are not detected, and hence the analysis data requires correction to allow for carbon. Data collected as part of the carbon x-ray mapping using wavelength dispersive spectroscopy (WDS) has enabled the carbon contents to be determined for the various microstructural phases present in the vacuum cast samples.

Similar EDS results for the eutectic carbide found in Zone 4 are provided in Figure 4.15 and for the changing ferrous matrix composition across the interface in Figure 4.16.

The EDS data for the carbon-corrected analysis for the sample positions shown in Figure 4.16 is tabulated in Tables 4.1. The EDS data shows the compositional gradients for carbon and chromium as the position of the analysis progresses across the interface, showing that these alloying elements are diffusing into the steel substrate from the white cast iron. The typical phase analysis obtained from EDS analysis for the white cast iron corrected for carbon content is also provided in Table 4.2.

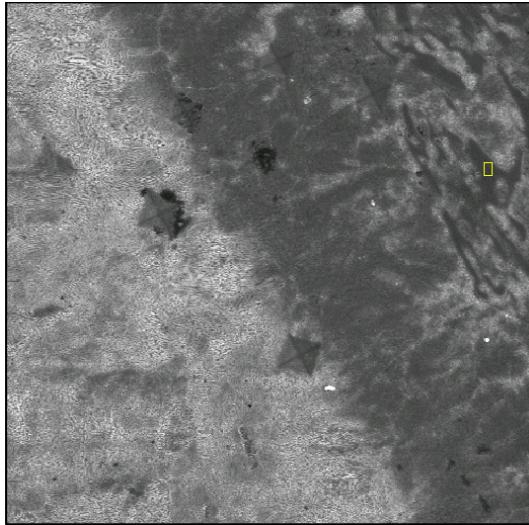
EDS analysis at these magnifications shown in Figures 4.14 to 4.16 are not capable of resolving the elemental differences between the two carbide types (M_7C_3 and M_3C) found in the white cast iron, and more detailed analysis using XRM and EBSD techniques is required to resolve these elemental and crystallographic changes.



21-June-07 22:39
 ID = 289 Points.
 Livetime = 21.86 Realtime = 31.61 Bulk STDLESS.
 kV= 30 Angle= 28

ELEMENT	WEIGHT %	+/- 2 SIGMA
Al	0.0	0.0
Si	0.871	0.290
Cr	6.92	0.495
Mn	1.26	0.252
Fe	89.3	2.18
Ni	1.67	0.356
Cu	0.0	0.0
W	0.0	0.0
TOTAL =	100	

Figure 4.14: EDS analysis for ferrous region in vacuum cast composite sample



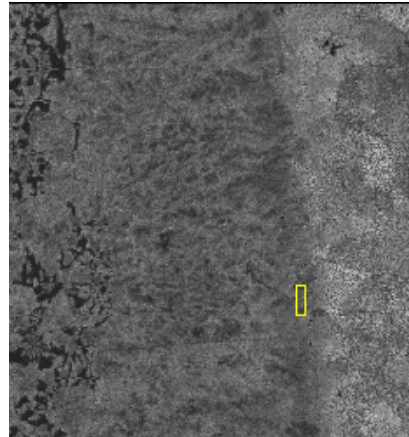
21-June-07 23:03
 ID = 40 Points.
 Livetime = 2.89 Realtime = 4.38 Bulk STDLESS.
 kV= 30 Angle= 28

ELEMENT	WEIGHT %	+/- 2 SIGMA
Al	0.333	0.240
Si	0.0	0.0
Cr	27.5	1.04
Mn	0.812	0.202
Fe	65.6	1.95
Ni	0.218	0.127
Cu	2.32	0.456
W	3.23	0.828
TOTAL =	100	

Figure 4.15: EDS analysis for eutectic carbide in vacuum cast white cast iron region (analysis region is shown in yellow).

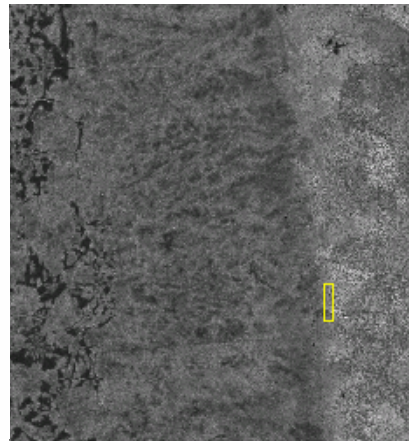
21-June-07 22:44
 ID = 133 Points.
 Livetime = 10. Realtime = 14.55 Bulk STDLESS.
 kV= 30 Angle= 28

ELEMENT	WEIGHT %	+/- 2 SIGMA
Al	0.0	0.0
Si	0.482	0.216
Cr	4.37	0.389
Mn	0.993	0.223
Fe	91.8	2.19
Ni	1.26	0.309
Cu	1.06	0.313
W	0.0	0.0
TOTAL =	100	



21-June-07 22:46
 ID = 161 Points.
 Livetime = 12.07 Realtime = 17.61 Bulk STDLESS.
 kV= 30 Angle= 28

ELEMENT	WEIGHT %	+/- 2 SIGMA
Al	0.0	0.0
Si	0.263	0.159
Cr	1.45	0.220
Mn	0.929	0.215
Fe	96.2	2.22
Ni	0.507	0.195
Cu	0.699	0.253
W	0.0	0.0
TOTAL =	100	



21-June-07 22:46
 ID = 125 Points.
 Livetime = 9.37 Realtime = 13.67 Bulk STDLESS.
 kV= 30 Angle= 28

ELEMENT	WEIGHT %	+/- 2 SIGMA
Al	0.0	0.0
Si	0.236	0.150
Cr	0.717	0.153
Mn	0.347	0.130
Fe	98.0	2.22
Ni	0.351	0.161
Cu	0.308	0.167
W	0.0	0.0
TOTAL =	100	

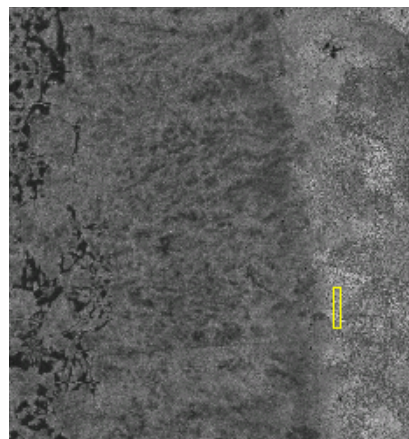


Figure 4.16: EDS analyses for vacuum cast sample interface for three ferrous zones

Table 4.1: EDS phase analysis after carbon correction for ferrous phase zones shown in Figure 4.16 for vacuum cast sample.

Element	Element weight %		
	Position 1	Position 2	Position 3
C	1.2	1.15	0.95
Cr	4.3	1.4	0.6
Mn	1.0	0.9	0.3
Si	0.5	0.3	0.1
Ni	1.2	0.5	0.3
Mo	0.0	0.0	0.0

Table 4.2: EDS phase analysis after carbon correction for vacuum cast sample.

Alloy Composition	Weight (%)	Element Weight %				Estimated Bulk Analysis
		Primary Carbide	Eutectic Carbide	Eutectic Matrix	Primary Matrix	
C	4.0	8.8	8.8	1.2	1.2	4.0
Cr	12.0	28.0	23.4	5.3	0.0	11.9
Mn	1.6	0.0	1.4	1.9	2.1	1.6
Si	0.6	0.0	0.0	0.8	1.0	0.5
Ni	1.0	0.0	0.8	1.1	1.3	1.0
Mo	0.0	0.0	0.0	0.0	0.0	0.0
Volume Fraction (%)		0.0	36.8	61.0	2.2	100.0
ECT%	4.06					
ECVF%	37.7					
Cr/C Ratio	3.0					

4.3.3 SEM XRAY MAPPING

High quality x-ray mapping (XRM) and quantitative x-ray mapping (QXRM), using wavelength dispersive spectroscopy (WDS) detectors has been used for over 30 years by researchers to quantify chemical phase within alloy samples [52]. Manufacturers of SEM equipment have been developing similar techniques using energy dispersive spectroscopy (EDS) over the last 20 years. At the early stages of mapping using EDS methods, producing a quality map has been difficult due to a number of problems such as poor computer specifications, cost, time to map and generally poor peak to background ratios (P:B).

Improvements in SEM equipment have allowed a more substantial development and usage of mapping techniques, with a significant improvement of P:B ratios, and time reductions to produce a quality x-ray map. The development of high count rate detectors and multi-detector systems has resulted in the time required to acquire an x-ray map decreases [53-56]. Using a single EDS detector at 20kcps output, a reasonably good 128x128 quantitative map can be obtained in approximately fifteen minutes for major elements (>10wt% evenly distributed) and minor elements (>1wt% localised). It is now possible to quantitatively map using multi-detectors and combined detectors such as WDS-EDS, resulting in not only reduced mapping time but also improving the ability to map trace elements very accurately.

In addition, EDS and WDS x-ray mapping may now also be combined with cathodoluminescence (CL) and electron back-scattered diffraction (EBSD) [56]. However, the combining of detectors and the data from the detectors whether multi-EDS detectors, multi-WDS detectors or combined EDS-WDS has to be done with utmost care [55, 56].

Carbon x-ray mapping for this study was conducted using a multi-detector EDS and WDS x-ray mapping system incorporated on a Jeol 733 microprobe with three

EDS x-ray detectors and three WDS detectors (see Figure 4.17). The carbon mapping was conducted courtesy of Moran Scientific [57].

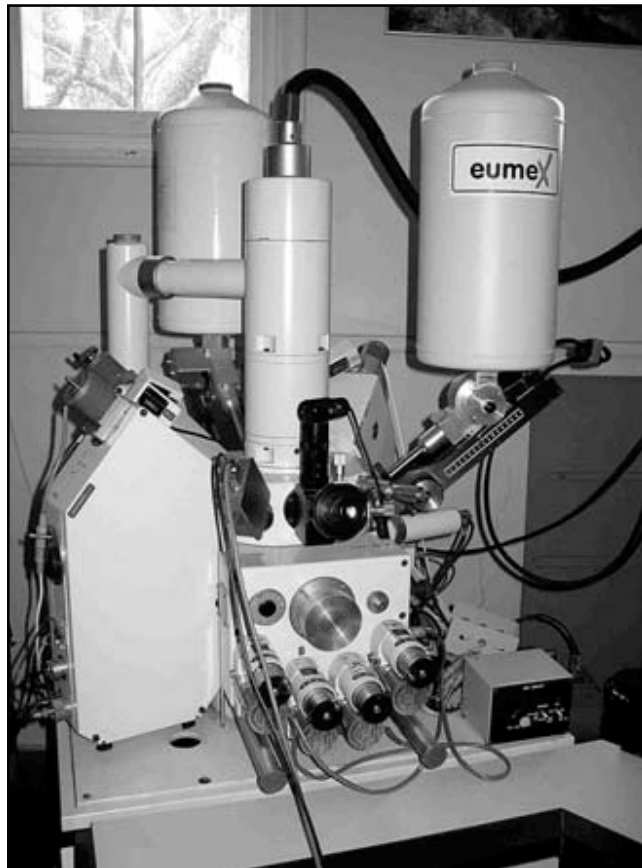


Figure 4.17: Moran Scientific Jeol 733 microprobe with three EDS x-ray detectors and three WDS detectors

Multi-element x-ray maps were collected at 20kV and 30kV accelerating voltage using a Moran Scientific energy dispersive x-ray analysis and mapping system attached to a Jeol 35CF SEM fitted with two EDS detectors (see Figure 4.13).

A typical pseudo colour x-ray map produced for the white iron in Zone 4 of the vacuum cast samples is shown in Figure 4.18. Using the Moran Scientific computer software and analysis package [58] the x-ray maps can be processed to

produce individual element compositional maps for the sample being studied. Three individual element x-ray maps can then be selected and overlaid on the SE image or BSE image for the sample to produce the pseudo-coloured map which effectively represents an elemental compositional image for the sample being examined.

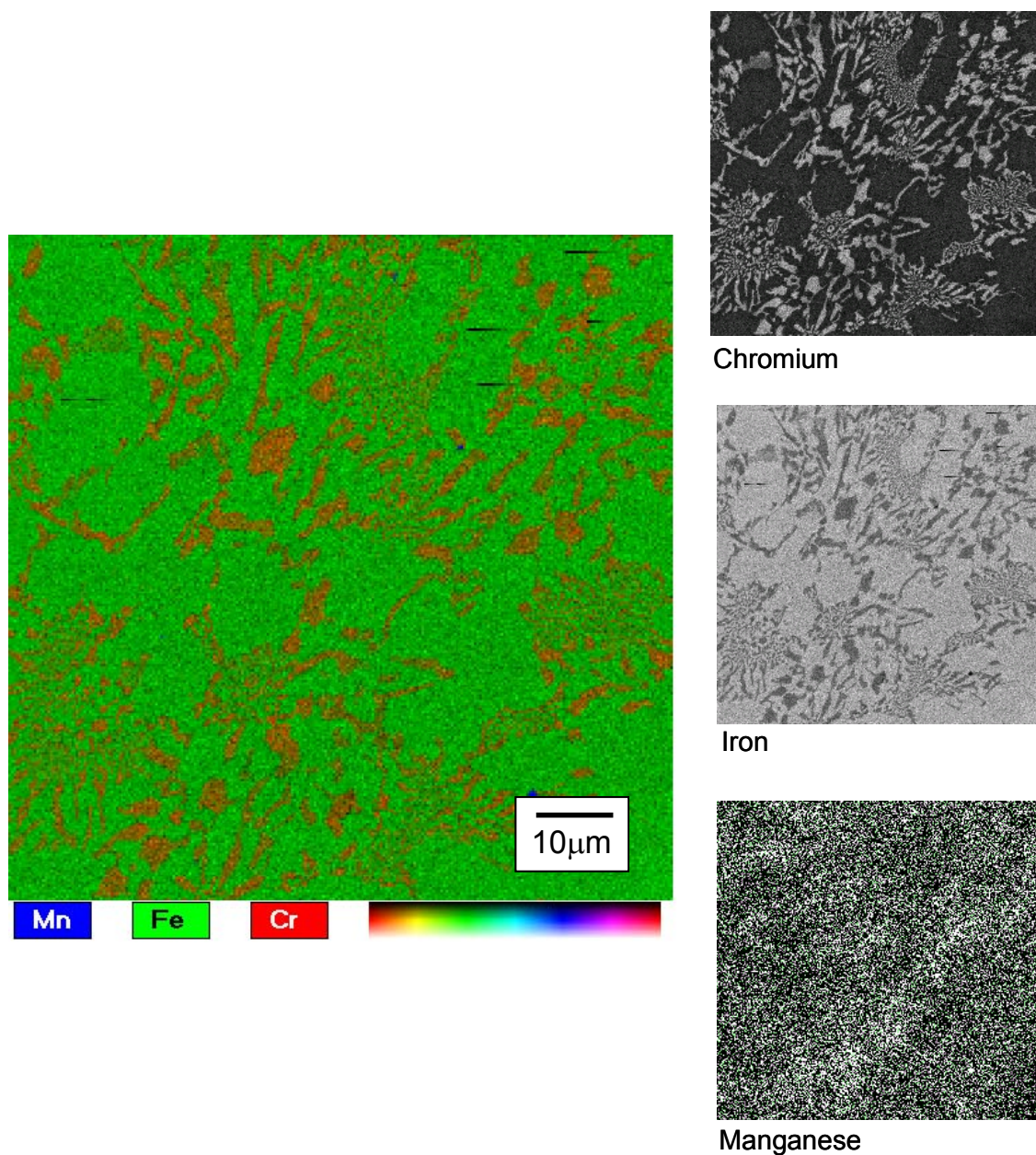


Figure 4.18: Pseudo colour x-ray map for low chromium white cast iron (red = chromium; green = iron; blue = manganese)

After selecting three elements of interest from the x-ray maps, a compositional scatter plot can be extracted for either two element combinations or all three elements selected. The compositional scatter plots for the x-ray maps allow chemical phases to be highlighted as “hot spots” on the scatter plots. If the compositional “hot spots” are highlighted, a threshold density image of the SE image or BSE image can be highlighted and superimposed over the image which can then be used to produce a multi-phase pseudo-colour x-ray map. Figure 4.19 shows the threshold density image for the compositional region shown highlighted within the three elemental scatter plots.

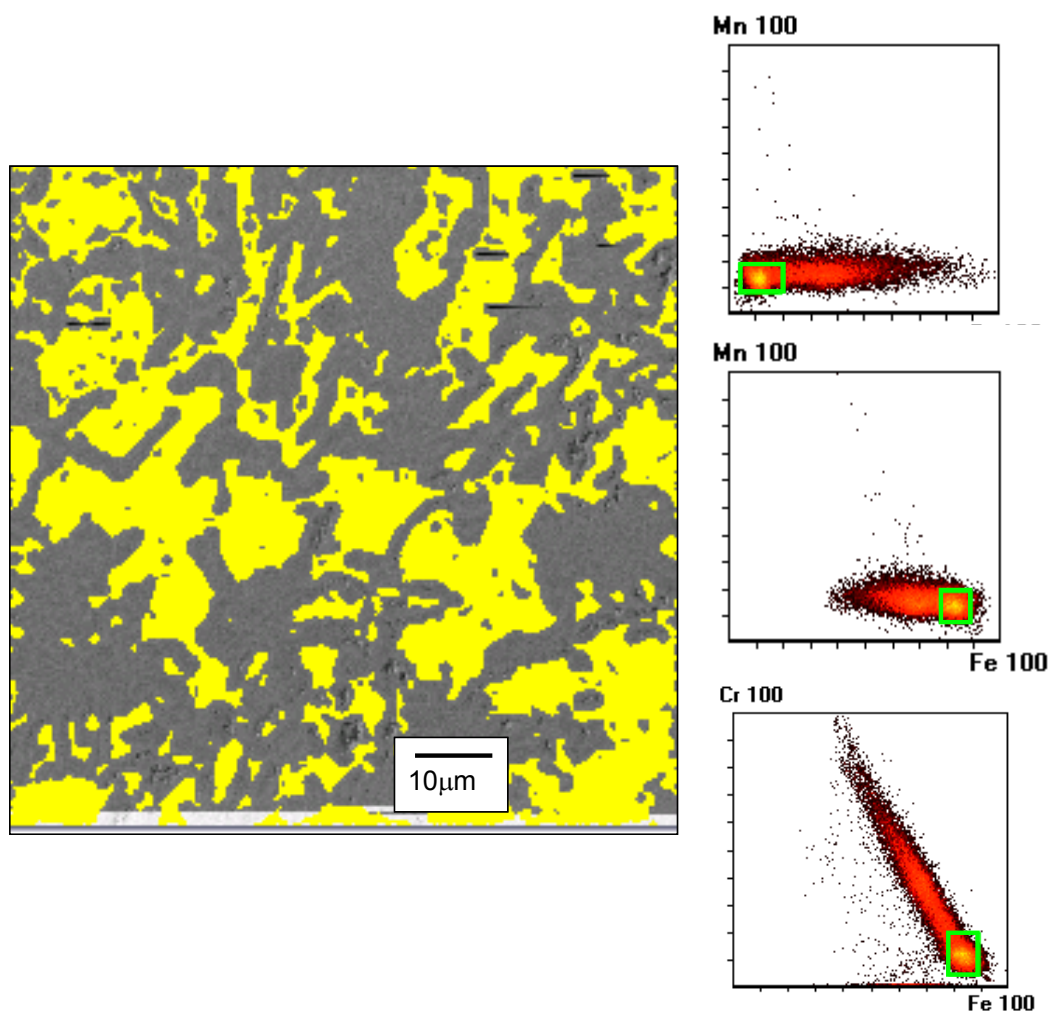


Figure 4.19: Compositional map for iron rich phase in low chromium white cast iron. Yellow colouring represents location of iron rich phase. Green borders on compositional scatter plots represent area of interest.

Additional compositional areas of interest can then be selectively highlighted and assigned pseudo image overlay colours within the Moran Scientific software, and overlaid on to the SE image or BSE image for the sample. Figures 4.20 to 4.22 show additional compositional phases selected for the Zone 4 white iron, and the complete set of colourised compositional images are shown in Figure 4.23.

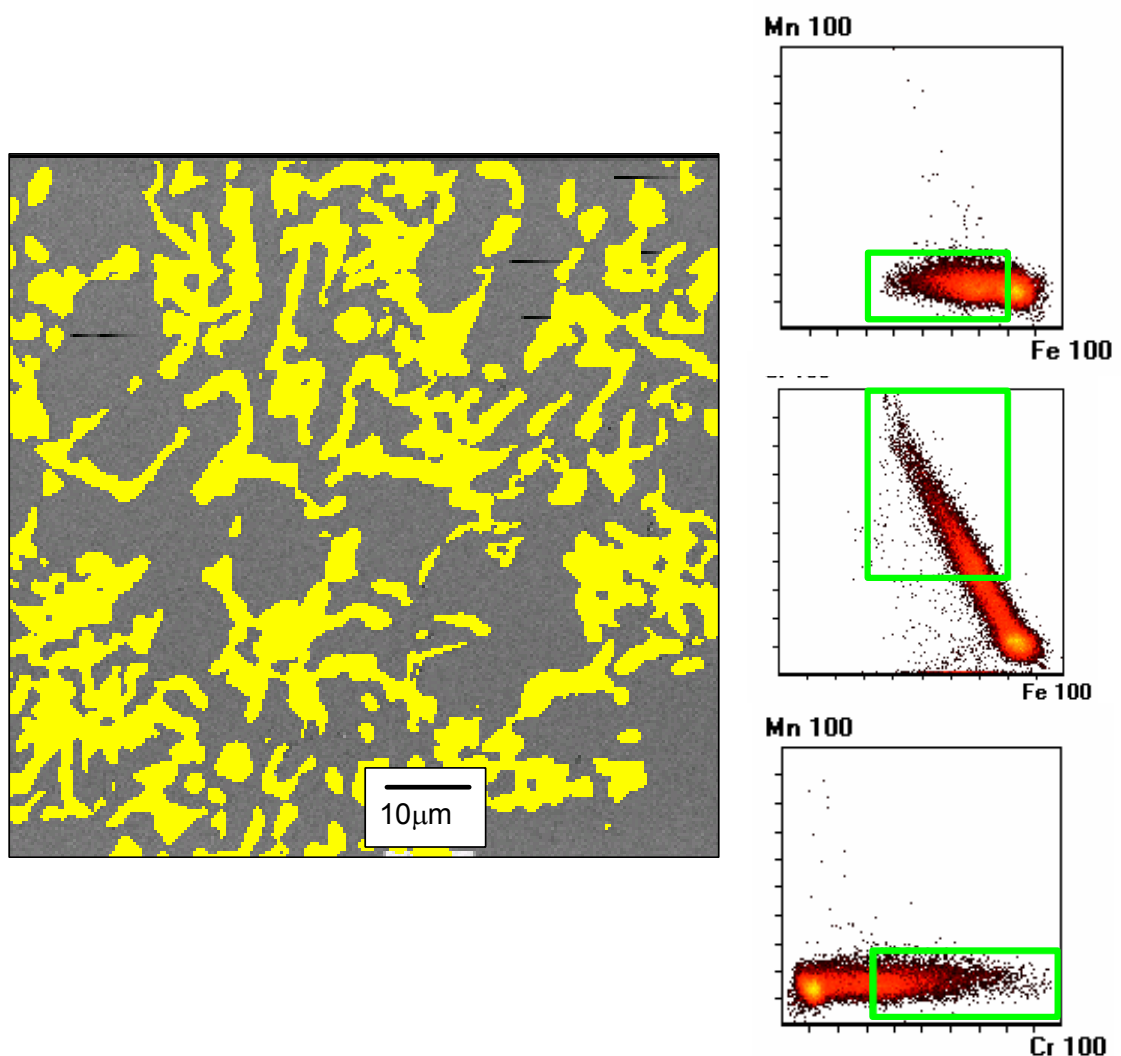


Figure 4.20: Compositional map for chromium rich carbides in low chromium white cast iron. Yellow colouring represents location of chromium rich phase. Green borders on compositional scatter plots represent area of interest.

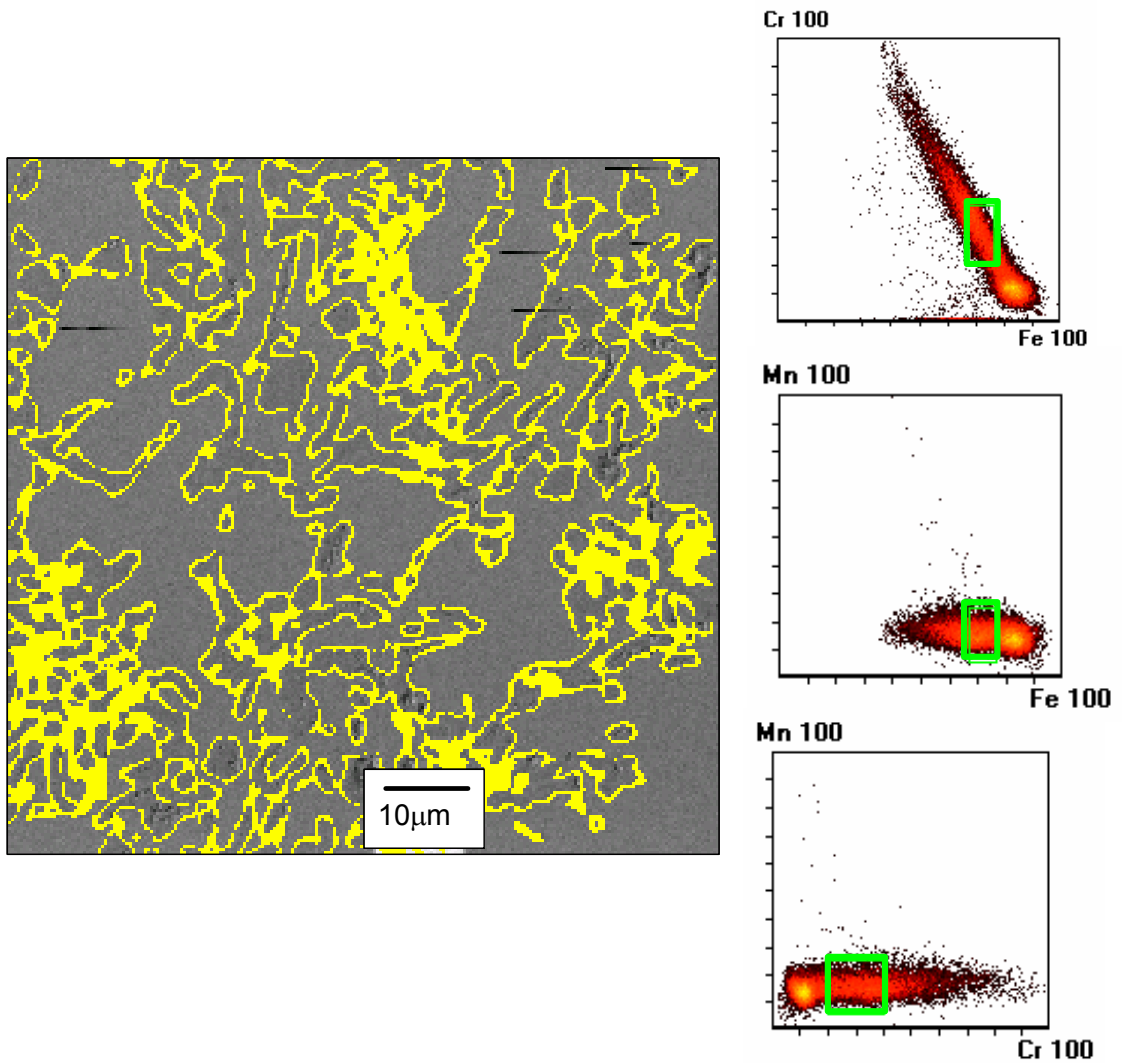


Figure 4.21: Compositional map for low chromium carbides in low chromium white cast iron. Yellow colouring represents location of low chromium carbides. Green borders on compositional scatter plots represent area of interest.

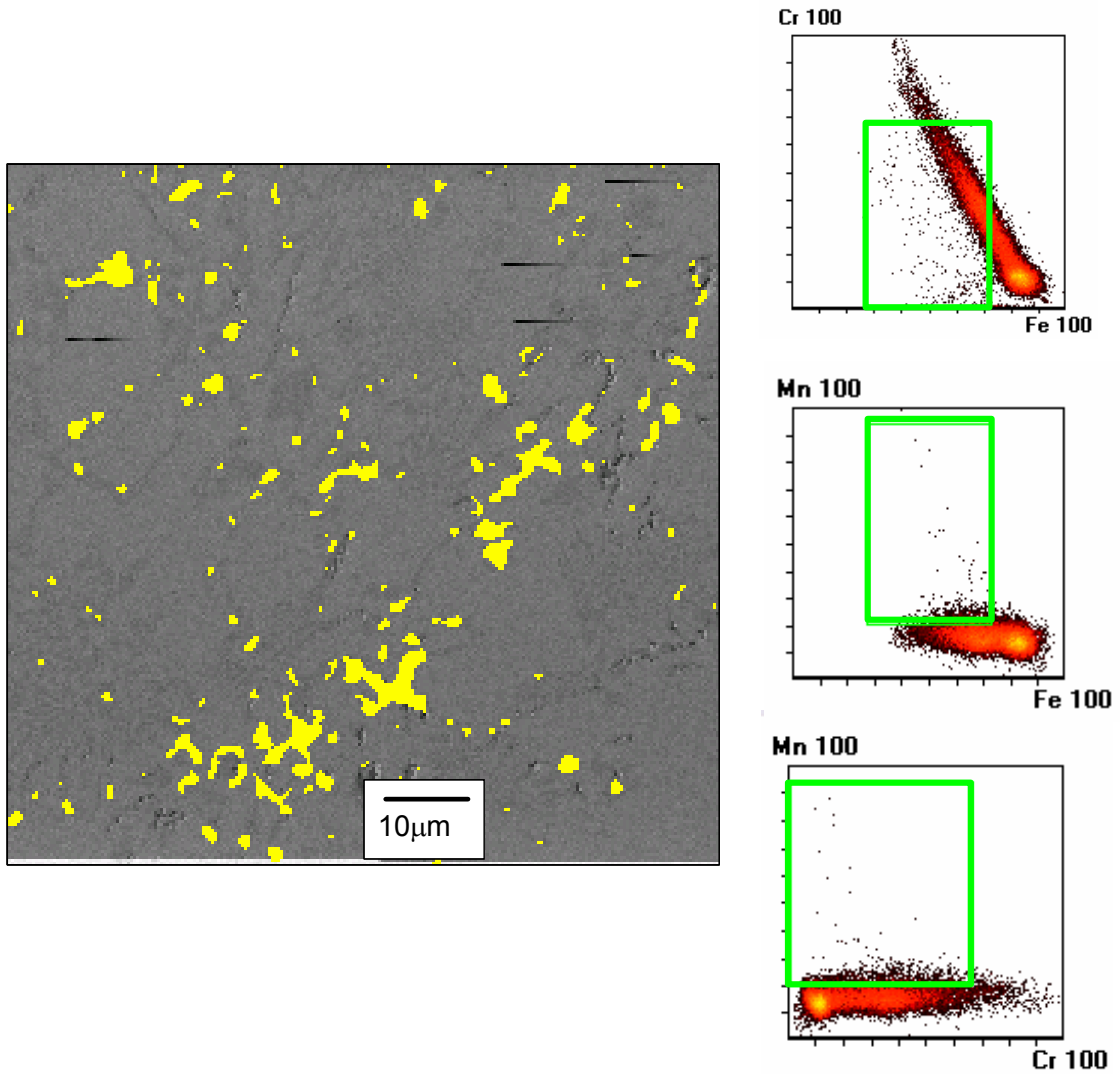


Figure 4.22: Compositional map for manganese rich phase in low chromium white cast iron. Yellow colouring represents location of manganese rich phase. Green borders on compositional scatter plots represent area of interest.

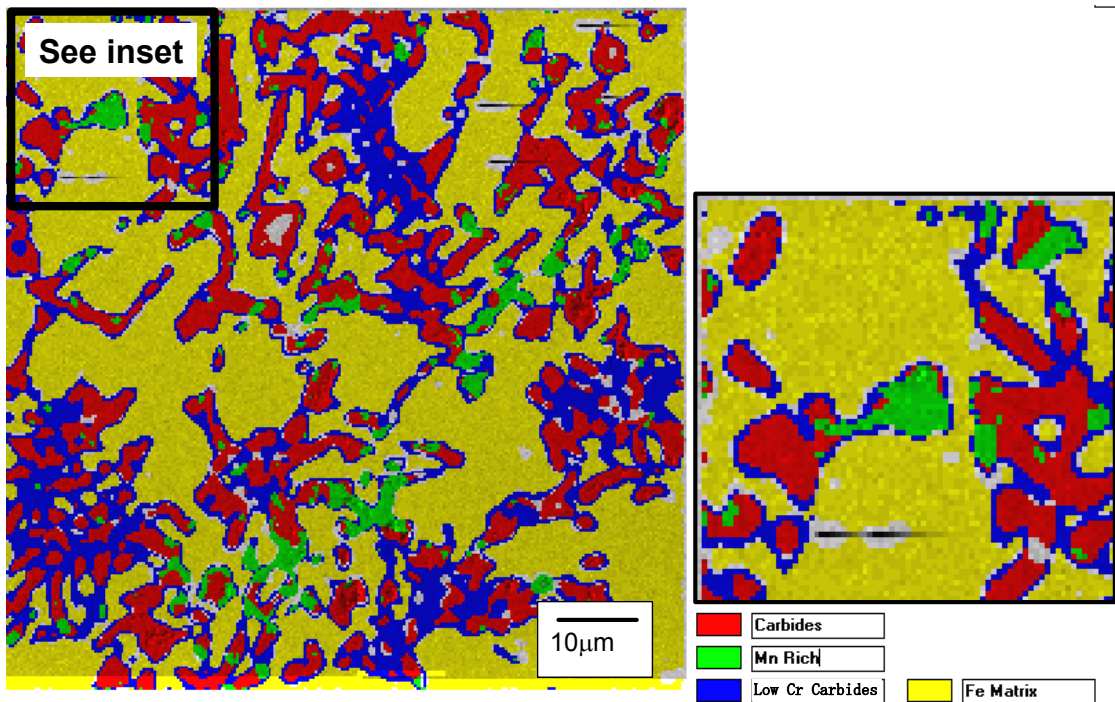


Figure 4.23: Composite colour x-ray map produced from overlay of selected compositional phase areas from Figures 4.19 to 4.22 for the low melting point alloy.

A significant advantage of processing the x-ray mapping data using the Moran Scientific software is the capacity to view compositional phases that may not be evident with single line scan profiles or spot EDS analysis. The map shown in Figure 4.23 shows the two carbide compositions present in the white cast iron, being the M_7C_3 carbide shown as red, and the M_3C carbide shown as blue. Two ferrous phases are also observed, one phase apparently richer in manganese (coloured green) compared to the other ferrous phase (coloured yellow).

XRM data was collected for a range of vacuum cast interface regions, and a typical sample of x-ray maps is shown in Figure 4.24. The x-ray maps have been processed using the Moran Scientific software to develop initially an understanding of the relationship between chromium, iron and manganese, and the results are provided in Figures 4.25 to 4.33.

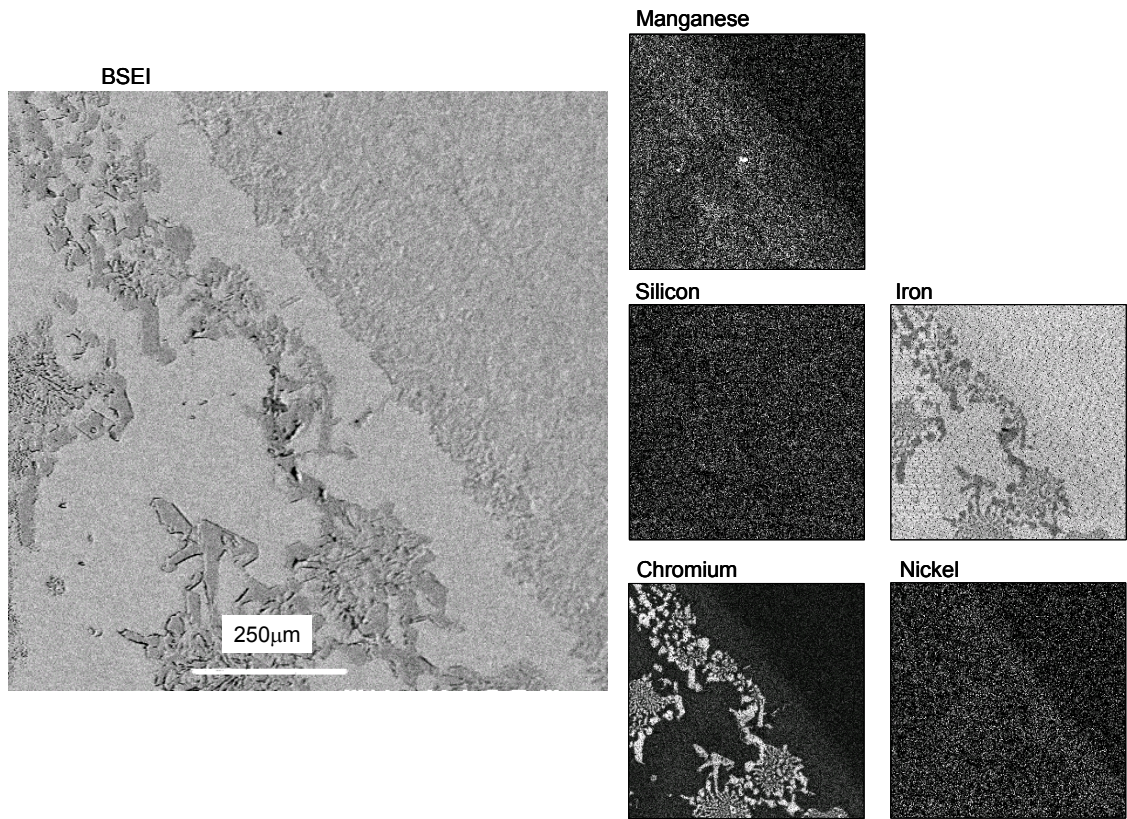


Figure 4.24: Back scattered electron (BSE) image and x-ray maps for vacuum cast sample interface colour x-ray map for low chromium white cast iron

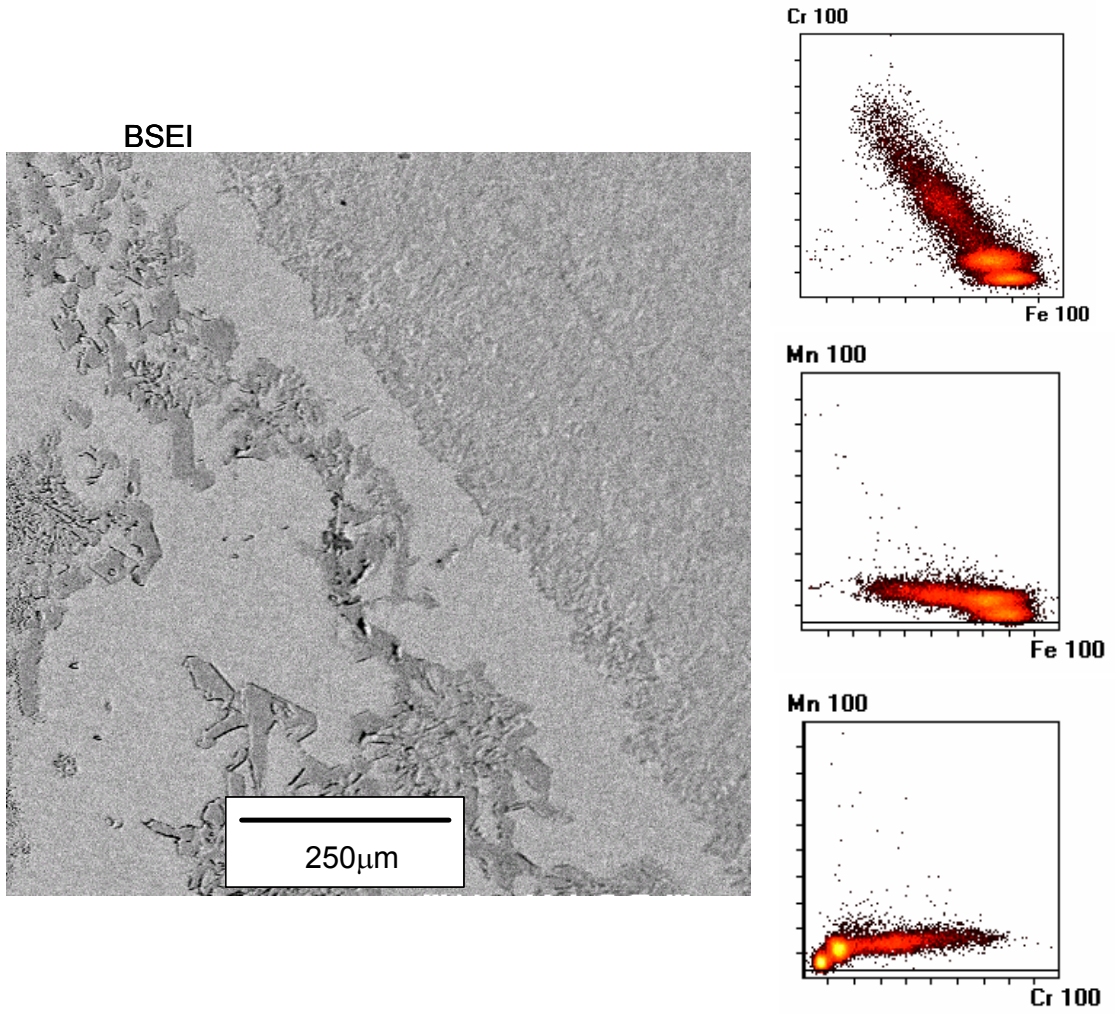


Figure 4.25: Back scattered electron (BSE) image and compositional scatter plots for vacuum cast composite interface region for chromium, iron and manganese.

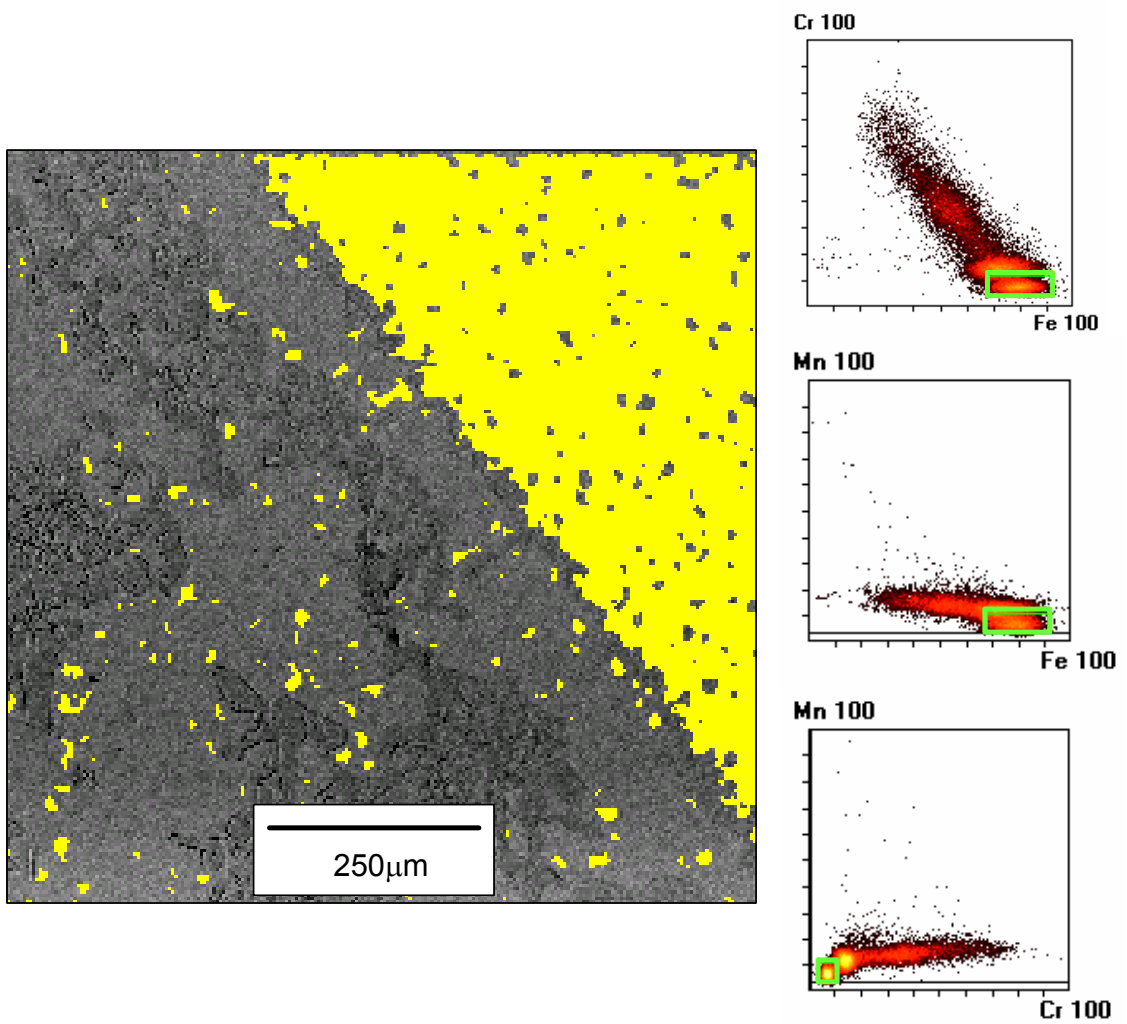


Figure 4.26: Compositional map for iron rich phase in vacuum cast composite. Yellow colouring represents location of iron rich phase. Green borders on compositional scatter plots represent area of interest.

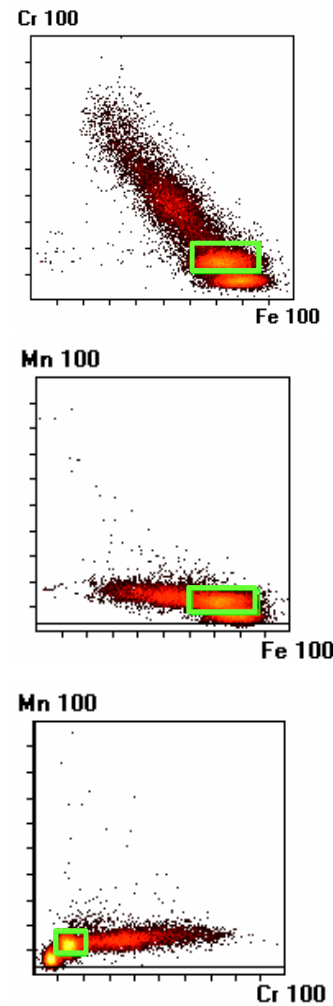
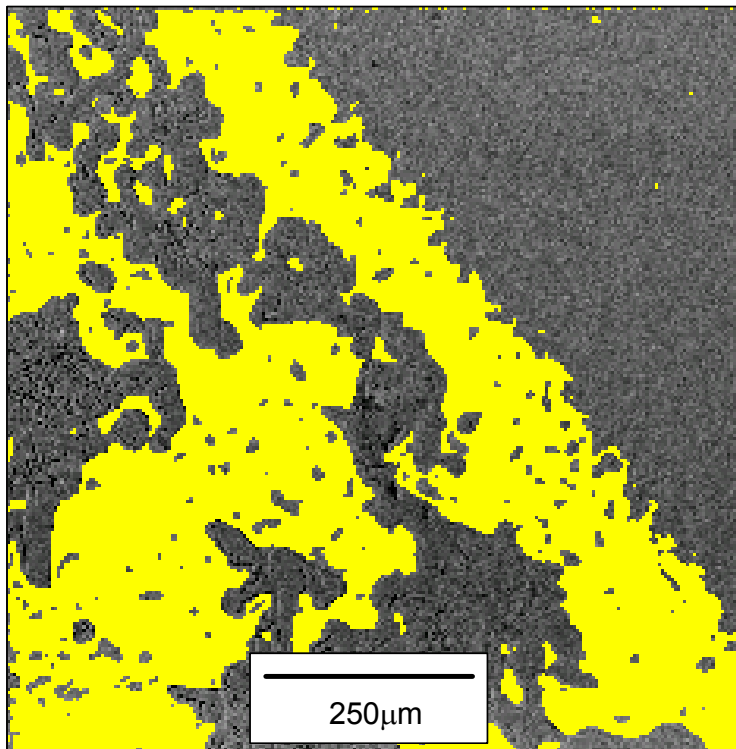


Figure 4.27: Compositional map for chromium/iron phase in vacuum cast composite. Yellow colouring represents location of chromium/iron phase. Green borders on compositional scatter plots represent area of interest.

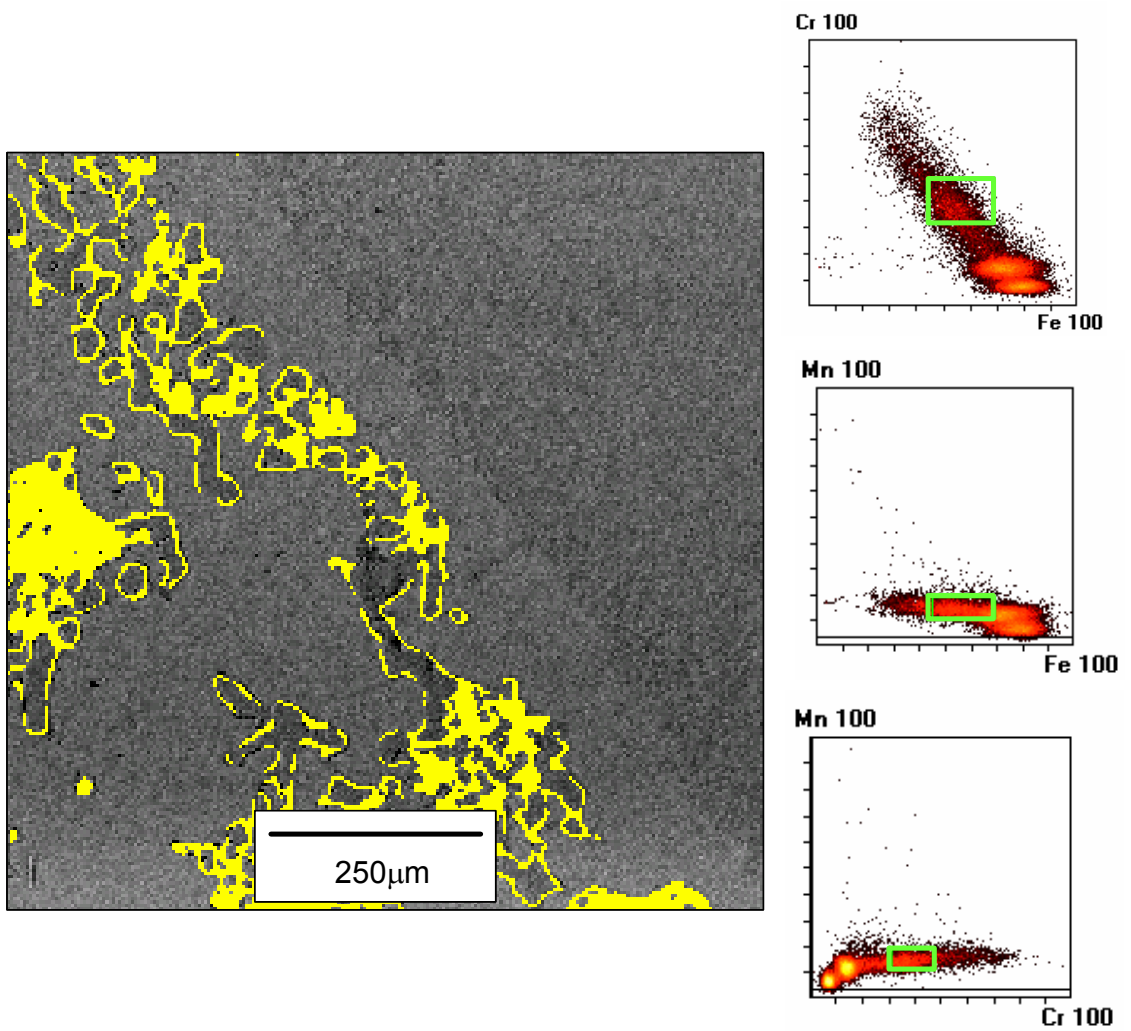


Figure 4.28: Compositional map for low chromium carbide phase in vacuum cast composite. Yellow colouring represents location of low chromium carbide phase. Green borders on compositional scatter plots represent area of interest.

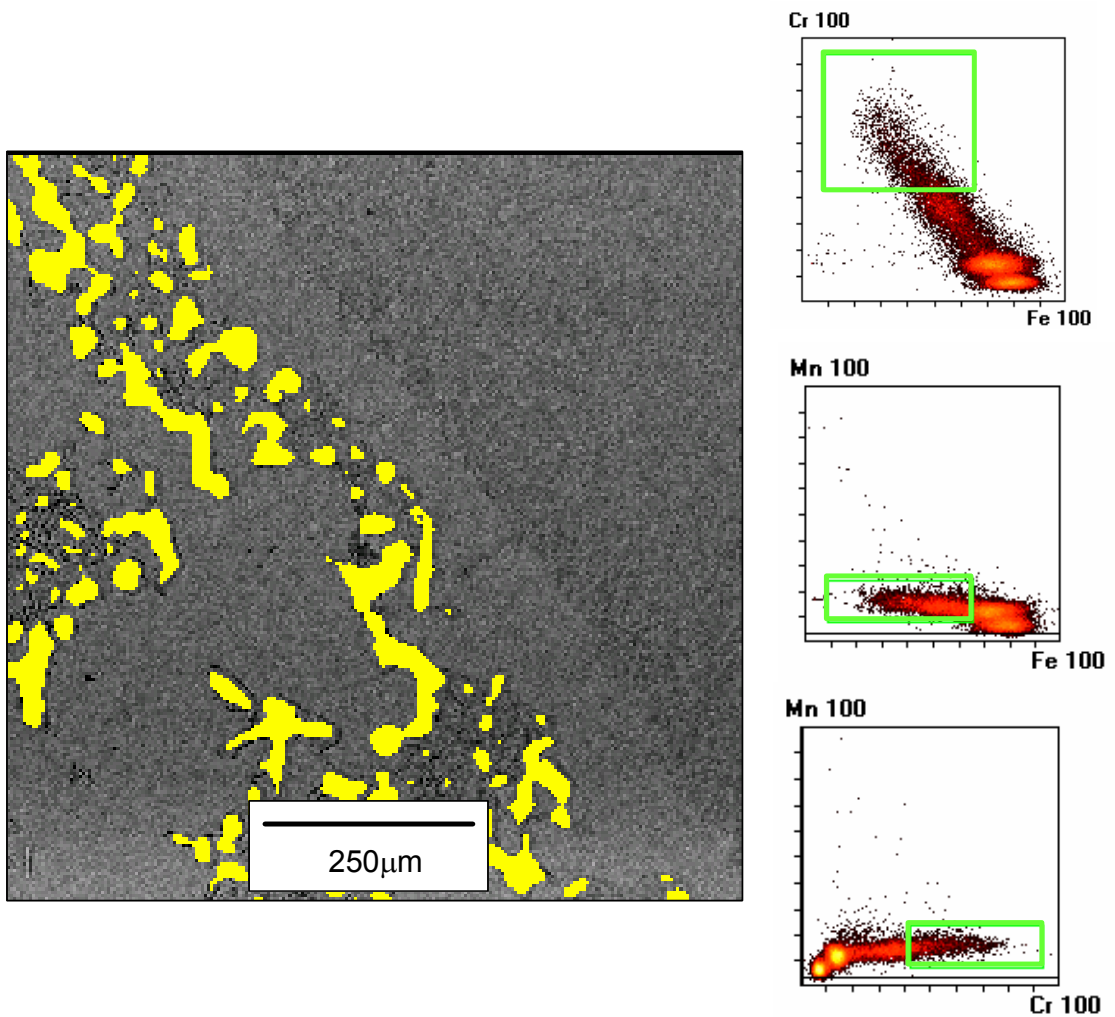


Figure 4.29: Compositional map for main chromium carbide phase in vacuum cast composite. Yellow colouring represents location of chromium carbide phase. Green borders on compositional scatter plots represent area of interest.

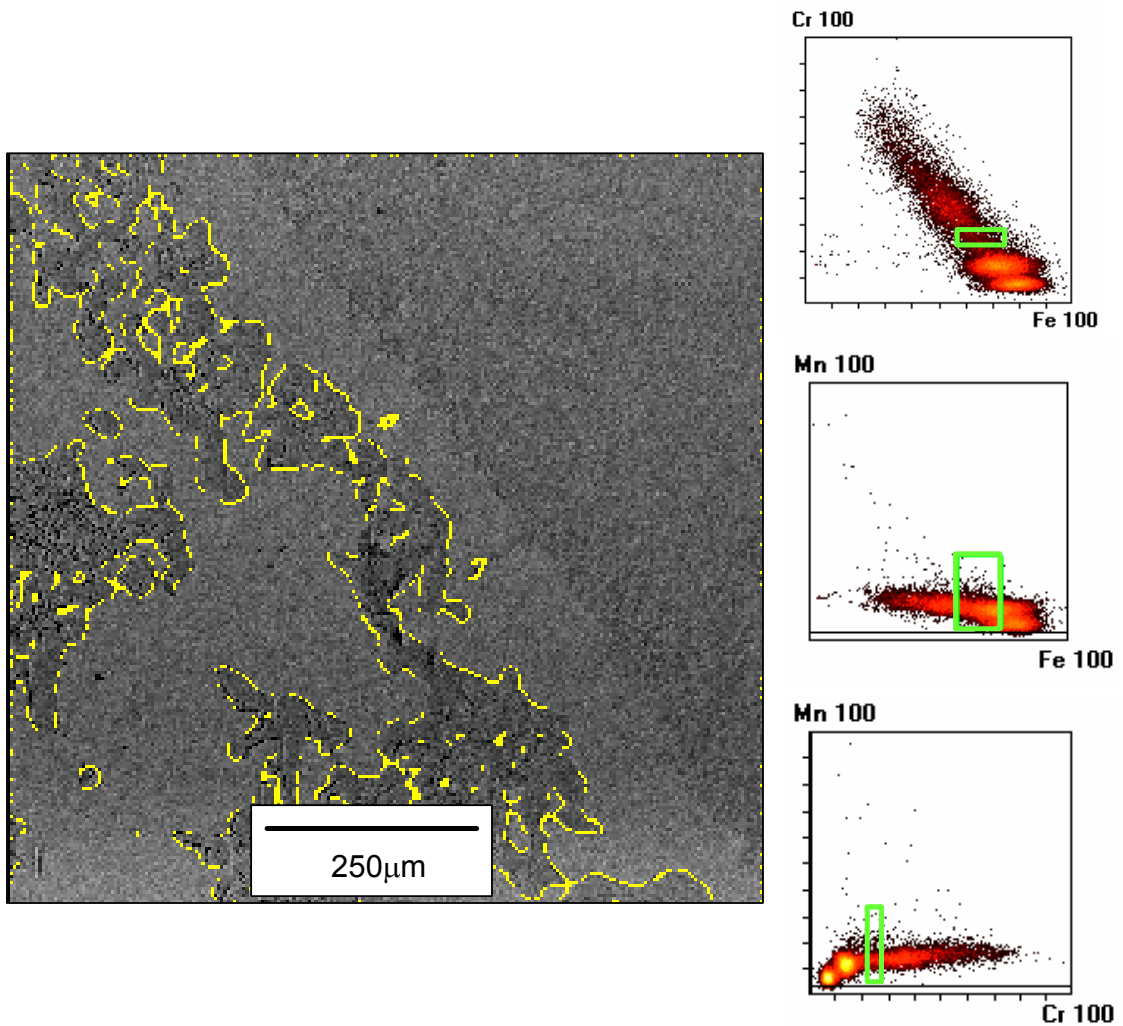


Figure 4.30: Compositional map for chromium depleted carbide phase in vacuum cast composite. Yellow colouring represents location of chromium depleted carbide phase. Green borders on compositional scatter plots represent area of interest.

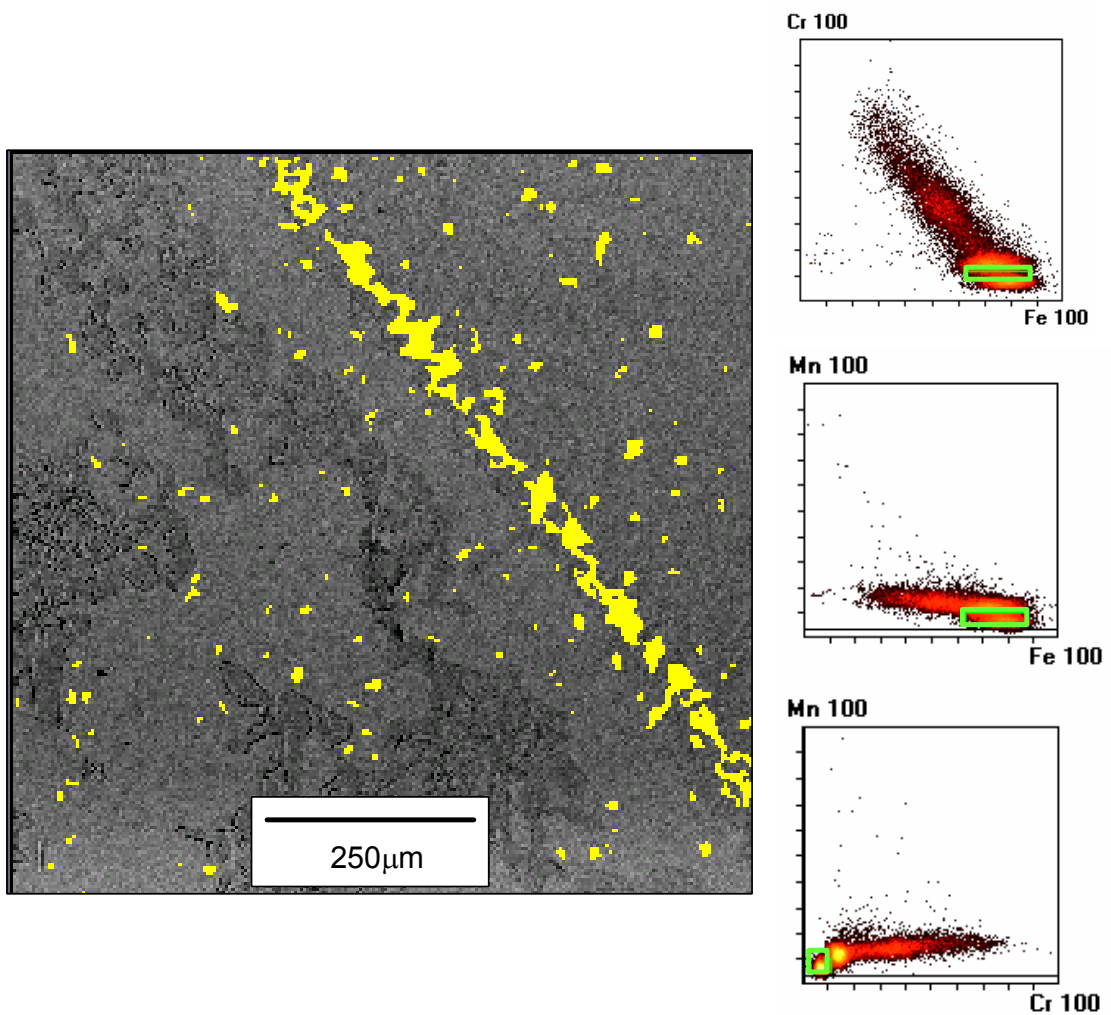


Figure 4.31: Compositional map for second chromium/iron phase in vacuum cast composite. Yellow colouring represents location of second chromium/iron phase. Green borders on compositional scatter plots represent area of interest.

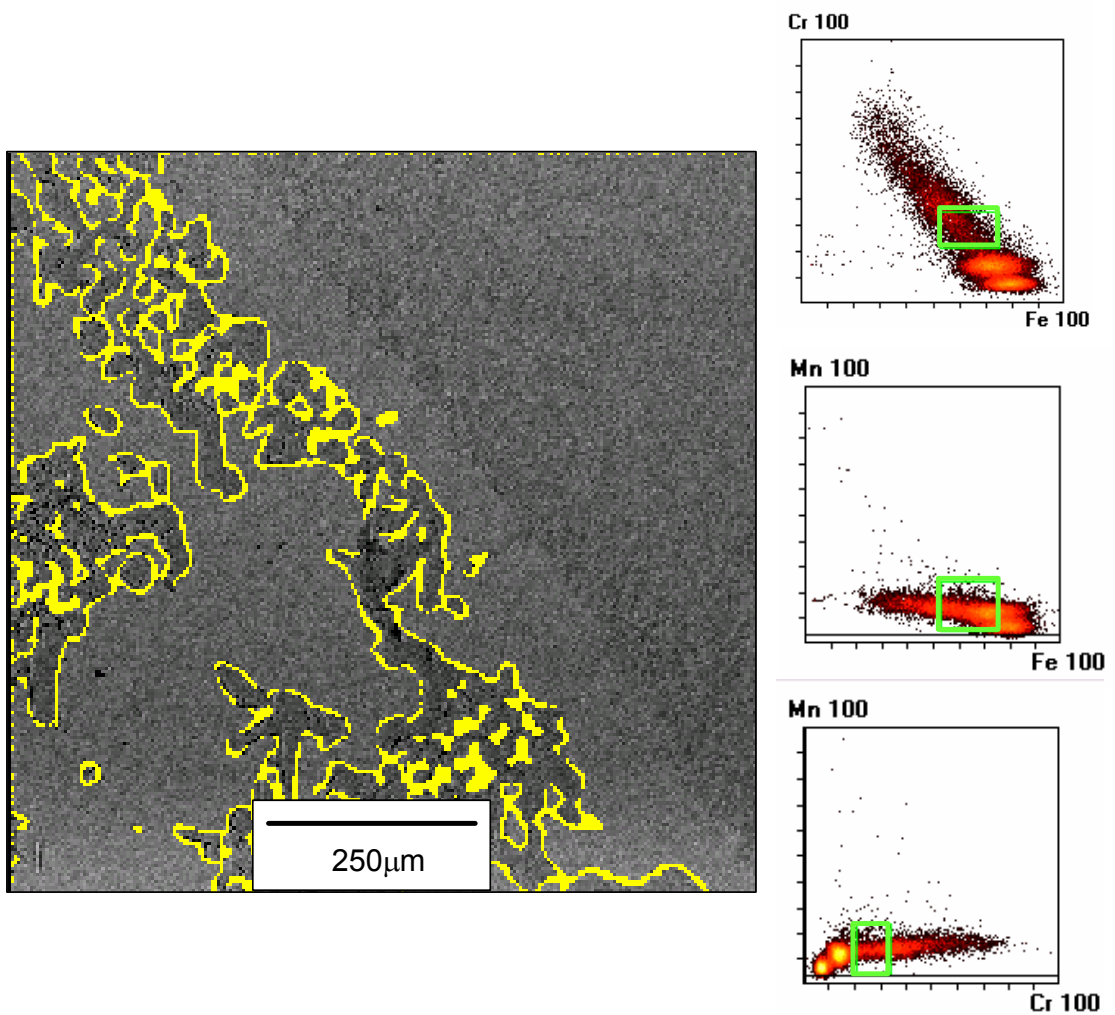


Figure 4.32: Compositional map for chromium rich matrix phase in vacuum cast composite. Yellow colouring represents location of chromium rich matrix phase. Green borders on compositional scatter plots represent area of interest.

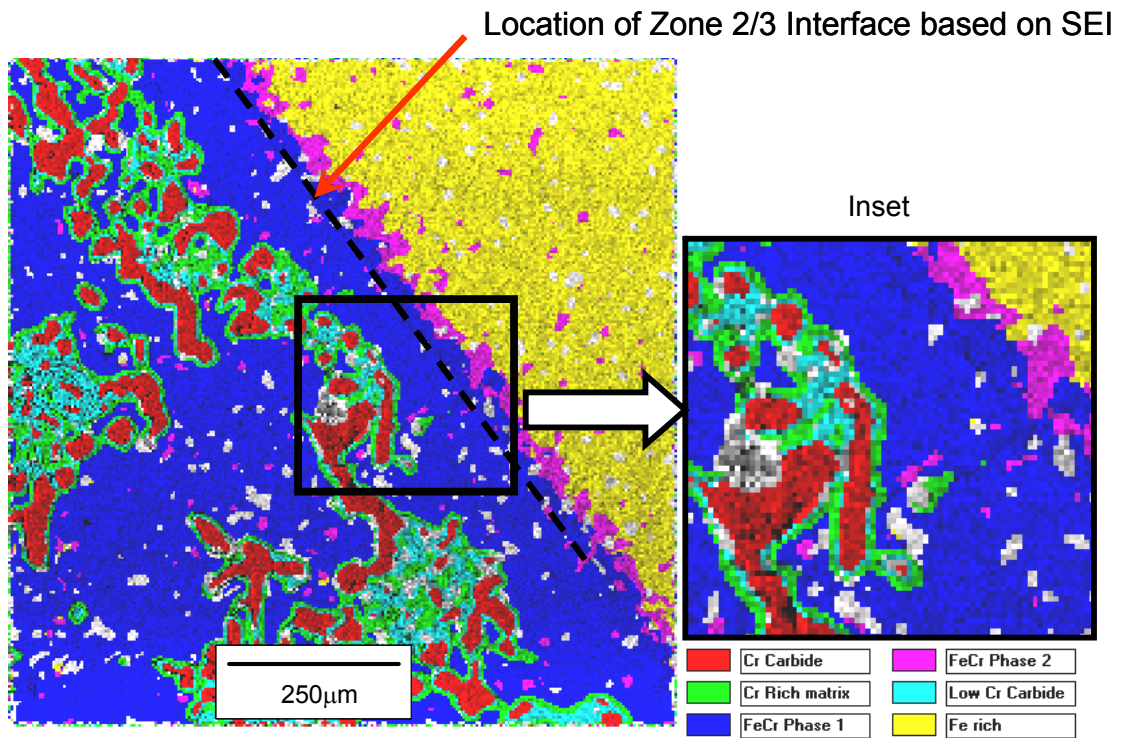


Figure 4.33: Composite colour x-ray map produced from overlay of selected compositional phase areas for chromium, iron and manganese from Figures 4.26 to 4.32 for the steel/white iron interface area.

The x-ray pseudo colour map shown above in Figure 4.33 shows the chromium has diffused across the vacuum cast interface into the steel substrate, resulting in a low chromium phase (coloured magenta) in the steel. The physical location of the vacuum cast interface based on the overlaid BSE image is shown as a dashed line on the pseudo colour map. Similar to the results shown in Figure 4.23, the x-ray mapping confirms the presence of two carbide compositions, representing the M_7C_3 (red) and M_3C (cyan) carbides.

The x-ray maps compared between chromium, iron and manganese in Figure 4.33 show only a minor effect from the influence of manganese. The same image and XRM data was then compared between chromium, iron and nickel, and are shown

in Figures 4.34 and 4.35. The use of nickel as the third comparative element instead of manganese has resulted in additional phase data being revealed, as shown in Figure 4.35.

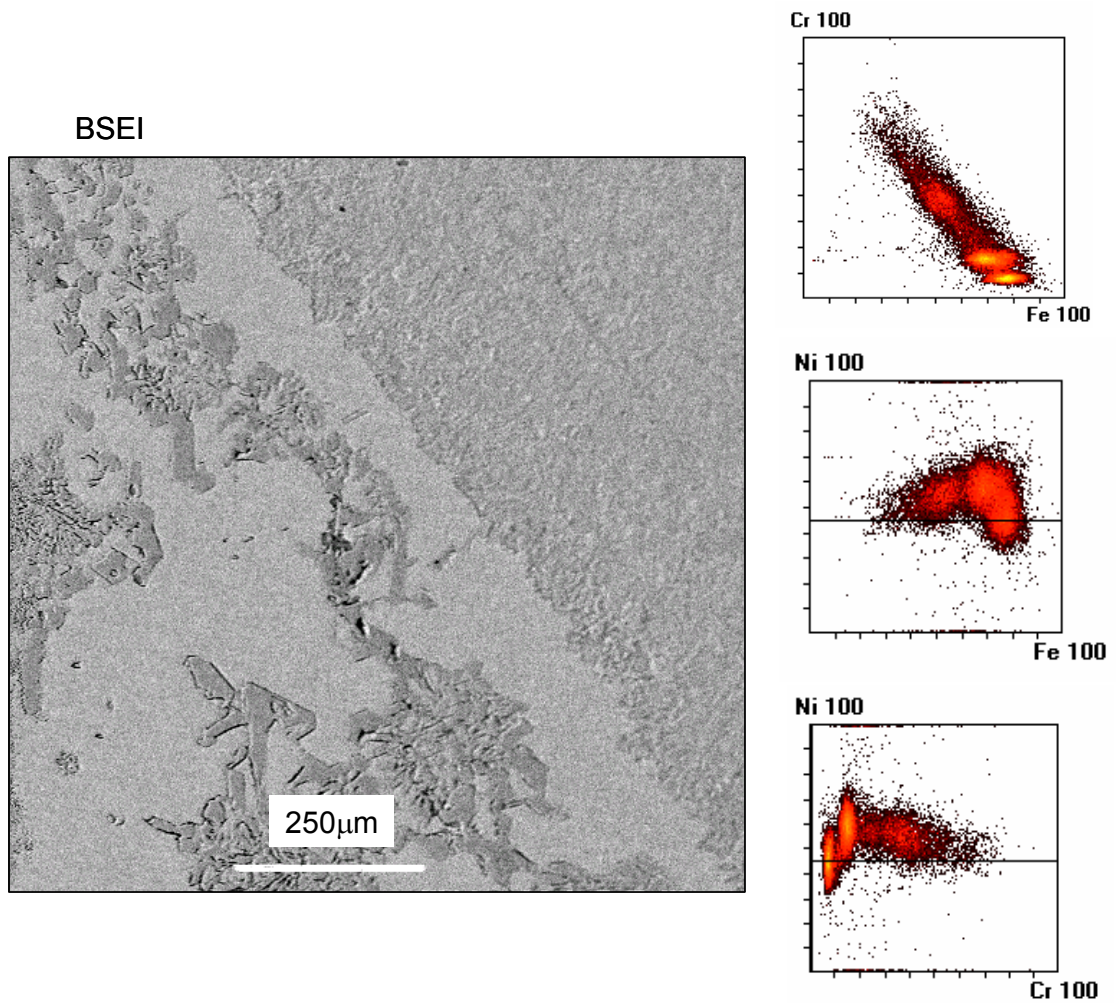


Figure 4.34: Back scattered electron (BSE) image and compositional scatter plots for vacuum cast composite interface region for chromium, iron and nickel.

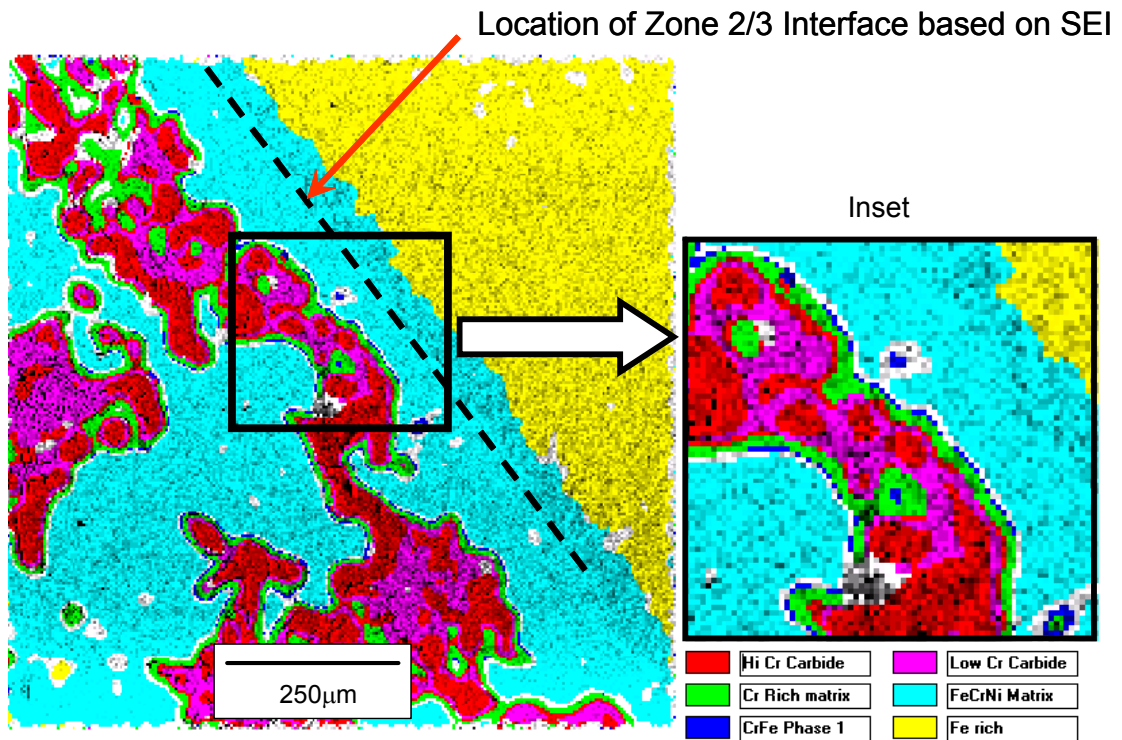


Figure 4.35: Composite colour x-ray map produced from overlay of selected compositional phase areas for chromium, iron and nickel for the steel/white iron interface area.

The use of nickel rather than manganese highlights the diffusion zone into the steel for chromium and nickel better compared to the chromium/iron/manganese map shown in Figure 4.33.

In addition, more compositional variation around and within the carbides has been identified, suggesting some chromium depletion is occurring at the carbide/ferrous matrix boundaries.

Using the Zeiss Supra 55VP SEM, x-ray maps were collected for the carbides within the white cast iron to enhance the compositional differences between the two types of carbides.

Figure 4.36 shows the In-lens secondary electron image and several elemental maps, including carbon, for the typical carbides observed in the low melting point white cast iron.

The following observations can be made from the data shown in Figure 4.36:

- i. Carbon content in the centre of the carbide is higher compared to the surrounding edges, representing the centre of the carbides as the M_7C_3 type, and the edges as the quasi-peritectic M_3C type;
- ii. Silicon is essentially partitioned wholly to the ferrous matrix of the white cast iron, indicating low or negligible solubility in the carbides;
- iii. Chromium content is highest in the M_7C_3 carbides compared to the M_3C carbides; and
- iv. Nickel has partitioned slightly more towards the ferrous matrix.

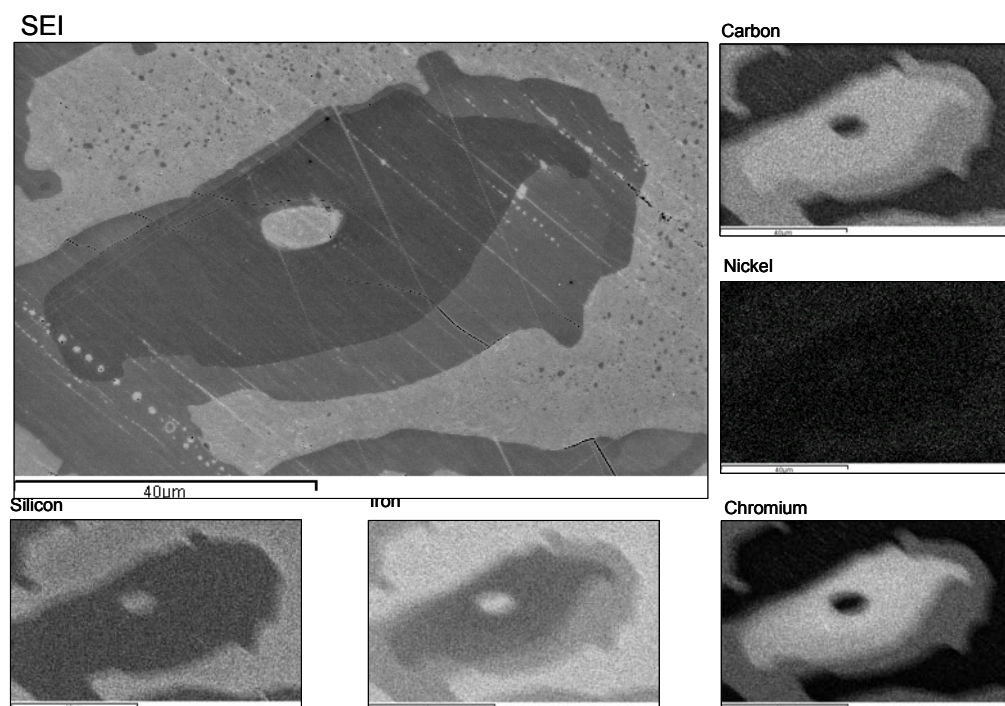


Figure 4.36: Secondary electron (SE) image and x-ray maps for vacuum cast sample white cast iron carbides

The typical carbon x-ray map produced using the Jeol 733 microprobe is shown in Figure 4.37. General observation of the carbon maps reveal a small reduction in carbon content as a thin band running parallel to the vacuum cast interface. This band may be a result of solid state diffusion during the cooling of the samples after completion of the vacuum casting process.

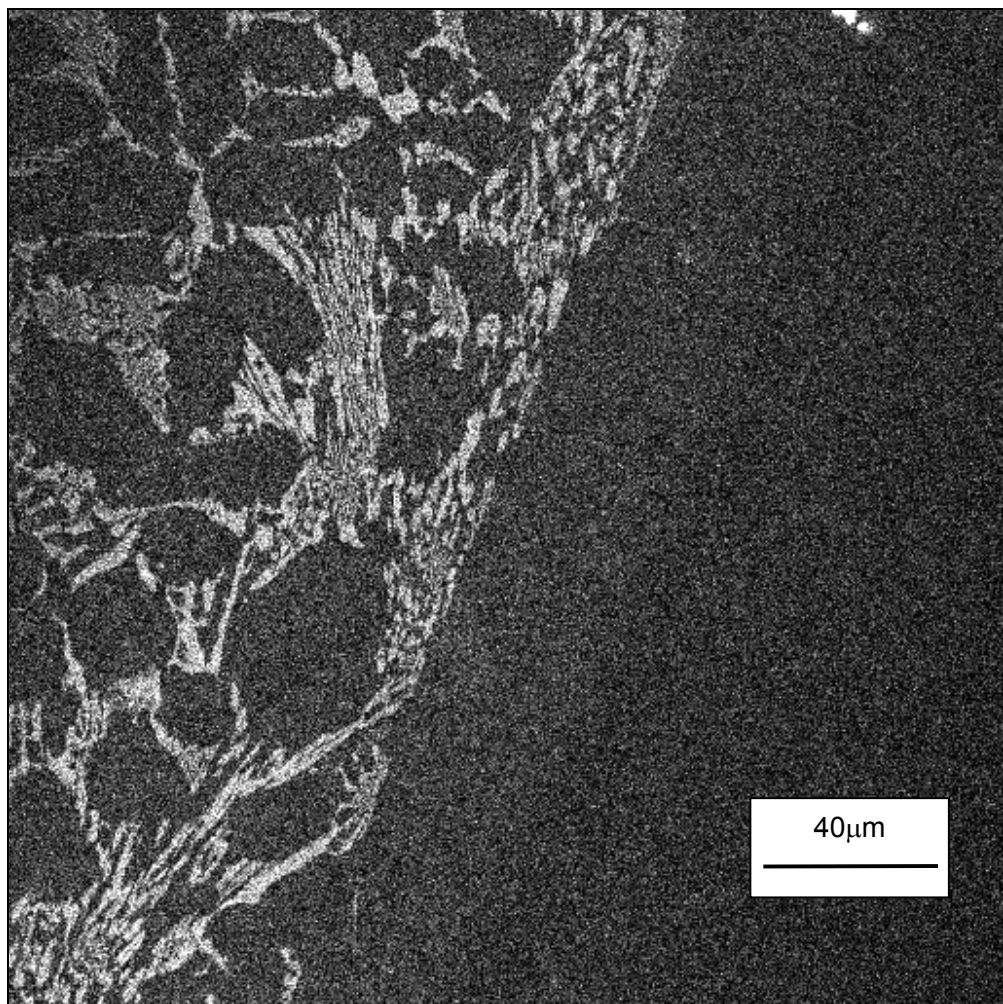


Figure 4.37: Carbon x-ray map for vacuum cast white iron/steel interface performed on a Jeol 733 Microprobe SEM

Using the carbon x-ray map from Figure 4.37, single line scan profiles can be selected along lines perpendicular to the vacuum cast interface. A typical single line scan profile for carbon is shown in Figure 4.38. The data for the line scan has been averaged to remove extraneous peaks and troughs, and it can be seen how the carbon content decreases as the position of analysis moves into the steel substrate.

Using the carbon data for the positions shown marked on Figure 4.38, the raw intensity data can be corrected for estimated carbon contents based on the stoichiometric composition of the M_7C_3 carbides and known carbon content of the steel. The relationship between carbon raw intensity and weight percent is shown in Figure 4.39. The data is observed to follow an exponential relationship, which can then be used to permit the raw intensity values for a given location to be converted to calculated carbon contents in weight percent.

The estimated carbon content in weight percent for the positions as shown marked in Figure 4.38 are shown in Table 4.3.

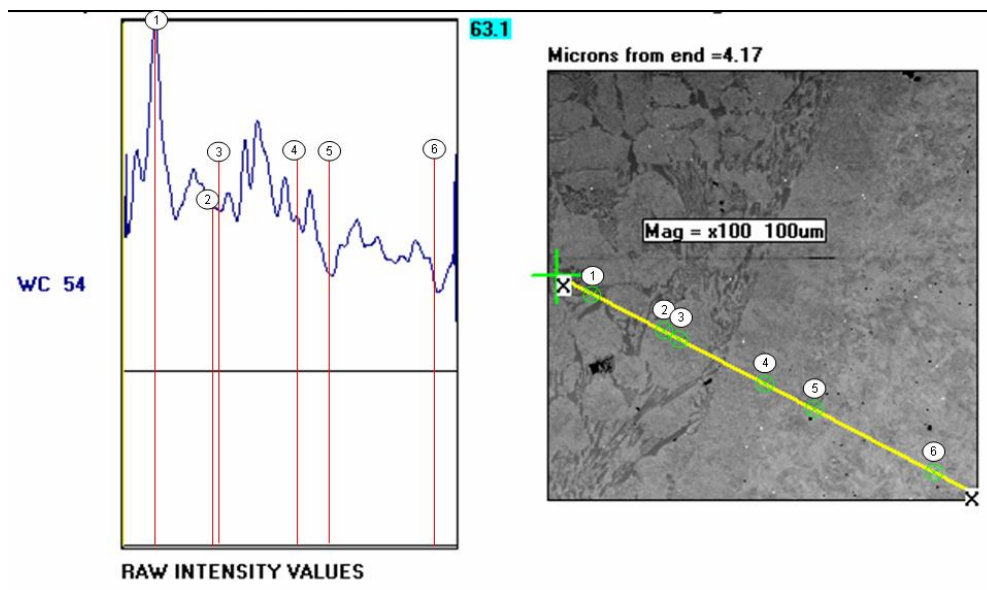


Figure 4.38: Single line profile from x-ray map for carbon WDS scan

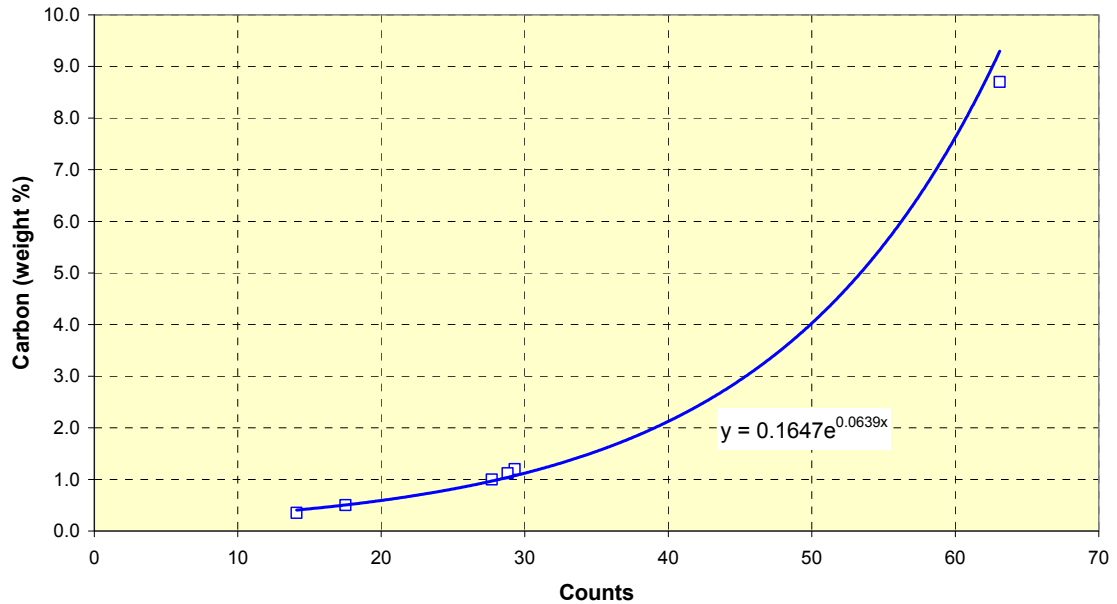


Figure 4.39: Relationship between carbon x-ray counts and carbon weight percent for vacuum cast alloy sample from Figure 4.38.

Table 4.3: Estimated carbon weight % based on carbon calibration curve shown in Figure 4.39 for positions on x-ray line scan shown in Figure 4.38.

Position	Position (μm)	Carbon Intensity (counts)	Estimated Carbon (weight %)	Expected Carbon (weight %)	Variance (%)
	0	54.0			
1	209	63.1	9.29	8.70	6.7%
2	588	29.3	1.07	1.20	-10.7%
3	626	28.8	1.04		
4	1110	27.7	0.97		
5	1320	17.5	0.50		
6	2010	14.1	0.41	0.35	15.9%

The estimated carbon content for the M_7C_3 carbide based on the curve shown in Figure 4.39 is high compared to the expected value of 8.7 weight %. The data shown in Table 4.3 shows the carbon content follows a trend similar to that expected for non-steady state diffusion of carbon into the steel, and this is discussed further in Section 4.4 of this study.

The carbon x-ray map and single line profile data has been overlaid and compared to the original position of the vacuum cast interface and is shown in Figure 4.40 and 4.41. In the example shown in Figures 4.40 and 4.41, the line profile is observed to vary substantially with several peaks and troughs within single phase regions. This suggests the accuracy of the WDS spectra is limited, and can only be used as a qualitative analysis rather than a quantitative analysis.

However the data shows the high level of carbon in the steel beyond the vacuum cast interface, and confirms the high quality of the bond that enables the ready diffusion of carbon into the steel substrate.

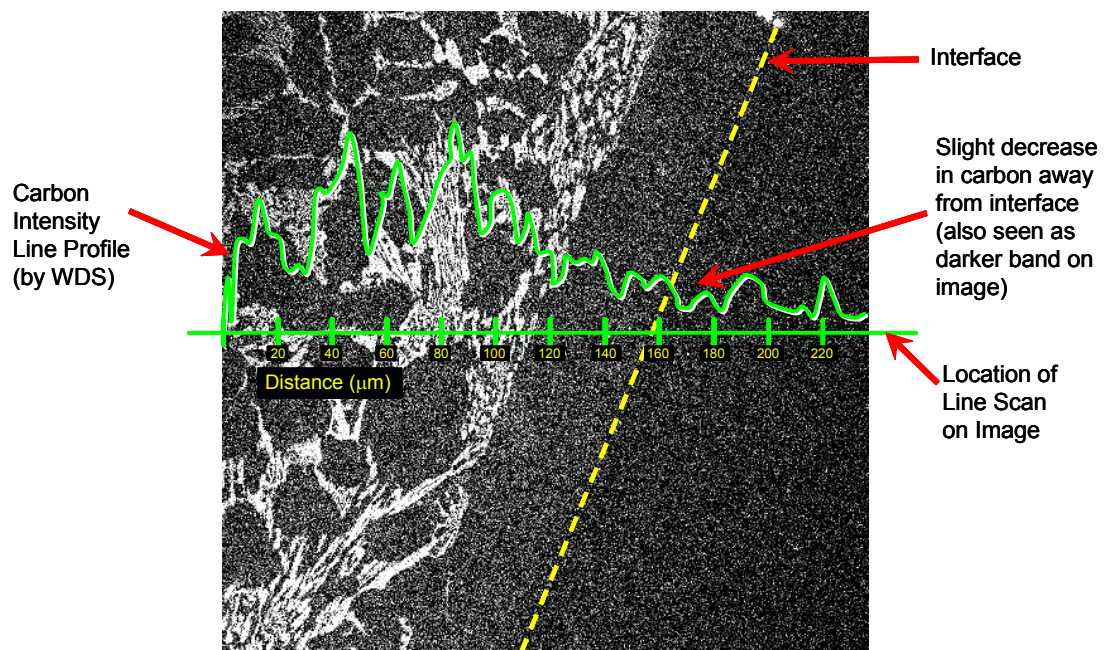


Figure 4.40: Carbon x-ray map for vacuum cast white iron/steel interface with x-ray line scan profile overlaid showing decrease in carbon content through a linear band parallel to the interface.

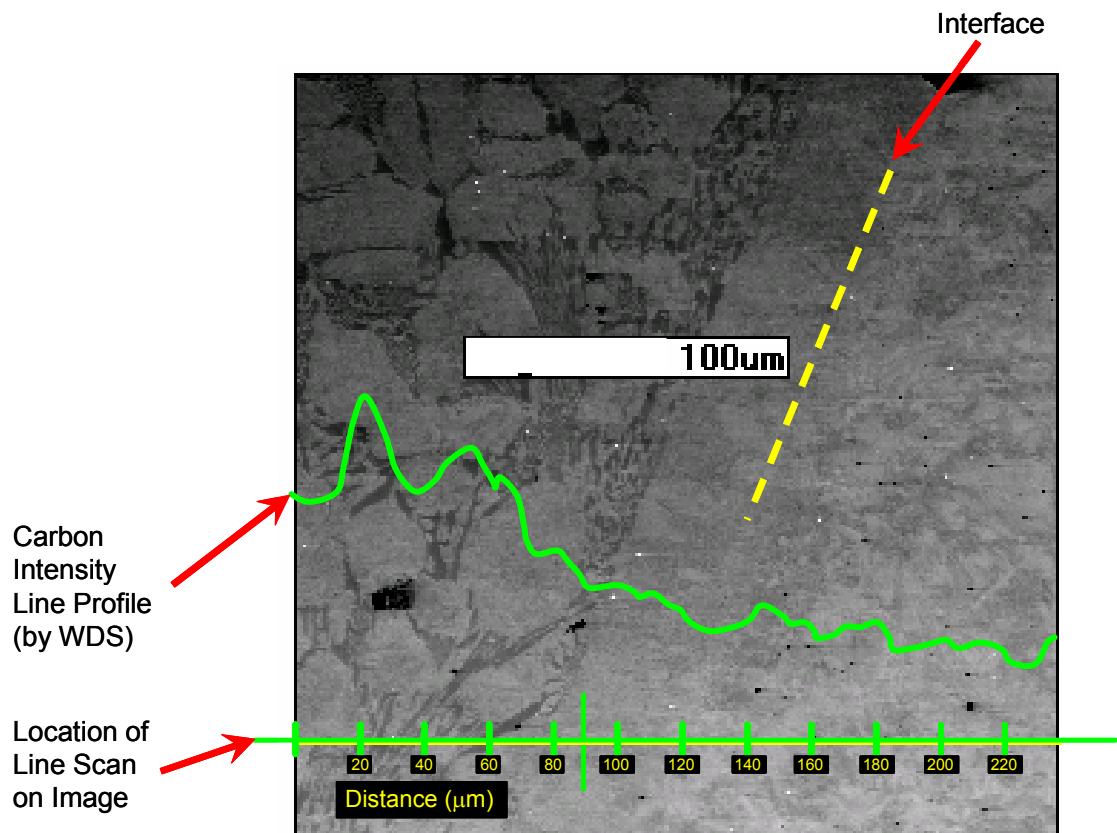


Figure 4.41: BSE image of sample shown in carbon map in Figure 4.37 for vacuum cast white iron/steel interface with x-ray line scan profile overlaid.

Using the multi element x-ray maps produced from the Jeol 35CF SEM, single line scan profiles can be selected along lines perpendicular to the vacuum cast interface. A typical single line scan profile for multi elements is shown in Figure 4.42. The data for the line scan has been averaged to remove extraneous peaks and troughs, and it can be seen how the carbon content decreases as the position of analysis moves into the steel substrate.

Based on the multi element data for the positions shown marked on Figure 4.42, the raw intensity data can be corrected for estimated carbon contents based on the stoichiometric composition of the M_7C_3 carbides and known carbon content of the

steel. The relationship between chromium, manganese and nickel raw intensity and weight percent are shown in Figures 4.43 to 4.45. The data can then be used to permit the raw intensity values for a given location to be converted to calculated chromium, manganese and nickel contents in weight percent.

The estimated chromium, manganese and nickel content in weight percent for the positions as shown marked in Figure 4.42 are shown in Tables 4.4 to 4.6.

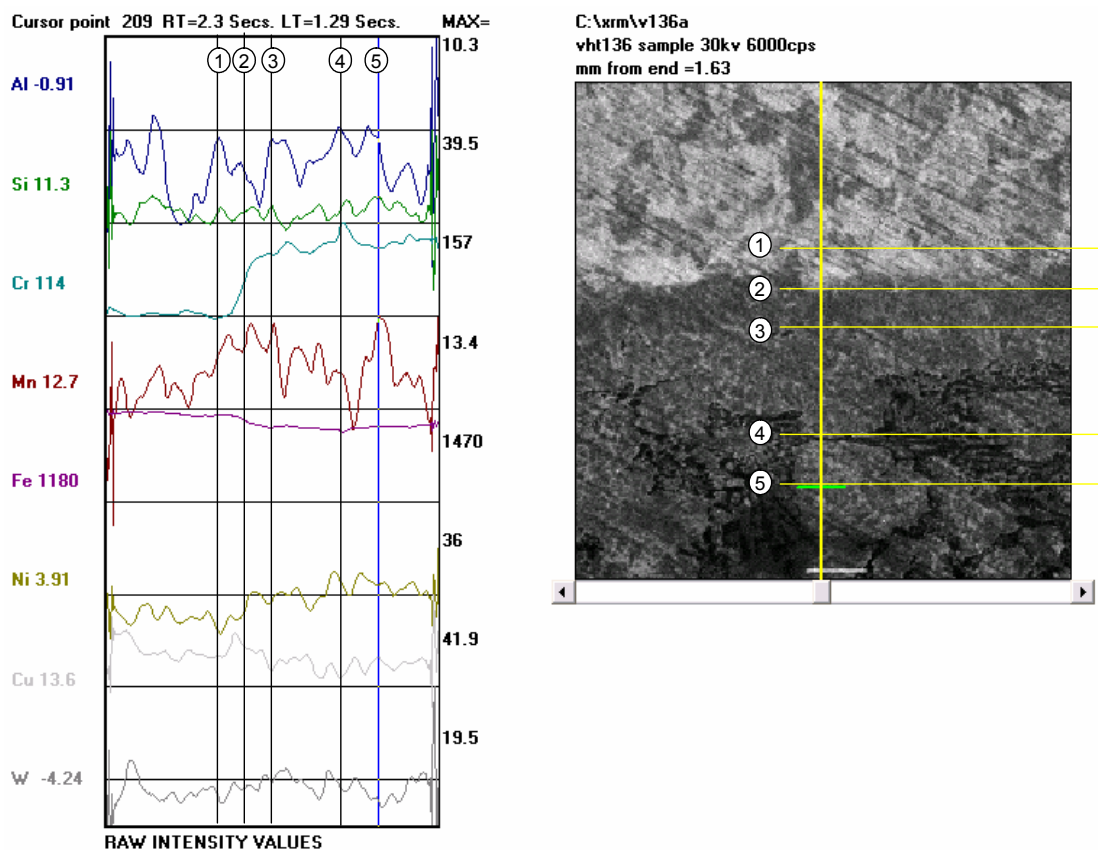


Figure 4.42: Single line profile from x-ray map for multi-element EDS scan.

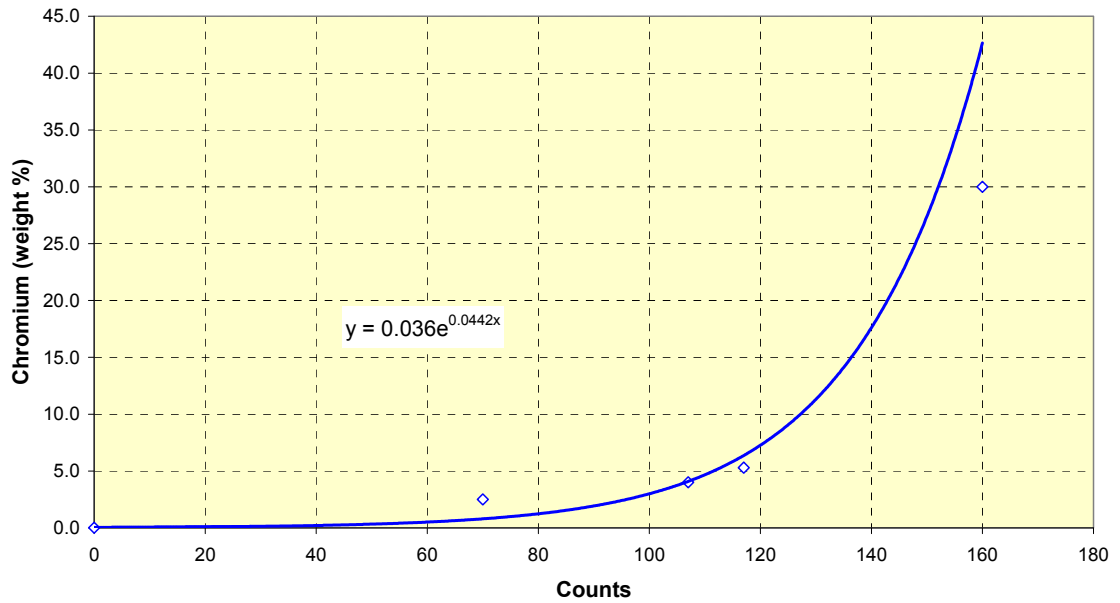


Figure 4.43: Relationship between chromium x-ray counts and chromium weight percent for vacuum cast alloy sample from Figure 4.42.

Table 4.4: Estimated chromium weight % based on chromium calibration curve shown in Figure 4.3 for positions on x-ray line scan shown in Figure 4.42.

Position	Position (μm)	Chromium Intensity (counts)	Corrected Intensity (counts)	Estimated Chromium (weight %)	Expected Chromium (weight %)	Variance (%)
	0					
1	680	-3.39	0	0.02	0.02	0.0%
2	844	66.6	69.99	3.00		
3	1000	104	107.39	4.04		
4	1430	157	160.39	30.5	28	8.8%
5	1630	114	117.39	5.37	5.3	1.3%

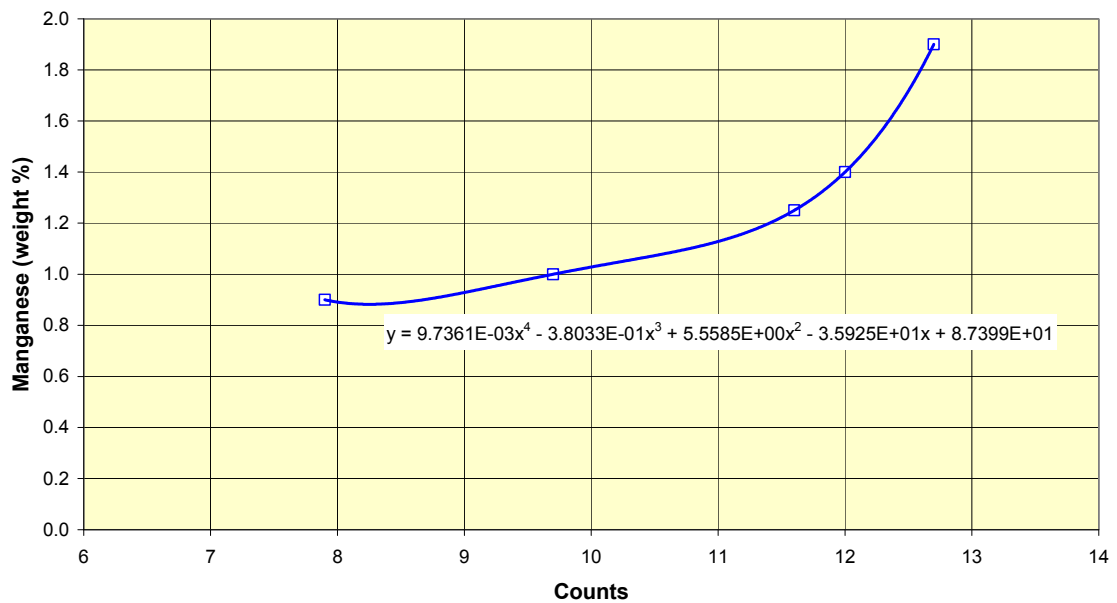


Figure 4.44: Relationship between manganese x-ray counts and manganese weight percent for vacuum cast alloy sample from Figure 4.42.

Table 4.5: Estimated manganese weight % based on manganese calibration curve shown in Figure 4.44 for positions on x-ray line scan shown in Figure 4.42.

Position	Position (μm)	Manganese Intensity (counts)		Estimated Manganese (weight %)	Expected Manganese (weight %)	Variance (%)
	0					
1	680	7.9	7.9	0.90	0.90	0.2%
2	844	9.7	9.7	1.00		
3	1000	11.6	11.6	1.25		
4	1430	11.8	11.8	1.32	1.4	-6.0%
5	1630	12.7	12.7	1.90	1.9	0.0%

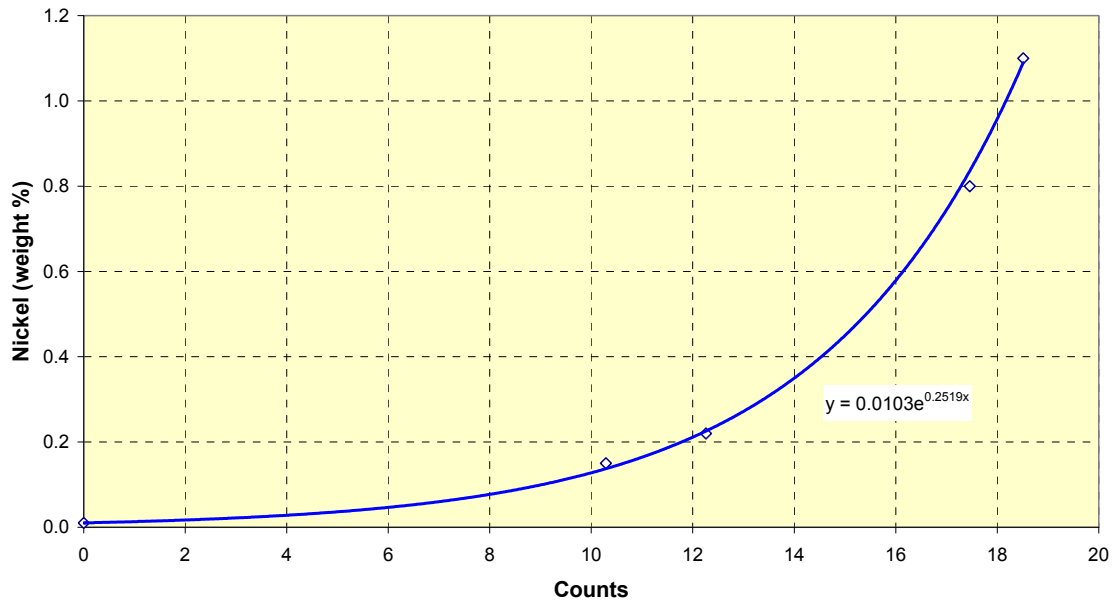


Figure 4.45: Relationship between nickel x-ray counts and nickel weight percent for vacuum cast alloy sample from Figure 4.42.

Table 4.6: Estimated nickel weight % based on nickel calibration curve shown in Figure 4.45 for positions on x-ray line scan shown in Figure 4.42.

Position	Position (μm)	Nickel Intensity (counts)		Estimated Nickel (weight %)	Expected Nickel (weight %)	Variance (%)
	0					
1	680	-14.6	0	0.01	0.01	3.0%
2	844	-4.31	10.29	0.14		
3	1000	-2.34	12.26	0.23		
4	1430	2.86	17.46	0.84	0.8	4.7%
5	1630	3.91	18.51	1.09	1.1	-0.8%

The relative variance between the estimated and expected weight percent values for chromium, manganese and nickel are low and therefore provide a high confidence level of utilizing the x-ray mapping data for quantitative work. The estimated element weight percent values across the vacuum cast interface and into the steel substrate have been used in Section 4.4 of this study to review the diffusion processes within the vacuum cast interface.

4.3.4 SEM ELECTRON BACKSCATTERED DIFFRACTION (EBSD) MAPPING

Electron back scattered diffraction (EBSD), also called EBSP, BKD, and OIM™ is an SEM technique that can be applied in theory to any crystalline material. The technique provides the absolute crystal orientation with sub-micron resolution and is a useful tool for discriminating between phases and for identifying unknown phases. EBSD mapping is emerging as an excellent tool for microstructural categorisation as it provides a more extensive analysis of phase crystallography and location of phases compared to more traditional x-ray diffraction techniques.

EBSP like patterns were first observed by Kikuchi (1928) in the Transmission Electron Microscope (TEM). Von Boersch (1937) extended Kikuchi's work and developed further the use of Kikuchi patterns as a method for characterizing crystallographic phases. As the electron beam strikes the specimen inside an electron microscope, scattering produces electrons travelling in all directions. The electrons that satisfy the Bragg condition for a plane (hkl) are channelled forming Kikuchi bands. Electrons strike the phosphor screen and produce light which is detected by a CCD camera and digitized. The resulting EBSP is automatically analysed and indexed using computer hardware and software.

EBSD mapping requires the sample to be tilted to an angle of approximately 70° on the SEM stage. Tilting the sample to such a high angle limits the working distance range of the microscope, and makes positioning and focusing of the sample difficult. Coupled with the fact the EBSD samples were examined unetched to remove edge effects on the diffraction patterns, initial setup of each sample for EBSD mapping required patience and time in order to achieve the best results. Despite the time and effort required to setup EBSD samples, the results have proven to be very worthwhile.

A typical EBSD setup for a scanning electron microscope is shown in Figure 4.46 [59].

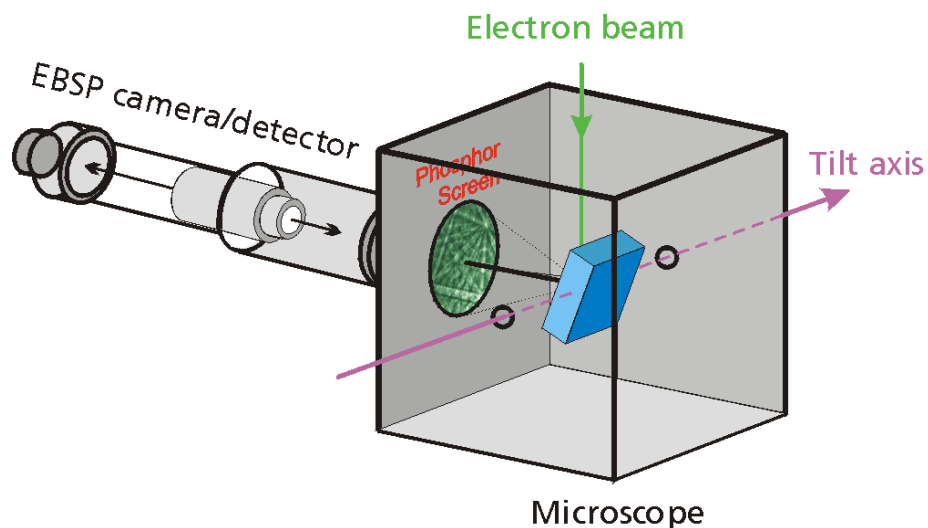


Figure 4.46: Typical EBSD SEM arrangement [59].

EBSD requires particularly flat sample preparation to provide scratch free surfaces in order to enable the correct indexing of the x-ray diffraction data collected. The samples examined for EBSD as part of this study were first polished to a 1 μm finish, then further chemical-mechanical polishing was conducted using colloidal silica to further improve the surface finish of the samples. Automatic polishing machines were used when available to produce ultra flat samples as well as electro polishing.

A HKL Technology EBSD system attached to the Zeiss Supra 55VP FEG SEM was operated at 20kV accelerating voltage and 20mm working distance for EBSD mapping.

An EBSD map was collected for a vacuum cast sample produced at 1274°C with a 60 minute soak for the region highlighted in Figure 4.47, which represents the interface and white cast iron region. The sample was chosen as it represented the highest degree of casting superheat with a significant soak period and therefore would produce the maximum amount of compositional changes.

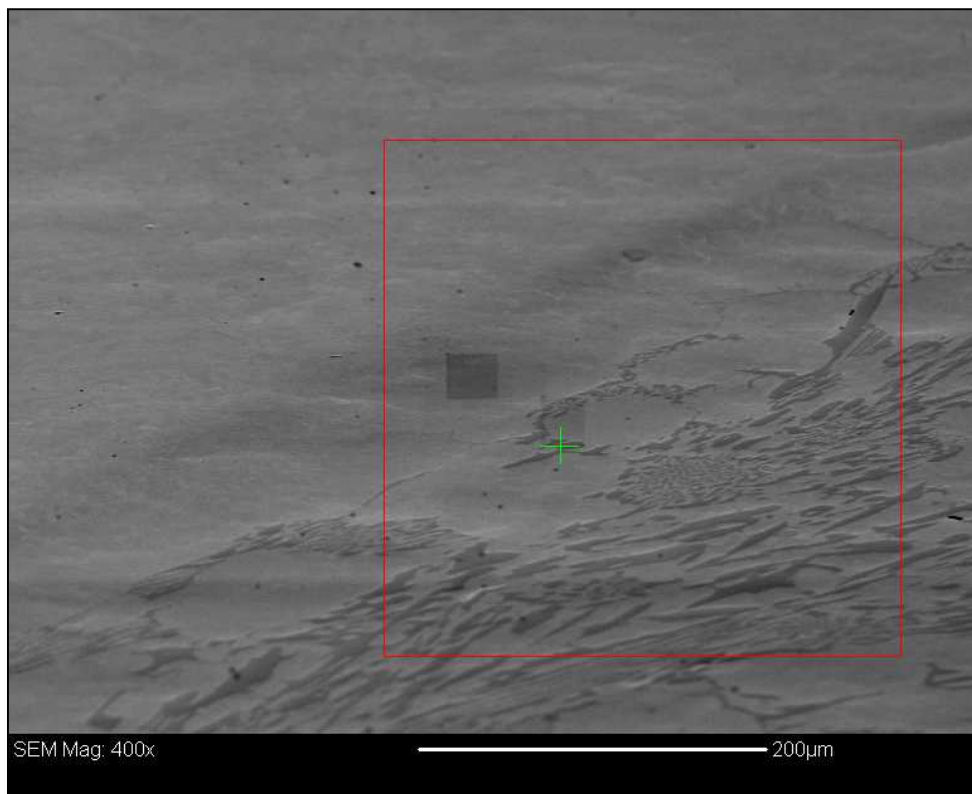
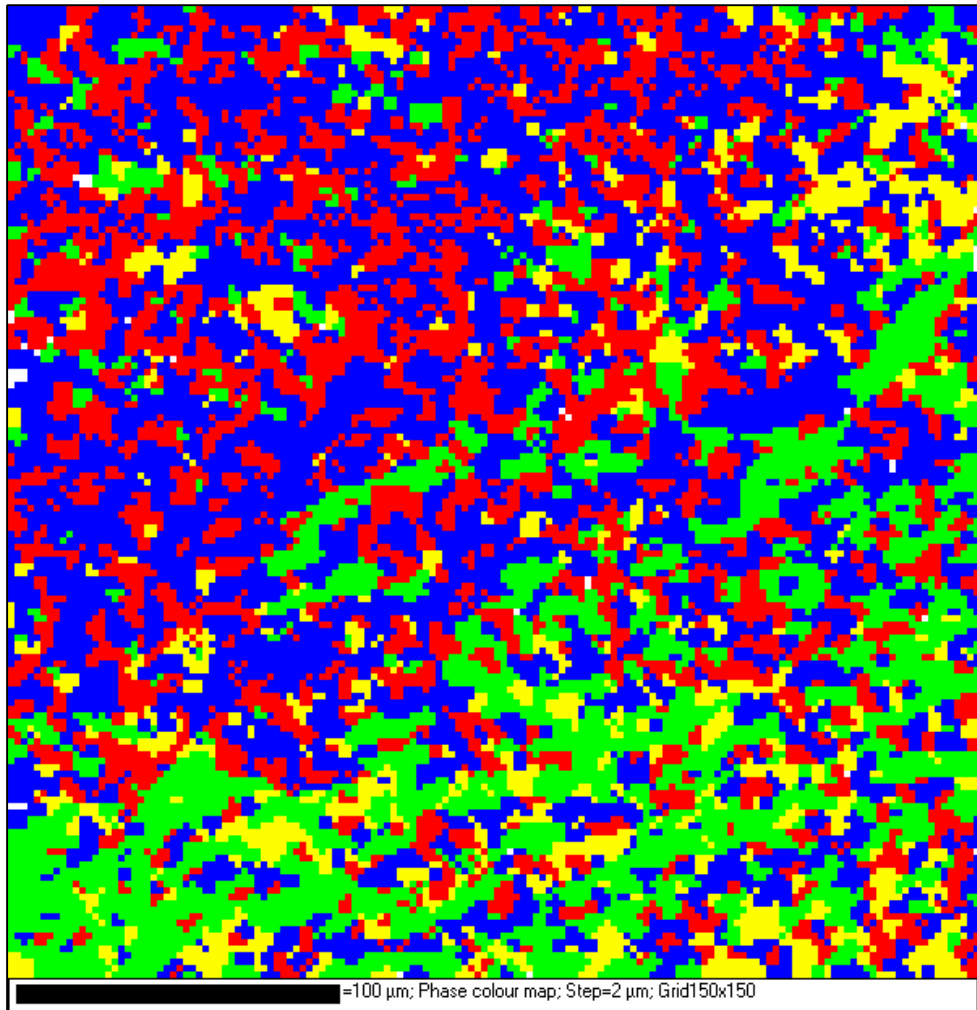


Figure 4.47: Location of EBSD map for vacuum cast composite bond produced at 1274°C for 60 minute soak.

The collected EBSD map for the region highlighted in Figure 4.47 is shown in Figure 4.48 along with the phase colour identification and the percentage of indexing achieved. The EBSD map has then been overlaid onto the SEI shown in Figure 4.47 to allow the phase regions identified from EBSD to be compared to the normal microstructural features, and is shown in Figure 4.49.

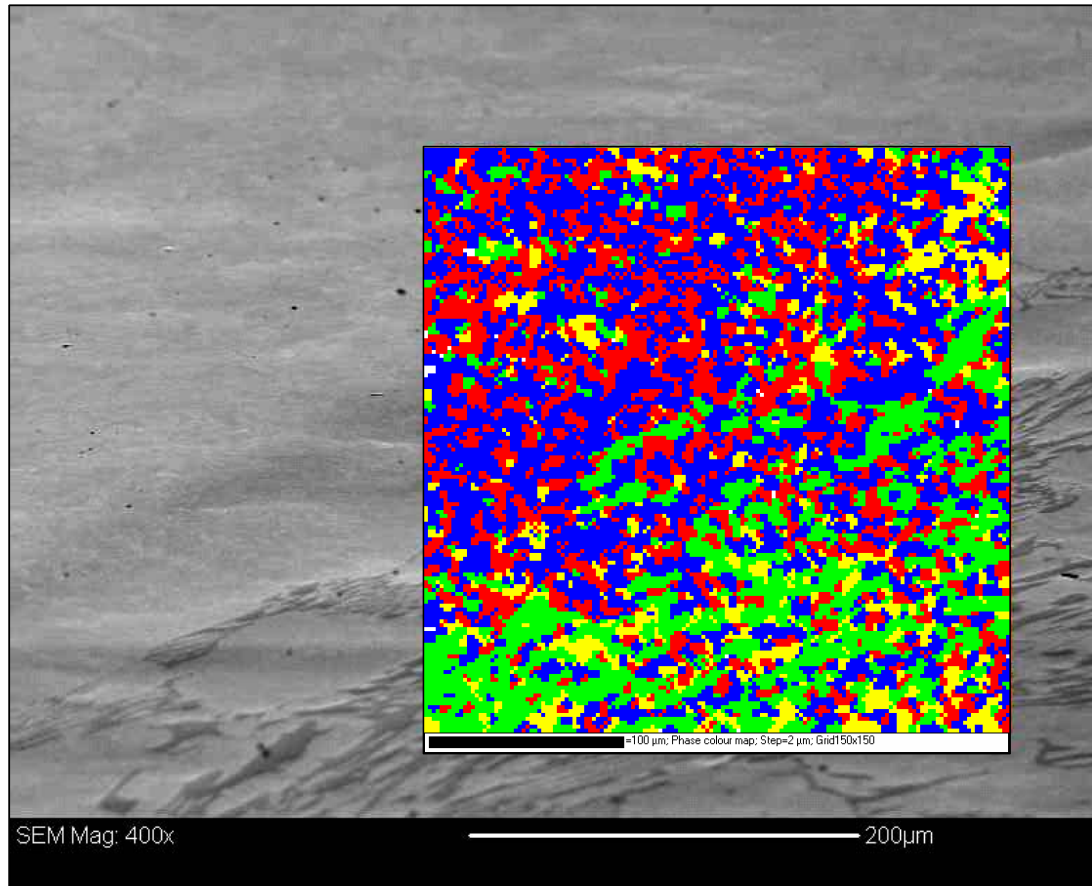


■ = Austenite, FCC
 ■ = Ferrite, BCC
 ■ = M_7C_3 Carbide
 ■ = M_3C Carbide

Phase	%	mean BC	mean BS	mean MAD
Zero solutions	28.62	85.75	41.11	n/a
Iron bcc	24.9	109.4	49.57	0.8034
Iron fcc	19.09	111.8	50.87	0.792
Fe3C	11.86	95.93	44.09	0.9199
C3Fe7	15.53	128.4	52.04	0.7725
Total	100	104.4	47.13	0.813

Analyzed: 100.0%

Figure 4.48: EBSD Map for vacuum cast composite bond produced at 1274°C for 60 minute soak for region shown in Figure 4.47



■ = Austenite, FCC
 ■ = Ferrite, BCC
 ■ = M_7C_3 Carbide
 ■ = M_3C Carbide

Figure 4.49: EBSD Map for vacuum cast composite bond produced at $1274^{\circ}C$ for 60 minute soak overlaid onto SE image from Figure 4.47

The EBSD map confirms the presence of the M_7C_3 and M_3C carbides within the white iron based on the reported crystal structures of these two phases, and also shows the presence of the M_3C carbides within the “carbide-free” zone of the white cast iron adjacent to the interface with the steel substrate. The results of the EBSD at this magnification also show the presence of ferrite and austenite within the white iron ferrous matrix, and also across the “carbide-free” white iron zone.

A higher magnification EBSD region is shown in Figure 4.50. Typical Kikuchi patterns and indexing results for several phases observed within the sample are shown in Figures 4.51 to 4.54, and shown with respect to the EBSD map in Figure 4.55.

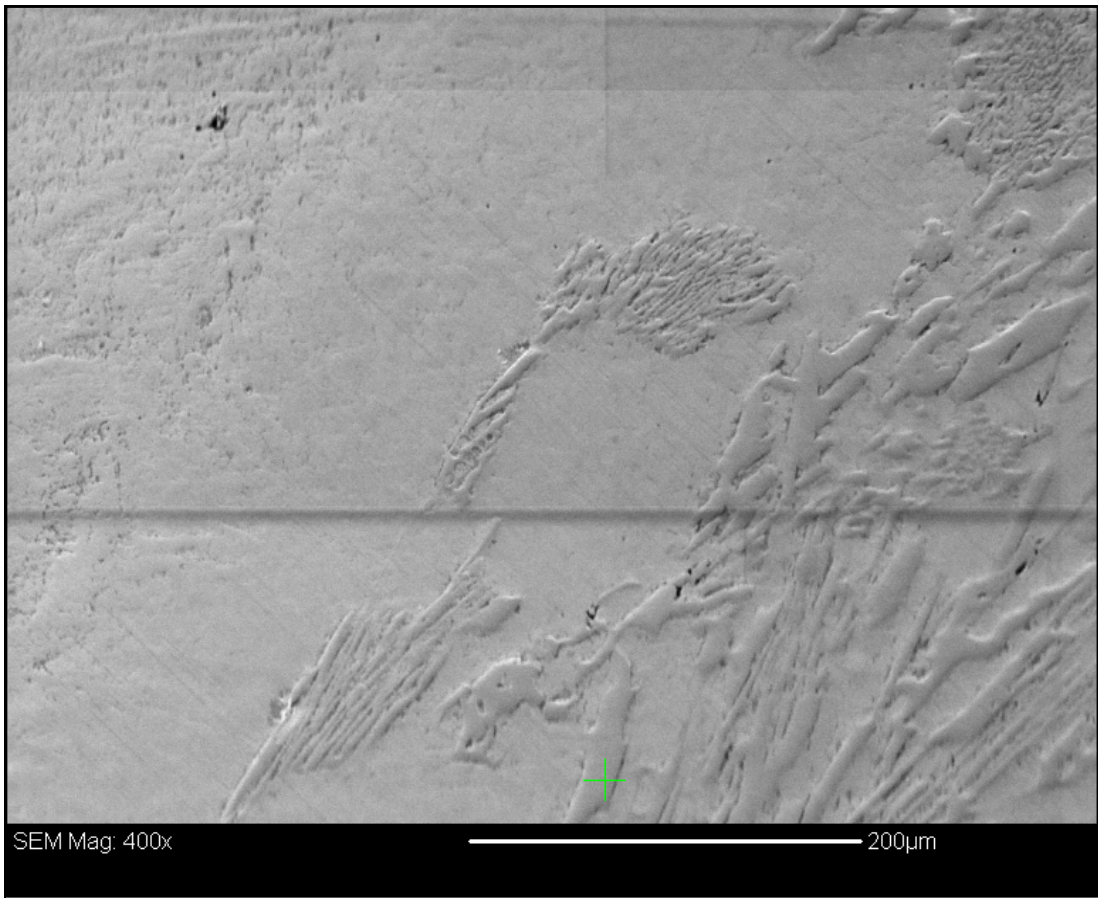
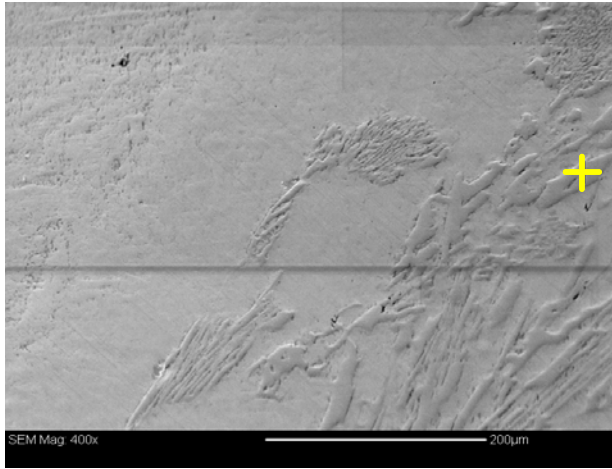
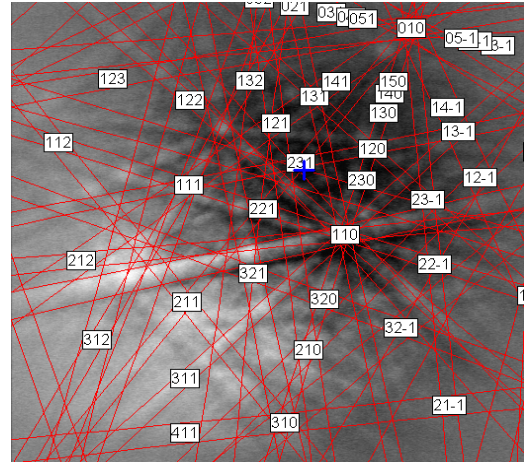
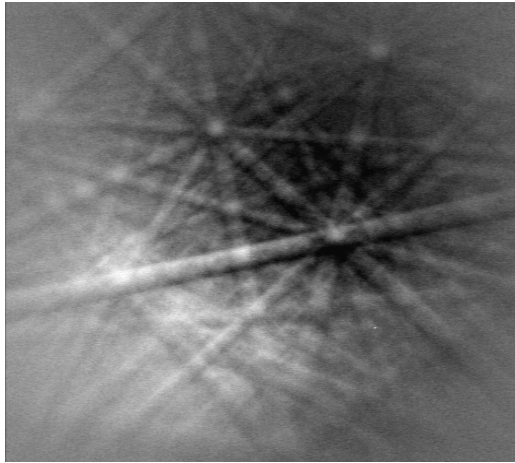


Figure 4.50: Higher magnification image of EBSD sample produced at 1274°C for 60 minute soak



Composition:

n/a



BC = 255, BS = n/a

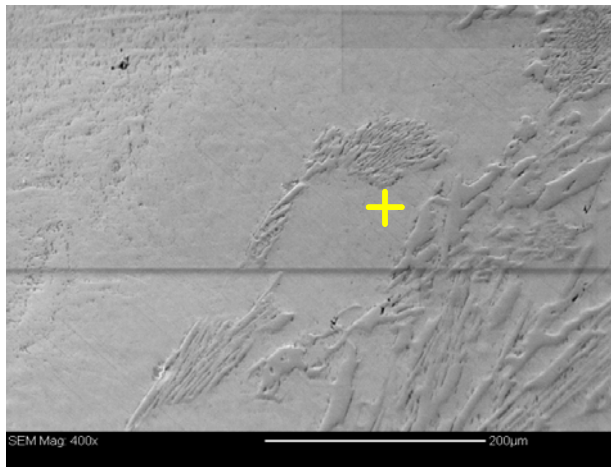
MAD = 2.246°, Orientation = (79.7, 108.4, 3.4)°

Phase:

Name:	cementite
Data source:	[Fe3c.cry]
Database name:	CHANNELPhaseDatabase
Laue group:	3, mmm
Unit cell lengths:	5.09, 6.74, 4.52 Å
Unit cell angles:	90.0, 90.0, 90.0 °
Composition:	C(25 at%), Fe(75)

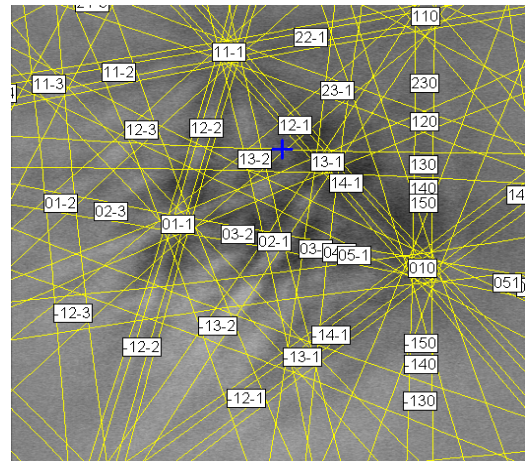
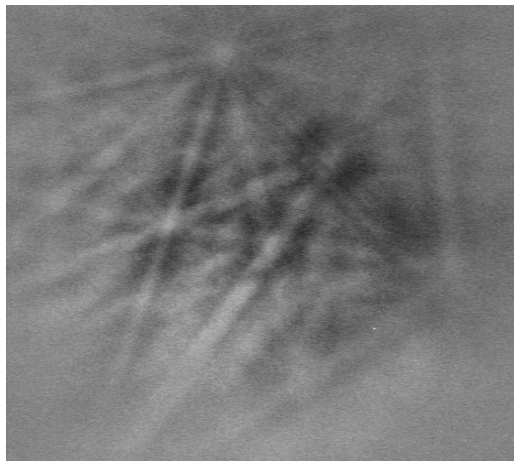
13/11/02 - 14:27:

Figure 4.51: Kichuchi patterns and indexing data for M_3C carbide found in sample shown in Figure 4.50



Composition:

n/a



BC = 196, BS = n/a

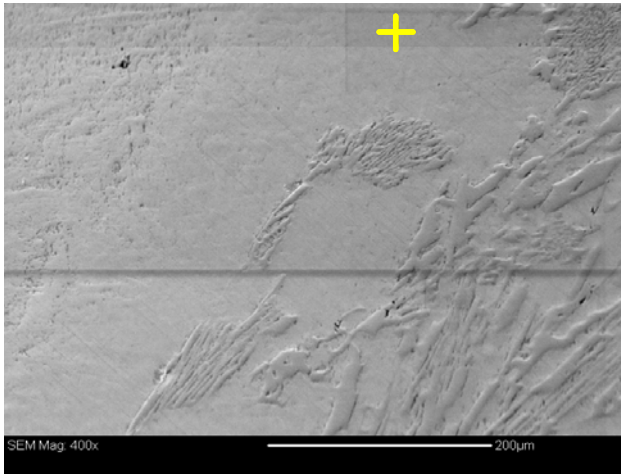
MAD = 0.733°, Orientation = (162.6, 40.9, 38.0)°

Phase:

Name:	Iron-BCC
Data source:	[Febcc.cry]
Database name:	CHANNELPhaseDatabase
Laue group:	11, m3m
Unit cell lengths:	2.69, 2.69, 2.69 Å
Unit cell angles:	90.0, 90.0, 90.0 °
Composition:	Fe(100 at%)

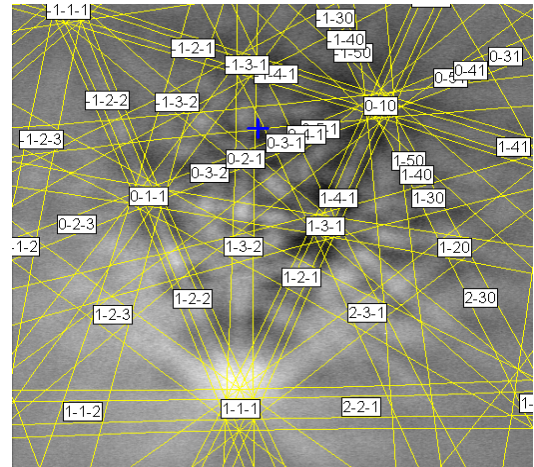
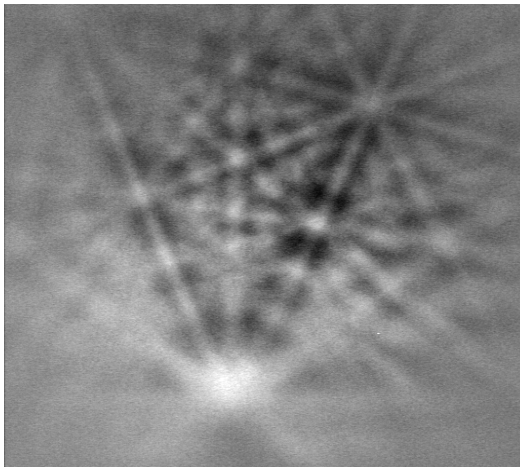
13/11/02 - 14:31z

Figure 4.52: Kichuchi patterns and indexing data for BCC ferrite found in white iron ferrous matrix shown in Figure 4.50



Composition:

n/a



BC = 169, BS = n/a

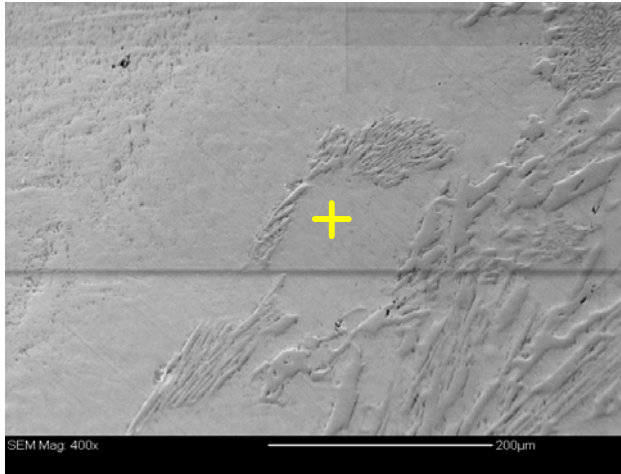
MAD = 0.476°, Orientation = (41.9, 34.5, 77.4)°

Phase:

Name:	Iron-BCC
Data source:	[Febcc.cry]
Database name:	CHANNELPhaseDatabase
Laue group:	11, m3m
Unit cell lengths:	2.69, 2.69, 2.69 Å
Unit cell angles:	90.0, 90.0, 90.0 °
Composition:	Fe(100 at%)

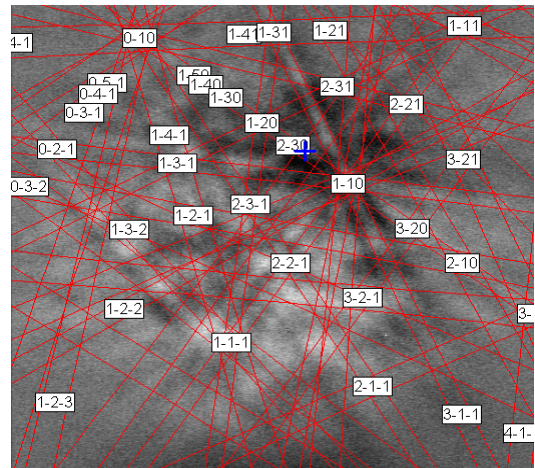
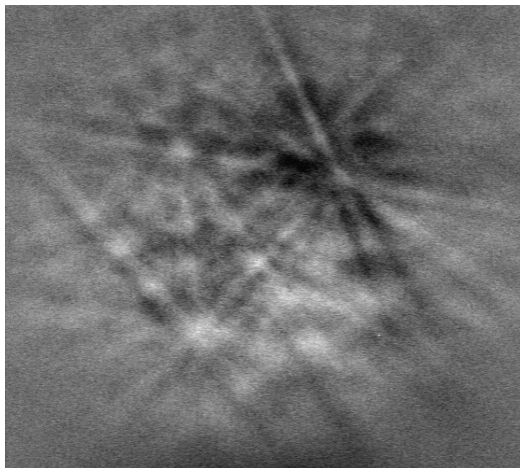
13/11/02 - 14:35:

Figure 4.53: Kichuchi patterns and indexing data for BCC ferrite found in the “carbide-free” zone shown in Figure 4.50



Composition:

n/a



BC = 121, BS = n/a

MAD = 1.981°, Orientation = (138.5, 65.3, 171.6)°

Phase:

Name:	cementite
Data source:	[Fe3c.cry]
Database name:	CHANNELPhaseDatabase
Laue group:	3, mmm
Unit cell lengths:	5.09, 6.74, 4.52 Å
Unit cell angles:	90.0, 90.0, 90.0 °
Composition:	C(25 at%), Fe(75)

13/11/02 - 14:25

Figure 4.54: Kichuchi patterns and indexing data for Fe₃C carbide found as pearlite in the sample shown in Figure 4.50

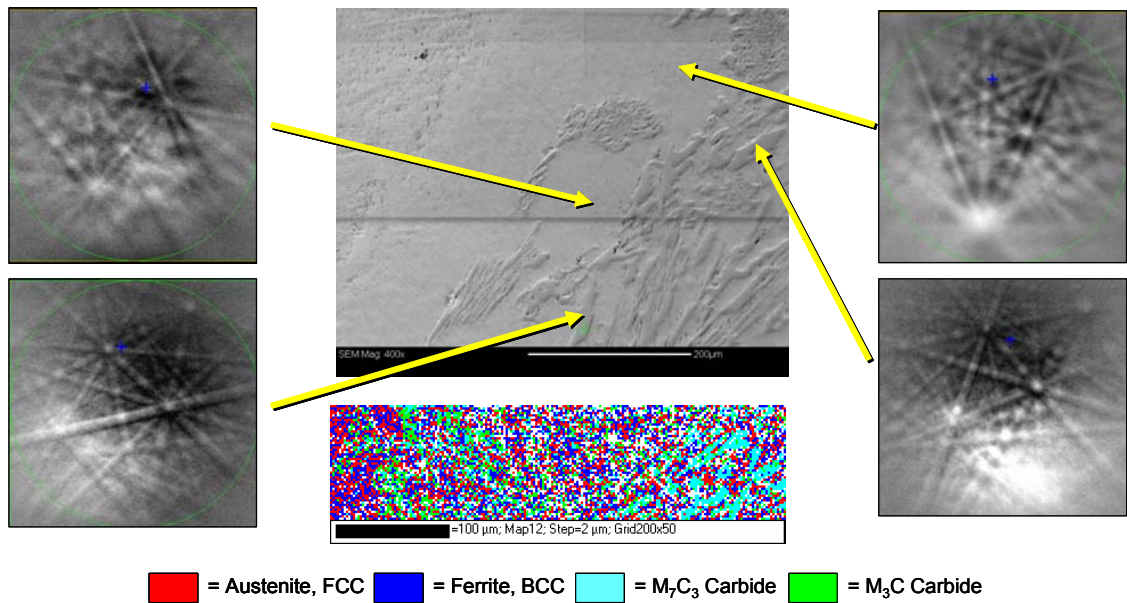


Figure 4.55: Correlation of Kichuchi patterns to vacuum cast interface based on Figure 4.50 and portion of EBSD map for selected region.

The carbide-free zone observed in the white cast iron (Zone 3) based on the x-ray mapping data suggests the ferrous matrix should contain austenite (face centred cubic, FCC), ferrite (body centred cubic, BCC) and cementite (Fe_3C carbide, or M_3C carbide). A more detailed EBSD map was conducted on the Zone 3 area to examine the phase microconstituents. Figure 4.56 shows the area where the EBSD map was taken, and Figures 4.57 to 4.60 provide more detail on the resulting maps and phases present.

It can be seen from Figure 4.60 that a substantial amount of Fe_3C carbide is present (yellow phase), and the ferrous matrix of the white iron in Zone 3 is perhaps made up of even amounts of pearlite plus retained austenite. Based on the HKL indexing from the Kikuchi patterns, the intergranular carbides within the Zone 3 ferrous matrix have been confirmed as the M_3C type.

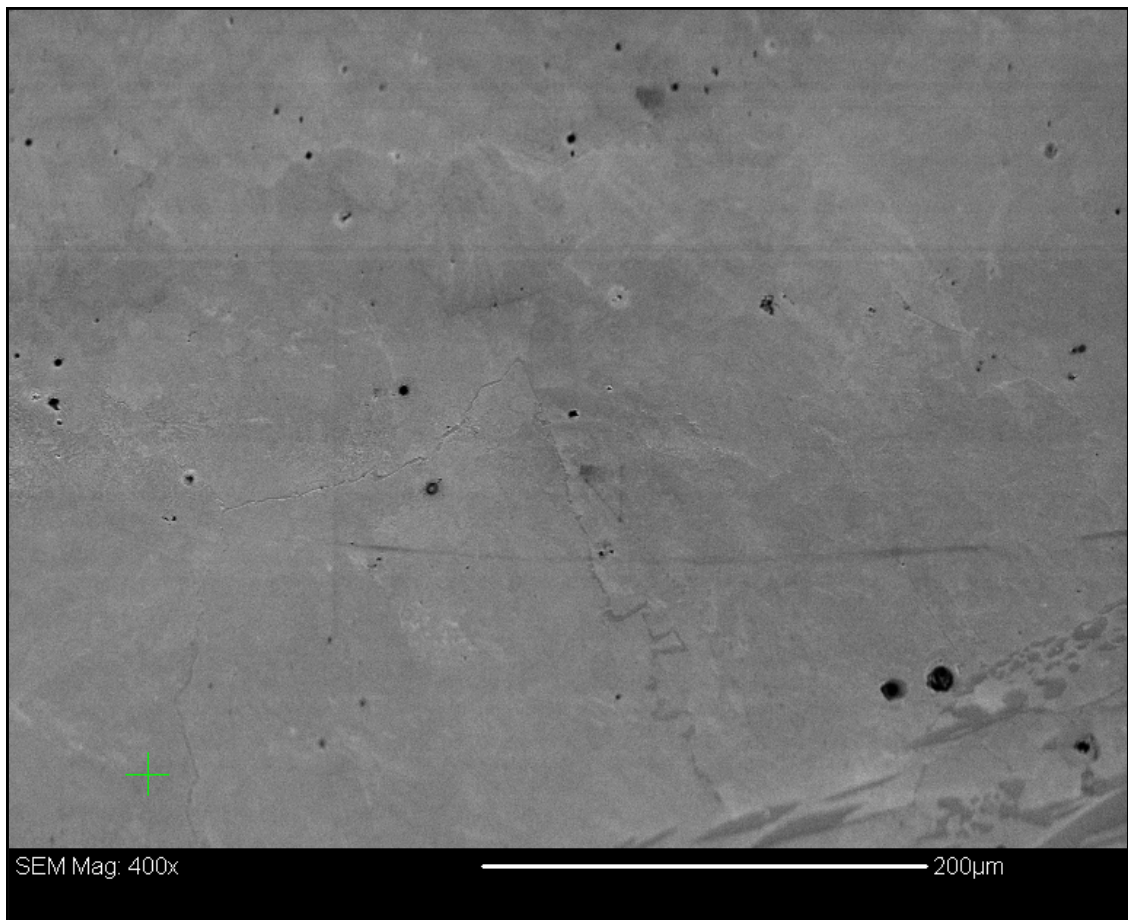


Figure 4.56: SE image for “carbide-free” region of the sample produced at 1274°C for 60 minute soak at higher magnification compared to Figures 4.47 and 4.50.

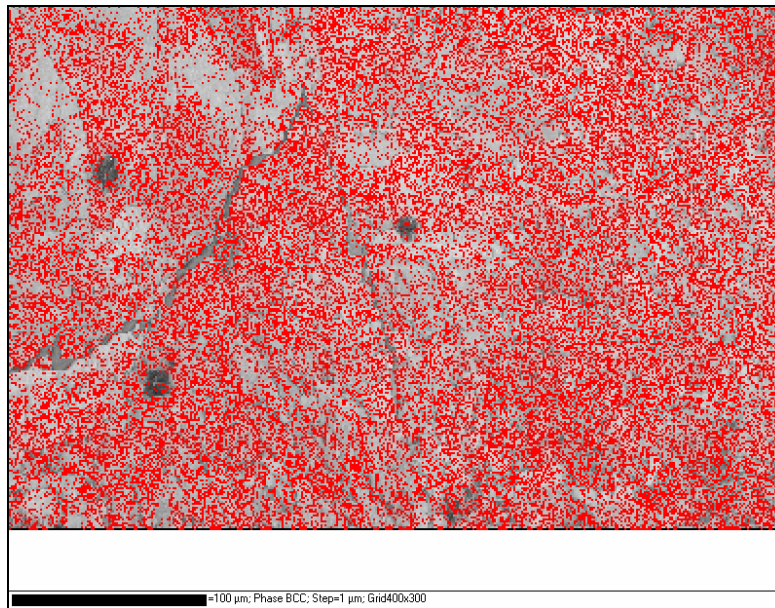


Figure 4.57: Overlay of EBSD data for BCC ferrite onto the SE image for “carbide-free” region of the sample produced at 1274°C for 60 minute soak based on Figure 4.56.

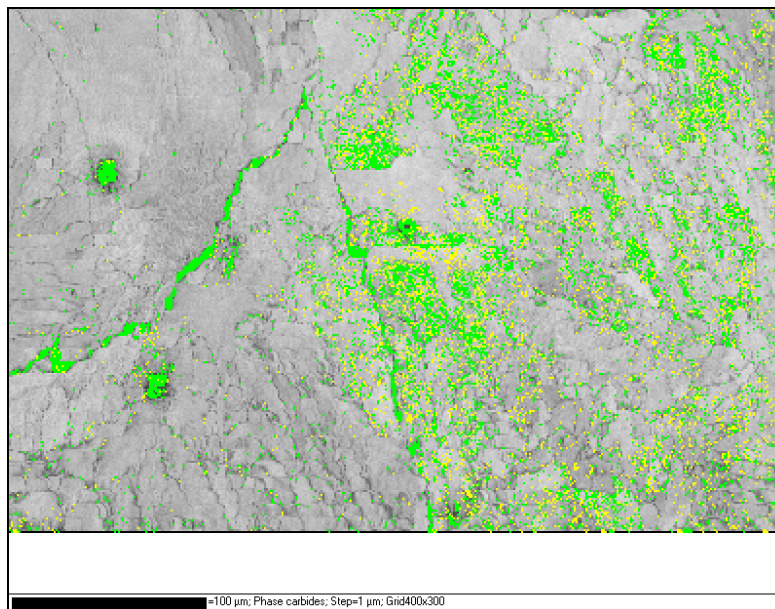


Figure 4.58: Overlay of EBSD data for M₃C carbides onto the SE image for “carbide-free” region of the sample produced at 1274°C for 60 minute soak based on Figure 4.56.

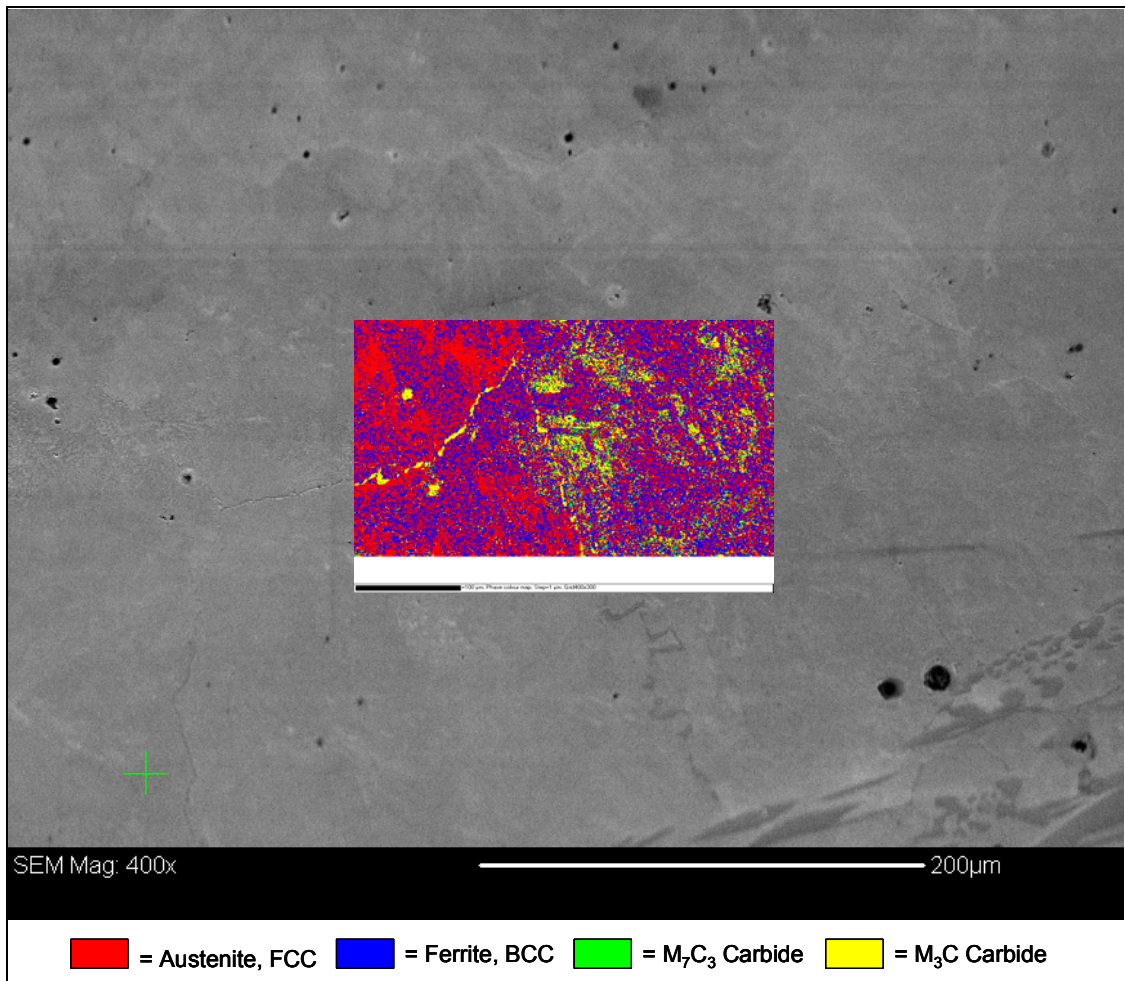


Figure 4.59: Overlay of complete EBSD map onto the SE image for “carbide-free” region of the sample produced at 1274°C for 60 minute soak based on Figure 4.56.

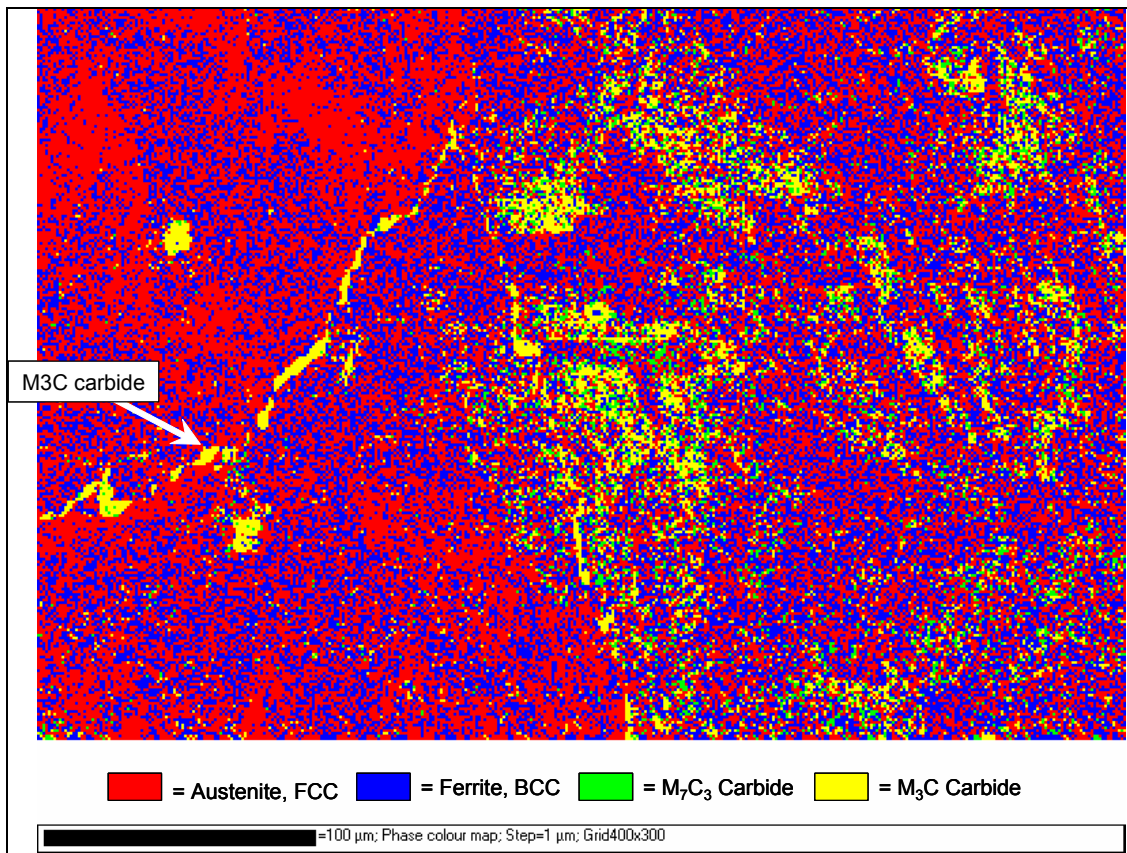


Figure 4.60: Detail of EBSD map for “carbide-free” region of the sample produced at 1274°C for 60 minute soak based on Figure 4.56.

Similar EBSD maps to that shown in Figures 4.47 to 4.49 are also provided in Figures 4.61 and 4.62.

A more detailed EBSD map was conducted for the eutectic carbides within the white cast iron region (Zone 4) to further identify the carbide phases present in the alloy. Figure 4.63 shows the location of the EBSD map.

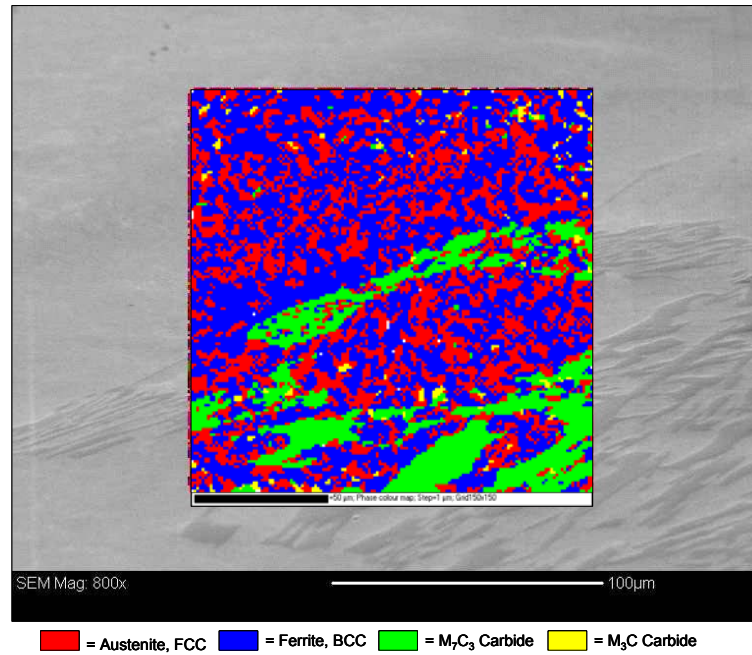


Figure 4.61: EBSD map overlaid onto SE image for vacuum cast interface between white cast iron and steel substrate.

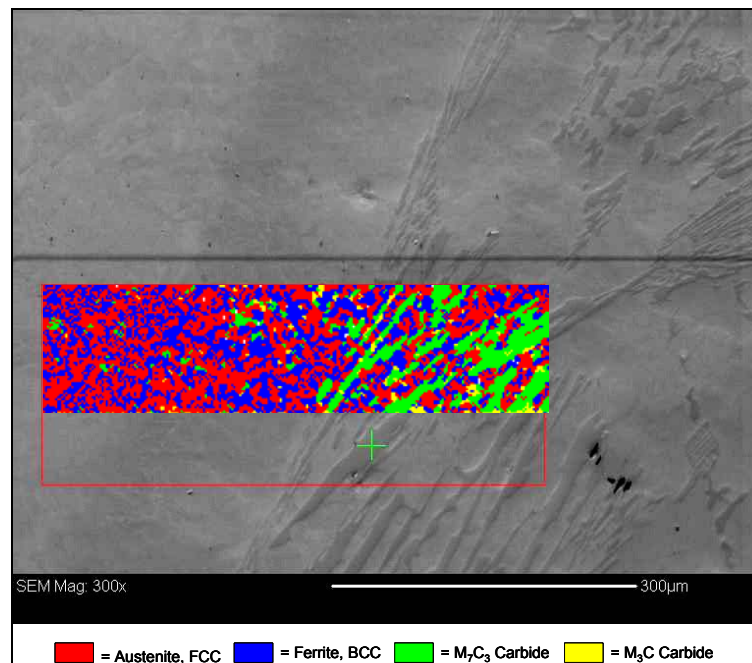


Figure 4.62: Lower magnification EBSD map overlaid onto SE image for vacuum cast interface between white cast iron and steel substrate.



Figure 4.63: Location of higher resolution EBSD map for eutectic carbides in the white cast iron (Zone 4) of the vacuum cast composite.

The resulting EBSD map obtained from the region shown in Figure 4.63 is shown in Figures 4.64 and 4.65. It can be seen from the EBSD map that the centres of the carbides are of the M_7C_3 type, with the M_3C carbides forming around the M_7C_3 carbides. This is consistent with the expected phases based on the phase diagram study conducted in Chapter 2 of this study, and the presence of the M_3C carbides is a result of the quasi-peritectic reaction of the M_7C_3 carbide with remaining liquid alloy to form the M_3C carbides.

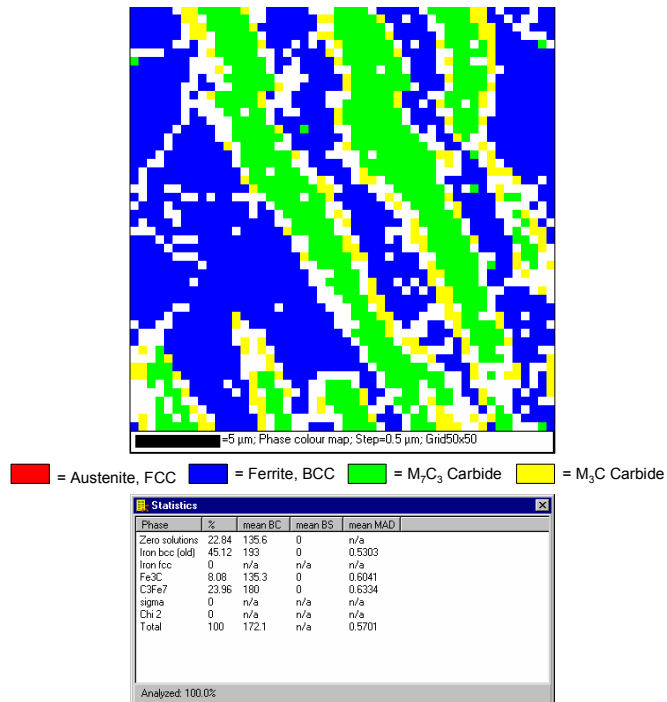


Figure 4.64: EBSD map for eutectic carbides in the white cast iron (Zone 4) of the vacuum cast composite.

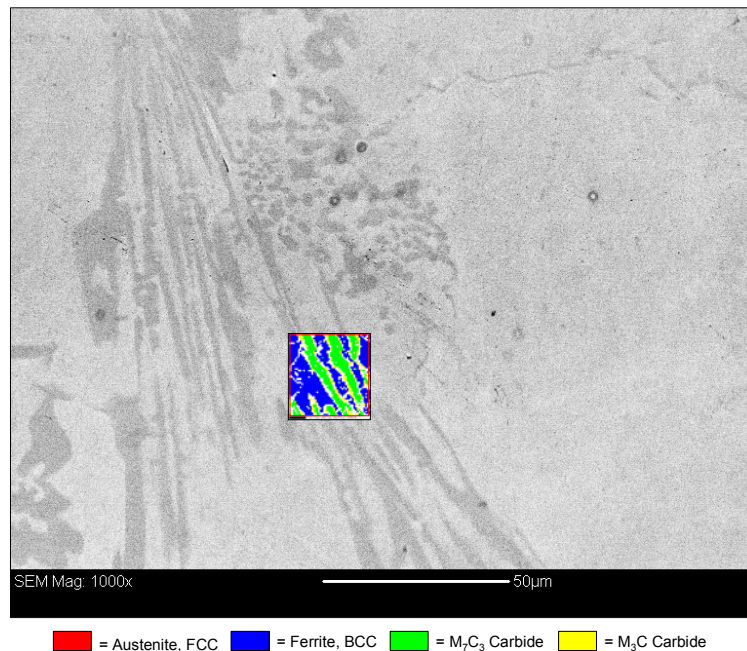


Figure 4.65: Overlay of EBSD map onto SE image for eutectic carbides in the white cast iron (Zone 4) of the vacuum cast composite.

4.4 DIFFUSION OF ELEMENTS ACROSS INTERFACE

A method of determining the success and quality of the bond between the vacuum cast white iron and the steel substrate is to measure the diffusion of alloying elements into the steel substrate and compare to theoretical diffusion rates based on the known concentration gradients.

The basic principles of diffusion and general equations are summarised in Appendix A [60].

The values for the diffusion coefficients, D_0 and the activation energy, Q_d have been published for many diffusion couples, and the values for carbon, chromium and nickel in austenitic steel are shown in Tables 4.7 to 4.9 along with the calculated diffusion coefficients for a range of temperatures using Equation A.4.

Table 4.7: Carbon Diffusion Coefficients in γ iron

$$\begin{aligned} D_0 &= 2.30E-05 \text{ m}^2/\text{s} \\ Q_d &= 1.48E+05 \text{ J/mol} \\ R &= 8.314 \text{ J/mol.K} \end{aligned}$$

Temperature		D (m ² /s)
(°C)	Kelvin	
1000	1273	1.944E-11
1100	1373	5.383E-11
1200	1473	1.298E-10
1209	1482	1.397E-10
1234	1507	1.705E-10
1259	1532	2.067E-10
1274	1547	2.314E-10

Table 4.8: Chromium Diffusion Coefficients in γ iron

$$\begin{aligned} D_0 &= 1.08E-03 \text{ m}^2/\text{s} \\ Q_d &= 2.91E+05 \text{ J/mol} \\ R &= 8.314 \text{ J/mol.K} \end{aligned}$$

Temperature		D (m ² /s)
(°C)	Kelvin	
1000	1273	1.237E-15
1100	1373	9.166E-15
1200	1473	5.173E-14
1209	1482	5.977E-14
1234	1507	8.843E-14
1259	1532	1.292E-13
1274	1547	1.612E-13

Table 4.9: Nickel Diffusion Coefficients in γ iron

$$\begin{aligned} D_0 &= 2.70E-04 \text{ m}^2/\text{s} \\ Q_d &= 3.00E+05 \text{ J/mol} \\ R &= 8.314 \text{ J/mol.K} \end{aligned}$$

Temperature		D (m ² /s)
(°C)	Kelvin	
1000	1273	1.322E-16
1100	1373	1.042E-15
1200	1473	6.202E-15
1209	1482	7.197E-15
1234	1507	1.078E-14
1259	1532	1.593E-14
1274	1547	2.002E-14

During the vacuum casting process, the white iron becomes liquid and creates a liquid/solid interface between the solid steel substrate. Providing surface wetting occurs, which is achieved through the minimization of surface oxidation of the steel within the vacuum/inert gas atmosphere, then the liquid white iron will begin to dissolve the steel substrate. The typical amount of steel dissolution resulting from the vacuum casting process is shown in Figure 4.66. In this example an average of 1.6mm of the internal steel wall thickness has been dissolved into the liquid white iron.

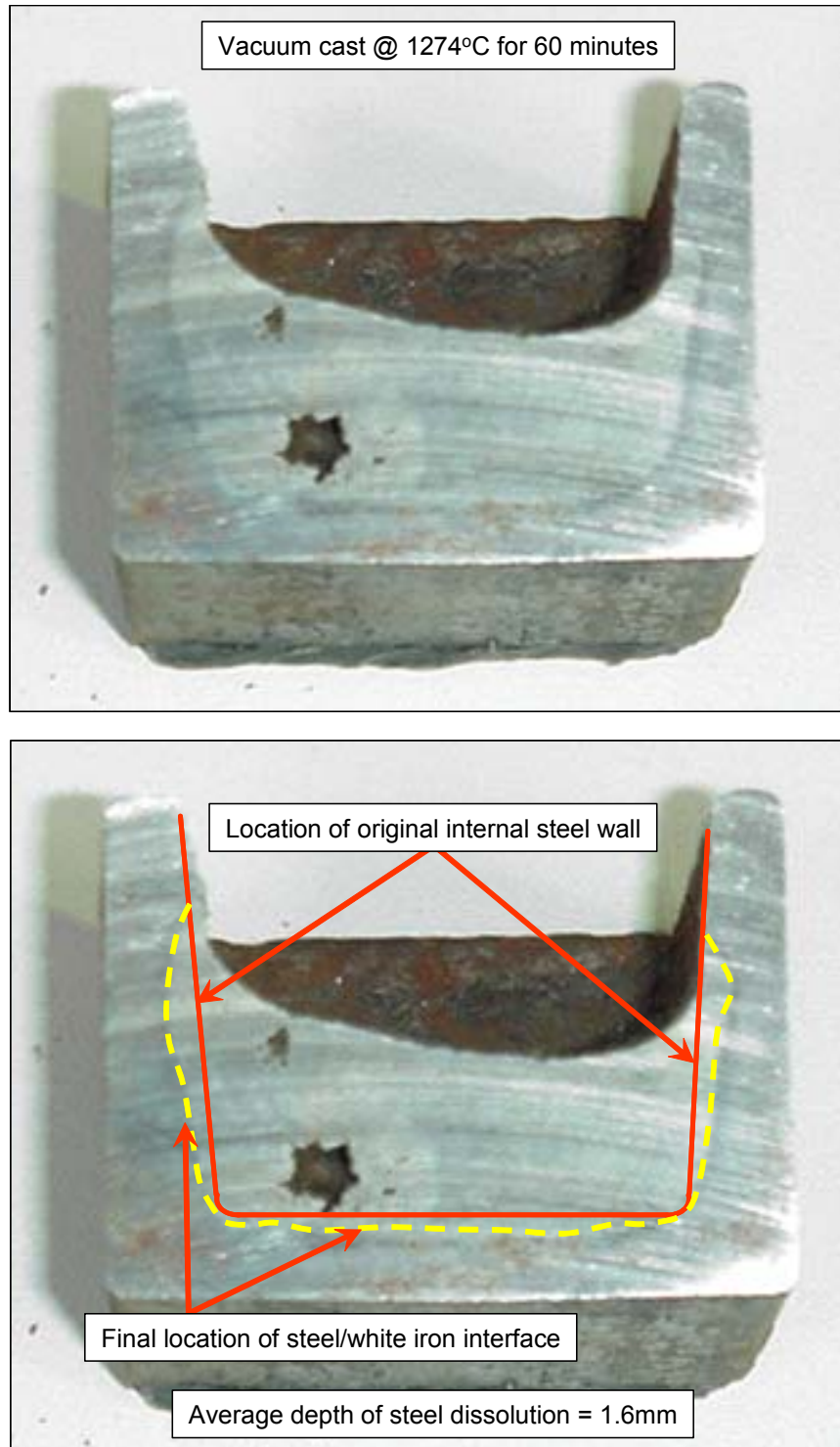


Figure 4.66: Typical steel dissolution as a result of the contact with liquid white cast iron during the vacuum casting process.

When the liquid white iron is in direct contact to the steel substrate, diffusion of elements will occur into the steel as a liquid/solid state diffusion process, and depending on the duration of the soak period at the melting temperature, the rate of the dissolving of the steel is competing with the diffusion rate of the elements such as carbon, chromium and nickel into the steel substrate. If the soak period is short and process temperature is close to the liquidus temperature of the white iron, negligible dissolution of the steel will occur, and the diffusion of elements will be essentially the direct result of the heat treatment process.

If the soak period is extended, and the process temperature is elevated significantly above the liquidus of the white cast iron, the significant dissolution of the steel surface will occur into the liquid white iron, removing the bulk of the diffusion zone prior to the cooling and resolidification of the alloy white iron.

The use of x-ray mapping has been an essential tool to enable the study of the diffusion process for the white iron / steel composite, and allows the compositional variations to be studied in detail as compared to single line profiles. Standard metallurgical analysis methods, such as optical microstructure phase analysis and microhardness profile testing are also valuable in demonstrating the amount and effect of the diffusion, however they are not capable of resolving with sufficient accuracy the depth of diffusion as compared to electron microscopy methods such as line profiles and x-ray mapping.

Figure 4.67 shows the comparison of microhardness and carbon content for the vacuum cast sample shown in Figure 4.66 above. The microhardness test results suggest the depth of carbon diffusion is approximately 1.25mm, whilst the compositional data obtained from carbon x-ray mapping shows the actual depth is closer to 2.1mm. A further example of the improved accuracy of the x-ray mapping compared to the microhardness data is shown in Figure 4.68 which also shows a difference between the predicted depths of diffusion.

It can also be seen by comparing Figures 4.67 and 4.68 that the longer soak and higher process temperature for the results in Figure 4.67 have resulted in a larger depth of diffusion compared to the zero soak and low process temperature shown in Figure 4.68.

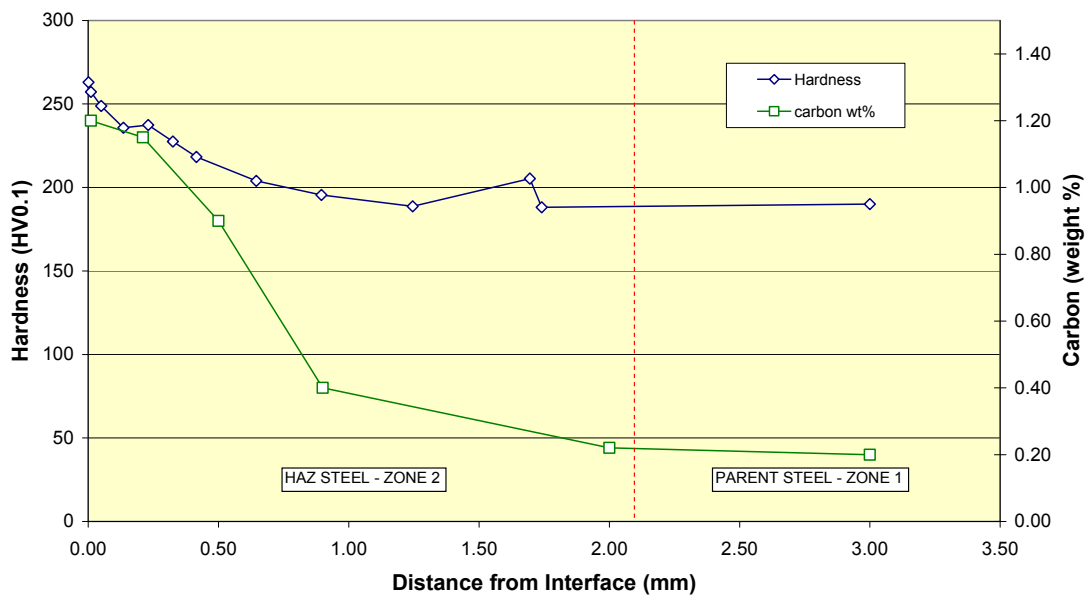


Figure 4.67: Comparison between microhardness and carbon content for diffusion away from the interface in the steel substrate for the vacuum cast white iron/steel composite produced at 1274°C with a 60 minute soak. (100g HV load used).

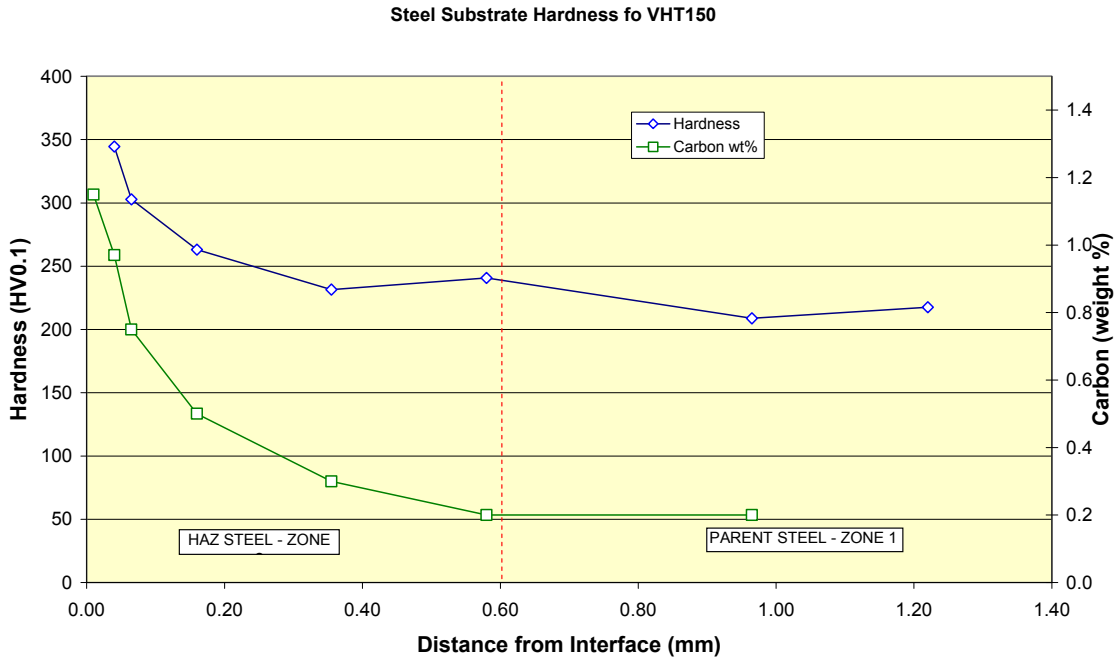


Figure 4.68: Comparison between microhardness and carbon content for diffusion away from the interface in the steel substrate for the vacuum cast white iron/steel composite produced at 1209°C with a zero soak. (100g HV load used).

Using the diffusion data in Tables 4.7 to 4.9 it is possible to calculate the expected elemental diffusion concentrations for the vacuum cast white irons.

The calculated diffusion data for the vacuum cast sample produced at 1274°C with a 60 minute soak is shown in Figure 4.69. The measured and calculated data for carbon compare favourably, and confirm in this case that the liquid/solid diffusion component of the process has been essentially re-dissolved as a result of the steel dissolution into the white cast iron. The resulting carbon diffusion profile is essentially the result of the solid state diffusion after the white iron has solidified.

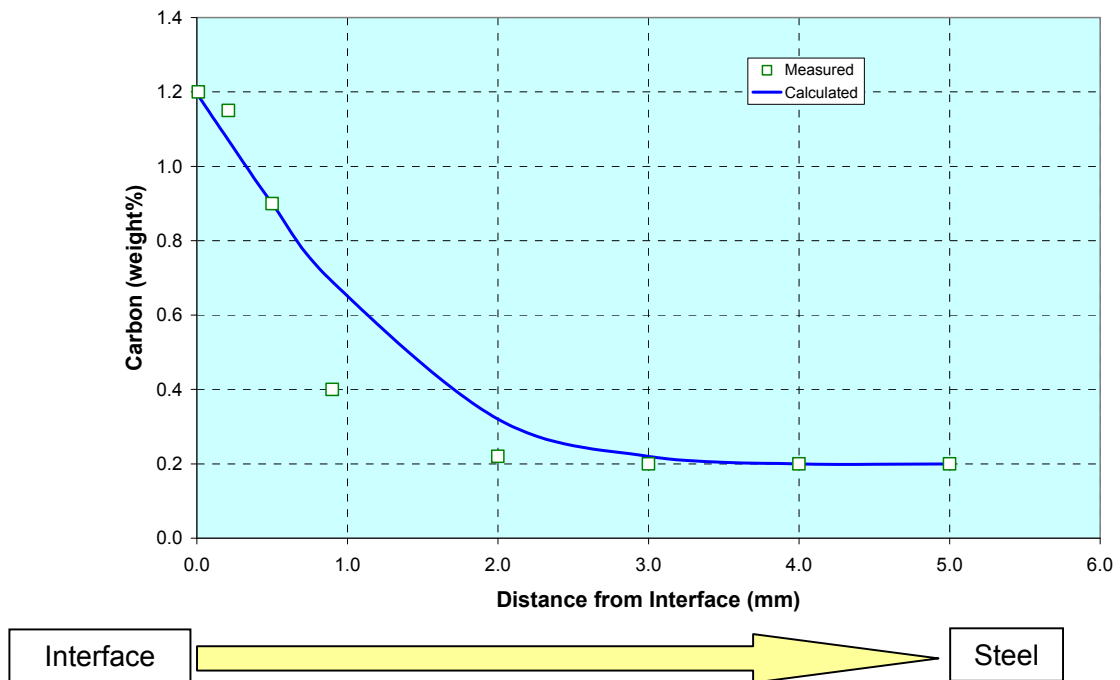


Figure 4.69: Comparison between measured and calculated carbon content in steel substrate adjacent to vacuum cast interface. Sample produced at 1274°C for 60 minute soak.

Figure 4.70 shows the calculated and measured carbon diffusion profile for the lower process temperature of 1209°C with a zero soak period. In this case there has not been sufficient time for significant melting of the white cast iron, and limited dissolution of the steel. The subsequent carbon diffusion profile is consistent with the solid state diffusion of carbon and the measured and calculated data compare favourably. The variation in measured carbon content at 1.00mm distance is most likely due to the presence of some liquid-solid state diffusion and the partial dissolution of the steel substrate into the liquid white cast iron prior to the solidification of the white iron.

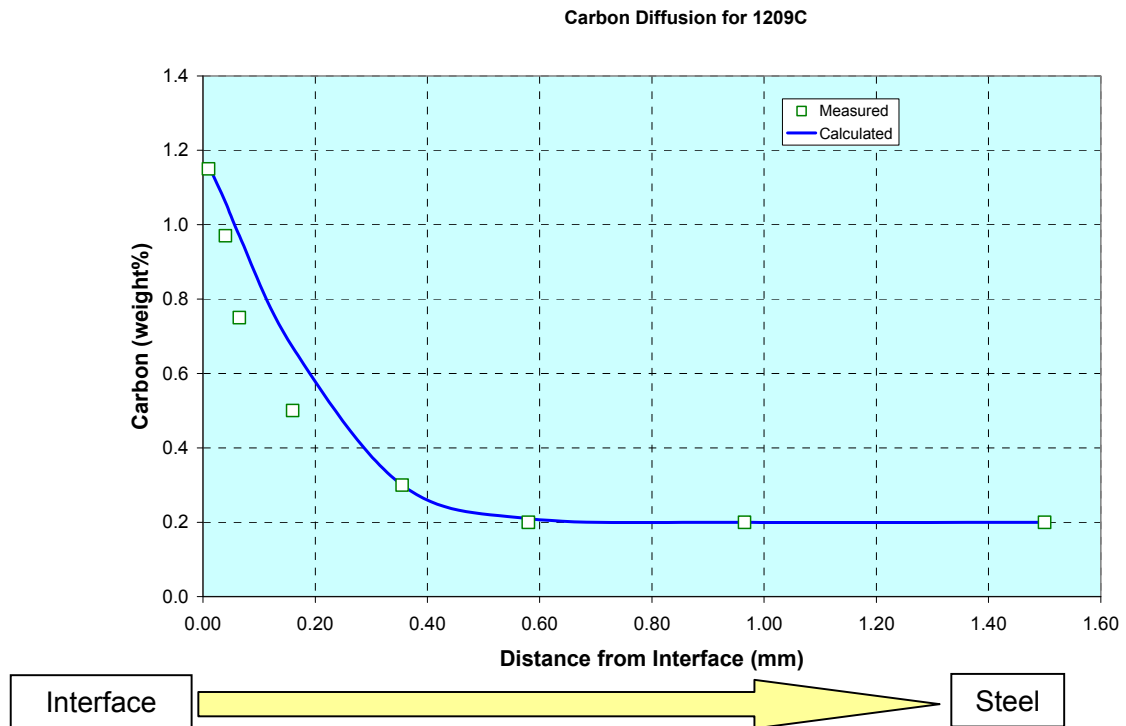


Figure 4.70: Comparison between measured and calculated carbon content in steel substrate adjacent to vacuum cast interface. Sample produced at 1209°C for zero soak.

Similar diffusion profiles comparing the measured and calculated diffusion composition curves have been conducted for chromium and nickel and are shown in Figure 4.71 and 4.72. The chromium and nickel diffusion curves show a consistent comparison between the measured and the calculated diffusion profiles.

The results of the diffusion calculations and measured x-ray mapping data demonstrate the classical non-steady state relationships represented by Fick's second law are a suitable method for predicting the compositional changes in the steel substrate resulting from the vacuum casting process.

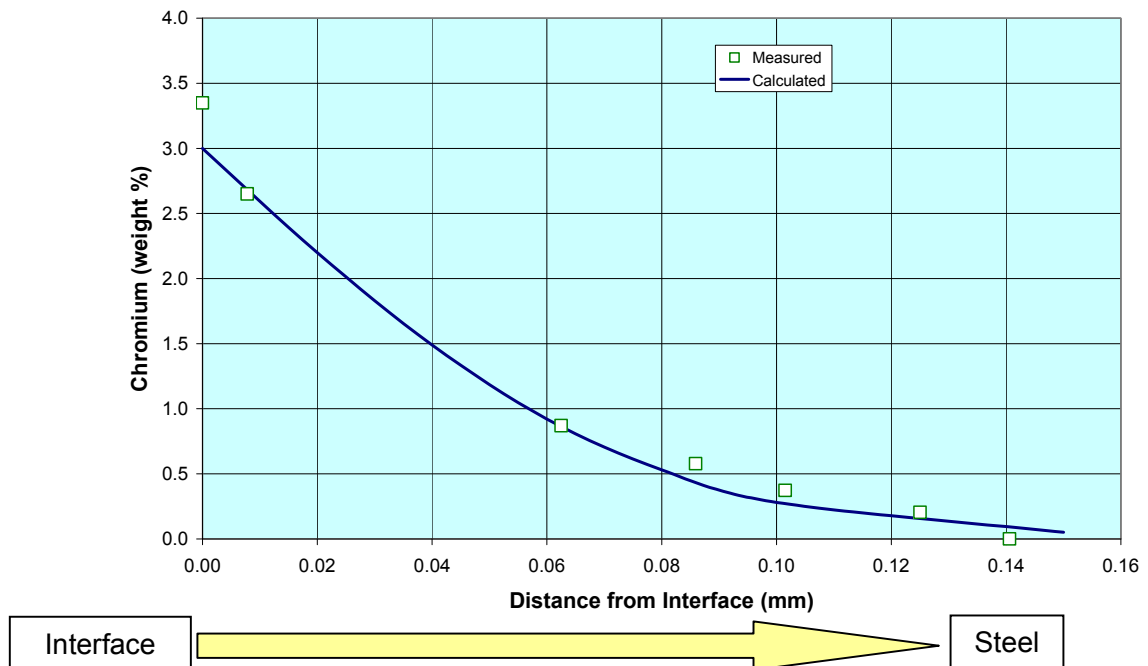


Figure 4.71: Comparison between measured and calculated chromium content in steel substrate adjacent to vacuum cast interface. Sample produced at 1274°C for 60 minute soak.

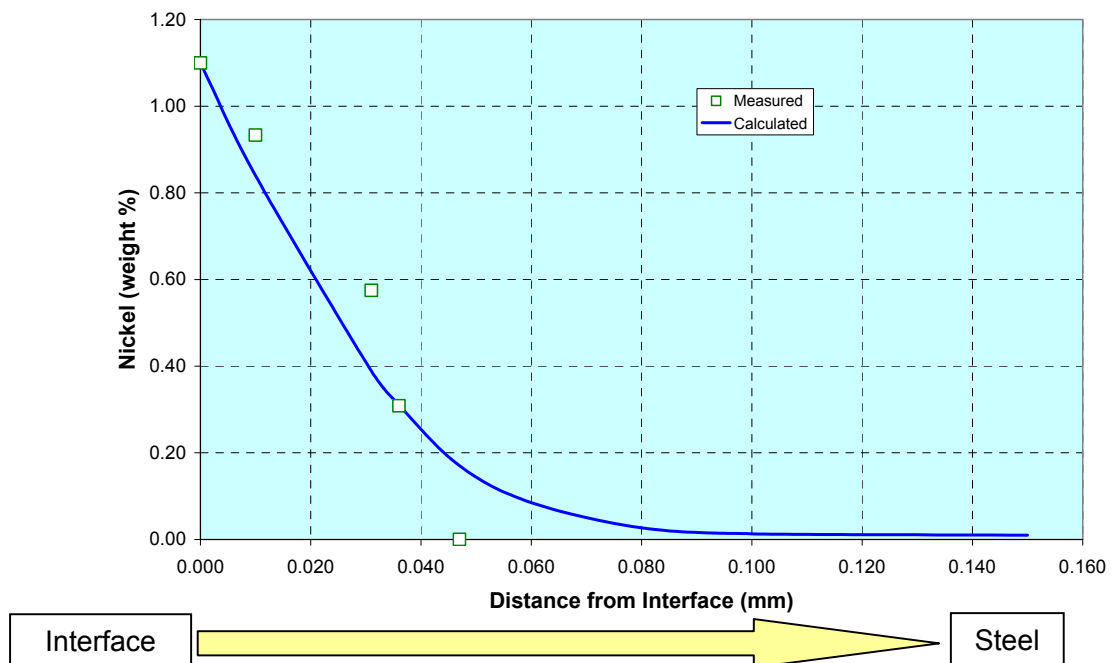


Figure 4.72: Comparison between measured and calculated nickel content in steel substrate adjacent to vacuum cast interface. Sample produced at 1274°C for 60 minute soak.

4.5 SUMMARY AND OUTCOMES

Optical and SEM imaging of the vacuum cast samples show the presence of four zones within the interface region, as previously discussed in Chapter 3 of this study. The higher resolution SEM imaging was able to show in detail the classical lamella structure for the pearlite present in the various zones of the composite alloys. The in-lens SEI obtained from the Zeiss Supra 555VP FEG SEM show clearly the compositional differences between the centre and the outside of the eutectic carbides, and this difference has been confirmed by both EBSD and x-ray mapping to relate to the formation of the quasi-peritectic M_3C carbide around the M_7C_3 carbides.

The use of x-ray mapping has proven to be an essential tool to allow the vacuum casting process to be understood and modelled with respect to chemical phases present and diffusion of elements into the steel substrate. The x-ray mapping has permitted a more detailed phase mapping to occur, and has precipitated the need to study the presence of various phases within the four interface zones by the use of EBSD mapping. The x-ray mapping, EDS data and line profiles all show a close correlation to the expected and stoichiometric phase chemical compositions. The carbon mapping requires further work to provide a higher level of accuracy, and was made difficult in this study due to the low concentrations of carbon in the steel substrate and white cast iron ferrous matrix.

EBSD mapping has allowed the crystal structure for the phases present within the vacuum cast samples to be determined with a high level of confidence. The results of the EBSD mapping show the following data:

- i. Zone 1 – original steel substrate, consisting of hypoeutectoid steel with BCC ferrite and pearlite (BCC ferrite and Fe_3C cementite);
- ii. Zone 2 – heat affected zone (HAZ) steel substrate consisting of pearlite (BCC ferrite and Fe_3C cementite) and some proeutectoid Fe_3C carbide;

- iii. Zone 3 – “carbide-free” area of low melting point white cast iron adjacent to interface, consisting of a ferrous matrix of pearlite (BCC ferrite and Fe₃C cementite) and retained austenite with intergranular M₃C carbide running perpendicular to the interface; and
- iv. Zone 4 – low melting point white cast iron, consists of M₇C₃ eutectic carbides which are surrounded by M₃C quasi peritectic carbides, with a ferrous matrix of pearlite (BCC ferrite and Fe₃C cementite) and retained austenite.

The results of the EBSD mapping are consistent with the expected results from the phase diagram analysis conducted in Chapter 2 of this study, and also consistent with the x-ray mapping conducted on the vacuum casting samples.

Diffusion calculations have been successfully compared to the measured diffusion profiles for carbon, chromium and nickel within the steel substrate, with a close correlation between the calculated and measured data. The presence of a classical non-steady state diffusion profile is consistent with a bonding process that has resulted in a high quality contact and diffusion joint.

CHAPTER 5

An important requirement for this study was to evaluate the composite white cast iron/steel wear parts in actual mining conditions by conducting field trials. A significant effort has been made to review published data on mining based field trials, and only a limited number of relevant articles could be found.

Review of patent data shows that a large volume of work within the wear parts industry has been conducted on developing technology for composite wear parts. The majority of these patents either deal with process based patents where the method of manufacture is unique or provides a unique product, or alternatively the design and materials used in the product provide some level of improvement over conventional wear parts.

Discussions with senior personnel at Westrac, a Western Australian distributor of Caterpillar (CAT) manufactured products and equipment suggests the issue of trialling composite parts, and any set of ground engaging tools (GET) for that matter, are more about overall performance of the equipment rather than just the wear life of the bucket teeth. The engine efficiency, fuel consumption, design loads and stresses are all claimed to be effected by the nature and wear of the ground engaging tools, and are related to the penetration performance, mass of the equipment, and material flow patterns into the buckets.

Based on the above issues of the effect of the GET on overall equipment performance, it is therefore difficult to define the success or failure of a given wear product purely on comparative mass loss and overall wear life. Understandably equipment manufacturers are therefore reluctant to provide detailed and quantified data on the performance of new GET, particularly with composites.

The following section of this study provides background to the types of materials used within the mining industry for GET and information from some published data on field trialling of GET components. The manufacturing of the prototype composite parts using the vacuum casting process is then detailed, and the field trial data for applications in dredging are provided.

5.1 PERFORMANCE OF EXISTING MATERIALS IN MINING APPLICATIONS

There are a range of wear materials used in the mining industry. A summary of the types of materials and their most common applications has been previously reported by Sare, Mardell and Hill [61], and is shown in Table 5.1

A study was conducted on the field trial performance of several white cast iron compositions on the wear rates of liner plate material [62]. The wear test data in Table 5.2 shows the liner plate relative wear rate changed with composition of the white iron, and the data presented showed the improved performance was the result of improved hardness of the wear plate after heat treatment.

In general ferrous metal alloys are used extensively across the mining industry due to their lower cost and ease of fabrication and repair compared to other materials. Elastomers and other polymers have begun to gain acceptance for use in chute liners and applications where heavy impact wear is experienced, and especially in slurry based applications.

Only limited data is available on published field trial performance of mining ground engaging tools (GET). A study by Mashloosh *et al* [63] on the wear of digger teeth was conducted to establish a correlation between laboratory wear tests and field data. Data from Pin-on-Drum wear tests [64] was found to produce similar wear ranking to the field trial data, and it was observed that the hardness of the steel was the major factor in controlling abrasion resistance.

Table 5.1: Summary of materials used in mining applications [61]

Information on material varieties and their characteristics		
Material class	Material sub-class	Application areas
White cast iron	High chromium	Casings, liners, chutes, hopper plates
	Chromium molybdenum	Cogs for rotor excavators, wet milling, pumps
	Weld-deposited hardfacings	Teeth, blades, liners, slurry piping, screen decks
Steel	Austenitic manganese	Pins, bushings
	AISI 1040-45	Slurry piping
	Tempered AR plate	Hopper plates, liners
	Martensitic	Teeth, pulleys, chain links
	Pearlitic	Liners
Alloys	Ni-Co alloys	High temperature piping, overlays, nozzles
Polyurethanes	Ester	Idlers, cyclones, screens
	Ether	Idlers, cyclones, screens
Natural rubber		Tyres, belts, hoses
Synthetic rubber	Nitrile	Oil seals, hoses, gaskets, linings
	Neoprene	Oil seals, hoses, gaskets, linings
	Silicone	Gaskets, cables
	Fluorocarbon	Gaskets, cables
	Ethylene propylene diene	Tyres, belts, hoses

Material class	Material sub-class	Application areas	Perceived advantages	Perceived disadvantages
White cast iron	High chromium	Casings, liners, chutes, hopper plates	High abrasion and erosion resistance, high hardness, superior corrosion	Moderate impact resistance
	Chromium molybdenum	Cogs for rotor excavators, wet milling, pumps	Corrosion-abrasion resistance	Toughness, fabrication and weldability limitations, cost
	Weld-deposited hardfacings	Teeth, blades, liners, slurry piping, screen decks	Excellent sliding abrasion resistance	Labor intensive, limited hardness
Steel	Austenitic manganese	Pins, bushings	High toughness, high work hardenability	Poor sliding abrasion resistance, embrittlement at elevated temperatures
	AISI 1040-45	Slurry piping	Cost, moderate impact-abrasion resistance	Low hardness
	Tempered AR plate	Hopper plates, liners	Moderate to good abrasion and gouging resistance, cost	Toughness, fabrication and weldability limitations
	Martensitic	Teeth, pulleys, chain links	Good impact-abrasion resistance, weldability	Low hardness
	Pearlitic	Liners	Good under impact-abrasive conditions	Poor corrosion-abrasion
Alloys	Ni-Co alloys	High temperature piping, overlays, nozzles	Oxidation and corrosion resistance, high hot-hardness	Cost, brittle nature
Polyurethanes	Ester	Idlers, cyclones, screens	Abrasion erosion resistance	Hydrolysis, operating temperature < 70°C
	Ether	Idlers, cyclones, screens	Abrasion erosion resistance	Poor high impact performance
Natural rubber		Tyres, belts, hoses	Tear, impact and abrasion resistance	Poor hydrocarbon and ozone resistance
Synthetic rubber	Nitrile	Oil seals, hoses, gaskets, linings	High hydrocarbon resistance, good abrasion and tear	Poor hydrocarbon, ketone, and ozone resistance
	Neoprene	Oil seals, hoses, gaskets, linings	High hydrocarbon resistance, good abrasion and tear	Poor solvent and acid resistance
	Silicone	Gaskets, cables	Low temperature flexibility	Poor petroleum product and abrasion resistance
	Fluorocarbon	Gaskets, cables	Chemical resistance, operating temperature range	Poor ketone resistance
	Ethylene propylene diene	Tyres, belts, hoses	Excellent resistance to hydraulic and silicone fluids	Poor petroleum product resistance

Table 5.2: Relative wear rates for white cast irons used for liner plates [62]

TABLE 5. Relative wear rates of the field liner tests and dry-sand-rubber wheel tests (reference sample, 16.5Cr-1.5Mo iron)

Wear test	Relative wear rate		
	10Cr-3.5Ni iron	16.5Cr-1.5Mo iron	15Cr-3Mo iron
Field liners, central	1.18	1	0.50
Field liners, bottom	1.64	1	0.50
DSRW	1.32	1	0.76

Heat treatment of the steel to produce high surface hardness [65] has also provided increases in wear life for bucket teeth. The wear of steels under abrasive wear modes with granular abrasive material decreased with increasing steel hardness.

Excavator bucket teeth in operation within open pit mining environments undergo significant gouging abrasion, and the comparison of wear rates to laboratory tests using smaller abrasive particles such as the Dry Sand Rubber Wheel test [66] may not be applicable. A typical example of an excavator in operation and the bucket teeth used are shown in Figures 5.1 and 5.2.

In a study by Fernandez *et al* [67], the laboratory and field trial wear data were compared for excavator teeth used on a large bucket-wheel excavator. The data summarized in Tables 5.3 and 5.4, and Figure 5.3 show a significant variation in wear rates irrespective of the limited range in overall hardfacing layer hardness. The laboratory and mine based wear test data shown in Table 5.4 show a close correlation between the ranking of the materials. These results suggest laboratory wear test data can provide a guide to the relative wear performance of the actual ground engaging tools (bucket teeth).



Figure 5.1: Excavator application in open pit mining



Figure 5.2: Typical bucket tooth installation on large mining excavator bucket

Table 5.3: Abrasive wear rates for hardfacing alloys [67]

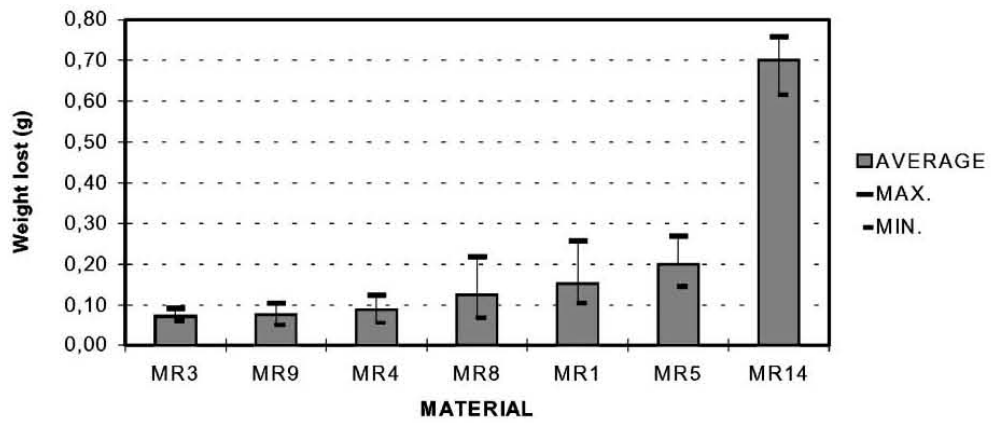


Table 5.4: Summary of wear part life for laboratory and mine based testing

Materials duration in comparison with MR5, in field and laboratory, and hardness (HRC) of material^a

Material	Duration (% MR5)						Average hardness
	Laboratory			Mine			
	Average	Maximum	Minimum	Average	Maximum	Minimum	
MR1	14866	19961	11766	9841	39257	5166	62.2
MR3	31139	34129	22833	14199	66065	6159	64.7
MR4	21954	34027	15882	12579	21597	6921	65.6
MR5	10000	14310	7112	10000	20023	5417	62.1
MR8	15830	30101	12416	10136	19870	4195	62.7
MR9	26152	39817	18512	11506	20437	5427	62.7
MR14	3005	3507	2724	9869	20237	2642	66.1

^a The laboratory–field duration correlation: 0.85.

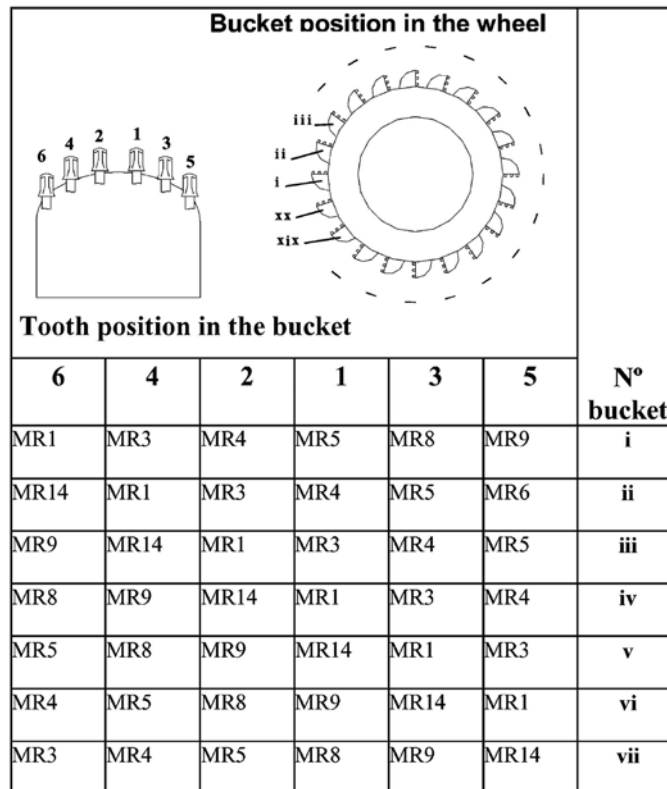


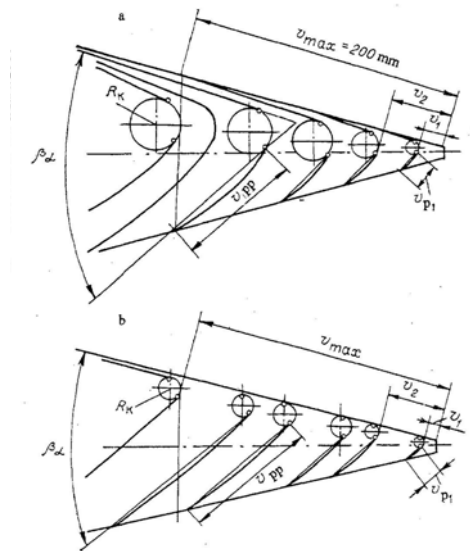
Fig. 11. Disposition of 42 teeth in seven buckets, indicating respective material name.

Figure 5.3: Bucket teeth test position

Further work by Polovinko and Fedulov [68-70] has been conducted to understand the wear kinetics of steel bucket teeth in mining applications. In general it was observed that wear rates for excavator bucket teeth decreased with increasing steel hardness. The wear patterns of the bucket teeth were measured during the course of the trials, and a summary of the measured wear geometries is shown in Figure 5.5.

There is some suggestion within the literature that a better understanding on the performance of bucket teeth would be provided by a pendulum groove test. [71,72]. The pendulum groove test was used to rank several materials based on their resistance to high stress gouging abrasion, and the data is summarized in Table 5.5.

Work conducted by Liu, Li and Man [73] on pendulum groove testing of Nihard alloys showed the energy of the wear and the microstructure of the white iron were related.



(a) bedrock, (b) frozen large-block rock; v_1 , v_2 and v_{max} are linear tooth wear, v_{p1} and v_{p2} are the wear platform sizes; R_K is the radius acquired by the cutting edge; β_α is the acquired sharpening angle [after Polovinko and Fedulov]

Figure 5.5: Geometry of the wear of excavator bucket teeth [68]

In a study by Sare *et al* [74], the wear rates for rotating impact crusher bars were shown to decrease with decreasing carbide volume fraction and increasing material hardness. The results of this study suggest the impact resistance of high carbide volume fraction white irons is poor compared to low carbide volume fraction hypereutectic white irons, having more primary austenite dendrites within the microstructure.

The performance of surface coatings on bucket teeth in field conditions has been reported by Polovinko and Fedulov [69, 70]. The study found that adding a coating of wear resistant hard facing had the potential to increase the wear life from between 1.4 to 2.0 times compared to the original steel material.

Table 5.5: Summary of pendulum groove test data [71]

Sample	Steel Alloy	Hardness (HV)	Relative Abrasion Resistance	
			Field Testing	Pendulum Groove
1	0.35C,1.3Cr	545	1.00	1.00
2	0.3C,1.4Cr	510	0.90	0.90
3	0.4C,5.3Cr,1.4Mo,1V	560	1.25	1.15
4	0.33C,3Cr,1Mo,0.3V	430	0.95	0.98
5	0.25C,0.6Cr	505	0.75	0.82

Fernandez *et al* [67] showed during field trials that overall wear performance was a function of the location of the wear parts on the bucket. The data shown in Figure 5.6 shows the teeth located in the centre of the bucket experience a faster wear rate compared to the outside teeth. The study by Fernandez *et al* suggested their results would be true for bucket-wheel style excavators, however historically hydraulic excavators and shovels with a single bucket tend to experience higher wear rates for the outer bucket teeth, and slower rates for the centre teeth.

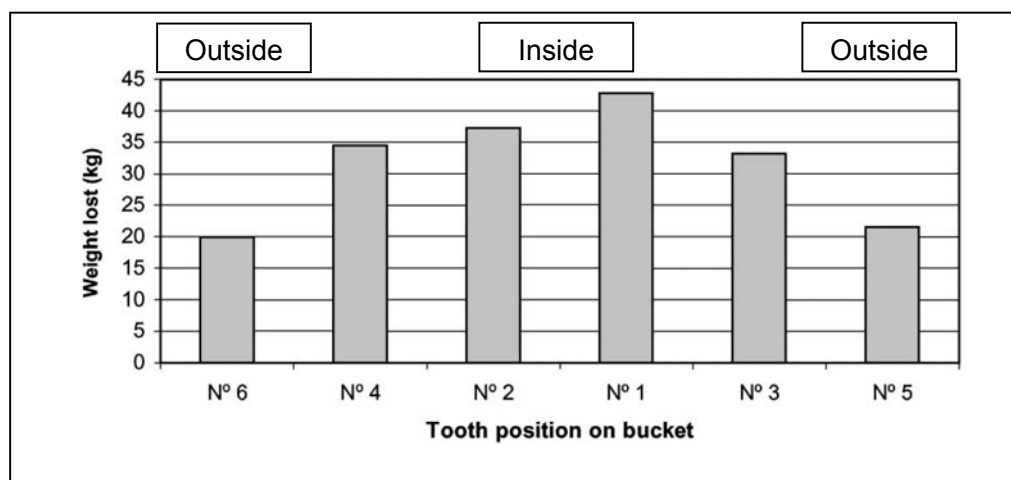


Figure 5.6: Effect of bucket tooth position on wear rate for bucket-wheel excavator trials [67]

A guide to the types of wear experienced on ground engaging tools is presented in Figure 5.7. The bucket teeth used on excavators would be characterized as experiencing high impact and high stress gouging abrasion. Applications such as chute liners and wear pads experience low impact and high sliding abrasion.

In open pit mining, at the start of operations the ore is typically weathered and exhibits a high degree of fracturing, and is relatively soft compared to unweathered rock. As the mining progresses the ore moves into the transition zone, becoming less fractured and harder. At the base of the mining operations, the ore is unweathered and commonly termed “blue rock”, exhibiting low degree of fracturing

and low weathering. These mining zones are shown diagrammatically in Figure 5.8. Excavator applications in the weathered zone are normally low impact and often associated with “free-digging” of the excavator, and not requiring specific drill and blast operations. These types of operations in the weathered zone are also often over-burden stripping applications.

There is a high potential to use composite excavator teeth in the weathered zone applications, where the low degree of impact will be better suited to the potentially lower impact strength of composite bucket teeth. Another application where impact stresses are lower compared to excavator applications are the bucket teeth used on front end loaders.

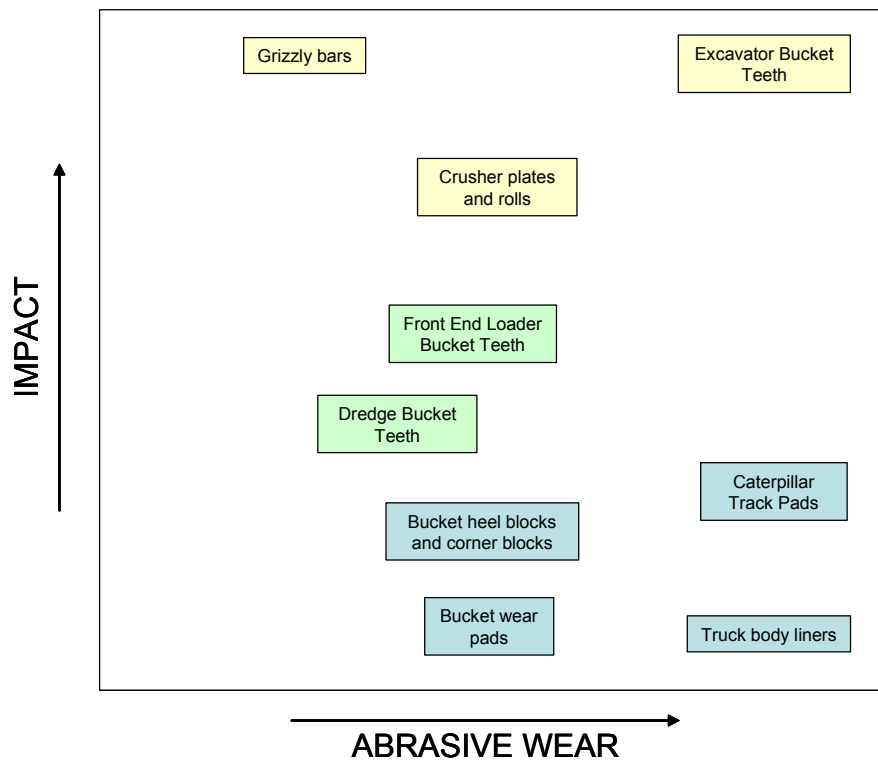


Figure 5.7: Relationship of wear and impact levels for different mining applications

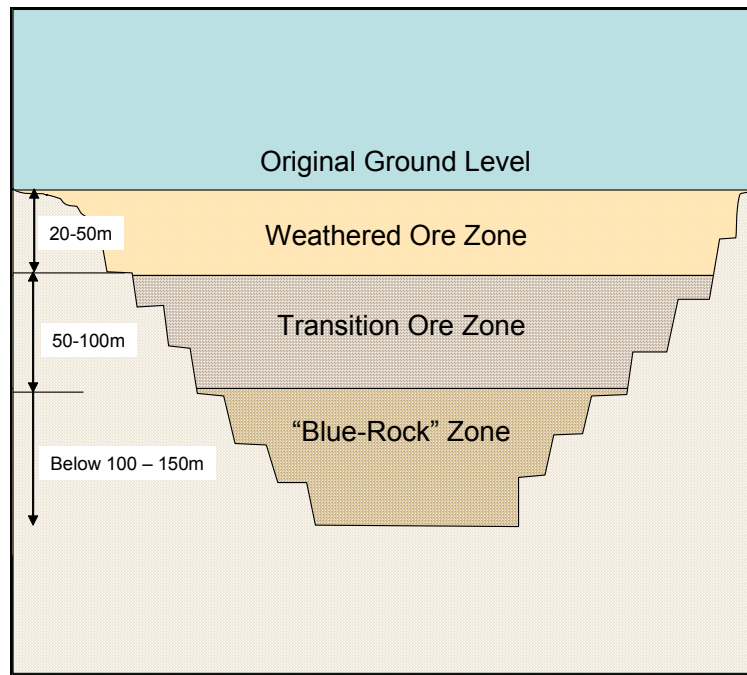


Figure 5.8: Types of rock zones experienced in open pit mining operations

5.2 MANUFACTURE OF PROTOTYPE PARTS

The aim of the prototype production was to produce representative samples for field trial evaluation in direct comparison to existing wear parts. Several types of parts were manufactured to enable the evaluation of the composite white cast iron/steel components in different applications, including:

- i. Composite bucket tooth for use on a suction-cutter dredge used for mineral sands mining;
- ii. Composite wide bucket lip for use on a suction-cutter dredge used for mineral sands mining;
- iii. Composite excavator bucket tooth tip
- iv. Composite wear bars for general abrasion protection of bucket undersides

Prior to conducting field trials on composite parts, it was considered necessary to test a full sized non-composite part produced using normal foundry methods from white cast iron to confirm potential performance and issues of toughness.

Following the testing of the full sized non-composite bucket tooth in white iron, the next stage of testing was to manufacture and trial a single laminate and multi-laminated vacuum brazed sample, which would have combination of wear resistance and toughness, and could be potentially compared to the vacuum cast products. The vacuum brazed parts were trialled as they represented composite parts that could be produced using existing technology and equipment.

5.2.1 MANUFACTURE OF FULL WHITE IRON EXCAVATOR BUCKET TOOTH

In order to answer the question as to the potential performance of a full white iron bucket tooth in excavator applications (considered to be high impact, gouging abrasion), several teeth were cast to suit a Komatsu PC1000 excavator, being the part equivalent to an ESCO V66RDX bucket tooth. The standard ESCO V66RDX bucket tooth is manufactured from a medium carbon chromium/molybdenum steel, and is typically hardened by quench and temper prior to use, providing a balance of impact toughness and wear resistance for general mining conditions.

Charges of Cr27 white cast iron were melted in a 75kW high frequency induction furnace with an 80kg tilt furnace, and poured into resin-bonded silica sand moulds with a superheat at time of pouring of 100°C to simulate standard foundry conditions. The castings were allowed to cool to room temperature prior to removing from the sand moulds and fettling. A finished white cast iron bucket tooth is shown in Figure 5.9 and shown compared to the original ESCO V66RDX bucket tooth in Figure 5.10.



Figure 5.9: Full white iron cast bucket tooth (equivalent to ESCO V66RDX tooth)



Figure 5.10: Comparison of cast white iron and cast steel bucket teeth

5.2.2 MANUFACTURE OF LAMINATED WHITE IRON/STEEL BUCKET TOOTH

The full sized non-composite white iron bucket tooth failed on the excavator application as the tip cracked and fractured after only one hour of operation (see Section 5.6.1 later in this Chapter). The failure of the brittle white cast iron component was believed to be the result of low impact toughness. It was decided to determine the effect of having a laminated composite bucket tooth produced by vacuum brazing a plate of white cast iron onto the machined face of the standard chromium/molybdenum steel bucket tooth. Using the steel bucket tooth as a substrate would provide excellent impact toughness, whilst the white cast iron would provide high wear resistance.

Two V66RDX bucket teeth were machined across the front face of the part as shown in Figure 5.11 to a tolerance/flatness of 0.1mm to enable vacuum brazing of a white cast iron wear plate to the surface.

Each part was vacuum brazed using a copper brazing paste at a temperature of 1120°C for 60 minutes and allowed to furnace cool to 1000°C, followed by forced gas quenching to room temperature.



Figure 5.11: Machined V66RDX steel bucket tooth ready to vacuum braze white iron wear plate on front tip

Following the limited success of the field trial (see Section 5.6.2 later in this Chapter) on the Komatsu PC1000 excavator at Greenbushes for the vacuum brazed single wear plate, a more complex multi-laminated wear tip was produced for trial.

The multi-laminated wear tip consisted of three layers of Cr27 alloy white cast iron sandwiched with two layers of manganese steel, as depicted in Figure 5.12. The white cast iron and manganese steel layers were cast using standard foundry

methods into resin-bonded silica sand moulds, then surface ground as required to a tolerance of 0.100mm flatness. The middle layers required machining on both mating surfaces.

The assembled sandwich composite was placed on a support frame as shown in Figure 5.12, then vacuum brazed at 1120°C for 60 minutes using copper brazing paste. The furnace was allowed to cool to 1000°C prior to removal and allowed to air cool to room temperature.

The final brazed multi-laminate wear tip is shown in Figure 5.13. The size of the wear tip was manufactured to suit an ESCO V71RDX bucket tooth.

The final brazed laminate was then welded to a previously sectioned bucket tooth using austenitic welding wire to produce a full composite wear part for trial testing.

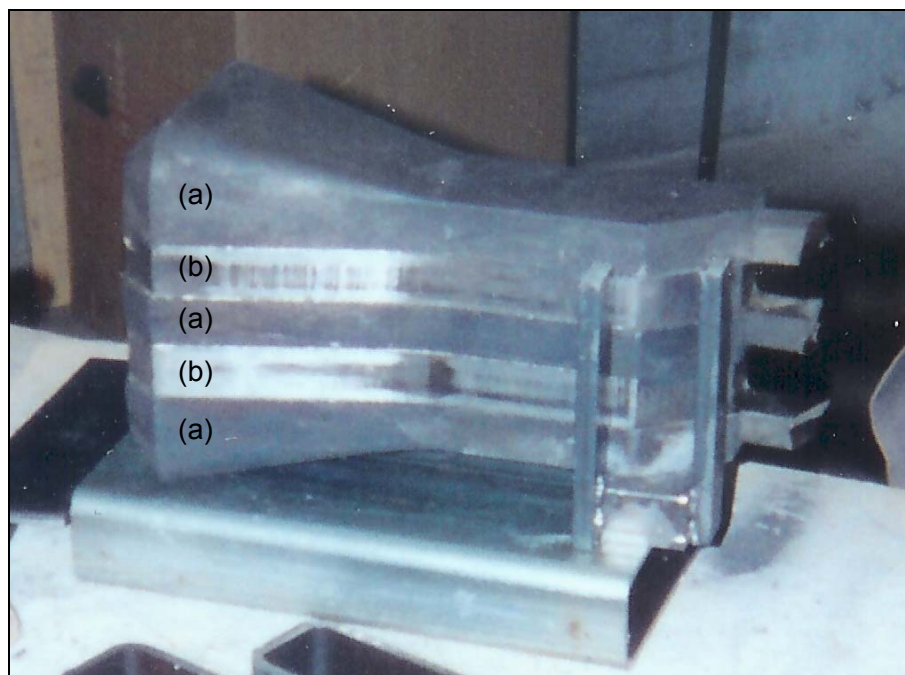


Figure 5.12: Multi-laminate bucket tooth tip. Layers of white cast iron (a) laminated with manganese steel (b)



Figure 5.13: Finished vacuum brazed multi-laminated bucket tooth tip.

Details of the field trialling of the multi-laminated bucket tooth tip are provided in Section 5.6.2 later in this Chapter.

The outcome from the field wear testing of the vacuum brazed samples was as follows:

- The single layer brazed composite provided a modest 10-15% wear life improvement
- The multi-layered tip failed after 10-12 hours of operation with the welded joint cracking and the tip falling off.

The manufacture of the vacuum brazed parts was technically difficult and at a high cost considering the machining required at high tolerances to achieve a suitable end-product. The vacuum brazed samples were not considered to be a commercially viable solution for the application of ground engaging tools.

The development of the vacuum casting process was seen as a method for producing a commercial product with a combination of high toughness and wear resistance, and with a reasonably low cost of production.

5.2.3 MANUFACTURE OF DREDGE SMALL BUCKET TEETH

In order to test the composite parts manufactured from the new vacuum casting process, an application was selected for a suction-cutter dredge bucket tooth. The dredge bucket teeth are relatively smaller compared to larger open pit mining equipment, and therefore presented an opportunity to establish a small pilot plant production facility. The standard part that was used by the client was an ESCO V19TY style bucket tooth, and a new and worn part is shown in Figure 5.14.

The ESCO part design and attachment system incorporates a patented helix-shaped twist locking mechanism, which would have been too complicated to replicate and potentially infringing the intellectual property owned by ESCO USA. To enable the trial parts to be produced it was decided to reuse the worn ESCO V19TY bucket teeth, and vacuum cast the extra white iron material over the worn part to produce a recycled new composite tooth.

The client who was located at the Jangardup Mine, near Capel, Western Australia, provided approximately 20 worn bucket teeth to permit production trials to proceed.



Figure 5.14: New and worn original Cr/Mo steel dredge bucket teeth (ESCO V19TY)

The worn bucket teeth were grit blasted to remove any residual rust/oxide and to provide a clean surface for bonding to the white iron.

Steel moulds were produced based on the method shown in Section 3 of this study, and the inside of the mould coated with a ceramic layer of magnesite refractory paint (Foseco Isomol Red) to prevent the liquid white iron bonding to the mould. Each worn steel part was then weighed and the white iron charge for each sample calculated on the basis of a required finished mass of the composite part of 3.0kgs.

The worn steel part was then positioned in the mould using a coated steel plate which slides into the locking pin arrangement on the worn part. The white iron charge was then positioned into the side chute of the mould, and whole assembly was placed onto a steel grid/tray to enable loading into the hot walled vacuum furnace. The moulds with white iron charge loaded on the furnace tray are shown in Figures 5.15 and 5.16.

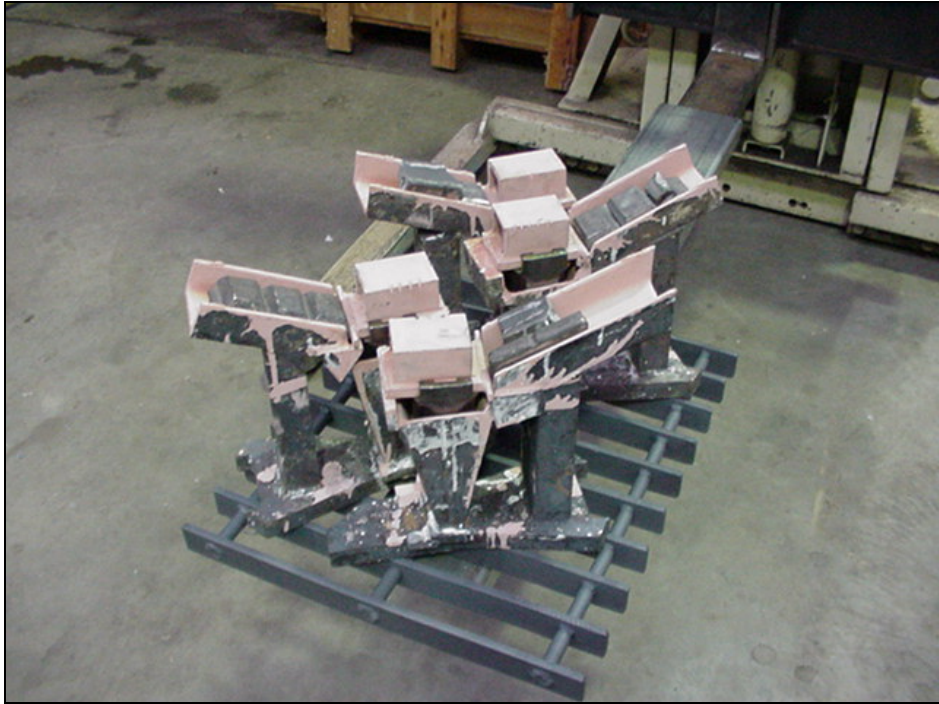


Figure 5.15: Steel moulds coated with refractory ceramic paint, with steel parts inserted and measured white iron charge positioned in side chutes.



Figure 5.16: Closer view of steel part positioned with steel plate, and white iron charge located in side chute

The set of moulds was then positioned into the hot walled furnace using an electric forklift, and the chamber closed and pumped down to a vacuum of 0.1mbar (see Figures 5.17 to 5.19).

The vacuum casting cycle was then run with a ramp at full power to a temperature of 1100°C, at which time the vacuum valve was closed and a partial pressure of nitrogen introduced into the furnace chamber to increase the pressure to 200mbar. The furnace temperature was then increased to the soak temperature of 1250°C, and held at this temperature for a period of 60 minutes to allow the liquid white iron to dissolve and bond with the solid steel parts. As the white iron melts, it flows down the chute into the mould cavity until the full white iron charge has melted.



Figure 5.17: Loading the hot walled vacuum furnace with trial composite white iron/steel parts in steel moulds

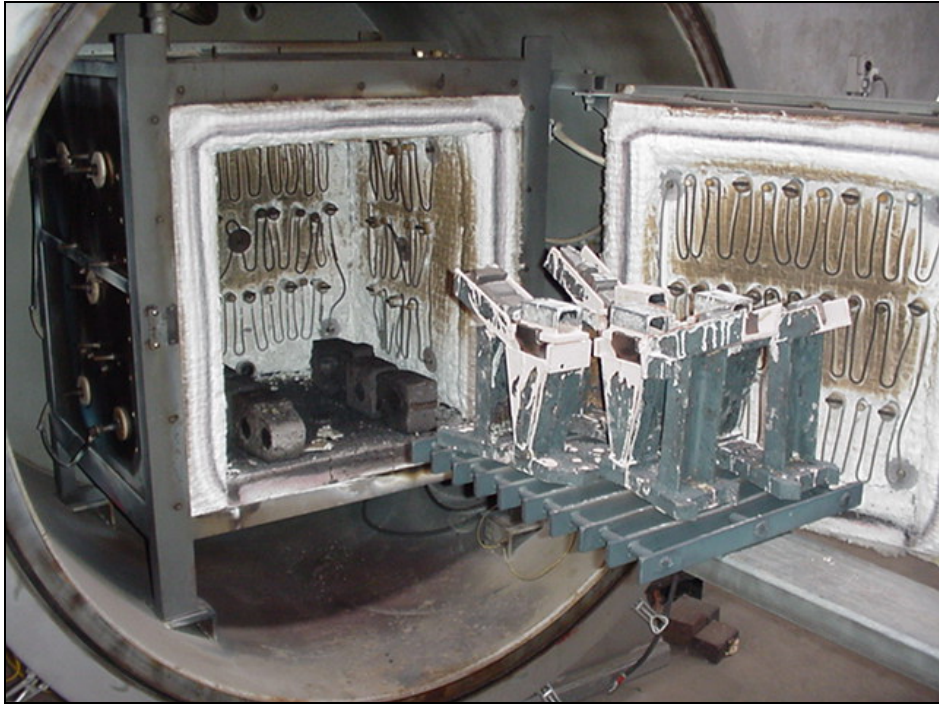


Figure 5.18: Close up view of hot walled vacuum furnace showing arrangement of steel moulds on furnace tray prior to final placement



Figure 5.19: View of multiple steel moulds for composite white iron/steel parts placed into hot walled vacuum furnace

After the completion of the 60 minute soak, the furnace was allowed to cool to a temperature of 1000°C, at which point the vacuum chamber was vented to atmospheric pressure, and the furnace load removed and placed on refractory bricks for air cooling.

The final cooled parts were then removed from the mould, lightly cleaned to remove any residual ceramic paint, then painted ready for trial. Examples of the finished parts are shown in Figures 5.21 to 5.23.

It is significant to note that no standard foundry methoding has been used to produce the composite parts. There are no in-gates, runner bars, down sprues and shrinkage feeders, yet the castings have been completed without the presence of any porosity, and the final castings as removed from the mould did not require any fettling to remove feeder blocks, and in-gates. Since there are no major additions of standard casting feeders, the casting yield for the process is very high. There is typically a very small amount of white iron surface skin left in the mould chute, weighing in this case typically less than 20 grams. The casting yield is therefore in the high 95% range.

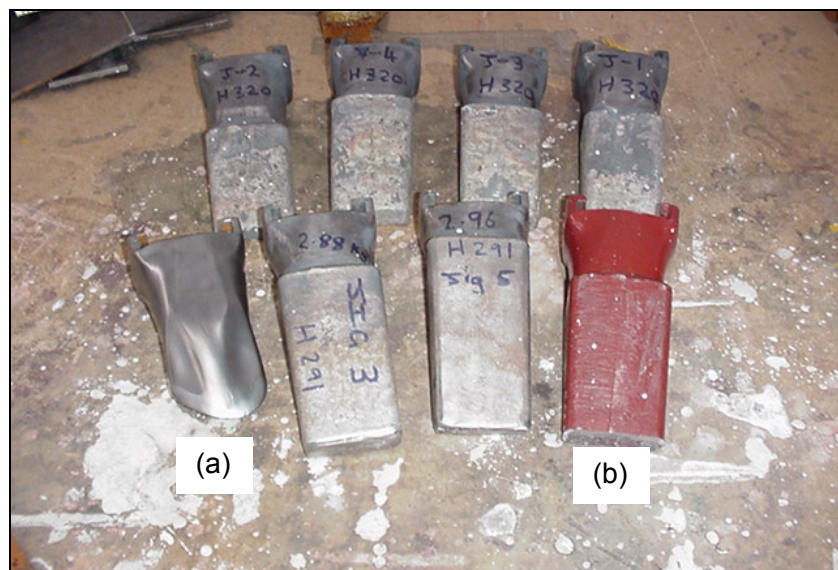


Figure 5.20: Several finished composite white iron/steel bucket teeth with original worn steel part (a) and painted composite part (b)

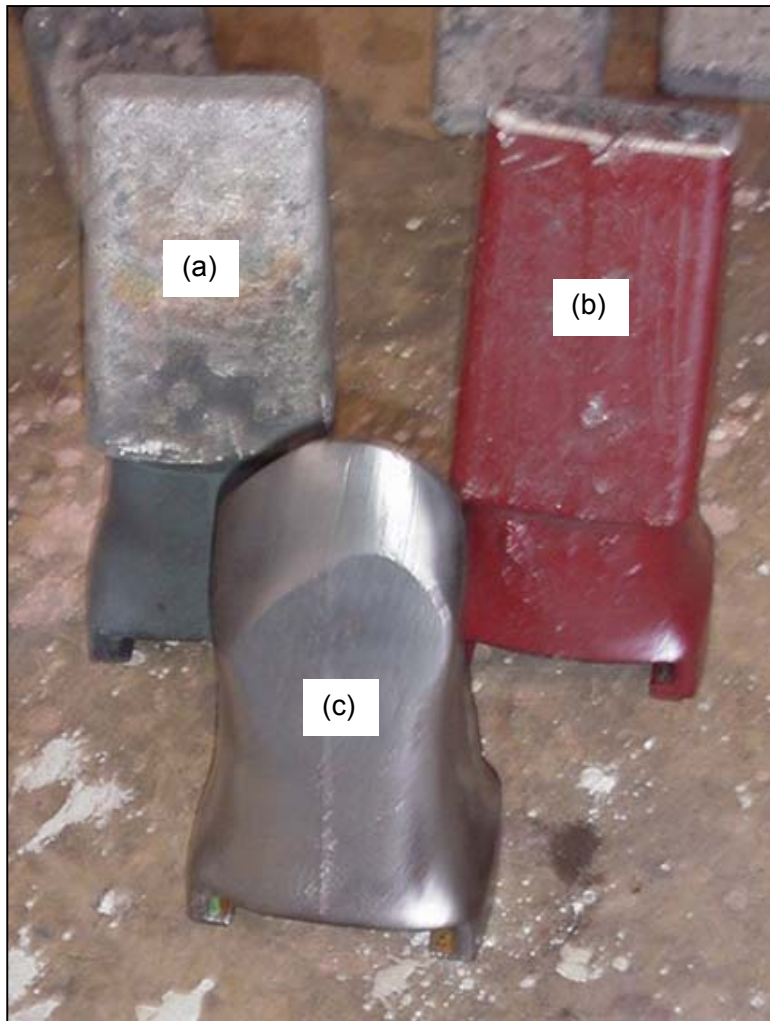


Figure 5.21: Detail of finished composite tooth (a), painted composite tooth (b) and original worn Cr/Mo steel tooth (c)

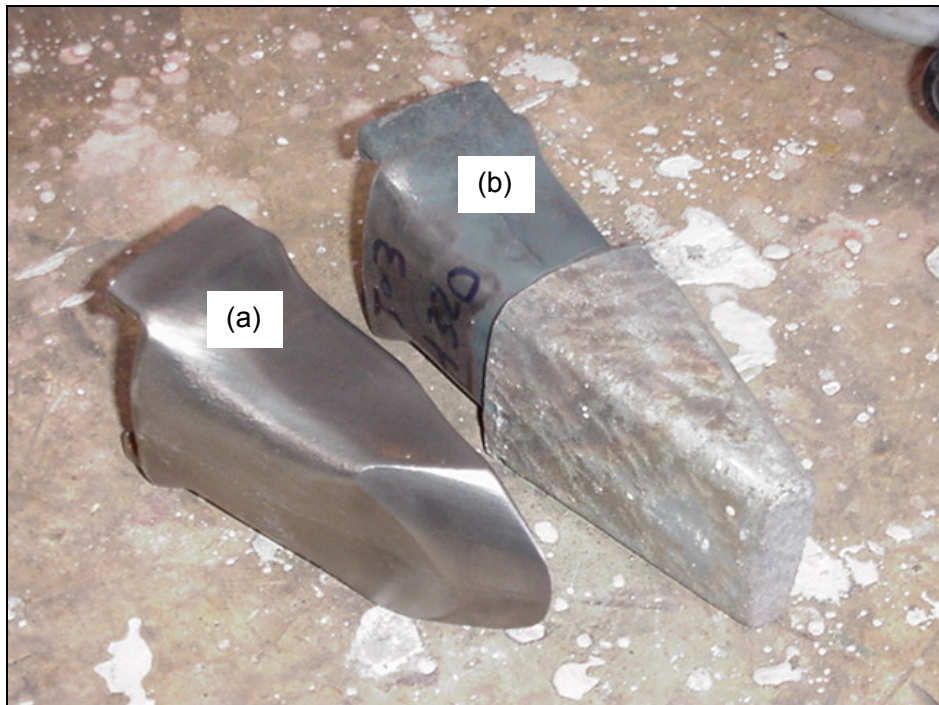


Figure 5.22: Detail view of comparison between worn original Cr/Mo steel bucket tooth (a) and new composite white iron/steel bucket tooth (b)

The steel moulds after use in the vacuum casting cycle were then grit blasted and cleaned, then re-coated with the refractory paint ready for the next furnace cycle. The hot walled vacuum furnace was capable of fitting five moulds for a given cycle. Based on the production trials with these small parts, it would be expected that at least 200 or more cycles could be achieved using the metal moulds using a vacuum based system.

The vacuum casting process with these steel moulds provides a cost effective means for producing a composite white iron/steel bucket tooth.

5.2.4 MANUFACTURE OF WIDER COMPOSITE DREDGE BUCKET TOOTH

Based on the original ESCO V19TY bucket tooth, a slightly wider tip style was requested by the client at the Jangardup Mine. The worn steel castings and moulds were prepared following the same method as outlined in Section 5.2.3 of this study. The prepared mould ready for inserting the steel part is shown in Figure 5.23, and with the steel part positioned in Figure 5.24.

The mould, steel part and white iron charge were then placed into the hot walled vacuum furnace and the cycle operated as described previously in Section 5.2.3.



Figure 5.23: View of steel mould with ceramic coating on inside surfaces to assist with stopping bonding of white iron to the steel mould



Figure 5.24: View of steel mould with steel part positioned using retaining plate. White iron charge is weighed and placed into chute on the right of the mould. During the heat treatment cycle, the white iron melts and flows down the chute and fills the mould cavity coming into contact with the steel part.

After the part had cooled, it was removed from the steel mould and is shown in Figures 5.25 to 5.28. The original steel part as-received from the mine site is shown alongside the new composite part in Figures 5.27 and 5.28.

Note from Figure 5.26 the undercutting of the steel surface resulting from the dissolution process with the liquid white cast iron. The strong degree of surface wetting between the steel and white cast iron is demonstrated by the meniscus shown at the joint. The part as-removed from the mould shows negligible oxidation of the bulk steel section, and therefore the original steel thickness for the areas of the adapter fitting are maintained. The surface finish of the white cast iron is also excellent being in contact with the ceramic coated steel mould. The steel mould is in perfect condition after removal of the finished part, as shown in Figure 5.29.



Figure 5.25: Completed wider tip composite part after removal from the metal mould



Figure 5.26: Side view of wider tip composite white iron/steel bucket tooth



Figure 5.27: Original as-received steel part and new wide tip composite wear part



Figure 5.28: Front view of original as-received steel part and new wide tip composite wear part



Figure 5.29: Ceramic coated mould after removal of the finished composite part

5.2.5 MANUFACTURE OF DREDGE WIDE BUCKET LIP

Using the vacuum casting process the wide bucket lip on the suction-cutter dredge was also prepared for the production of a composite wear part. The worn part after grit blasting is shown in Figures 5.30 to 5.32.



Figure 5.30: Worn steel dredge wide bucket lip

Similar to the production of the smaller dredge bucket teeth, a steel mould was fabricated with a suitable side chute to contain the charge of white iron. The finished mould was then coated with the refractory paint, part positioned and charge weighed and placed prior to placement into the hot walled vacuum furnace, as shown in Figure 5.33. This part had a larger total finished mass of approximately 9.4kgs, compared to the smaller bucket teeth finished mass of 3.0kg.



Figure 5.31: Side view of worn steel dredge wide bucket lip



Figure 5.32: Dual attachment cavities for wide bucket lip



Figure 5.33: Wide bucket tooth lip part inserted into furnace ready to start the cycle

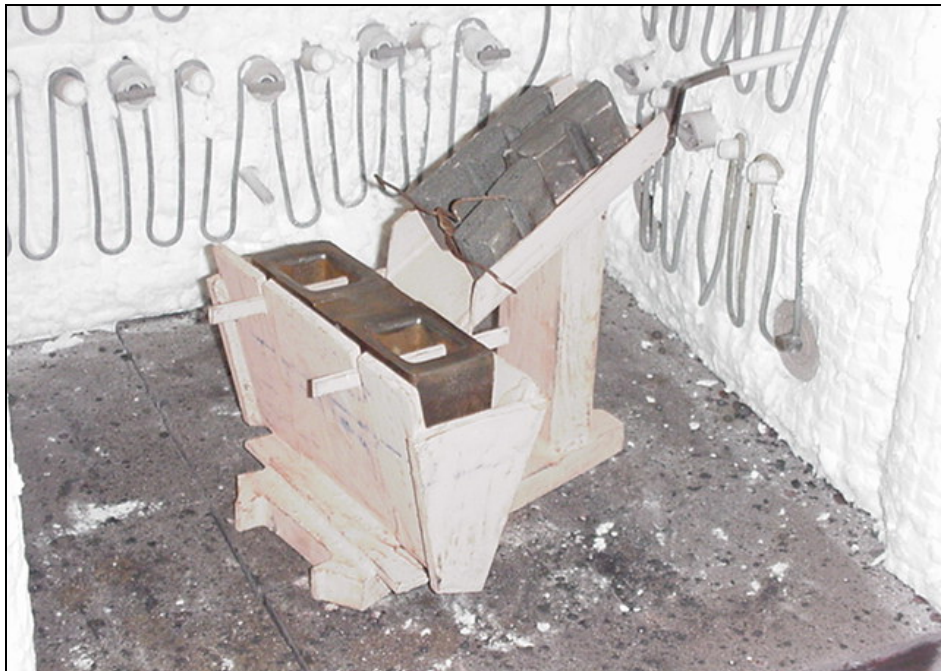


Figure 5.34: View of mould, white iron charge and steel part placed into position

The hot walled furnace cycle was then conducted based on the same procedure as used previously in Section 5.2.3 and 5.2.4. At the completion of the cycle, the mould and finished part were removed and examples of the finished part still inside the mould are shown in Figures 5.35 to 5.38.

The high quality of wetting between the white iron and the steel is highlighted in Figure 5.37. Note also from Figure 5.38 the white iron charge has fully melted and flowed down the chute, leaving essentially no residual white iron in the chute.

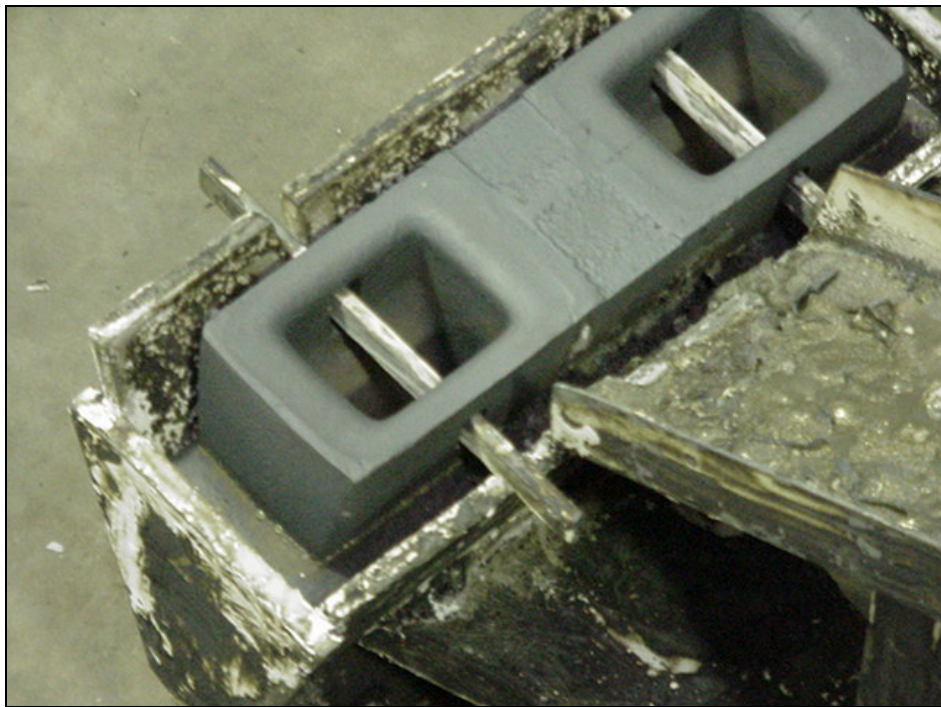


Figure 5.35: View of completed wide bucket lip still in the mould after casting

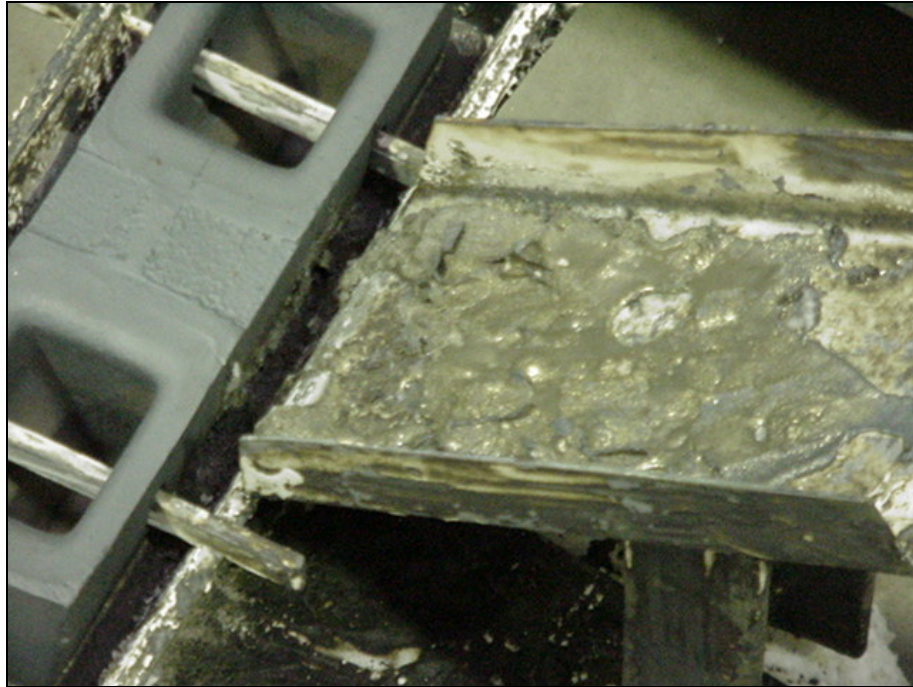


Figure 5.36: Detail view of completed wide bucket lip still in the mould after casting. Note the presence of a small amount of white iron “skin” left in the chute.

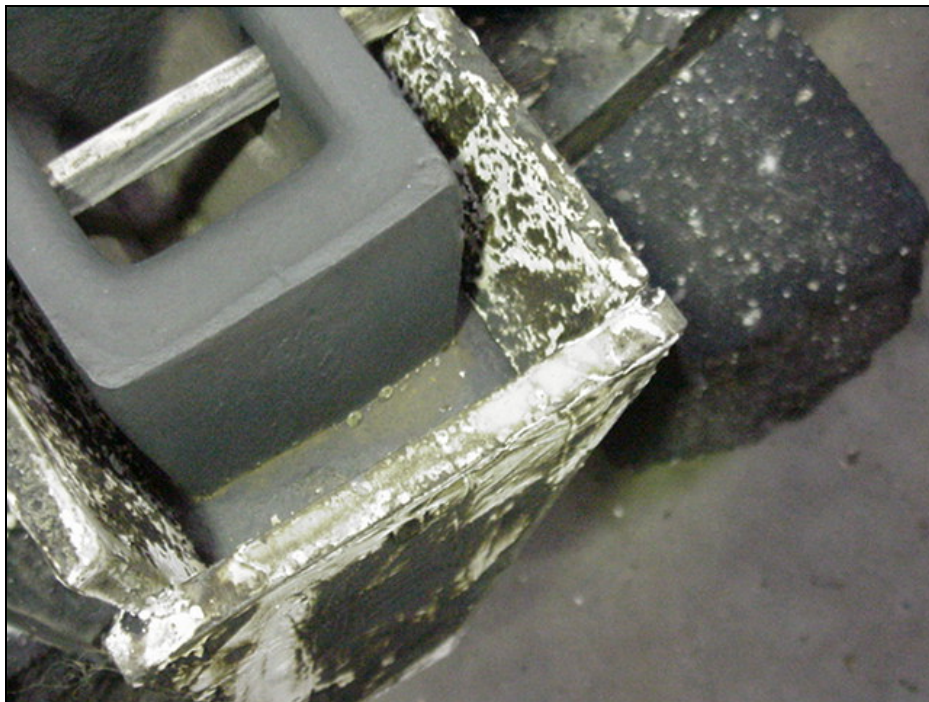


Figure 5.37: View of excellent wetting between the white iron and the steel



Figure 5.38: Side view of steel mould and composite part after removal from the furnace



Figure 5.39: Finished composite wide bucket lip after removal from the mould

The very first wide bucket lip part produced was based on a finished mass of 9.0 kg. At the completion of the test production cycle it was noted the composite white iron had not covered sufficient amount of the steel base, as can be seen in Figure 5.42, where the white iron only covers approximately 50% of the original steel part, and sections of the worn side faces can still be seen at the base of the white iron.

Subsequent production trials were run with an increased total mass of 9.40kgs, and the final result was the part shown in Figures 5.40 and 5.41.

The size of the finished composite wide bucket lip compared to the original ESCO V19TY steel parts is shown in Figure 5.43.



Figure 5.40: View of the finished composite wide bucket tooth prior to final painting



Figure 5.41: End view of wide bucket lip showing excellent bonding around the complete part



Figure 5.42: First production trial part with a final mass of 9.02kg. Subsequent cycles were adjusted for a total composite mass of 9.40kg.



Figure 5.43: Comparison of sizes of wide bucket lip composite part to ESCO V19TY bucket teeth

5.2.6 MANUFACTURE OF EXCAVATOR BUCKET TOOTH TIP

A future concept for the production of a composite white iron/steel bucket tooth was to incorporate a cavity in the original steel casting into which the white cast iron could be cast using the vacuum based process.

Excavator bucket teeth tips of the size consistent with the ESCO V71 RDX commonly used in the mining industry were cast from the chromium/molybdenum steel with a cavity as shown in Figure 5.44. The volume of the cavity was equivalent to a white iron charge of approximately 3.5kgs, and the centre rib was added to the design of the cavity to provide additional strength to the composite part.



Figure 5.44: Cast chromium/molybdenum steel bucket tooth tip with cavity to receive white iron

The cast steel tip was placed onto a furnace tray and levelled so that the white iron charge could be placed directly into the cavity. The required charge of 3.5kgs was weighed and placed into the cavity, and then the whole assembly placed into the hot walled vacuum furnace.

The furnace cycle was conducted as described previously, and after the completion of the cycle the white iron had been observed to have completely filled the cavity, as shown in Figure 5.45.

The finished part was then sectioned through the white iron/steel composite section to check the bonding and casting quality. After sectioning, no porosity in the cast white iron was observed, and full bonding had been achieved between the steel substrate and the white cast iron.



Figure 5.45: As-cast composite steel/white cast iron bucket tooth tip. Note the white iron has completely filled the cavity, and the absence of any significant surface scale.

5.2.7 MANUFACTURE OF WEAR BARS

A number of experimental wear bars were produced using the vacuum casting process, including:

- i. a segmented “chok” bar commonly used as wear protection on excavator buckets;
- ii. a 50mm x 50mm x 230mm wear bar manufactured using a wrought steel “C” section with welded end caps as the substrate/mould

The “chok” bars were produced using a ceramic coated steel mould with the white iron placed on the bottom of the mould, and the steel backing plates laid across the top. Small weights were placed onto the steel backing plates to provide sufficient downward pressure to ensure filling of the mould cavity. The mould after removal from the hot walled furnace at 1000°C is shown in Figure 5.46. The mould allowed two “chok” bars to be produced at a time, and the steel mould could be reused several times.



Figure 5.46: Hot “chok” bar mould with cast parts after removal at 1000°C from furnace

The finished composite white iron/steel “chok” bar is shown in Figures 5.47 and 5.48. Further work is required with these types of parts to refine the production and eliminate small porosity gaps along the perimeter of the samples.

Figure 5.48 shows the excellent bonding achieved between the white cast iron and the steel during the vacuum casting process.

The as-cast composite wear bar is shown in Figure 5.49. Note the surface has not been touched since casting of the white iron, and there is no evidence of scale of casting defects on the wear face.



Figure 5.47: Finished composite white iron/steel “chok” bar after casting using vacuum based process



Figure 5.48: Detail view of excellent bonding between white cast iron and steel backing plate. Some minor edge gaps are present which need to be eliminated by future modifications to the method of moulding.



Figure 5.49: As-cast composite wear bar manufactured from "C" channel with welded end caps

5.2.8 MANUFACTURE OF DEBONDING (TENSILE) TEST SAMPLE

Several debonding (tensile) test samples were manufactured based on the diagram and dimensions shown in Figure 5.50. The design was developed to provide a test sample of a convenient size for use with standard tensile test equipment, whilst allowing the composite alloy process to be used for its manufacture. The samples are a non-standard design specific to this study. The purpose of the debonding test samples was to attempt to measure the bond strength between the steel and the white cast iron.

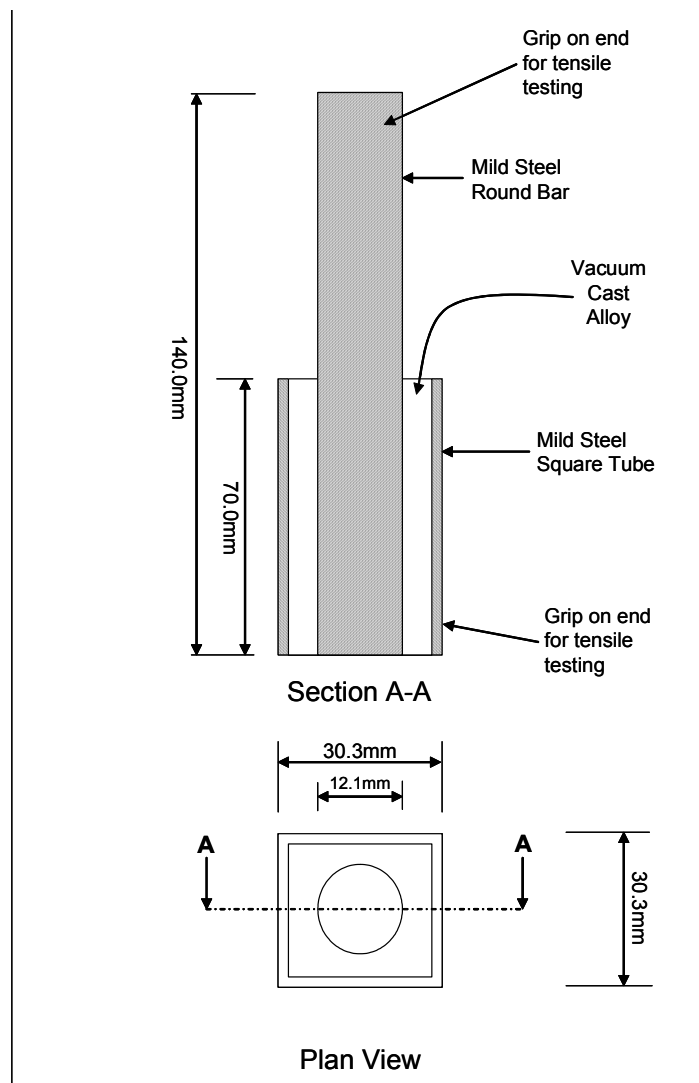


Figure 5.50: Vacuum cast composite tensile test sample dimensions

The completed debonding test samples after conducting the standard vacuum casting cycle are shown in Figures 5.51 to 5.53. A total of three samples were produced, and each sample showed excellent surface wetting between the steel and the white cast iron.

Each test sample was then attached to a standard tensile testing machine and tested under tensile load until failure. The final load at break was recorded, and the data used to determine the shear load across the contact surface area of the white cast iron to the steel.

In all three cases the tensile test samples fractured through the centre steel rod, and not through the white iron bonded area. The centre steel rod was of insufficient diameter to prevent failure prior to the bond undergoing failure. However the test data can be used to determine a minimum bond strength for the white iron to steel.



Figure 5.51: End view of completed composite debonding test sample



Figure 5.52: Composite debonding test sample



Figure 5.53: Detail of bonding/interface between centre rod, white cast iron and outer shell of composite tensile test sample

5.3 LABORATORY WEAR TESTING

Dry Sand Rubber Wheel (DSRW) wear tests according to ASTM G65-04 [66] were conducted on samples machined from the Fe-12Cr-1.6Mn-1.0Ni-0.6Si-C alloy series for variations in carbon from 2.9 to 4.3 weight %. The DSRW wear tests were all conducted compared to the same alloy composition of Cr/Mo steel used for the standard bucket teeth.

The test conditions used for the DSRW wear tests were as follows:

- Wheel Rotating Speed (rpm) = 200
- Wheel Diameter (mm) = 221.6
- Total Wheel Revolutions = 6000
- Applied Load (N) = 130
- Dead Weight (kg) = 3.75
- Abrasive Sand = Imdex 50/100 screened

Two samples of each alloy composition were abrasion tested. The results of the wear testing are provided in section 5.7.1 of this study.

5.4 DEBONDING (TENSILE) TESTING

The debonding test data is summarized in Table 5.6. Based on the average failure load of 45.7kN, the calculated minimum strength for the white iron to steel bond is 405 MPa. This value of the bond strength compares favourably with the generic strength of the white cast iron. Typical bond strengths for vacuum brazed white iron to steel samples using copper are in the order of 400 to 450MPa, and are comparable with the test data obtained in this study.

Table 5.6: Debonding (Tensile) test results for composite white cast iron/steel

Sample	Load (kgs)	Load (Newtons)	Stress (MPa)
1	4,509	44,188	391
2	4,734	46,393	410
3	4,770	46,746	413
Ave	4,671	45,776	405

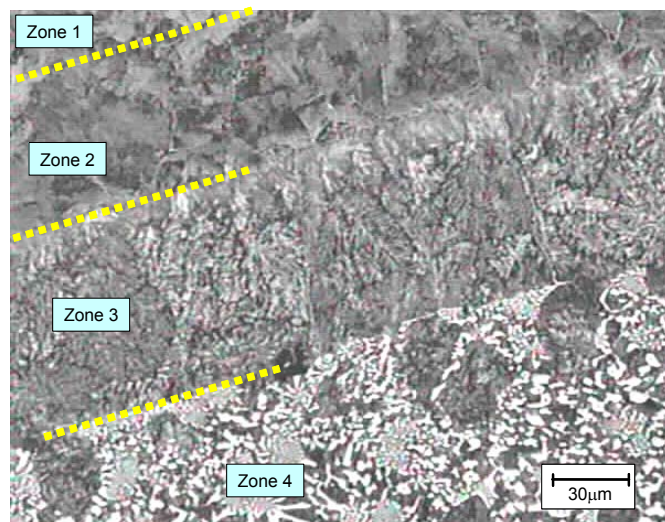
5.5 COMPOSITE WHITE IRON/STEEL MATERIAL DATA SHEET

Description: White Cast Iron and Steel Composite

Chemical Composition: (based on results from Chapter 2)

Alloy	Element (Weight %)								
	C	Si	Mn	Cr	Mo	Ni	S	P	Fe
White Cast Iron	4.1	0.6	1.6	12.0	<0.1	1.0	0.03	0.03	Bal
Cr/Mo Steel	0.35	0.6	0.9	2.3	0.3	<0.01	0.02	0.02	Bal

Microstructure: (based on analysis from Chapter 4)



White cast iron consisting of eutectic M_7C_3 carbides with M_3C carbides surrounding M_7C_3 carbide particles, with a ferrous matrix of ledeburite with retained austenite. Substrate is a medium carbon steel with ferrite and pearlite.

Mechanical & Physical Properties:

Hardness = 550 HV as-cast
Density = 7.7 g/cm^3
Bond Strength = 405 MPa (minimum)

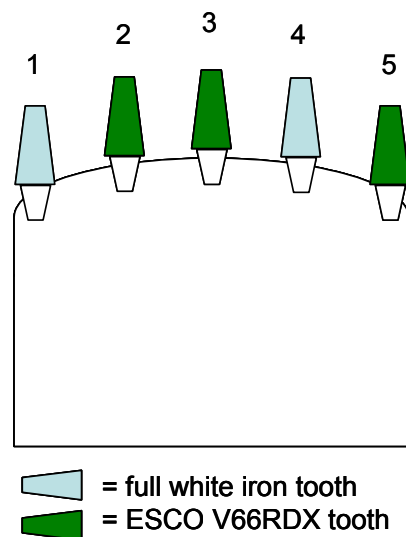
5.6 FIELD TRIALS

5.6.1 FIELD TRIAL OF FULL WHITE IRON NON-COMPOSITE BUCKET TEETH ON AN EXCAVATOR

The full white iron non-composite bucket teeth were tested on a Komatsu PC1000 excavator in operation at the Greenbushes Mine Site, south west of Perth, in Western Australia. The excavator was operating in an open pit mine, digging freshly blast rock consisting of spodumene, and having typically a very high impact load and high wear rate.

The Komatsu PC1000 bucket had five teeth located across the front of the bucket lip. Typical wear life for the standard ESCO V66RDX bucket teeth was 10-12 hours per set of five teeth.

Two trial full white iron bucket teeth were installed onto the Komatsu PC1000 bucket as shown diagrammatically in Figure 5.x.



Tooth position 1 closest to driver's cabin

Figure 5.54: Location of trial full white iron bucket teeth on Komatsu PC1000 excavator bucket

The result of the trial of the full white iron non-composite material was the two trial teeth cracked and fractured after 1 hour of operation. The cracking and fracturing confirm the brittle nature of white cast iron and the unsuitability of white cast iron for high impact applications.

5.6.2 FIELD TRIAL OF LAMINATED BUCKET TEETH ON EXCAVATOR

The single wear plate vacuum brazed bucket teeth were trialled at the Greenbushes Mine Site for the same duty as the trial described in Section 5.6.1. Two trial bucket teeth were installed against three new ESCO V66RDX bucket teeth for comparison of wear rates.

The position of the trial wear teeth on the excavator bucket are shown in Figure 5.55.

The parts were trialled for a duration of 12 hours then removed from the excavator to compare the weight loss and material remaining.

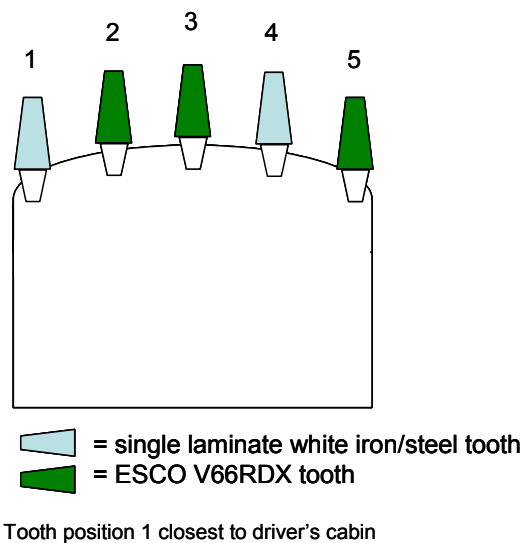


Figure 5.55: Location of trial single laminate white iron/steel bucket teeth on Komatsu PC1000 excavator bucket

The multi-laminated V71RDX sized bucket tooth was tested on an Hitachi EX1800 excavator located at the Golden Feather Mine, near Kalgoorlie, Western Australia. Typical wear life for a set of bucket teeth at this site was 100 hours. The excavator was operating in a freshly blasted area of “blue” rock, typically considered high impact and high wear.

The test position for the two multi-laminated bucket teeth are shown in Figure 5.56.

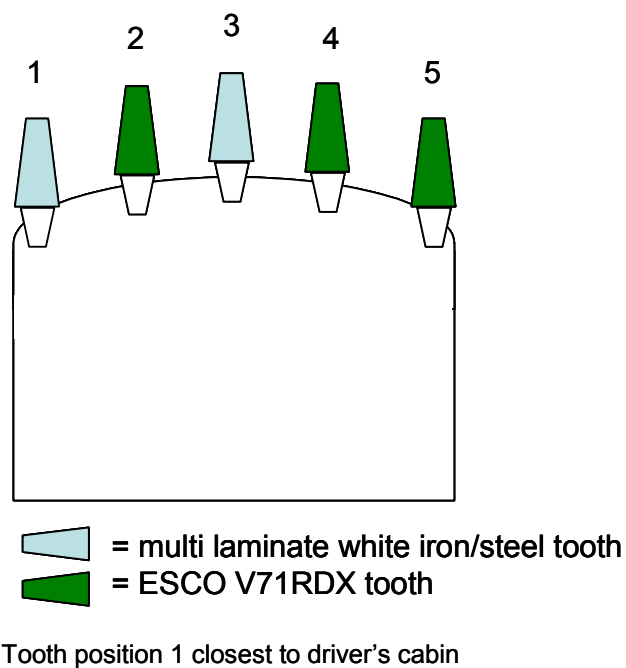


Figure 5.56: Location of trial multi-laminated white iron/steel bucket teeth on Hitachi EX1800 excavator bucket

5.6.3 FIELD TRIAL OF BUCKET TEETH IN DREDGING APPLICATIONS

The new vacuum casting process was used to manufacture a range of composite wear parts for use in mining applications. One particular trial incorporated a white iron/steel composite ground engaging tool (GET) located on a suction-cutter dredge at a mineral sands mine in Capel, Western Australia (see Figures 5.57 and 5.58).

A suction-cutter dredge has a rotary cutting head that operates in a submerged condition against the mining face. The rotary cutting head normally consists of multiple buckets which cut into the mining bed and the loose material is then commuted to the surface using a heavy duty slurry pump where the suction eye of the pump is connected to the outlet of material from the cutter head. Each of the buckets on the cutter head have a number of wear teeth to enable a satisfactory cutting action of the mining bed.

The dredge that was to be used at the Jangardup Mine, near Capel, south-west from Perth, Western Australia had a cutting head fitted with ten buckets, each fitted with a wide wear lip across the front of the bucket, and several smaller bucket teeth along the sides of the bucket. Typical wear life for a set of bucket teeth was 2 weeks operation. The dredge was mining mineral sands.

The composite wear parts manufactured in Section 5.2.3, 5.2.4 and 5.2.5 were installed on multiple buckets to compare to the operation and performance of the standard chromium/molybdenum steel components. The performance of the trial composite wear parts was monitored on a regular basis during the trial to check for possible failure and wear problems. After a period of approximately two weeks, the original steel wear parts were removed and replaced, and the trial composite wear parts were kept in service to continue the trial. This procedure was repeated until the end of the field trial.

At the completion of the field trial, the various wear parts were weighed to determine the average mass and volume loss and an overall wear rate determined based on the life of the parts.



Figure 5.57: View of suction-cutter dredge head raised from the water for maintenance.



Figure 5.58: Closer view of bucket arrangement on suction-cutter dredge head. Note wide bucket lip and smaller side bucket teeth.



Figure 5.59: Vacuum cast small composite bucket teeth trialled at Cable Sands Mine, Capel, Western Australia (New composite on left)

5.7 RESULTS AND DISCUSSION

5.7.1 LABORATORY WEAR TESTING

The results of the laboratory wear tests are shown in Table 5.7 and shown graphically in Figure 5.60 for the Fe-12Cr-1.6Mn-1.0Ni-0.6Si-C alloy series. The data presented is based on as-cast samples, and would be representative of the microstructures resulting from the standard vacuum casting cycles.

As expected, the wear test data shows a strong correlation with carbon content of the alloy and the volume loss. Based on the Dry Sand Rubber Wheel wear test results, as the carbon content increases the material volume loss decreases. The decrease in volume loss with increasing carbon would relate directly to the increase in carbide volume fraction of the alloy.

The volume loss data for the white cast irons are also less compared to the Cr/Mo steel values, and hence it would be anticipated that the white cast irons from this alloy series would have an improved wear life in the actual field conditions compared to the Cr/Mo steels.

Table 5.7: Dry Sand Rubber Wheel Wear Test Results (according to ASTM G65-04)

Fe-12Cr-1.6Mn-1.0Ni-0.6Si-C Series

Carbon	Average Mass Loss (g)	Average Volume Loss (mm ³)
2.9	0.1053	13.7
3.3	0.0891	11.4
3.7	0.0724	9.8
4.1	0.0578	7.5
4.3	0.0485	6.3
Cr/Mo Steel	0.1211	15.5

**Dry Sand Rubber Wheel Wear Test Results
Fe-12Cr-1.6Mn-1.0Ni-0.6Si-C Alloy Series**

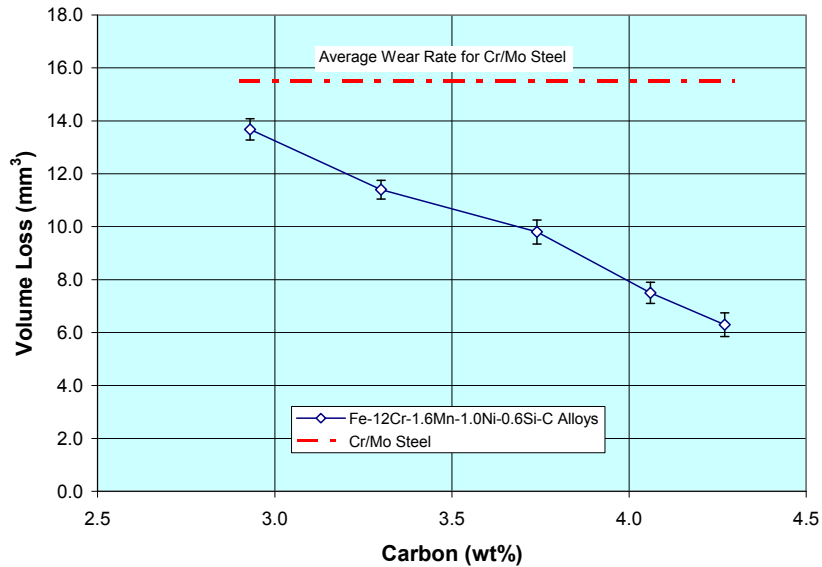


Figure 5.60: Relationship Between Carbon Content and Abrasive Wear Rate for Fe-12Cr-1.6Mn-1.0Ni-0.6Si-C Alloy Series (DSRW Test based on ASTM G65-04)

The laboratory wear test data presented in this study compares favourably with previously published data on abrasive wear testing for white cast irons, as previously discussed in Section 2 of this study. The laboratory wear testing suggests the low melting point alloy C1 having a near eutectic microstructure would provide the best wear performance under abrasive conditions. The impact properties of the high carbide volume fraction alloys would be poor compared to standard quench and temper steels.

The laboratory test data also suggests that hypoeutectic white iron compositions with low carbide volume fractions will have only minor wear life improvements compared to the standard chromium/molybdenum quench and tempered steels.

5.7.2 SUMMARY OF FULL SCALE FIELD TRIALS

The results of the initial field trials using the full white cast iron bucket teeth, and the composite white iron/steel parts produced from vacuum brazing are summarized in Table 5.8. and Table 5.9.

The use of full white cast iron bucket teeth would not be recommended for excavator applications since the impact toughness for the white iron is not sufficient to withstand the high impact conditions experienced by excavators in open pit mining operations.

Table 5.8: Summary of field trial data for full white iron and vacuum brazed wear parts, Greenbushes Mine

Site: Greenbushes Mine
Company: Sons of Gwalia
Trial Date: February-1997
Equipment: Komatsu PC1000

Description	Material	SG Alloy	Average Mass (g)			Volume Loss (mm ³)	Average Life (hrs)	Wear Rate (mm ³ /h)	Wear Rate Ratio (Comp/Steel)
			New	Worn	Loss				
ESCO V66RDX	Chrome/Moly Steel	7.8	21.00	15.4	5.60	718	12	59.8	1.00
Full White Iron Tooth	Cr27 Alloy	7.6	20.8	20.4	0.40	53	1	52.6	0.88
Vacuum Brazed Single Plate	Cr27 Alloy/Chrome/Moly Steel	7.8	21.20	16.50	4.70	603	12	50.2	0.84

Table 5.9: Summary of field trial data for full white iron and vacuum brazed wear parts, Golden Feather Mine

Site: Golden Feather
Company: Roche Mining
Trial Date: February-2000
Equipment: Hitachi EX1800

Description	Material	SG Alloy	Average Mass (g)			Volume Loss (mm ³)	Average Life (hrs)	Wear Rate (mm ³ /h)	Wear Rate Ratio (Comp/Steel)
			New	Worn	Loss				
ESCO V71RDX	Chrome/Moly Steel	7.8	44.00	22.6	21.40	2744	100	27.4	1.00
Vacuum Brazed Multi Plate	White Iron/Manganese Steel	7.8	44.60	42.90	1.70	218	10.5	20.8	0.76

NB: part fractured after 10.5 hours

The trial multi-layered composite part tested at the Golden Feather mine failed after 10.5 hours operation due to the weld failure between the sectioned steel base and the laminated tip.

The wear performance in excavator applications of the composite parts compared favourably to the steel parts, as shown in Figure 5.61 and 5.62, however the risk of failure due to cracking of the vacuum brazed composites was considered too high for satisfactory use in the mining industry.

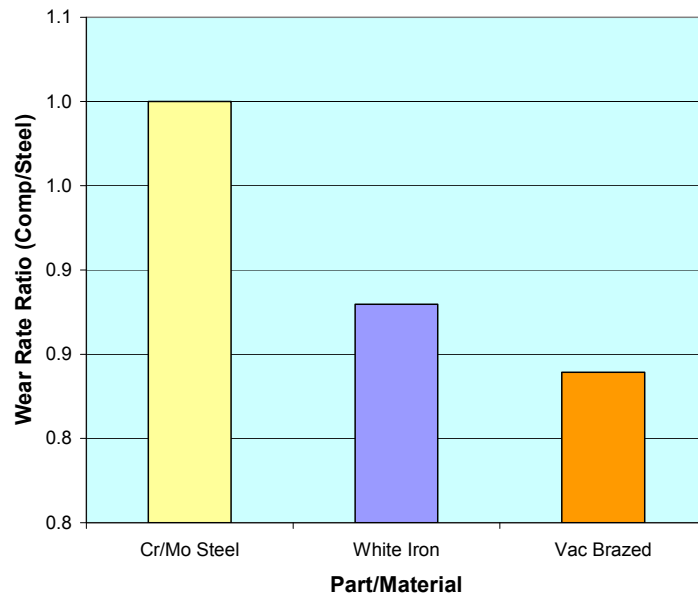


Figure 5.61: Comparative wear rates for chromium/molybdenum steel and white cast iron in excavator application (Greenbushes Mine)

The results of the field trials conducted at the Jangardup Mine dredge are shown in Table 5.10. The data clearly shows the vacuum brazed composites have significantly outperformed the original chromium/molybdenum steel components. The wear rate improvement was observed to be three to four times better compared to the original chromium/molybdenum steel.

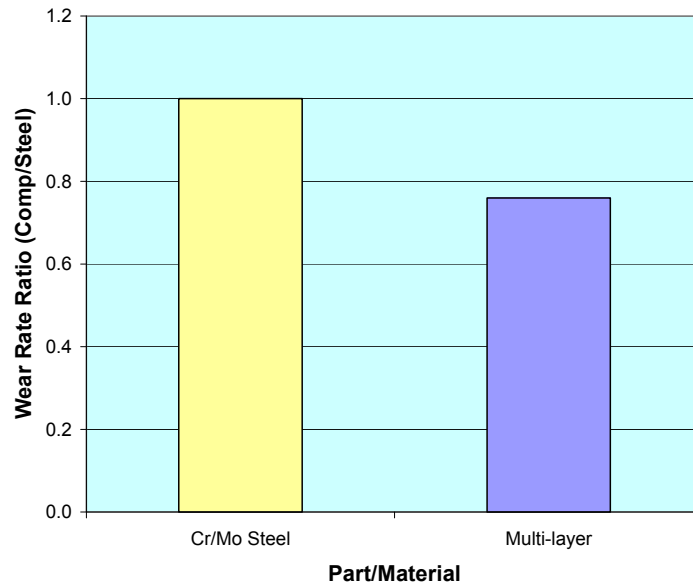


Figure 5.62: Comparative wear rates for chromium/molybdenum steel and multi-layer vacuum brazed white cast iron in excavator application (Golden Feather Mine)

Figure 5.63 shows the relative wear performance of the white iron vacuum cast composite compared to the steel. It can be seen from Figure 5.63 that the wide bucket lip experiences a significantly faster wear rate compared to the side teeth. In both examples of the field trial parts, the composite white iron/steel part has outperformed the original steel part.

Table 5.10: Summary of field trial data for composite wear parts in dredge application

Site: Jangardup Mine Site, Capel, Western Australia **Site Contact:** John Wishart
Company: Cable Sands
Trial Date: August-2001

Description	Material	SG Alloy	Average Mass (g)			Volume Loss (mm ³)	Average Life (hrs)	Wear Rate (mm ³ /h)	Wear Rate Ratio (Comp/Steel)
			New	Worn	Loss				
ESCO V19TY	Chrome/Moly Steel	7.8	2.40	1.89	0.52	66	308	0.214	1.00
Composite Bucket Tooth	Fe-12Cr-1.6Mn-1.0Ni-0.5Si-4.1C	7.6	2.98	2.32	0.66	87	1232	0.070	0.33
Wide Bucket Lip	Chrome/Moly Steel	7.8	9.37	6.76	2.61	335	308	1.086	1.00
Composite Bucket Lip	Fe-12Cr-1.6Mn-1.0Ni-0.5Si-4.1C	7.6	9.40	6.8	2.60	342	1232	0.278	0.26

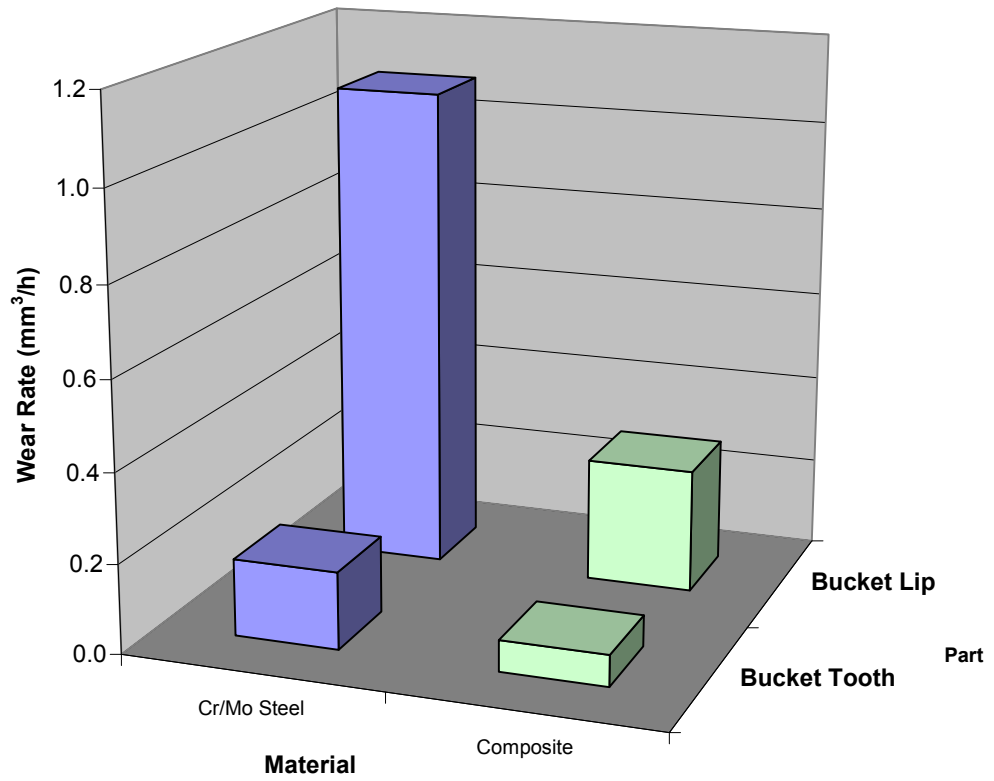


Figure 5.63: Comparison of Volumetric Wear Rates for Cr/Mo Steel and Composite Alloy Parts (Cable Sands Jangardup Mine Site)

5.8 SUMMARY OF OUTCOMES

Manufacturing and field trials have been conducted on a range of composite products to establish the potential benefit of using composite white iron/steel components in mining wear applications. The vacuum casting process has been used successfully to produce a significant volume of trial wear parts, including over forty small dredge bucket teeth and ten wide bucket lips, indicating the process is robust enough to be considered for repetitive production, and can also be adapted to manufacture a wide range of products.

The production and testing of a full white iron bucket tooth has demonstrated that parts manufactured from white iron and used in high impact applications are susceptible to fracture and premature failure. Additional attempts to manufacture laminated composites for trial had limited success due to the difficulties in integrating the composites fully within the parts, and the limited method of application these types of laminated composites provide.

No controlled impact testing has been conducted on composite samples to date due to the limited applicability of current standard impact tests (such as Charpy and Izod) with these sorts of composites. Basic drop impact tests may be of use providing sufficient energy can be applied to the samples. Fracture toughness testing using bend test methods would be difficult with composites of this nature due to the difficulty in manufacturing the test samples.

Laboratory wear tests conducted on the white cast iron used for the vacuum casting showed the alloy had the potential to offer significant wear life advantages compared to the original chromium/molybdenum steels. The trend observed from laboratory wear tests compared favourably with the measured field trial comparative wear rates.

The field trials conducted on the dredging application at the Jangardup Mine located near Capel, Western Australia, showed a significant wear life improvement for the composite white iron vacuum cast components of between 3 to 4 times compared to the original chromium/molybdenum steel parts. There was no evidence of part fracture or cracking for the composite wear parts tested on the dredge, indicating that providing satisfactory bonding occurs between the white iron and the steel, that significant impact toughness is achieved.

CHAPTER 6

A new process has been developed to enable the manufacture of composite wear parts for use in the mining industry. The new process typically involves the following:

- Placing a prepared steel substrate inside a ceramic mould
- A charge of white cast iron material is positioned inside a reservoir above the mould
- The mould and the reservoir are placed inside a vacuum heat treatment furnace
- The components are then heated to a temperature nominally 50°C above the liquidus of the white cast iron, and held at this temperature for nominally 60 minutes
- The white cast iron becomes liquid and flows from the reservoir into the ceramic mould and comes into contact with the steel substrate.
- The liquid white cast iron partially dissolves the solid steel substrate and upon cooling a full metallurgical bond is produced

This original process developed was conducted within a hot wall vacuum heat treatment furnace, with a relatively rough ultimate vacuum of 0.1mbar. When the white cast iron was molten, low vacuum chamber pressures resulted in cavitation bubbles within the white cast iron after solidification. It was found that increasing the partial pressure by the addition of an inert gas such as nitrogen to approximately 200mbar eliminated the porosity problems.

The method used for the casting of the white cast iron did not involve the use of feeders (risers), down sprues, runners and ingates. The absence of traditional casting methods has resulted in a significant increase in casting yield from normal foundry levels of nominal 60 – 65% to a high level of 95-98%. The ultimate yield of

100% can be achieved if the atmosphere control is optimum and all oxygen can be excluded.

Analysis of the interface region of the bond shows there are four unique microstructural zones formed after the casting process. Zone 4 is typically the normal as-cast microstructure of the white cast iron, with M_7C_3 carbides and quasi-peritectic M_3C carbides surrounded by a ferrous matrix typically of pearlite with some retained austenite. Zone 3 is the white cast iron material that has solidified adjacent to the bond interface, and is characterized by an essentially carbide-free microstructure with some intergranular M_3C carbides extending perpendicular to the interface boundary. Zone 2 is a carbon enriched steel region adjacent to the bond interface, where the carbon has diffused into the mild steel from the liquid high carbon white cast iron during the bonding process. Zone 2 is typically hypereutectoid steel with coarse M_3C carbides surrounding the prior austenite grain boundaries with eutectoid pearlite. Zone 1 is the original low carbon steel microstructure for the steel substrate which is typically ferrite and eutectoid pearlite.

Extensive SEM analysis and x-ray mapping has shown significant diffusion of elements occurs across the bond interface. Carbon, chromium and nickel have been observed to diffuse from the white iron into the steel substrate, whilst iron in the steel diffuses into the white iron. The bulk of the measured diffusion process occurs in the solid state. Some diffusion would occur with the liquid/solid system during the melting of the white iron, however the subsequent dissolution of the steel by the molten white cast iron removes much of this high temperature diffused layer. The diffusion of carbon, chromium and nickel were observed to follow the non-steady state diffusion process described by Fick's Second Law.

EBSM mapping of the interface has confirmed the presence of the dual carbide types within the white cast iron, and also has shown the ferrous matrix of the white

cast iron to consist of pearlite with retained austenite. The intergranular carbides within Zone 3 have been determined to be of the M_3C type.

Several wear parts have been manufactured using both the vacuum based casting process and inert gas based process for trials on Western Australian mine sites. The first trials using the vacuum process produced a 3kg white iron/steel composite bucket tooth for use on a suction-cutter dredge. The composite parts lasted 8 weeks in service compared to two weeks life for the standard quench and tempered steel parts. The wear part trials have proven the composite technology can produce a wear product with excellent performance for various applications within the mining industry, and have also shown the potential versatility of the vacuum casting process to manufacture complex shapes.

The overall success of this project has not only been in proving the initial theory behind the new bonding process, but also in further developing the technology into a robust manufacturing process, and along the way overcoming a number of barriers to achieve an extremely successful and high performing wear product for the mining industry.

The vacuum casting technology for the production of wear resistant composite parts has been successfully patented, with a full Australian Patent being awarded in March 2007 (see full patent specification and IP Australia Patent copy in Appendix B).

The vacuum casting technology was also successful in achieving the runner-up award in the Industry category of the inaugural Western Australian Inventor of the Year 2006, conducted by the Department of Industry and Resources. A copy of the WA Inventor award is attached in Appendix C.

7 FUTURE WORK

Since this is the first major study of the bonding of two alloys using a direct casting process within a vacuum or inert gas environment, there are a number of future projects that need to be considered. Suggested future projects include:

- Modelling of the dynamic interface that occurs between the liquid white cast iron and the solid steel substrate to enable the casting variables of time, temperature and pressure to be elucidated.
- Investigation of the fracture toughness and impact toughness of white cast iron/steel composites.
- Investigation of the addition of other particles such as tungsten carbide into the liquid white cast iron and understand the effects on solidification and bond quality.
- Investigation of the joining of other alloy combinations, such as titanium to aluminium, steel to aluminium, copper to aluminium.

8 REFERENCES

1. AS2027-2007, "Abrasive-resistant cast irons", Standards Australia, 2007
2. G.L.F. Powell and P.G. Lloyd, "A Deep Etching Technique for the Examination of the Carbide of High Chromium Cast Iron in a Scanning Electron Microscope", *Metallography*, Vol 14, No 1, pp 37 - 46, 1980.
3. G.L.F. Powell and P.G. Lloyd, "A Deep Etching Technique for the Examination of the Carbide of High Chromium Cast Iron in a Scanning Electron Microscope", *Metallography*, Vol 14, pp 271 - 274, 1981.
4. H.S. Avery, "The Measurement of Wear Resistance", *Wear*, Vol 4, pp 427-449, 1961.
5. K. Zum Gahr, "Microstructure and Wear of Materials", Tribology Series, Vol 10, Elsevier Press 1987.
6. P.J. Mutton, "Abrasion Resistant Materials for the Australian Minerals Industry", AMIRA HANDBOOK, 1988.
7. J.T. Burwell and C.D. Strange, "On the Empirical Laws of Adhesive Wear", *J App Phys*, Vol 23, pp 18 - 28, 1952.
8. S. Jahanmir, "On the Wear Mechanisms and Wear Equations", *Fundamentals of Tribology*, MIT Press, Cambridge, pp 455 - 467, 1980.
9. D. Godfrey, "Diagnoses of Wear Mechanisms", *Wear Control Handbook*, ASME, New York, pp 283 - 311, 1980.
10. S.L. Rice, "A Review of Wear Mechanisms and Related Topics", *Wear Control Handbook*, ASME, New York, pp 469 - 476, 1980.
11. DIN 50320, Verschleib - Begriffe, Analyse von Verschleibvorgangen, Gleiderung des Verschleibgebietes, Beuth Verlag, Berlin, 1979.
12. ASTM G40-83, "Standard Terminology Relating to Erosion and Wear", *Annual Book of ASTM Standards*, Vol 03.02, 1985.
13. J.D. Watson, P.J. Mutton and I.R. Sare, "Abrasive Wear of White Cast Irons", *Metals Forum*, Vol 3, No 1, 1980.

14. M.C. Roco, P. Nair and G.R. Addie, "Test Approach for Dense Slurry Erosion", *Slurry Erosion: Uses, Applications and Test Methods*, ASTM STP 940, pp 185 - 210, 1987.
15. P.G. Huggett and C.I. Walker "Development of Wear Test to Simulate Slurry Erosion", *Hydrotransport 11*, Stratford-upon-Avon, UK, pp 495-506, October 1988.
16. W. Day, "Carbide Morphology in Alloy White Iron", School Chemical Engineering, Georgia Institute of Technology, March 1982.
17. G.F. Truscott, "Wear in Pumps and Pipelines", BHRa Information Series No 1, *Wear in Slurry Pipelines*, 1980.
18. W.A. Stauffer, "The Abrasion of Hydraulic Plant by Sandy Water", *CE Trans 1799*, *Schweizer Archiv fur Angewandte Wissenschaft und Technik*, Vol 24, Nos 7/8, pp 3-30, 1958.
19. I.R. Sare, "Abrasion Resistance and Fracture Toughness of White Cast Irons", *Metals Technology*, pp 412-419, November 1979.
20. M.A. Moore, "Abrasive Wear", *Fundamentals of Friction and Wear of Materials*, ASM, 1980.
21. S.S. Aptekar and T.H. Kosel, "Erosion of White Cast Irons and Stellite", *International Conference on Wear of Materials*, Vancouver, pp 677-686, 1985.
22. A. Ball, "The Mechanisms of Wear, and the Performance of Engineering Materials", *JS Afr Inst Min Metall*, Vol 86, No 1, pp 1-13, January 1986.
23. A.G. Guy and J.J. Hren "Elements of Physical Metallurgy", 3rd Edition, Adison-Wesley, 1974.
24. C.J. Heathcock, "Cavitation Erosion Damage of Materials", PhD Thesis University of Cape Town, 1980.
25. C.J. Heathcock, B.E. Protheroe, A. Ball, "The Influence of Microstructure on the Cavitation Erosion of Materials", *Fifth Int Conf on the Strength of Metals and Alloys*, Aachen, 1979.
26. K.F. Dolman, "Alloy Development: Shredder Hammer Tips", *Proceedings of Australian Society of Sugar Cane Technologists*, 1983.

27. T. Foley and E. Levy, "The Erosion of Heat Treated Steels", *Wear*, Vol 91, pp 45-64, 1983.
28. J.T.H. Pearce, "Abrasive Wear Behaviour of Alloy Cast Irons", *British Foundryman*, pp 13-23, January 1985.
29. L.P. McCabe, G.A. Sargent, H Conrad, "Effect of Microstructure on the Erosion of Steel by Solid Particles", *Wear*, Vol 105, pp 257-277, 1985.
30. R.B. Gundlach and J.L. Parkes, "Influence of Abrasive Hardness on Wear Resistance of High Chromium White Irons", *Wear* Vol 46, pp 97-108, 1978.
31. K. Bungardt, E. Kunze and E. Horne, *Arch. Eisenhüttenwes.*, Vol. 29, pp 193-203, 1958.
32. R.S. Jackson, "The Austenite Liquidus Surface and Constitutional Diagram for the Fe-Cr-C Metastable System", *Journal of the Iron and Steel Institute*, pp 163-167, February 1970.
33. W.R. Thorpe & B. Chico, "The Fe-Rich Corner of the Metastable C-Cr-Fe Liquidus Surface", *Metallurgical Transactions*, Vol. 16A, pp 1541-1549, September 1985.
34. Thermo-Calc TCW3 Software, 2005, Foundation of Computational Thermodynamics, Stockholm, Sweden.
35. C.G. Schon and A. Sinatora, "Simulation of solidification paths in high chromium white cast irons for wear applications", *CALPHAD*, 1998, Vol 22, pp437-448.
36. H. Du and J. E. Morral, "Prediction of the lowest melting point eutectic in the Fe-Cr-Mo-V-C system", *Jour. of Alloys and Compounds*, 1997, Vol 247, pp122-127.
37. T. Gomez-Acebo, M. Sarasola and F. Castro, "Systematic search of low melting point alloys in the Fe-Cr-Mn-Mo-C system", *CALPHAD*, 2003, Vol 27, pp325-334.
38. T. Gomez-Acebo, Calculation performed on request based on correspondence, 2005.
39. FactSage Computer Software, 2005, Thermfact and GTT-Technologies
40. P.G. Huggett, "The relationship between microstructure and erosive wear for white cast irons", MSc Thesis, University of technology, Sydney, 1992.
41. ImageTool V3.0 Computer Software, University of Texas Health Science Centre, San Antonio, 2002.

42. M. Schwartz, "Modern Metal Joining Techniques", Wiley Interscience, 1969
43. G. Drach, "Application of Vacuum Brazing as a Metal Joining Technique", Vacuum, vol 24, number 2, pp95-99, Feb 1974
44. M.J. Fletcher, "Vacuum Brazing", Engineering (London), vol 223, number 6, ppI-VIII, June 1983
45. B. Edenhofer and J.W. Bouwman, "Vacuum Heat Treatment", Steel Heat Treatment Handbook, pp483-525, 1997
46. T. Yoshida and H. Ohmura, "Dissolution and Deposit of Base Metal in Dissimilar Carbon Steel Brazing", Welding Journal, vol 59, number 10, pp278-282, October 1980
47. T. Yoshida and H. Ohmura, "Dissolution and Deposit of Base Metal in Dissimilar Metal Brazing", Welding Journal, vol 64, number 1, pp1-12, January 1985
48. I.V. Etchells and P.M. Roberts, "Brazing Furnaces", Welding Metal Fabrication, vol 59, number 6, pp302-312, July 1991
49. G.S.A. Shawki and A.A.S. El-Sabbagh, "Shear Strength of Brazed and Soldered Joints", Welding Journal, vol 54, pp276-279, August 1975
50. B.K. Arnold, T. Heijkoop, P.G. Lloyd, G. Rubenis and I.R. Sare, "Wear of cast-bonded components in a coal pulveriser mill", Wear, 1997, Vol 203-204, pp663-670.
51. I.R. Sare, I.D. Henderson, T. Heijkoop, M.R. Bosworth, R.E. Aspin and B.K. Arnold, US Patents 4,635,701, 1987 and 4,953,612, 1990
52. R. Wuhrer, K. Moran and L. Moran, "Characterisation of materials through x-ray mapping", Materials Forum, 2006, Vol 30, pp63-70
53. R. Wuhrer and K. Moran, "Representation of microstructures through rapid x-ray mapping", Materials Australia, 2005, Vol 38, pp13-15
54. K. Moran and R. Wuhrer, "X-ray mapping and interpretation of scatter diagrams", Microchimica Acta, 2006, Vol 155, pp209-217

55. K. Moran and R. Wuhrer, "Quantitative bulk and trace element x-ray mapping using multiple detectors", *Microchimica Acta*, 2006, Vol 155, pp59-66
56. J.I. Goldstein, D.E. Newbury, P. Echlin, D.C. Joy, A.D. Romig Jr, C.E. Lyman, C. Fiori and E. Lifshin, "Scanning electron microscopy and x-ray microanalysis", 3rd Ed, Kluwer, Academic Plenum, New York, 2003.
57. K. Moran, In-house testing, Moran Scientific, 2005
58. Moran Scientific EDS, WDS and XRM Analysis Software, Moran Scientific, Goulburn, NSW, 2005.
59. P. Trimby, "ESBD General Introduction", HKL Technology ApS Publication, 2005, Denmark.
60. J.H. Brophy, R.M. Rose and J. Wulff, "The structure and properties of materials – Volume 2 – Thermodynamics of structure", John Wiley & Sons, 1964.
61. I.R. Sare, J.I. Mardel, A.J. Hill, "Wear-resistant metallic and elastomeric materials in the mining and mineral processing industries – an overview", *Wear*, 2001, Vol 250, pp1-10
62. L.Xu, C. Vose, and D. StJohn, "Abrasive wear study of selected white cast irons as liner materials for the mining industry", *Wear*, 1993, Vol 162-164, pp820-832.
63. K.M. Mashloosh, F.. Akbasoglu and T.S. Eyre, "Wear of digger teeth", I Mech E Conference Publications, 1984, pp29-34.
64. ASTM G132-96, "Standard test method for pin abrasion testing", ASTM International 2001
65. M. Matsunaga, Y. Ito and H. Kobayashi, "Wear test of bucket teeth", Electric Power Research Institute (Report) 1979, pp 336-342
66. ASTM G65-04, "Standard Test Method for Measuring Abrasion Using the Dry Sand/Rubber Wheel Apparatus", ASTM International, 2004
67. J.E. Fernandez, R. Vijande, R. Tucho, J. Rodriguez and A. Martin, "Materials selection to excavator teeth in mining industry", *Wear*, 2001, Vol 250, pp11-18.

68. V.A. Polovinko and A.I. Fedulov, "Bulk strengthening of excavator teeth with hard alloys", J. Mining Science, 1993, Vol 29, pp420-424
69. V.A. Polovinko and A.I. Fedulov, "Wear of a surface coating on an excavator tooth and development of its rational parameters", J. Mining Science, 1993, Vol 29, pp341-346
70. V.A. Polovinko and A.I. Fedulov, "Abrasive wear of excavator teeth", J. Mining Science, 1993, Vol 29, pp48-51.
71. O. Vingsbo, "Single pass pendulum grooving – A technique for abrasive testing", Wear, 1984, Vol 100, pp489-502
72. U. Bryggman, S. Hogmark and O. Vingsbo, "Prediction of gouging abrasion resistance of steel by pendulum grooving and other laboratory test methods", Wear, 1987, Vol 115, pp203-213
73. J. Liu, S. Li, Y. Man, "Wear resistance of Ni-hard 4 and high chromium cast iron re-evaluated", Wear, 1993, Vol 166, pp37-40
74. I.R. Sare, B.K. Arnold, G.A. Dunlop, and P.G. Lloyd, "Repeated impact-abrasion testing of alloy white cast irons", Wear, 1993, Vol 162-164, pp790-901

Appendix A: Basic Theory of Diffusion

Diffusion is the process whereby elements migrate between two materials (called a diffusion couple) to even out concentration gradients between the diffusion couple. The main result of diffusion is a normalization of the high concentration element to the low concentration material, and is a thermodynamically driven process. The migration of the alloying elements at the atomic scale erases free energy gradients within the material [60], and in all cases is activated by thermal energy.

The mathematical relationship in which the concentration differences reduce is expressed in Fick's First and Second Laws. Fick's First Law represents the change in concentration gradient across a diffusion couple interface under steady state conditions, and is shown in Equation A.1 [60].

$$J_x = -D \frac{dC}{dx} \quad \text{Equ A.1}$$

Where: J_x = flux of diffusing species
 D = diffusivity or diffusion coefficient
 $\frac{dC}{dx}$ = concentration gradient

The more common form of diffusion is where the concentration changes with time, and is represented by Fick's Second Law for non-steady state diffusion [60], as shown in Equation A.2.

$$\frac{dC_x}{dt} = \frac{d}{dx} \left[D \frac{dC_x}{dx} \right] \quad \text{Equ A.2}$$

Where: C_x = concentration of diffusing species that varies with distance x , and time t , and diffusivity D

Solving the differential equation A.2 produces the more common equation [60]:

$$\frac{C_x - C_0}{C_s - C_0} = 1 - \operatorname{erfc}\left(\frac{x}{2\sqrt{Dt}}\right) \quad \text{Equ A.3}$$

Where: C_s = surface concentration
 C_0 = concentration of semi-infinite solid
 $\operatorname{erfc}(y)$ = Gaussian Error Function (see Figure 1)

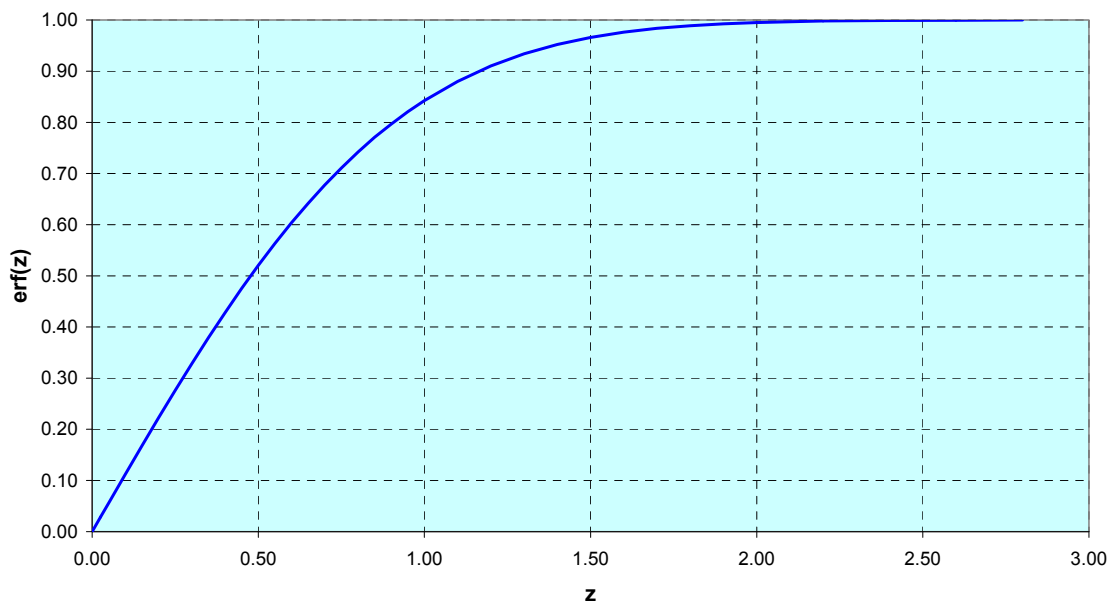


Figure 1: Gaussian error function for non-steady state diffusion

Through the use of measurements of concentration gradients on diffusion couples at different temperatures, it is possible to determine the diffusivity D at these temperatures using the Gaussian Error Function. The diffusivity has been found to follow the Arrhenius equation as shown in Equation A.4 [60].

$$D = D_0 \cdot \exp\left[\frac{-Q_d}{RT}\right] \quad \text{Equ A.4}$$

Where:

D_0	=	temperature independent pre-exponential, m^2/s
Q_d	=	activation energy for diffusion, J/mol
R	=	Gas constant, $8.314 \text{ J}\cdot\text{mol}^{-1}\cdot\text{K}^{-1}$
T	=	Temperature, Kelvin

Appendix B: IP Australia Full Patent Specification for the Vacuum Casting Process



Australian Government

IP Australia

LETTERS PATENT

STANDARD PATENT

2001277412

I, Fatima Beattie, the Commissioner of Patents, grant a Standard Patent with the following particulars:

Name and Address of Patentee(s):

Paul Graeme Huggett
16 Ferntree Close, Thornlie, WA, 6108, Australia

Name of Actual Inventor(s):

Huggett, Paul Graeme.

Title of Invention:

A method of manufacturing metallic composites and composites produced thereby

Term of Letters Patent:

Twenty years from 9 August 2001

Priority Details :

<i>Number</i>	<i>Date</i>	<i>Filed with</i>
PQ9334	10 August 2000	AU



Dated this 5th day of March 2007

Production Note:
Signature removed prior to publication.

PATENTS ACT 1990

Fatima Beattie
Commissioner of Patents

(12) STANDARD PATENT
(19) AUSTRALIAN PATENT OFFICE

(11) Application No. **AU 2001277412 B2**

(54) Title
A method of manufacturing metallic composites and composites produced thereby

(51) International Patent Classification(s)
B22D 19/08 (2006.01) **B22D 19/06** (2006.01)
B22D 18/06 (2006.01) **B22D 25/08** (2006.01)
B22D 19/04 (2006.01)

(21) Application No: **2001277412** (22) Date of Filing: **2001.08.09**

(87) WIPO No: **WO02/13996**

(30) Priority Data

(31) Number	(32) Date	(33) Country
PQ9334	2000.08.10	AU

(43) Publication Date: **2002.02.25**
(43) Publication Journal Date: **2002.05.23**
(44) Accepted Journal Date: **2006.11.16**

(71) Applicant(s)
Paul Graeme Huggett

(72) Inventor(s)
Huggett, Paul Graeme

(74) Agent / Attorney
Watermark Patent & Trademark Attorneys, The Glasshouse 290 Burwood Road, Hawthorn, VIC, 3122

Appendix C: Western Australia Inventor of the Year 2006 – Runner Up Award

